Global deformation and internal structure of Venus in the frame of its exploration missions

Christelle Saliby

UNIVERSITÉ CÔTE D'AZUR

ÉCOLE DOCTORALE
SCIENCES FONDAMENTALES ET APPLIQUÉES

THÈSE DE DOCTORAT

Déformation globale et structure interne de Vénus dans le cadre de ses missions d'exploration

Christelle SALIBY

UMR Géoazur

Présentée en vue de l'obtention du grade de docteur en Sciences de la Planète et de l'Univers
de l'Université Côte d'Azur.
Dirigée par :
Agnès Fienga
Co-encadrée par :
Anthony Mémin
Soutenue le: 10 Novembre 2022

Devant le jury, composé de :
Karin Sigloch, **présidente du jury**, Directrice de recherche, CNRS Géoazur
Nicolas Coltice, Professeur, PSL
Alexandre Correia, Professeur, Université de Coimbra
Mark Wieczorek, Directeur de recherche, OCA-Lagrange
Hauke Hussmann, Directeur de recherche, DLR
Nicolas Rambaux, Maître de conférences, Sorbonne Université
Giorgio Spada, Professeur, Université de Bologne

Déformation globale et structure interne de Vénus dans le cadre de ses missions d'exploration

Jury :

Présidente du jury

Karin, Sigloch, Directrice de recherche, CNRS Géoazur, Université Côte d'Azur

Rapporteurs

Nicolas Coltice, Professeur, Paris Science et Lettres (PSL), laboratoire de Géologie

Alexandre Correia, Professeur, Université de Coimbra

Examinateurs

Mark Wieczorek, Directeur de recherche, Observatoire de la Côte d'Azur (OCA), Lagrange

Hauke Hussmann, Directeur de recherche, Centre allemand pour l'aéronautique et l'astronautique (DLR), Berlin

Nicolas, Rambaux, Maître de conférence, Sorbonne Université

Giorgio Spada, Professeur, Université de Bologne

Global deformation and internal structure of Venus in the frame of its exploration missions

Résumé

La planète Vénus est souvent appelée la sœur de la Terre car elle a un rayon et une densité similaires. La structure interne des deux planètes est donc supposée similaire avec un noyau riche en fer, un manteau de silicate de magnésium et une croûte de silicate. Malgré ces similitudes, Vénus n'a pas de tectonique des plaques et de champ magnétique interne. Son atmosphère est épaisse, dense et riche en CO_2. Vénus a également une température et une pression de surface élevées de 737 K et 93 bars, respectivement. Les connaissances sur Vénus sont basées sur sa masse, son rayon, sa température de surface, sa topographie et son champ de gravité. De nombreuses informations sont encore inconnues comme la structure de son noyau, la viscosité du manteau et le degré de son activité issue des panaches du manteau. Cette planète est intéressante car elle a évolué très différemment de sa planète sœur et des indices récentes d'activité volcanique ont été observées. Dans le cadre des futures missions d'exploration de Vénus EnVision et VERITAS, nous étudions la structure interne de la planète et évaluons la détection de son activité géophysique.

Tout d'abord, nous utilisons la masse, le moment d'inertie, le nombre de marée Love k_2 et une plage attendue du facteur de qualité Q dérivé des observations géophysiques et géodésiques pour sélectionner, en utilisant une approche Monte-Carlo, les profiles probables des modèles de Vénus. Les modèles sélectionnés constitués de quatre ou cinq couches sont des descriptions radiales des paramètres rhéologiques de Vénus. Nos modèles sélectionnés montrent que des contrastes significatifs de viscosité existent entre le manteau supérieur et le manteau inférieur et favorisent un noyau sans sulfur. Deuxièmement, nous estimons l'effet d'une activité sismique sur le déplacement de surface et la variation de gravité. Pour ce faire, nous supposons l'occurrence d'un rifting sur Vénus de la même géométrie et de la même magnitude que l'événement sismique de 2005 de Manda Hararo-Dabbahu dans le système de rift Est-Africain sur Terre. Après avoir validé notre calcul pour la Terre, nous appliquons le même modèle de

dip-slip sur un modèle de Vénus et calculons les rebonds cosismiques et post-sismiques. Nous montrons qu'avec les futures mesures d'altimétrie des missions EnVision et VERITAS, les fractures sur Vénus seront mieux cartographiées et donc plus d'informations sur son activité géologique seront déduites. De plus, la relaxation de surface après un événement sismique sera observée avec Repeat Pass Interferometry (RPI) effectuée avec VERITAS qui donnera possiblement des indications sur la magnitude et la profondeur d'une dislocation sismique.

Mots clés : Vénus; géophysique planétaire; structure interne; rebond sismique

Abstract

The planet Venus is called the twin sister of the Earth since it has a similar radius and density. The internal structure of the two planets are therefore assumed to be close with an iron rich core, a magnesium silicate mantle and a silicate crust. Despite these similarities Venus lacks plate tectonics and an internal magnetic field. Its atmosphere is thick, dense and rich in CO_2. Venus also has high surface temperature and pressure of 737 K and 93 bars, respectively. The known facts about Venus are drawn from its mass, radius, surface temperature, topography and gravity field. Many information are still unknown as its core structure, mantle viscosity and extent of its activity driven from mantle plumes. This planet is of interest since it evolved very differently from its twin planet and recent proof of volcanic activity have been observed. In the frame of the future Venus exploration missions EnVision and VERITAS, we investigate the internal structure of the planet and assess the detection of its geophysical activity.

Firstly, we use the mass, the moment of inertia, the tidal Love number k_2 and an expected range of the quality factor Q derived from geophysical and geodetical observations to select, using a Monte-Carlo approach, the most probable interior models of Venus. The selected models made of four or five layers are radial descriptions of Venus rheological parameters. Our selected models show that significant contrasts in the viscosity are required between the upper mantle and the lower mantle and additionally favor a sulfur free core. Secondly, we estimate the effect of a Venus-quake on the surface displacement and gravity variation. To do so we suppose the occurrence of a dip-slip rifting on Venus of the same geometry and magnitude as the 2005 Manda Hararo-Dabbahu seismic event in the East-African rift system on Earth. After validating our computation for the Earth, we apply the same dip-slip model on a profile of Venus and calculate the coseismic and postseimic rebounds. We show that, with future EnVision and VERITAS altimetry data, the rifts on Venus will be better mapped and therefore more information on its geological activity might be obtained. Additionally, the

surface relaxation after a seismic event will be observed with Repeat Pass Interferometry (RPI) performed with VERITAS which will possibly give indications on the magnitude and depth of a seismic dislocation.

Keywords : Venus; planetary geophysics; internal structure; seismic rebound

Acknowledgments

I am grateful to my supervisors Agnes Fienga and Anthony Memin who made this PhD achievable. I thank them for their patience and help in my work. As my supervisors in my Master's degree and PhD, they have been a part of my guiding and tutoring in research.

I would like to extend my sincere thanks to Giorgio Spada and Daniele Melini who were an integral part of this work. In addition to providing the codes, they partook in discussions and answered questions that were crucial to complete the required tasks.

I thank the members of the jury for the time they provided to participate in this PhD defense despite their busy schedule. Many thanks to Nicolas Coltice and Alexandre Correia for accepting to be the reporters.

My warmest gratitude goes to my family: my parents Elias and Micheline and my sisters Maria, Perla and Rachelle. Finally, I could not have undertaken this journey without my cousin Sammy who is like a brother to me and has been my number one supporter since day one.

Contents

List of Figures

List of Tables

Abbreviations

The following abbreviations are used in this manuscript:

A: Asal-Ghoubbet rift

AL: Alayta volcano

ALMA: The plAnetary Love nuMbers cAlculator

ASTRA: A poSTseismic Rebound cAlculator

BAT: Beta-Atla-Themis

C: Carbon

CO_2: Carbon dioxide

EA: Erta'Ale volcano

EARS: East African Rift system

ESA: European Space Agency

Fe: Iron

GPS: Global Positioning System

GRACE: Gravity Recovery and Climate Experiment

INSAR: Interferometric Synthetic Aperture Radar

K: Potassium

LLN: Load Love number

LN: Love numbers

MER: Main Ethiopian Rift

MH: Manda Hararo volcanic complex

MH: Manda Hararo Goba'Ad rift

MI: Manda Inakir rift

Mg: Magnesium

N: Nitrogen

NASA: National Aeronautics and Space Administration

O: Oxygen

PREM: Preliminary Reference Earth Model

PVO: Pioneer Venus Orbiter

S: Sulfur

SAR: Synthetic Aperture Radar

SO_2: Sulphur dioxide

SPOT: Satellite for observation of Earth

Si: Silicate

T: Tadjoura region

TA: Tat'Ali volcano

TABOO: A posT glAcial reBOund calculatOr

TLN: Tidal Love number

Th: Thorium

U: Uranium

VERITAS: Venus Emissivity, Radio science, INSAR, Topography And Spectroscopy

VEx: Venus Express

VIRTIS: Visible and Infrared Thermal Imaging Spectrometer

VISAR: Venus Interferometric Synthetic Aperture Radar

VMC: Venus Monitoring Camera

VNM: Viscoelastic normal-modes

VenSAR: Venus Synthetic Aperture Radar

Symbols

The following symbols are used in this manuscript:

β Andrade's law creep amplitude

α Andrade's law creep duration

γ Angle divergence from the North

$\mathbf{F}$ Body forces tensor per unit volume

χ^2 Chi-squared distribution

U Deforming potential

ρ Density

d Depth

δ Dirac delta distribution

$\overrightarrow{d}$ Displacement vector

R_E Earth radius

e Exponential constant/Euler's number

U_1 External deforming potential

μ First Lamé constant/rigidity

F Forcing function

ν Frequency

M_g Geometric moment

g Gravity

n Harmonic degree

H Heaviside function

I Identity tensor

i Imaginary unit

K Incompressibility/bulk modulus

ϕ Incremental potential

U_2 Internal response potential

$\mathcal{L}^{-1}$ Inverse Laplace transform

$\mathcal{L}$ Laplace transform

φ Latitude

θ Longitude

M Mass

C Moment of inertia

MoI/$\tilde{C}$ Normalized moment of interia

ϵ Phase lag

P Pressure

V_P Primary (P) seismic wave propagation velocity

W Radial deformation

$\overrightarrow{d_r}$ Radial displacement vector

r Radius (or radial boundary) in a planet

p Rupture points number

λ Second Lamé constant

V_S Secondary (S) seismic wave propagation velocity

M_0 Seismic moment

$\vec{p}$ Source boundary conditions

ε Strain tensor

$\vec{b}$ Surface boundary conditions

$\mathbf{T}$ Surface forces/stress tensor

S Surface harmonic

R Surface radius of a planet

X Tangential deformation

$\overrightarrow{d_t}$ Tangential displacement vector

T Temperature

Γ The gamma function

τ Tidal period

ω Tidal frequency

t Time

σ Uncertainty

$\mathbf{e}$ Unit vector

G Universal gravitational constant

Δ Variation/difference

$\overrightarrow{v}$ Velocity vector

M_V Venus mass

R_V Venus radius

η Viscosity

V Volume

Introduction

The planet Venus is the closest planet to the Earth and is similar to it in density and size, both being only 5% smaller for Venus than its neighboring planet. Despite these similarities Venus evolved differently than the Earth. The most notable differences are the lack of plate tectonics and an internal magnetic field in Venus. Its atmosphere is approximately one hundred times denser than that of the Earth, rich in CO_2 and almost lacks H_2O. These discrepancies indicate that Venus and the Earth have different internal structures hence have probably evolved differently. The interior of Venus can be constrained with its global properties (radius, mass and distance to the Sun) and geophysical data such as the topography and the gravity field. The topography gives insight on its surface deformation and the gravity field provides its global deformation due to tidal forces from the Sun. The topography and gravity field of Venus have been most recently mapped by Magellan and Pioneer Venus orbiter (hereafter PVO). Furthermore, proof of present volcanic activity have been detected from thermal emissivity maps of Venus Express (hereafter VEx) [Shalygin et al., 2015; Stofan et al., 2016]. The surface temperature of Venus is 737 K which is the highest of the Solar System planets and its surface pressure is of 93 bars. The high surface temperature and pressure might cause the crust to be more ductile than that of the Earth, therefore more resistant to deformation. Magellan and VEx missions provided the currently best topography, thermal emissivity and gravity field data. There is no indication that Venus has plate tectonics [Crameri and Kaus, 2010; Bercovici and Ricard, 2014], its geological activity and surface deformation are caused by mantle plumes approaching the surface. Despite new information from Magellan and VEx several questions have not been answered yet, such as what is the extent of the activity of Venus? What is its internal structure? Why did Venus evolve so differently than the Earth? Future NASA and ESA Venus exploration missions VERITAS and EnVision [Ghail et al., 2017; Smrekar et al., 2020] aim to answer these questions and several more by mapping with a better

resolution the topography and the thermal emissivity as well as the gravity field. We aim to better understand the inner structure of Venus and assess the detection of its geophysical activity. Therefore we first make constrains on the internal structure of Venus with already estimated parameters. Then we estimate the seismic rebounds for a model of Venus to investigate future detection of seismic activity in the context of the next missions (future topography and gravity field data).

Tidal forces exerted on a planetary body cause deformations and mass redistributions in its interior. They lead to surface deformations and variations of its gravity field that can be observed with geophysical and geodetical experiments. Love [1909] studied the tidal deformation of a homogeneous compressible model of the Earth and introduced the so-called Love numbers (hereafter LNs) which describe the deformation of a planet. A planet deforms dependently to its internal structure, therefore the LNs are an indication of its interior. The change in the gravitational field of a planet due to an external gravity field is described by the tidal Love number (hereafter TLN) k of degree 2, denoted by k_2 since it is predominantly of degree 2. The TLN k_2 of Venus describes its gravity field variation from tidal excitation induced by the Sun. It is estimated from spacecraft radio tracking data and it has been most recently estimated to be $k_2 = 0.295 \pm 0.066$ (2σ) [Konopliv and Yoder, 1996]. This value is denoted in what follows by k_2^{MPVO} since it has been evaluated from Doppler tracking of Magellan and PVO. This present uncertainty of k_2 is too big to constrain the core structure (solid, fluid, part solid and part fluid) [Dumoulin et al., 2017]. The lack of an internal magnetic field is not a constrain either since both a fluid and a solid core are compatible with this observation [Stevenson, 2003]. The energy loss of a planet is caused from its delayed response to the tidal forces and it is due to its viscoelastic nature. It is quantified by the quality factor Q and it is estimated from the real and imaginary parts of the TLNs [Murray and Dermott, 2000]. The quality factor of Venus has been approximated to be between 20 to 100 from general studies about energy loss [Goldreich and Soter, 1966] and long term spin evolution [Correia et al., 2003]. The TLN k_2 can be calculated for a planetary model under periodic tidal forcing of frequency ω. Therefore comparing the estimated k_2 from spacecraft navigation with the theoretical calculation constrains the possible models to a certain limit depending on its uncertainty. In the first part of this work we first calculate the tidal deformations to explore the

internal structure of the planet Venus from available observations as its mantle viscosity for each possible core structure. The TLN k_2 is calculated for different profiles of Venus and then we use geophysical and geodetical data as k_2^{MPVO} to filter the possibilities.

Venus has been shown to have recent volcanic activity from VEx data but the extent of this activity has not been explored yet. Future Venus exploration missions VERITAS and EnVision will be launched in the near future and one of their main goals is to explore the geological activity of Venus. They will map the topography and gravity field of the planet with a better resolution than the present map acquired from Magellan and PVO data. The second part of this work is to explore future detection of seismic activity from the future topography and gravity field data. A code called `ASTRA` [Melini et al., 2008] calculates the coseismic and postseismic rebounds of a planet due to a fault dilocation. We calculate with `ASTRA` the possible effect of a Venus-quake on the surface deformation and gravity variation and whether it can be detected from orbiters. The Beta Regio is a rift system on Venus found similar to the East-African rift system (hereafter EARS) on the Earth [Surkov et al., 1976], [Saunders and Malin, 1977], [Mcgill et al., 1981] and [Basilevsky, 2008]. A seismic dislocation in 2005 took place in the EARS in the Manda Hararo-Dabbahu area. Based on the comparison between the rift system in Beta Regio and the one of the EARS, we estimate the effect of a seismic dislocation of the same magnitude and geometry as the 2005 Manda Hararo-Dabbahu event on Venus.

Chapter 1 introduces the general information we currently know about Venus. First, geological features at its surface, the mechanism at its mantle which drives the surface deformation and the recent proof of volcanism observed from VEx data. Afterwards we give current observations deduced from geophysical and geodetic experiments. And finally the past missions (flybys, orbiters, atmospheric probes and landers) and the future missions that will be launched to explore Venus in the near future. Chapter 2 explains the theory behind the calculation of the deformations which is used to solve tidal and load problems Lambeck [1980]. We then describe how the tidal and load Love numbers came to be introduced in 1909 by A. E. H. Love [Love, 1909]. Next we list different rheologies applied in the deformation calculation for planetary models as Maxwell, Burgers and Andrade rheologies. At last we explain how the rheology is introduced in the calculation of the Love numbers. This chapter also explains the theory behind

open source fortran codes: the plAnetary Love nuMbers cAlculator `ALMA3` [Melini et al., 2022] and A poSTseismic Rebound cAlculator `ASTRA` [Melini et al., 2008]. The `ALMA3` is a fortran code that was originally created for the computation of the Earth loading LNs (hereafter LLNs). The most recent version of the code [Melini et al., 2022] calculates the TLN k_2 and the quality factor Q of Venus and was also applied in Briaud et al. [2022] for the study of the Moon. `ALMA3` is applied in chapter 3 for the study of Venus. In chapter 3 we explore the interior of the planet Venus from its tidal deformation from the Sun. First we explore the effect of two different rheologies (Andrade and Maxwell) and the influence of the thick and dense Venusian atmosphere on k_2 and Q. Then we explore with random Monte-Carlo sampling a large range of internal structure parameters of Venus (densities, viscosities and thicknesses) for 4 and 5-layer models. We use the mass and the total moment of inertia to filter out the models that are not consistent with these parameters. Afterwards we calculate k_2 and therefore Q with `ALMA3` for each model. Finally the value k_2^{MPVO} derived from observations and the expected limits for the quality factor Q to filter out models that are not consistent with these constraints. We deduce that the core of Venus can be entirely fluid, entirely solid or part solid and part fluid. We also show that the mantle of Venus has a contrast in viscosity for each of the possible core structures. This chapter is a part of my first publication as the lead author which is currently in revision, you will find the submitted version to Planetary and Space Science (PSS) journal in Appendices. I am also the second author of [Melini et al., 2022] where I wrote section 5.1 titled "tidal deformation of Venus" as part of the benchmarking of `ALMA3`. In chapter 4 we explore the seismic rebound of a Venus model possibility to detect past or present Venus-quakes. A fault dislocation deforms a planet with surface displacements and gravity field variations. We first model the geometry and magnitude of the 2005 Manda Hararo-Dabbahu seismic event. We apply it to a model of the Earth and compare the results to a previous study done by Grandin et al. [2009]. We assume that Venus is subjected to the same rifting event. We then calculate the coseismic and postseismic rebounds on a model of Venus with `ASTRA`. This study is done in the frame of the future Venus exploration missions EnVision and VERITAS which will provide new data on the topography and altimetry of Venus. Chapter 5 is a conclusion of this work and discusses the open questions and perspectives in the frame of the future exploration missions to Venus. Finally the Appendices include Appendix A with

the scientific communications (submitted and published papers I authored and co-authored) and two of these publications. The Appendix B includes additional tables and figures related to chapter 3.

1. The planet Venus

The four planets closest from the Sun are called terrestrial planets for their similarities with the Earth structure. The planet Venus size and density are only 5% smaller than that of the Earth, therefore it is often called its twin planet. Venus orbits around the Sun with a 224 days period. Contrary to the Earth, it does not have natural satellites and has a retrograde spin with a period of 243 days. Venus is seen as having a core rich in iron, a magnesium silicate mantle and a silicate crust [Morgan and Anders, 1980]. Its atmosphere is 90 times denser than that of the Earth, it is mostly carbon dioxide (symbol CO_2), also rich in nitrogen (symbol N) and sulfur dioxide (symbol SO_2). This thick and dense atmosphere causes the surface temperature to approach 740K which does not allow any water to exist on the surface. It is the planet with the highest surface temperature in the Solar System. The atmosphere causes a green-house effect and additionally, without water, the planet struggles to form plate tectonics. Presently, Venus shows no proof of plate tectonics activity. It is assumed to have a stagnant-lid regime. This regime does not allow the temperature of the planet to cool, instead the heat gets trapped inside.

1.1 Venus, an active planet

1.1.1 Geological features

Similarly to the Earth, it has been proposed that Venus has buoyant mass rising from the mantle, called mantle plumes. Based on the gravity field and the topography from Magellan Smrekar and Sotin [2012] proposed that Venus has approximately 9 mantle plumes which, when approaching the lithosphere, cause surface deformation. The plumes cause surface fracturing and consequently they formed over 85000 volcanoes. Crustal fracturing on Venus caused by a rising mantle plumes frequently manifest by the formation of novae, arachnoids and

coronae on its surface.

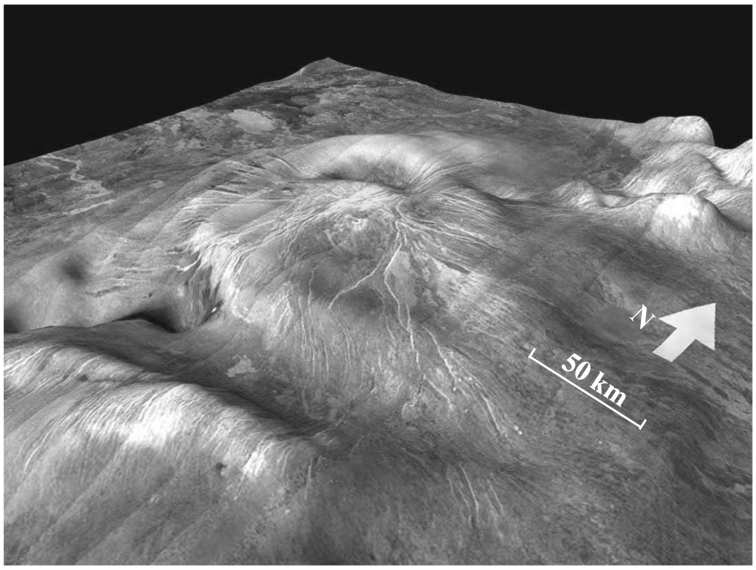

Figure 1.1: 3D image of Anala Mons nova of 200 km diameter situated at (14.5°E,11°N) from Krassilnikov [2002b]. The image is a superposition of Magellan radar image and altimetry data, it is in a N-E direction and the vertical scale is expanded by 20 times.

Novae are uplifted domes on the surface of the planet of $100 - 300$ km diameters and were first discovered with radar images from Magellan. Krassilnikov [2002b] proposed that they form when material from mantle plumes ascend and approach the surface which causes an uplift of the lithosphere creating a dome at the surface. Fig. 1.1 from Krassilnikov [2002b] is an image of the Anala Mons nova obtained from superposition of Magellan radar image and altimetry data. Venus has 64 identified novae. Following a gravitational relaxation of the lithosphere the dome-like shape of the uplift flattens laterally and becomes similar to a plateau. Finally, the hot mantle plume cools down and the plateau transforms into a circular rim with a subdued trough. These circular shapes with uplifted shoulders at the border and a relaxed subsidence in the middle are called coronae [Krassilnikov, 2002b] and arachnoids [Krassilnikov, 2002a]. Coronae and arachnoids were first discovered from the Venera 15 and 16 radar images which were missions of the Lavochkin space agency of the Soviet Union. An arachnoid has a radius from 50 to 175 km with a uniform topographic shape [Head et al., 1992]. A corona has a complex structure and topography with a radius of a several hundred kilometers. There are at least 90 arachnoids and 209 coronae on Venus. Figs. 1.2 and 1.3 from Krassilnikov [2002a] and Krassilnikov [2002b] are images

of arachnoid no. 186 and Pavlova Corona, respectively. They are obtained from superposition of Magellan radar image and altimetry data.

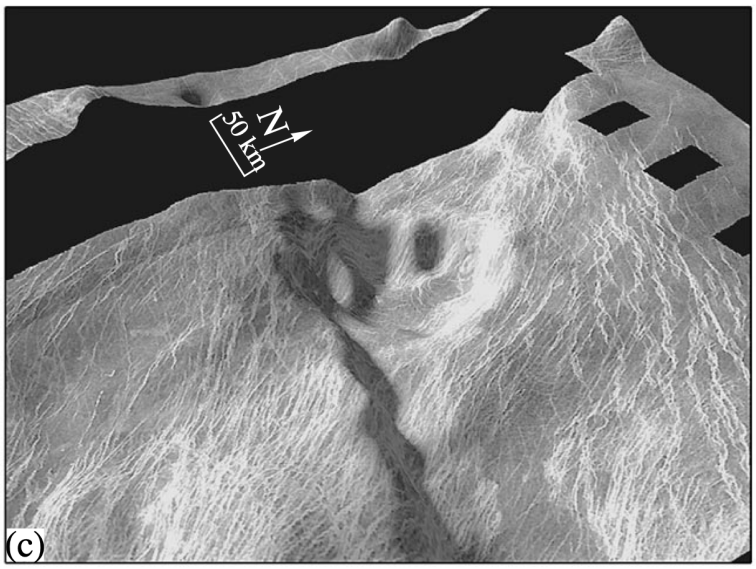

Figure 1.2: 3D image of arachnoid no. 186 from Krassilnikov [2002a] situated at (227°E,17.5°S) [Crumpler and Aubele, 2000]. The image is a superposition of Magellan radar image and altimetry data, it is in a W–NW direction and the vertical scale is expanded by 30 times.

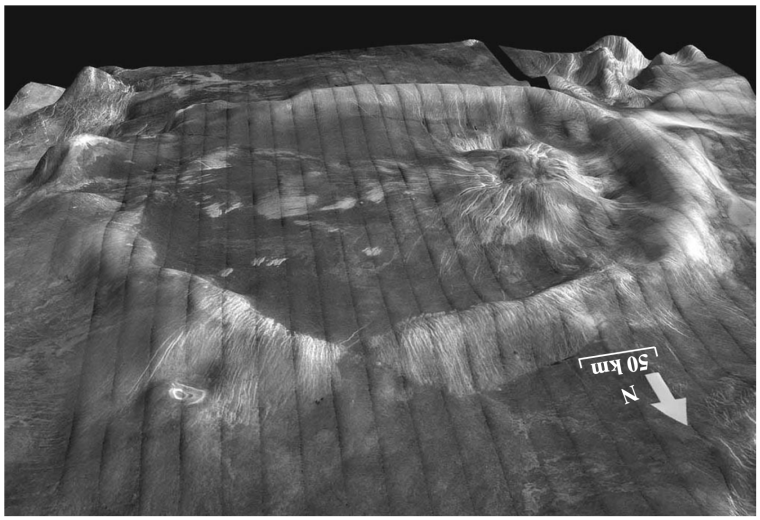

Figure 1.3: 3D image of Pavlova Corona of 400 km diameter situated at (40°E,14.5°N) from Krassilnikov [2002b]. The image is a superposition of Magellan radar image and altimetry data, it is in a S direction and the vertical scale is expanded by 20 times.

Davaille et al. [2017] made observational evidence for subduction on Venus. They produced in laboratory experiments, with a lithosphere-like skin and fluid

heated below, the up-welling of a mantle plume which causes fractures and sometimes spread of the material (volcanism) and afterwards the formation of coronae. They compared the laboratory observation with combined radar and topography images of coronae on Venus. Davaille et al. [2017], in this way, reproduced the Artemis and the Quetzalpetlatl coronae in shapes and features (rift segments, a subduction trench, fractures and volcanic flows) and showed that mantle plumes trigger subduction and is favoured by a hot lithosphere. Gülcher et al. [2020] made morphological analysis of the coronae of Venus. The goal was to discern if the existing coronae are active or inactive and, if active, to recognize at what stage they are. They used 3D thermomechanical numerical simulation to mimic realistic thermorheological lithosphere and mantle dynamics. They identified 4 different regimes of coronae formation and each goes through different stages of evolution. They found that different coronae structures indicate different regimes of interactions between the mantle plume and lithosphere as well as different stages of evolution. After comparing the numerical simulation with morphological analysis of coronae on Venus from topographic data they deduced that at least 37 large coronae as the Artemis corona are active. This led to the conclusion that extensive plume activity on Venus is still ongoing.

1.1.2 Recent activity

The surface of Venus is rich in volcanoes, rift zones and other geological features as novae, arachnoids and coronae. The BAT (Fig. 1.4) region is located within $180° - 300°$E and $50°$S $- 50°$N in coordinates and it is of interest for future Venus exploration missions since it contains well preserved tectono-magmatic structures. A chasma is an extended, narrow, deep depression, its plural is called chasmata. Venus has many chasmata which include the Hecate Chasma (between Atla Regio and Beta Regio), the Devana Chasma (South of Beta Regio) and the Parga Chasma (between Atla Regio and Themis Regio). VEx was the most recent ESA mission to Venus which had a role to study its atmosphere and clouds. The VIRTIS (Visible and Infrared Thermal Imaging Spectrometer) and the VMC (Venus Monitoring Camera) on-board instruments provided new information on the geological activity of Venus. High emissivity data from the VIRTIS instrument indicate the existence of unweathered basalt on the surface. From VIRTIS maps Smrekar et al. [2010] showed that three regions on Venus

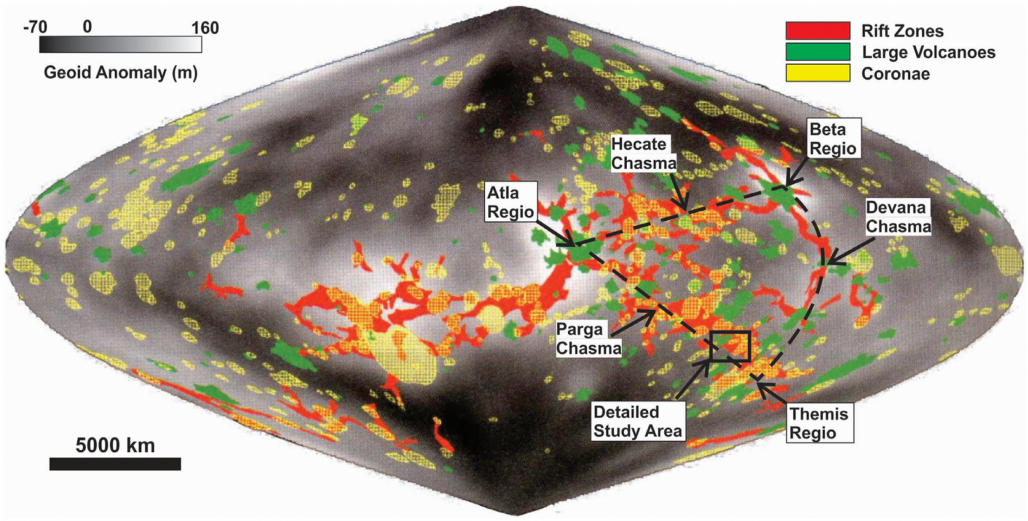

Figure 1.4: A sinusoidal projection of the surface of Venus from Graff et al. [2018] with the central meridian at 180°E. The map shows the major structures as rift zones (red), large volcanoes (green), and coronae (yellow). The Beta-Atla-Themis (BAT) region is outlined by dashed lines. The black square indicates the location of the area of Parga Chasma studied by Graff et al. [2018].

show high emissivity. They are Imdr Regio located South of Parga Chasma outside the BAT Region, Themis Regio and Dione Regio located near the Themis Regio. Smrekar et al. [2010] estimated the volume of the basalt flow on Venus from the surface of the emissivity at these three areas with an approximation of flow thickness from the Earth basaltic flows. After estimating the flow volume, new hypothesis about the age of the basalt flows were proposed. The first is that Venus experienced a catastrophic resurfacing 2.5 million years ago with little present volcanism (0.01 km^3/year). The second is that Venus has equilibrium resurfacing (1 km^3/year) which sets the age of the basalt flows between hundreds to thousands of years extending to tens of thousands as an upper boundary. The last hypothesis shows that the flows can be largely younger than estimated. Until then, no evidence for present volcanism has been shown.

Ganiki Chasma of Venus is located near Atla Regio (Fig. 1.4). Shalygin et al. [2015] studied the VMC maps from VEx which observed bright spots in the data in 2008 near the Ganiki Chasma. They showed that it indicates a sharp rise in the SO_2 in the upper atmosphere which witnessed a gradual decrease in the following 5 years. Shalygin et al. [2015] therefore showed that, while it was orbiting Venus, VEx witnessed a volcanic activity which was the first proof that Venus is presently active and changing. Stofan et al. [2016] analysed

VIRTIS maps from VEx which show emissivity anomalies in Themis Regio (Fig. 1.4). This is an indication of atmospheric spike in SO_2. Combining the data with geologic mapping and gravity anomaly Stofan et al. [2016] found that the emissivity are plausible evidence of recent volcanic activity. Graff et al. [2018] studied the complex morphology of Parga Chasma and Hecate Chasma (Fig. 1.4) and compared them to the Atlantic rift on the Earth. They found that they are a consequence of the formation of local triple-junction rifting. This triple junction was caused by the arrival of several mantle plumes. The difference between the rift systems on the two planets is that on Venus the rift failed to progress and achieve an ocean opening stage. As for the Earth, the Central, Southern, and Northern Atlantic Oceans were formed.

The Beta Regio (Fig. 1.4) is a complex feature rich in rifts and volcanoes, and it is part of the BAT region on Venus. The Earth based radar observations first indicated a bright spot at 22° N and 280° E on Venus which was called "Beta". It appeared to be caused by an elevation of the surface and was suggested to be a large shield volcano [Saunders and Malin, 1977]. Later with gamma-ray experiments from Venera 9 and 10 (both from the Lavochkin space agency), after an estimation of the K, U and Th abundance it was shown that the Eastern part of Beta is rich in basalt. This validates the first suggestion of a volcanic area proposed by Surkov et al. [1976] in 1976. The "Beta" reference was later transferred to a wider surface now called "Beta Regio" which includes the original shield volcano. This alternate interpretation of the location is based on topographic maps [Mcgill et al., 1981] where it includes elongated depressions spanning South the original identification. The Beta Regio therefore refers to the extended area from 25° to 50° N in latitude and from 270° to 300° E in longitude [Basilevsky, 2008]. In what follows we refer by Beta Regio rift system to the entire systems spanning from Beta Regio South to Phoebe Regio.

Smrekar [1994] used spectral methods from Magellan gravity data to estimate the elastic thickness of the Venusian lithosphere in Beta Regio and they found it to be 30 ± 5 km. Upcott et al. [1996] used forward modeling of free air gravity anomalies to estimate the effective elastic thickness of the Western branch of the EARS and they found it to be 25 ± 5 km. Ebinger et al. [1989] found the effective elastic thickness of the Eastern branch of the EARS to be 29 ± 2 km by studying the wavelength dependence of the correlation between the topography and the Bouguer gravity anomaly. Therefore the Beta Regio and the EARS have similar

effective elastic lithosphere thickness. Foster and Nimmo [1996] compared the two rifts systems of 100 km length. They found that main difference between the Beta Regio and the EARS is that they have half-grabens (distance between rift faults) of 100 km and 50 km, respectively. This observation is an implication of the higher fault strengths on Venus [Foster and Nimmo, 1996]. These results corroborate the findings of Montesi [2013] that, without plate tectonics, the crust requires additional sources of stress as mantle plumes (buoyant uplift) to perform rifting. Therefore mantle plumes played a role in developing the Beta Regio rift system [Montesi, 2013]. Venus is therefore an active planet and more details on the extent of this activity will be revealed with future missions. Regions identified as likely sites of mantle plumes, show:

- active novae, coronae and arachnoids on the surface;
- mantle plume triggered subduction;
- high surface emissivity anomalies which are at times proof of volcanism.

The BAT region is of interest since it has locations with mantle plumes that are possibly of volcanic activity such as Ganiki Chasma and Themis Regio. As well as regions rich in geological features and rifts similar to the Earth as the Parga Chasma and Hecate Chasma and Beta Regio.

1.2 Geophysical and geodetical observations

Strom et al. [1994] found that the surface of Venus is relatively young with an age from 300 Myr to 1 Gyr based on crater counting. This might be caused by a global catastrophic resurfacing $\approx$ 1Gyr ago which covered the planet with younger material [Romeo and Turcotte, 2010]. The global catastrophic resurfacing can be explained by resonant core-mantle friction [Touma and Wisdom, 1998; Greff-Lefftz and Legros, 1999]. Another argument for the young surface age is that Venus has episodic subduction with intervals between 500 and 700 Myr with global lithospheric overturn [Turcotte et al., 1999]. Noack et al. [2012] studied the interaction between interior dynamics and atmosphere thermal evolution by calculating 2D and 3D mantle convection models with digitized atmosphere temperatures. They found that an increase of the surface temperature causes a greenhouse effect. Noack et al. [2012] also found that an increase of the surface

temperature to a critical value causes the lithosphere to become locally mobile. Venus might have had plate tectonics [Moresi and Solomatov, 1998; Schubert et al., 2001] before achieving the stagnant lid regime [Nimmo and McKenzie, 1998]. There is no proof that it presently has plate tectonics which might be due to the high surface temperature [Bercovici and Ricard, 2014]. Therefore Venus evolved differently than the Earth and has now a different geology and climate [Phillips et al., 2001; Noack et al., 2012; Gillmann and Tackley, 2014]. This fact drives the conclusion that Venus and the Earth have different internal mechanisms and structures. Constraining the interior of Venus can be made from geophysical and geodetical observations of past exploration missions. The most recent have been made from Magellan, PVO and VEx.

The 1990 NASA Magellan mission which ended in 1994 provided the best available gravity topography data and SAR (Synthetic Aperture Radar) images. From the topography and radar data of Magellan the topographic features, geologic structures and their surroundings as rift systems [Graff et al., 2018], volcanoes, mantle plumes [Smrekar, 1994; Smrekar and Sotin, 2012], arachnoids [Krassilnikov, 2002a], novae and coronae [Krassilnikov, 2002b] were studied. The gravity field has been determined from the combination of Magellan and PVO [Konopliv et al., 1999] and from these new data the TLN has been estimated (Table 1.1). The ESA mission VEx ($2005-2014$) focused on studying its atmosphere (section 1.1.2) and did not allow a big improvement of the gravity field determination from Magellan and PVO due to its high eccentric orbit [Rosenblatt et al., 2012].

Table 1.1: The Venus parameters derived from geophysical parameters used to constrain its interior. The mass M_V is without the atmosphere.

Constant	Value	$\pm 1\sigma$	References
R_V (km)	6051.8	-	Rosenblatt et al. [1994]
M_V ($\times 10^{24}$ kg)	4.8673	1.1×10^{-4}	-
MoI	0.337	0.024	Margot et al. [2021]
k_2	0.295	0.033	Konopliv and Yoder [1996]

For the size and internal structure the mean radius of Venus has been estimated from Magellan topography data to be 6051.9 km [Rosenblatt et al.,

1994]. The basaltic crust of Venus has been determined from the gravity and topography data of Magellan mission to have a thickness of 30 km by geoid to topography ratios [James et al., 2010]. The crustal density was measured from gamma-ray back-scattering of the Venera 8 mission of Lavochkin space agency to be $2700 - 2900$ kg/m^3 [Fegley, 2004]. The total mass with its atmosphere is denoted by M_{V+a}. It is determined with its uncertainty from the gravitational constants G and GM_{V+a}. The values used are of $G = (6.67430 \pm 0.00015) \times 10^{-11}\mathrm{m}^3\mathrm{kg}^{-1}\mathrm{s}^{-2}$ as CODATA recommended in 2018 [Tiesinga et al., 2021] and $GM_{V+a} = 324858.592 \pm 0.006$ km^{3}s^{-2} from `MGNP180U` gravity field [Konopliv et al., 1999]. Hence M_{V+a} is deduced. The mass of the atmosphere equal to 4.77×10^{20} kg [Taylor, 1985] is therefore subtracted to obtain the mass M_V without the atmosphere and is given in Table 1.1. Several parameters of Venus are used to constrain its interior in addition to its mass without the atmosphere. These parameters are R_V, the normalized moment of inertia $\tilde{C} = C/M_V R_V^2$ (hereafter MoI) [Margot et al., 2021], such that C is its moment of inertia and finally its TLN k_2 are shown in Table 1.1.

There are no additional data to assess the density profile of the whole planet which led past profiles of Venus to be a rescaled version of the Earth. The model of the Earth usually used is the Preliminary Reference Earth Model (hereafter PREM) [Dziewonski and Anderson, 1981] which is a 1D seismological model of its density ρ, pressure P and elastic properties such as primary seismic wave propagation velocity V_P and secondary seismic wave propagation velocity V_S. Previous studied rescaled the Earth PREM taking into account the slightly lower mass and smaller radius of Venus [Zharkov, 1983; Yoder, 1995; Mocquet et al., 2011]. Aitta [2012] calculated a rescaled model of Venus from the pressure of PREM. They assumed that there is a relation between the mantle density of the two planets written as a function of pressure. Considering that Venus has an iron fluid core, they modeled its density from the theory of tricritical phenomena [Aitta, 2010a,b]. They finally obtained a complete density profile of Venus. Dumoulin et al. [2017] also calculated several rescaled models by modeling the mantle density and seismic velocities from thermodynamical equilibria of mantle minerals. They assumed two different hypothesis on the temperature: a cold mantle [Steinberger and Werner, 2010] and a hot mantle [Armann and Tackley, 2012]. Dumoulin et al. [2017] assumed in their study different core structures: an entirely fluid core, an entirely solid core and a part solid and part fluid core.

The models of Aitta [2012] and Dumoulin et al. [2017] are used later in chapter 3 for comparison with our work.

1.3 Past and future missions

Venus, as our closest planetary neighbor other than the Moon, was the first planet to be explored by a spacecraft. The first successful exploration was done by Mariner 2 of the NASA. It performed a successful scan as it flew by Venus on the 14^{th} of December 1962. The most successful landing missions on Venus till the present day were executed by the Venera missions (Lavochkin space agency). Landing spacecrafts did not survive for long due to the high temperature and pressure at the surface. The Venera 4 capsule entered the atmosphere of Venus on the 18^{th} of October 1967 which was the first space-probe to provide measurements from the atmosphere of another planet. It measured the temperature, pressure and density of the atmosphere. In addition it discovered by performing multiple chemical experiments that its atmosphere is made of 95% CO_2. Mariner 5 of the NASA also flew by Venus in 1967. It collected data on the radiation and magnetic field of the planet and, in combination with the Venera 4 data about the atmosphere. It showed that the surface pressure is very high in comparison to the Earth (75 to 100 times). These observations were confirmed and improved later by Venera 5 and 6 which entered the atmosphere in 1969. Until then no spacecraft were able to reach the surface of Venus while functioning and transmitting.

The first successful landing on another planet, therefore did not crash or perform a soft landing (as Venera 7), was done by Venera 8. It landed on Venus on the 22^{nd} of July 1972. Two years later, Mariner 10 (NASA) had a successful flyby by Venus. In 1975 a Lavochkin space agency mission, Venera 9, became the first orbiter of Venus and its lander successfully landed on its surface. It provided the first images from the surface of another planet. This mission was followed in the same year by Venera 10 which consisted in another successful orbiter and lander. Afterwards in 1978 Venera 11 and 12 both landed on the surface of Venus and had instrument failures. Pioneer Venus Orbiter (hereafter PVO) and Pioneer Venus Multiprobe (hereafter PVM) from the NASA are also called Pioneer Venus 1 and Pioneer Venus 2, respectively. PVO entered the orbit of Venus on the 4^{th} of December 1978 and decayed after 14 years. PVO was followed by PVM which entered the atmosphere the 9^{th} of the same month.

PVM consisted in five spacecraft, one of which briefly continued transmitting after reaching the surface. One of the multiprobes survived for about an hour after reaching the surface. From 1981 to 1983 Lavochkin successfully executed 4 missions (Venera 13 to 16) which consisted of orbiters and landers. From which Venera 13 sent the first recording of sounds from another planet. After the end of the Venera missions, Lavochkin sent in 1984 Vega 1 and 2 which executed flybys and deployed landers and atmospheric probes which operated for 2 days. The Magellan topography and SAR data [Crumpler and Aubele, 2000] provided the catalog of volcanic structures on the surface of Venus. This catalog was the basis of the novae and coronae study [Krassilnikov, 2002b] as well as the arachnoids study [Krassilnikov, 2002a]. It was followed by a ESA mission, VEx (section 1.1.2), which operated after orbit insertion from 2006 to 2014 and provided the first proof of present Venusian volcanic activity [Shalygin et al., 2015]. Finally, the most recent missions to reach Venus are Akatsuki and its IKAROS from the JAXA (Japan Aerospace Exploration Agency). These are the only successful Venus missions from Japan. Akatsuki performed a flyby in 2010 and successfully entered the orbit in the 7^{th} December of 2015. IKAROS was an experimental spacecraft released from the Akatsuki mission and it made a flyby on the 8^{th} December of 2010 and failed to make observations.

Three NASA and ESA missions have been chosen to explore Venus and will be launched in the near future. VERITAS (Venus Emissivity, Radio Science, InSAR, Topography, and Spectroscopy) from the NASA is an orbiter and will be launched to Venus in 2027. It will be followed by DAVINCI (Deep Atmosphere Venus Investigation of Noble gases, Chemistry, and Imaging) from the NASA. It will carry an atmospheric descent probe and its goal is to explore the atmosphere of Venus: its chemistry, temperature, pressure and winds. EnVision from the ESA will be launched in 2031. VERITAS and EnVision aim to provide a detailed radar imagery and topography maps of the planet with special focus on areas with present potential geological processes. They will map the surface of Venus with altimetry with a better resolution than that of Magellan. The gravity field tidal Love number k_2 will also be determined with a better uncertainty than the one achieved by Magellan and PVO (Table 1.1) by both EnVision [Rosenblatt et al., 2021] and VERITAS [Cascioli et al., 2021]. These missions will constrain the internal structure of the planet as its core state and its mantle viscosity, surface composition, weathering, active volcanism and explore more the possibility of

active subduction and tectonic processes. They will also provide the first maps of rock composition at the surface and estimate surface weathering. Finally they will search for thermal and chemical signatures from active or recent volcanism.

2. Global deformations and internal structure

2.1 Modeling deformations

The deformation of the planet depends on its shape, density and elastic parameters which variate relatively with its depth. Lambeck [1980] explained in details the Love numbers (hereafter LNs) history and mathematical basis used for their calculation. In this chapter we introduce the concepts behind the LNs definition as well as open source codes that can be used in the present day.

2.1.1 Fundamental equations

Describing the deformation in an element of volume requires several equations [Lambeck, 1980]:

1. The linear momentum of a body (also simply called momentum) is its mass, which depends on its density, multiplied by its velocity. Applied body forces per unit volume $\overrightarrow{F}$ and surface forces (also called stress) $\overline{\sigma}$ change the linear momentum of an element of volume of density ρ. The rate of the velocity $\overrightarrow{v}$ of the element relates to $\overrightarrow{F}$ and $\overline{\sigma}$ as:

$$\rho \frac{\mathrm{d}\overrightarrow{v}}{\mathrm{d}t} = \overrightarrow{F} + \overrightarrow{\nabla} \cdot \overline{\sigma}, \tag{2.1}$$

   where $\overrightarrow{\nabla} = (\frac{\partial}{\partial x_1}, \frac{\partial}{\partial x_2}, \frac{\partial}{\partial x_3})$ and $\cdot$ represents the scalar product. This equation is called the equation of conservation of the linear momentum.

2. The deformation of the element is described by two relations. The first is between the displacement $\overrightarrow{d}$ of components d_i and strain tensor $\overline{\varepsilon}$ of

components ε_{ij}:

$$\varepsilon_{ij} = \frac{1}{2}(\partial d_i/\partial x_j + \partial d_j/\partial x_i), \quad \text{where } i,\ j = 1,\ 2,\ 3. \tag{2.2}$$

The second is a relation between stress and strain. If the body is elastic, this relation is called the Hooke's linear law of elasticity:

$$\sigma_{ij} = \lambda\ tr(\bar{\varepsilon}) I_{ij} + 2\mu\varepsilon_{ij}, \tag{2.3}$$

with $tr(\bar{\varepsilon}) = \sum_k \varepsilon_{kk}$, the cubic dilatation, $\overrightarrow{I}$ the identity matrix and μ and λ are the Lamé constants. While μ is the rigidity (also called shear modulus), $\lambda = K - \frac{4}{3}\mu$ such that K is the incompressibility (also called bulk modulus). This stress-strain relation depends on the rheology of the planet, it can be replaced by another anelastic (non elastic) rheology. Section 2.1.2 details the process of calculating the deformation for anelastic rheologies.

3. A continuity equation ensures the mass conservation of the planet, where t stands for time:

$$\partial\rho/\partial t + \nabla \cdot (\rho \overrightarrow{v}) = 0. \tag{2.4}$$

The planet is considered to be spherically symmetrical (a sphere). It is also assumed to be in hydrostatic equilibrium and we study the small perturbations from this state. Therefore the perturbation equations of conservation of linear momentum (Eq. 2.1) is linearized for small perturbations:

$$\rho\frac{\partial^2 \overrightarrow{d}}{\partial t^2} = \nabla \cdot \bar{\sigma} - \nabla(\rho g \overrightarrow{d} \cdot \overrightarrow{e_r}) - \rho\nabla U + g\nabla \cdot (\rho \overrightarrow{d})\overrightarrow{e_r}. \tag{2.5}$$

where now $\bar{\sigma}$ is the non-hydrostatic stress tensor and ρ and g respectively the density and gravity of the deformed state. The unit vector is denoted by $\overrightarrow{e}$ with radial component $\overrightarrow{e_r}$ and tangential component $\overrightarrow{e_t}$. The potential U is the sum of two potentials $U = U_1 + U_2$, such that U_1 is of the external force $\overrightarrow{F}$ and U_2 is of the non-hydrostatic internal response or in other words the self-attraction after deformation. The potential U is subject to Poisson's equation

$$\nabla^2 U = -4\pi G \nabla \cdot (\rho \overrightarrow{d}). \tag{2.6}$$

inside the planetary body. We denote the surface harmonic of degree n by S_n and the radius (also called radial boundary) in the planetary body by r. We assume the potential U is harmonic and of frequency ν:

$$U = \sum_n U_n(r) S_n e^{i\nu t}, \tag{2.7}$$

where i is the imaginary unit. In this case, partial solutions of Eqs. 2.5 and 2.6 exist [Love, 1909], where the displacement vector, $\overrightarrow{d}$, can be replaced by:

$$\overrightarrow{d} = \sum_n [W_n(r) S_n \overrightarrow{e_r} + X_n(r) \nabla S_n \overrightarrow{e_t}] e^{i\nu t}, \tag{2.8}$$

where $W_n(r)$ and $X_n(r)$ are unknown functions describing respectively the radial and tangential deformations. Alterman et al. [1959] transformed Eqs. 2.5, 2.6 and 2.8 for realistic Earth models. The results are six first-order differential equations also called fundamental solutions:

$$\frac{\mathrm{d}y_\alpha}{\mathrm{d}r} = \sum_{\beta=1}^{6} a_{\alpha\beta} y_\beta, \qquad \alpha = 1, \cdots, 6. \tag{2.9}$$

The parameters y_α are radial functions such as:

$$\begin{aligned}
&y_1 = W_n(r) \text{ is the radial displacement,} \\
&y_2 \text{ is the radial stress,} \\
&y_3 = X_n \text{ is the tangential displacement,} \\
&y_4 \text{ is the tangential stress,} \\
&y_5 = U_n(r) \text{ is the potential perturbation,} \\
&y_6 = \partial U_n/\partial r - 4\pi G \rho W_n \text{ is the perturbation in potential gradient.}
\end{aligned} \tag{2.10}$$

The $a_{\alpha\beta}$ are functions of the frequency ν, the harmonic degree n, $\rho(r)$, $g(r)$, Lamé constants $\lambda(r)$ and $\mu(r)$. Boundary conditions are set to solve Eqs. 2.9 such as

- regularity at the origin
- no stress at the surface,
- the deformation and stress are continuous at surface discontinuities in the

interior,

- internal and external gravitational potentials and their respective gradients must be equal at free surfaces and surface discontinuities.

The above expressions (Eqs. 2.9) were formulated to resolve the Earth surface and internal loading as well as its the tidal deformations. Therefore the equations of Eq 2.10 become six differential equations to solve. This method can be applied to any planetary body. Other geophysical problems can also be resolved by the same formulation as a planet rotational deformations and its free oscillations [Alterman et al., 1959, 1974]. For deformation processes other than the oscillating problem (tidal, internal loading, surface loading and rotational) a deforming potential is required. In the case of tidal deformations the fundamental solutions of Eq. 2.9 are solved by assuming that the external (in this case tidal) potential $U_1(r)$ acts on the planet without surface loading. Therefore there are no surface stresses and the observed values are the surface deformation (W_n and X_n) and change in gravitational potential U_n (section 2.1.2 for more details). The rotational deformation is equivalent to the tidal deformation problem by replacing the tidal potential with a potential of centrifugal force. In the case of surface loading deformations the external potential $U_1(r)$ is considered to be the gravitational potential of the applied load. The main difference between this problem and the tidal deformation problem is the boundary conditions since in this case the surface stresses are continuous on the surface (section 2.1.2 for more details). The internal loading problem is similar to the surface loading as it relates to estimating the stress and density anomalies resulting from an external gravitational potential. The linearized momentum equation (Eq. 2.5) serves to validate the linear momentum conservation of the planet. The continuity equation (Eq. 2.4) validates its mass conservation. The stress-strain relation called constitutive equation (as Eq. 2.3) depends on the rheology of the body which can be anelastic, for an elastic body the law of Hooke presents convenient solutions of the fundamental equations (Eq. 2.9). In what follows these three equations along with the Laplace equation of Eq. 2.7 obtained in assuming the deforming potential U is harmonic outside the planet (four equations in total) are called the governing equations. These governing equations are the basis for solving the deformation problems of a planet. Love [1909] set forth parameters describing the loading and tidal deformations derived from their consequent surface and po-

tential deformations called respectively the Load Love numbers (hereafter LLN) and the Tidal Love numbers (hereafter TLN).

2.1.2 Loading and tidal deformations

For the loading and tidal problems, the external deforming potential U_1 is assumed to be linear as the total deforming potential U (Eq. 2.7). It is also harmonic of the same degree n and is written as:

$$U_1 = \sum_n U_{1,n}(r) S_n e^{i\nu t}, \tag{2.11}$$

with

$$\begin{pmatrix} W_n(r) \\ X_n(r) \\ U'_{2,n}(r) \end{pmatrix} = U_{1,n}(r) \begin{pmatrix} h_n(r) \\ l_n(r) \\ k_n(r) \end{pmatrix}. \tag{2.12}$$

Regarding the fundamental solutions (Eq. 2.10):

$$\begin{aligned} y_1 &= h_n(r) U_{1,n}/g(r), \\ y_3 &= l_n(r) U_{1,n}/g(r), \\ y_5 &= (1 + k_n(r)) U_{1,n}. \end{aligned} \tag{2.13}$$

To calculate these parameters on the surface, r is replaced by R:

$$\begin{aligned} \overrightarrow{d_r}(R) &= \overrightarrow{e_r} y_1(R) S_n e^{i\nu t} = [h_n(R)/g] U'_{1,n}(R) \overrightarrow{e_r}, \\ \overrightarrow{d_t}(R) &= \overrightarrow{e_t} y_3(R) \nabla S_n \mathrm{e}^{i\nu t} = [l_n(R)/g] \nabla U'_{1,n}(R) \overrightarrow{e_t}, \\ \Delta U(R) &= y_5(R) S_n e^{i\nu t} = [1 + k_n(R)] U'_{1,n}(R), \end{aligned} \tag{2.14}$$

where $U_1 = \sum_n U'_{1,n}$. Love [1909] introduced the constants k_n and h_n of degree n, afterwards Shida [1912] introduced the constant l_n. These three parameters k, h and l are called the Love numbers which as stated before are denoted in this manuscript by LNs. This notation is reserved for the LNs resulting of an external, in this case tidal, potential (section 2.1.1) without loading the planet. They are therefore called the tidal Love numbers (TLNs). If the potential loads the planet, the corresponding parameters describing the deformation are denoted by k', h' and l' and called the load Love numbers (LLNs). If tangential stresses are applied to the planetary surface, the parameters describing this deformation are denoted

by k'', h'' and l'' and called shear Love numbers [Saito, 1978; Lambeck, 1980]. In this work we focus on the LLNs and TLNs. These three sets of Love numbers are related in three equations [Molodensky, 1977]:

$$\begin{aligned} k'_n &= k_n - h_n \\ h''_n &= 3n(l_n - l'_n)\frac{n+1}{2n+1}, \\ 1 + k''_n &= 3nl_n\frac{n+1}{2n+1}. \end{aligned} \tag{2.15}$$

The LNs were first defined and used on the basis of an elastic Earth model. The work of William Thomson, referred to by Kelvin, greatly impacted the study of the Earth response to deformations. Thomson [1863] considered that the Earth is elastic, spherically symmetrical, homogeneous and incompressible. This model is now called the Kelvin model. Assuming a Kelvin model of a planet, its deformation as a response to a harmonic potential of degree $n = 2$ only depends on four parameters: ρ, μ, g in addition to its radius R. The TLNs become simply [Thomson, 1863]:

$$k_2 = \frac{3/2}{1 + \frac{19\mu}{2\rho g R}}, \quad h_2 = \frac{5/2}{1 + \frac{19\mu}{2\rho g R}}, \quad l_2 = \frac{3/4}{1 + \frac{19\mu}{2\rho g R}}, \tag{2.16}$$

and the LLNs

$$k_2{}' = -\frac{1}{1 + \frac{19\mu}{2\rho g R}}, \quad h_2{}' = -\frac{5/3}{1 + \frac{19\mu}{2\rho g R}}. \tag{2.17}$$

The Kelvin model is a simplified approach to solve the deformation problems. More realistic models as heterogeneous compressible models of the Earth were studied afterwards [Takeuchi, 1950]. Takeuchi [1950] first studied the tidal deformation of an elastic, compressible heterogeneous Earth model. They fixed several Earth models based on seismology profiles and K. E. Bullen's work [Bullen, 1936], [Bullen, 1940] and [Bullen, 1942] on the Earth internal density distribution. They solved the differential equations of stress and motion of these models with numerical integrations. This theoretical work was based on assuming an elastic response, therefore an elastic planetary body. When an elastic body is subjected to stress, the strain is instantaneous and the initial strain fully then recovers. For an anelatic body, the response is instead time-dependent and the initial shape and volume of the body can not always be fully recovered. The Earth and other

planetary objects are not purely elastic. To solve the LNs problem for a realistic planetary model anelasticity is crucial to take into consideration. The same notations for the LNs were later (and untill the present day) used to also describe the anelastic, more specifically viscoelastic deformation. Therefore assuming in Eq. 2.3 a stress and strain relation different than the law of Hooke of elasticity. In the next section we explain the different between an elastic and an anelastic medium. Additionally we explain how an elastic or an anelastic deformation of a body is theoretically displayed.

2.1.3 Elastic and anelastic deformations

To estimate the response of a body to external or internal potentials, we have to understand its rheology, which describes its instantaneous deformation and relaxation (also called flow) after an applied stress. For an anelastic planetary body, the LNs are time-dependent and they depend on its rheology. The simplest linear rheology, as already stated in section 2.1.1, is the rheology of Hooke corresponding to an elastic (also called a Hookean) body. We refer to a Hookean body simply by "elastic body" (Fig. 2.1). If the body is a 1D body, the stress is scalar denoted by σ and it is proportional to the strain which is also a scalar denoted by ε. The Eq. 2.3 becomes in 1D:

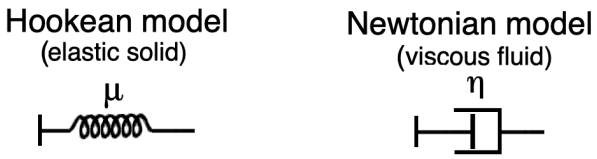

Figure 2.1: Representation of the elastic (Hooke) model and the fluid (Newton) model.

$$\sigma = 2\mu\varepsilon. \tag{2.18}$$

At the other end of the spectrum of linear rheological bodies there is the viscous (also called Newtonian) body, in which the stress σ is proportional to the strain rate $\dot{\varepsilon}$ [Ranalli, 1995]:

$$\sigma = 2\eta\dot{\varepsilon}, \tag{2.19}$$

such as η is the linear or Newtonian viscosity, simply referred to as viscosity. We refer to a Newtonian body simply by "fluid body" (Fig. 2.1). A fluid body does not deform instantaneously due to stress as an elastic one, instead it exhibits a delay or flow in its response. In what follows, a spring (labeled with its rigidity μ) represents the elastic properties of the medium, while a dashpot (labeled with its viscosity η) stands for its viscous properties. Dashpots are also sometimes called dampers since they dampen the deformation. The Maxwell model can be described as a combination of a spring and a dashpot in series. The Kelvin-Voigt model is a combination of a spring and a dashpot in parallel. As for the Burgers model, it is both Maxwell and Kelvin-Voigt models in series. Maxwell, Kelvin-Voigt and Burgers are also linear rheologies which are described as viscoelastic since they include both an elastic and a fluid component (Fig. 2.2).

The LNs are calculated for an anelastic body as it is believed to be more realistic than the elastic one. In this case the LNs are not constant parameters as in Eqs. 2.16 and 2.17 but become time-dependent. Peltier [1974] was first to extend the theory of the LNs calculation to a viscoelastic rheology. It was done for a Maxwell body based on the correspondence principal of linear viscoleasticity which states that the time-dependent viscoelastic response can be simplified to be solved as the elastic problem [Peltier, 1974]. More specifically, the correspondence principal states that with no initial conditions the Laplace transform or Fourier transform of functions of a viscoelastic body are equivalent to the equations for an elastic body. It was done in Peltier [1974], Vermeersen et al. [1996] and Soldati et al. [1998] with the Laplace transform which converts the time-dependent fundamental equations (Eq. 2.13), to the Laplace domain as an s-dependent function where s is the Laplace variable. For an incompressible planetary model the rheology contributes in the theoretical computation of k_2 through a single parameter: the complex rigidity $\tilde{\mu}(s)$ (also referred to as complex shear modulus and effective shear modulus). The complex rigidity is a function of s and it is equal to μ for the elastic rheology (Table 2.1). The form of the s-dependent complex rigidity $\tilde{\mu}$ depends upon the kind of constitutive law hence the rheology of the planetary body [Patrick Wu, 1982]. Tables 2.1 and 2.2 display the complex rigidity for several different rheologies as a function of s, μ and η.

To calculate the time-dependent viscoelastic LNs the fundamental equations (Eq. 2.10) are put in terms of the LNs (Eq. 2.13). In these fundamental equations

the rigidity μ is replaced by the complex rigidity $\tilde{\mu}$. The equations are solved and the viscoelastic LNs are calculated in the Laplace domain, the Laplace transform is denoted by denoted by $\mathcal{L}$. To calculate the time-dependent viscoelastic LNs for an applied forcing $F(t)$, an inverse Laplace transform $\mathcal{L}^{-1}$ is applied. We denote by $\mathbf{l}(s)$ a LN in the Laplace domain (which is $k_2(s)$ for the TLN k of degree 2 for example). Its Laplace inverse transform $\mathbf{L}_\delta(t) = \mathcal{L}^{-1}[\mathbf{l}(s)]$ is the time-dependent response to an impulsive δ forcing. The time-dependent LN, denoted by $\mathbf{L}(t)$ response to a forcing $F(t)$ is then calculated as:

$$\mathbf{L}(t) = \mathcal{L}^{-1}\Big[\mathbf{l}(s)\mathcal{L}[F(t)]\Big] \tag{2.20}$$

For the loading deformation, the forcing is set to be step-wise with $F(t) = H(t)$ with$H(t)$ is a Heaviside function for the LLNs. In this case $\mathcal{L}[H(t)] = \dfrac{1}{s}$, therefore $\mathbf{L}(t)$ is:

$$\mathbf{L}(t) = \mathcal{L}^{-1}\Big[\frac{\mathbf{l}(s)}{s}\Big] \tag{2.21}$$

which is equivalent to

$$\mathbf{L}(t) = \mathbf{L}_\delta(t) * H(t) \tag{2.22}$$

where $*$ represents the convolution operation. For the tidal deformation, the forcing is set to be periodic of frequency ω, with $F(t) = e^{st}$ where $s = i\omega$ and $\omega = \dfrac{2\pi}{\tau}$ if τ is the tidal period. The time-dependent TLNs become:

$$\mathbf{L}(t) = \mathbf{L}_\delta(t) * e^{i\omega t}. \tag{2.23}$$

For a Kelvin model (homogeneous model) the LNs for an anelastic rheology is calculated by replacing the rigidity μ by the complex rigidity $\tilde{\mu}(s)$ in Eqs. 2.16 and 2.17. Therefore the LNs become the frequency s-dependent:

$$k_2(s) = \frac{3/2}{1 + \dfrac{19\tilde{\mu}(s)}{2\rho g R}}, \quad h_2(s) = \frac{5/2}{1 + \dfrac{19\tilde{\mu}(s)}{2\rho g R}}, \quad l_2(s) = \frac{3/4}{1 + \dfrac{19\tilde{\mu}(s)}{2\rho g R}}, \tag{2.24}$$

and the LLNs

$$k_2{}'(s) = -\frac{1}{1 + \dfrac{19\tilde{\mu}(s)}{2\rho g R}}, \quad h_2{}'(s) = -\frac{5/3}{1 + \dfrac{19\tilde{\mu}(s)}{2\rho g R}}. \tag{2.25}$$

These are the s-dependent LNs for a Kelvin model. Finally, after applying Eq. 2.22 for the LLNs and Eq. 2.23 for the TLNs, the LNs are obtained as functions of time. The tidal perturbations result from periodic perturbations, hence the TLNs could be better calculated by a Fourier transform than by a Laplace transform. Despite this fact `ALMA` uses the Laplace transfrom since it calculates both the TLNs and the LLNs, with a modification of the tidal forcing function done to the periodic function corresponding to the TLNs (Eq. 2.23). Section 2.2 explains in details several rheologies as Maxwell, Burgers and Andrade and gives their complex rigidity.

2.2 Rheologies

An anelastic rheology is described by the combination of one or several springs with one or several dashpots. They can be connected either by series or parallel to each other. A rheology is called linear if its strain-rate is a linear function of stress and/or stress-rate as the Hookean (Eq. 2.18) and the Newtonian (Eq. 2.19) rheologies. Other linear rheologies are the rheologies of Maxwell, Kelvin-Voigt and Burgers [Ranalli, 1995]. A nonlinear rheology as the rheologies of Andrade and Sundberg-Cooper have a non-linear power-law exponent strain-rate [Weertman et al., 1978]. Laboratory experiments suggest that dislocations inside the grains, might explain the long-term deformation of mantle materials: non-linear stress-strain relationship [Weertman et al., 1978; Ranalli, 1995].

2.2.1 Linear rheologies

Maxwell's model (Fig. 2.2 (a)) can be described as a combination of a spring of rigidity μ and a dashpot of viscosity η in series. The Kelvin-Voigt model (Fig. 2.2 (b)) can be described as a combination of a spring of rigidity μ' and a dashpot of viscosity η' in parallel. Burgers' model (Fig. 2.2 (c)) can be described as the Maxwell model and the Kelvin-Voigt model in series.

After an applied stress on the Maxwell model the spring and dashpot deform independently. Therefore there is both the instantaneous deformation of the spring and the time-dependent deformation $\varepsilon(t)$ of the dashpot. The resulting time-dependent deformation has an almost linear ($\sim t$) term only if, as this case, a fluid body is connected in series with other elements [Spada, 2008]. This

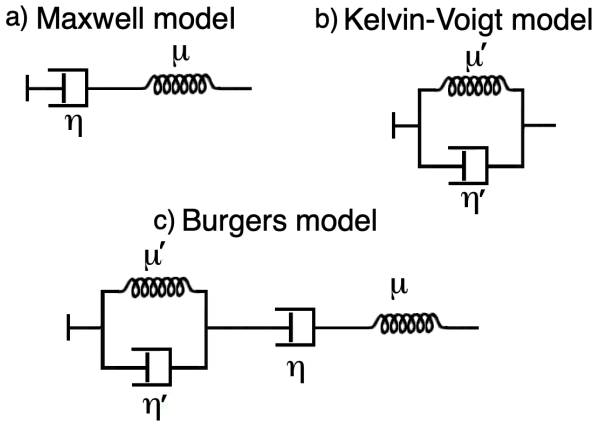

Figure 2.2: Representation of the Maxwell model, Kelvin-Voigt model and Burgers model.

response is called a steady-state response and such a rheology is called a steady-state rheology. Once the stress is removed the elastic spring will recover its initial state (for a spring it is its length). The remaining final strain corresponds to the deformed dashpot which, unlike the spring, does not recover its initial state. In the case of the Kelvin-Voigt model after a stress the dashpot will cause a delay of the deformation of the spring, which is called a transient creep. The deformation is therefore not instantaneous. The total initial state of the model will be recovered, because of the spring, after the stress is removed which is also a delayed response. Finally, for the Burgers model after a stress there is both the instantaneous elastic response of the spring in the Maxwell element and its total recovery afterwards. It also has the steady-state (almost linear $\sim t$) response resulting from the dashpot in series with the other components in the Maxwell element. In addition it has the transient creep caused by its Kelvin-Voigt element before achieving the steady-state and its full recovery afterwards. The deformation that will not be recovered, after the stress is removed, corresponds to the deformation of the dashpot of the Maxwell element.

The complex rigidities of the elastic (Hookean) model, the fluid (Newtonian) model, the Maxwell model, the Kelvin-Voigt model and the Burgers model are in Table 2.1. If $\eta \to +\infty$, the Maxwell model becomes equivalent to an elastic model with rigidity μ. It becomes equivalent to a fluid model with viscosity η if $\mu \to \infty$. The Kelvin-Voigt model becomes equivalent to an elastic model with rigidity μ' if $\eta' = 0$. And if $\mu' = 0$ it becomes equivalent to a fluid model with viscosity η'. If $\eta' \to +\infty$, the Burgers model becomes equivalent to the Maxwell

Table 2.1: The complex rigidities for the elastic (Hooke), fluid (Newton), Maxwell, Kelvin-Voigt and Burgers models.

Rheology	complex rigidity $\tilde{\mu}$	
Hooke	μ	-
Newton	$s\eta$	-
Maxwell	$\dfrac{\mu s}{s+\dfrac{\mu}{\eta}}$	if $\eta \to +\infty$: Hooke if $\mu \to +\infty$: Newton
Kelvin-Voigt	$\mu' + \eta' s$	if $\eta' = 0$: Hooke if $\mu' = 0$: Newton
Burgers	$\dfrac{\mu s(s+\dfrac{\mu'}{\eta'})}{s^2 + s(\dfrac{\mu}{\eta} + \dfrac{\mu+\mu'}{\eta'}) + \dfrac{\mu\mu'}{\eta\eta'}}$	if $\eta' \to +\infty$: Maxwell if $\eta \to +\infty$ and $\mu = 0$: Kelvin-Voigt

model with an elastic element and a fluid element of a rigidity μ and a viscosity η, respectively. And if $\eta \to +\infty$ and $\mu = 0$ it becomes equivalent to the Kelvin-Voigt model with an elastic (rigidity) and a fluid (viscosity) components of μ' and η', respectively.

2.2.2 Nonlinear rheologies

Andrade [1911] proposed a law describing the observed viscous flow in metals and allied phenomena. It is called the Andrade law and describes the transient deformation observed in experiments of materials under stress. They found that a lead wire under extension after the achieving its elastic phase, its deformation becomes proportional to the time, hence the flow becomes viscous. The difference between the rheology of Andrade and the rheology of Burgers is that the one of Andrade has a transient response with continuous infinite relaxation times. Therefore it can be represented with the Maxwell model in series with an added

component, representing the transient response, of an infinite number of springs in series in parallel with an infinite number of dashpots in series. This component represented on the left in Fig. 2.3 illustrates the infinite and continuous distribution of relaxation times observed in the Andrade rheology.

James et al. [1971]; Goetze and Brace [1972] conducted experiments studying the creep of rocks under high pressure (P) and temperature (T), such that the conditions simulate the interior of the Earth. They showed that rocks under stress and at high temperature show a transient creep that obeys the Andrade law. The mineral olivine is a magnesium iron silicate with the formula

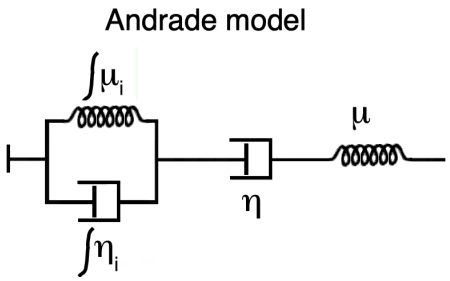

Figure 2.3: Representation of the Andrade modelwhere the transient component is illustrated by an infinite number of springs in series in parallel with an infinite number of dashpots in series as in Castillo-Rogez et al. [2011] .

$(Mg^{2+}, Fe^{2+})_2SiO_4$ such that Mg stands for Magnesium, Fe for Iron, Si for Silicate and O for Oxygen. It's the primary component of the upper mantle of the Earth and it is a common mineral in its subsurface. The creep function of the Andrade law was deduced from the work of both Jackson et al. [2002] and Castillo-Rogez et al. [2011]. It was done by measuring the energy dissipation from grain-size strain of fine grained polycrystalline olivine. The s-dependent creep function $J(s)$ is given by Castillo-Rogez et al. [2011] as:

$$J(s) = \frac{1}{\mu} + \beta\frac{\Gamma(\alpha+1)}{s^{\alpha}} + \frac{1}{\eta s} \tag{2.26}$$

such that Γ is the gamma function, α and β describe the transient response duration in the primary creep and its amplitude, respectively. More precisely β characterizes the intensity of the anelastic friction in the material. Castillo-Rogez et al. [2011] approximated β to be $\beta \simeq \mu^{\alpha-1}/\eta^{\alpha}$. the empirical (or experimental) parameter α has been determined for olivine-rich rocks to have a wide range of 0.1-0.5, most often within 0.2-0.4 [Castillo-Rogez et al., 2011]. Louchet and

Duval [2009] studied the relationship between strain and time, and found that α is close to 1/3 (which is the initial value found by Andrade) if the applied deformation is linear.

The complex rigidity of the Andrade rheology is calculated as $\tilde{\mu}(s) = \dfrac{1}{J(s)}$ (Table 2.2). The transient creep of this law is in the second addend in both $J(s)$ and $\tilde{\mu}$ in Eq. 2.26 and Table 2.2, respectively (which correspond to the left element in Fig. 2.3). The steady-state rheology of Maxwell (Fig. 2.2) lacks this component. Castillo-Rogez et al. [2011] and Dumoulin et al. [2017] have shown with applications to the Earth and with available experimental data for rock that the Andrade law is a better approximation to describe the anelastic attenuation at tidal frequencies. This is due to the transient nature of Andrade's rheological law which mimics well the transition from the elastic phase to the steady-state phase. The rheology of Andrade is used to estimate the deformation of terrestrial planets [Dumoulin et al., 2017; Melini et al., 2022; Goossens et al., 2022].

Table 2.2: The complex rigidities for the Sundberg-Cooper and Andrade models.

Rheology	complex rigidity $\tilde{\mu}$
Sundberg-Cooper	$\dfrac{\mu s\dfrac{\mu'}{\eta'} + s}{s^2(1+\mu^\alpha\Gamma(\alpha+1)(s\eta)^{-\alpha}) + s(\dfrac{\mu}{\eta} + \dfrac{\mu+\mu'}{\eta'} + \dfrac{\mu'}{\eta'}\mu^\alpha\Gamma(\alpha+1)(s\eta)^{-\alpha})}$
Andrade	$\dfrac{\mu s}{s + s\mu^\alpha\Gamma(\alpha+1)(s\eta)^{-\alpha} + \dfrac{\mu}{\eta}}$

As an example of another nonliner rheological law of Sundberg-Cooper [Sundberg and Cooper, 2010] is a recently developed rheology that is usually used for the study of Mercury. The Sundberg-Cooper model is represented as the Andrade model with the Kelvin-Voigt model in series, therefore having an additional purely transient component. It is applied on Mercury [Goossens et al., 2022] since laboratory experiments on materials simulating the mantle of this planet follow

Sundberg-Cooper's law [Renaud and Henning, 2018]. We give its complex rigidity $\tilde{\mu}$ (Table 2.2) that can be applied to any planetary model. In the next section we detail the theoretical basis `ALMA3` [Spada, 2008] [Melini et al., 2022], a code that calculates for a planetary model the LLNs and TLNs of any degree n and under different applied forcing functions $F(t)$. This code is then applied to Venus in chapter 3.

The first step in this PhD was to implement Andrade in the code `ALMA` to calculate the tidal deformation of Venus with this rheology as explained in section 2.3. It was done in this thesis in a collaboration with the referenced writer of the original code [Spada, 2008]. First, I did an analytical calculation of the TLN for an instantaneous (Heaviside $F(t) = H(t)$) forcing to have an outlook on the difference between Mawell and Andrade's rheological laws. This test consisted by analytically calculating the TLNs of degree 2 for a simple homogeneous model, hence a Kelvin model, of Venus using Eq. 2.21 with $l(s)$ represented in Eq. 2.24. The complex rigidity $\tilde{\mu}$ replaced in Eq. 2.21 was therefore the one in Table 2.2. After this test was done and an overview of an expected difference between Andrade and Maxwell was observed, the same complex rigidity $\tilde{\mu}$ was then implemented in a new version of `ALMA` called `ALMA2`. Finally the periodic tidal forcing was then implemented in the presently final version of `ALMA` called `ALMA3` [Melini et al., 2022] where the rheology of Andrade was preserved and tested again, this time, with a heterogeneous model of Venus (see section 3.1.1 in chapter 3). This benchmarking with the heterogeneous model of Venus from Dumoulin et al. [2017] detailed in section 3.1.1 is partially included in the paper Melini et al. [2022].

2.3 ALMA3 and ASTRA codes

We recall from section 2.1.1 that, for the deformation problems, the integration of the governing equations are linearized based on the assumption of small perturbations. These equations give expressions of the gravity field U_n, radial V_n and tangential W_n deformations (Eq. 2.10). For the loading and tidal deformations the fundamental solutions (Eq. 2.10) are written in terms of the LNs as in Eq. 2.13. In the case of the anelastic rheologies (section 2.2) Eq. 2.13 is hard to solve in the time domain. According to the correspondence principle [Peltier, 1974] the fundamental solutions can be written and solved in the Laplace domain.

One way to calculate the LNs with this technique is the viscoelastic normal-modes (hereafter VNM) method introduced in Peltier [1974] which solves the equations using matrix propagation method [Spada et al., 1992]. Afterwards, the LNs are transformed to the time domain with an inverse Laplace transform, numerically or analytically. A code called `TABOO` (a posT glAcial reBOund calculatOr) [Spada et al., 2004] is a fortran code that uses the VNM method and transforms the LNs analytically to the time domain. In `TABOO` only a limited number of layers (no more than 9) and only the Maxwell viscoelastic rheology can be applied. With added layers and complex rheologies the analytical inverse Laplace transform becomes more complicated. A step forward is the fortran code `ALMA3` (plAnetary Love nuMbers cAlculator) [Spada and Boschi, 2006; Spada, 2008] which also calculates the LNs using the VNM method similarly to `TABOO`. `ALMA3` applies the numerical Post-Widder [Post, 1930; Widder, 1934] inversion formula for the inverse Laplace transform. It is not limited to a certain number of layers and many more rheologies are already implemented and applied unto any layer. The linear rheologies of Hooke, Newton, Maxwell, Kelvin-Voigt and Burgers and the nonlinear rheology of Andrade are implemented in this version called `ALMA3` [Melini et al., 2022]. The code assumes a spherically symmetric (1 dimensional or simply 1D), incompressible, viscoelastic and self-gravitating model of a planet.

The response of a planet due to a deforming potential U is divided as stated in section 2.1.1 as a sum of two potentials U_1 and U_2. The external potential U_1 is the direct (or rigid) response of the planet and its internal response U_2 is its non direct incremental. On the surface of the planet we replace $r = R$ in Eq. 2.13. We recall that $k = \frac{U_2}{U_1}$, hence we write as Vermeersen et al. [1996]:

$$\begin{aligned} U &= U_1 + U_2, \\ &= U_1(1 + k). \end{aligned} \tag{2.27}$$

On the surface we have $U_1 = \frac{Rg_s}{M}$ where g_s is the planet surface gravity and M is its total mass. The TLN k can then be written from Eq. 2.27, h and l become

from Eq. 2.13 as in Spada and Boschi [2006]:

$$\begin{aligned} h &= y_1 \frac{M}{R}, \\ l &= y_3 \frac{M}{R}, \\ k &= \frac{M}{R g_s} U - 1. \end{aligned} \tag{2.28}$$

We denote by L the number of layers and r_i the radius (also called radial boundary) of each layer with $i \in \{1, \cdots, L\}$, $r_0 = 0$ being the center of the planet and r_1 the core radius. We have $r_1 < \cdots < r_L$ and r_L corresponds to its free surface. For an applied forcing $F(t)$, and its Laplace inverse $f(s)$, the VNM method consists of solving the governing equations which corresponds to using the technique of matrix propagation [Spada et al., 1992]. Here is an overlook of the equations behind the theoretical basis of `ALMA3` which is given in Spada and Boschi [2006] and Spada [2008] and most recently in Melini et al. [2022]. For a harmonic degree n the equations can be solved in the Laplace domain with the standard propagator methods. Their solutions for $r = R$ where R is the surface of the planetary body are such as

$$(y_1(s), y_3(s), U(s))^T = [P_1 W(s) J][P_2 W(s) J]^{-1} f(s) \vec{b}, \tag{2.29}$$

where J is the core-mantle-boundary interface matrix of 6×3 dimension (given analytically in Sabadini et al. [1982]). The three-component vector $\vec{b}$ corresponds to the surface boundary conditions therefore it depends on the deformation type (loading deformation or tidal deformation) [Sabadini et al., 1982]. The matrix P_1 (3×6 dimension) is a projection matrix which extracts the first, third and fifth components from $\vec{y}$ as:

$$P_1 \vec{y} \equiv (y_1, y_3, y_5)^T. \tag{2.30}$$

Additionally P_2 (3×6 dimension) is a projection matrix as:

$$P_2 \vec{y} = \vec{b} f(s). \tag{2.31}$$

The matrix W is called the propagator and it is such as:

$$W(s) = \Pi_{j=L-1}^{1} Y_j(r_{j+1}, s) Y_j^{-1}(r_j, s). \tag{2.32}$$

The matrix $Y_k(r, s)$ such that $k \in \{1, \cdots, L-1\}$ is the fundamental matrix of 6×6 dimension which propagates the solution from the core ($r = r_1$) to the surface ($r = R$). Since the planet is assumed to be incompressible Y_k depends on the rheology (specifically its complex rigidity $\tilde{\mu}$) of the layer. It contains the linearly independent solutions of the fundamental equations (Eq. 2.9). The three-component vector $\vec{b}$ expresses the surface boundary conditions corresponding to either the loading or tidal problems . Calculating the viscoelastic response consists on finding the roots and residues of the secular equation $|P_2 W J| = 0$. For an impulsive load ($f(s) = 1$) the s-dependent LNs are expressed as:

$$\mathbf{l}(s) = \mathbf{L}_e + \sum_{1}^{m} \frac{\mathbf{L}_i}{s - s_i}, \tag{2.33}$$

where m is the number of viscoelastic normal modes, $\mathbf{L}_e$ the elastic response ($s \to +\infty$) and s_i are the roots of the secular equation and $\mathbf{L}_i$ are the residues such that $i \in \{1, \cdots, m\}$. The LNs in the time domain are calculated in `TABOO` with complex contour integration on the Bromwich path. With the residue theorem of Cauchy where the Laplace inverse transform becomes equivalent to a sum of the viscoelastic responses. For an impulsive load ($F(t) = \delta(t)$) the LNs are obtained as the sum of the elastic and the viscoelastic responses as follows:

$$\mathbf{L}(t) = \mathbf{L}_e \delta(t) + \sum_{1}^{m} \mathbf{L}_i e^{s_i t}, \tag{2.34}$$

This method is applied in `TABOO` for the Maxwell rheology for the mantle and a limited number of layers. For a different rheology and more than 9 layers the root finding becomes a lot more complex and a different approach is needed. The Post-Widder [Post, 1930; Widder, 1934] Laplace inverse is a non-conventional method which is introduced and benchmarked in Spada and Boschi [2006] and it allows to overcome the limitations of the VNM method. The original version of `ALMA3` [Spada and Boschi, 2006; Spada, 2008] aimed at calculating the LNs for a forcing term following a Heaviside time-history ($F(t) = H(t)$ equivalently $f(s) = 1/s$). Spada et al. [2011] compared their new approach to different ones as

the original VNM method in TABOO [Spada et al., 2004] and the Spectral-finite elements method [Martinec, 2000]. The Heaviside forcing function is usually applied to the loading deformation. The latest version of this code called ALMA3 [Melini et al., 2022] accounts also for a periodic forcing that can be applied to the TLNs calculation. For the tidal deformation of period τ the forcing function is $F(t) = e^{i\omega t}$ where $\omega = \frac{2\pi}{\tau}$. In this case the TLNs are complex numbers with a real part and an imaginary part. The theory is explained in details in [Melini et al., 2022]. As stated in Eq. 2.23 the TLNs in the time domain is obtained by the convolution of $\mathbf{L}_\delta(t)$ and $F(t)$. Eq. 2.23 can be expressed as

$$\mathbf{L}(t) = e^{i\omega t} \int_0^\infty \mathbf{L}_\delta(t') e^{-i\omega t'} dt' = \mathbf{L}'(\omega) e^{i\omega t} \tag{2.35}$$

where $\mathbf{L}'(\omega) = \mathcal{L}\{\mathbf{L}_\delta(t)\}$. Therefore we obtain with $f(s) = 1$ and $s = i\omega$ in Eq. 2.29:

$$(y_1(\omega), y_3(\omega), U(\omega))^T = [P_1 W(i\omega) J][P_2 W(i\omega) J]^{-1})\vec{b}. \tag{2.36}$$

Finally the TLNs are expressed as in Eq. 2.28:

$$\begin{aligned} h(\omega) &= y_1(\omega)\frac{M}{R}, \\ l(\omega) &= y_3(\omega)\frac{M}{R}, \\ k(\omega) &= \frac{M}{R g_s} U(\omega) - 1. \end{aligned} \tag{2.37}$$

as a function of ω. The real and imaginary parts are the amplitude and lag of the response, respectively. The TLN k describes the change in the gravitational field of a planet due to the influence of an external gravity field. Its predominantly of degree 2, denoted by k_2. Its imaginary part is always negative therefore we denote $k_2 = {k_2}^r - i{k_2}^i$ where ${k_2}^r$ is the real part and ${k_2}^i$ the absolute value of the imaginary part. The phase lag $\epsilon = \frac{k_2^i}{k_2^r}$ which is $\epsilon = 0$ (since $k_2^i = 0$) if the planet is elastic. The energy dissipation of a planet is also estimated by the TLNs through its quality factor Q and it is defined in Murray and Dermott [2000]. It is expressed through the time lag as $Q = \frac{1}{\sin\epsilon} = \frac{\|k_2\|}{k_2^i}$ such that $\|k_2\| = \sqrt{{k_2^r}^2 + {k_2^i}^2}$, and its inverse Q^{-1} is called the dissipation.

The theoretical basis of the code ASTRA which solves the seismic rebound

problem is explained in details in Melini et al. [2008]. Unlike `ALMA` no update was made to the code in this PhD. Therefore we give a general outlook on it since it was simply used in the last chapter to provide preliminary results for future studies. `ASTRA` has the same basis than `ALMA` which solves the loading and tidal and deformations. More specifically the common basis is that the seismic rebound problem also requires the simultaneous solution of the constitutive equations, derived from the continuity equation (mass conservation, Eq. 2.4), the constitutive equation (stress-strain relation, Eq. 2.3) and the momentum equation linearized for small perturbations (linear momentum conservation, Eq. 2.5). Integrating these perturbation equations of conservation along with integrating the Poisson's equation for the deforming potential (Eq. 2.6) and assuming the potential is harmonic outside the planet (Laplace equation, Eq. 2.7) give expressions of the gravity field and the surface deformations (Eq. 2.10). Similarly to `ALMA`, `ASTRA` solves the equations using matrix propagation method [Spada et al., 2004] using the approach of the VNM method and the Post-Widder inversion formula. Main differences exist between the two codes, since differences exist between the seismic rebound problem and the loading and the tidal cases. First their are no surface stresses as the tidal deformation problem and contrarily to the loading deformation problem. Second, the forcing term for a seismic dislocation translates to an internal couple of forces: a dislocation force. This forcing couple has both spheroidal and toroidal components where the two other deformation problems (tidal and loading) have simply a spheroidal component. Denoting by $x(s)$ the solution for the seismic deformation, for the spheroidal and toroidal components the solution is such as:

$$x(s) = [P_1 W(s) J][P_2 W(s) J]^{-1} f(s)\vec{b} + \vec{p} \tag{2.38}$$

similarly to Eq. 2.29 where the three-component vector $\vec{p}$ corresponds to the source boundary conditions. In this particular code the seismic dislocation is assumed to be instantaneaous, therefore the forcing term is $F(t) = H(t)$ hence $f(s) = 1/s$ as the loading problem.

The time-dependent solution $x(t)$ is obtained from the inverse Laplace transform of $x(s)$ of Eq. 2.38. `ASTRA` uses the Post-Widder inversion formula [Post, 1930] and [Widder, 1934] for the Laplace inversion (section 2.3) as `ALMA`. Solving the seismic problem has a slower harmonic convergence in comparison to the

loading and tidal problems. The spheroidal and toroidal solution vectors contain harmonic coefficients for deformation, perturbation to the gravity field and incremental stress tensor. The observables given by $x(s)$ are the surface displacement ($\overrightarrow{d}$), the incremental gravitational potential (ϕ) and the variation of the gravity acceleration (Δg). They are obtained from harmonic summation of the spheroidal and toroidal components for a set of spherical coordinates (r, θ, φ) called the observation points. A semi-analytical approach was first developed to compute the postseismic deformation of a planet [Piersanti et al., 1995]. This approach extended the work of Sabadini et al. [1984] and is based on the VNM method. As in the case of the loading and tidal deformations the governing equations are solved in the Laplace domain instead of the time domain according to the correspondence principle of linear viscoleasticity [Peltier, 1974]. In the same paper [Melini et al., 2008] modeled accurately the Earth coseismic deformations induced by the 2004 Sumatra-Andaman earthquake. Their results reproduced the surface deformation observed from Global Positioning System (GPS) stations and the geoid signals observed by the satellite GRACE. The model of the planet is the same as the one applied in `ALMA`: a spherically symmetrical, incompressible and self-gravitating modeling. Any linear viscoelastic rheology can be implemented in the code with its corresponding rigidity (section 2.2). The rheologies already available in `ASTRA` are Hooke (elastic body), Maxwell, Burgers, Newton, Kelvin and Newtonian (fluid body). The non linear rheology of Andrade is also implemented.

In chapter 3 the k_2 and Q are calculated with `ALMA3` for different models of Venus. First (section 3.1) they are calculated for a model from Dumoulin et al. [2017] and the results are compared with theirs. Afterwards (section 3.2) with random Monte-Carlo sampling, a wide range of internal structure parameters of Venus is explored. This method enables the study of a high number of possible models with different assumptions on the structure. The most recently estimated value of $k_2 = 0.295 \pm 0.066$ (2σ) [Konopliv and Yoder, 1996] and an estimated range of Q between 20 and 100 [Correia et al., 2003; Dumoulin et al., 2017] are used as a filter the models and preserve the one that fall into these estimations. A 1D seismic source can be set in `ASTRA` (in other words aligned rupture points). The seismic source is defined in the code by the coordinates (longitude,latitude) of its center (θ,φ), its depth and seismic moment M_0, strike, dip and rake angles, length and number of rupture points p. For a source with $p > 1$, M_0 is divided

equally between the rupture points, therefore having each a seismic moment of M_0/p. The observables can either be computed for a 1D set of observations (segment) or a 2D set of observations (rectangle/map) within a certain depth. The spacial observation steps (distance between the points) is also chosen. The observation time can either be set to $t \to 0$ to calculate the coseismic (or elastic) rebound or set to $t > 0$ for the postseismic rebound calculation. In chapter 4 the code is applied for a seismic dislocation on the Earth model and a Venus model. We compute the observables $\mathbf{d}$ and Δg in a 2D space on the surface of the planet (observation depth equal to 0 km).

3. Venus tidal deformations

In what follows we use the tidal deformation of Venus from the periodic TLNs to constrain the internal structure of the planet. The most important tidal deformations are for a period of $\tau = 58.4$ days corresponding to the solar tides period [Cottereau et al., 2011]. We use the `ALMA` code (described in section 2.3) to estimate the periodic response of Venus to the tidal excitation. As we explained in section 2.3, `ALMA` needs some inputs for computing the TLNs. These inputs describe the rheological parameters of each layer: viscosity, density, rigidity and thickness. These properties are poorly known for Venus. So in order to explore the possible internal profiles and their expressions in terms of TLNs, we randomly sample intervals of possible values for each rheological parameter in using a Monte-Carlo approach. A Monte-Carlo simulation consists in randomly selecting a set of parameters that will follow, in our case, uniform distributions. We explore each one within a wide range of values leading to a large number of models of Venus internal structure. `ALMA` is then used to calculate the TLN k_2 for each model which will serve as a filter to filter out the models non consistent with the most recent observation of k_2^{MPVO} (Table 1.1). This way we obtain a set of possible models for the internal structure of Venus. We use homogeneous and incompressible layered models. The outputs of `ALMA3` are the real k_2^r and imaginary k_2^i parts of the TLN k_2 from both which we calculate the quality factor Q.

3.1 Adaptation of ALMA3 for Venus

In this section we present the results obtained using `ALMA3` to compute the k_2^r and k_2^i for Venus assuming its mantle follows the Andrade rheology and has four different viscosities $\eta \in \{10^{19}, 10^{20}, 10^{21}, 10^{22}\}$ Pa $\cdot$ s. As a model of Venus we use the radial profile from Dumoulin et al. [2017] plotted in Figs. 3.1 and 3.2.

3.1.1 Comparison with previous work

In the work of Dumoulin et al. [2017], the TLN k_2 is computed by integrating the radial functions associated with the gravitational potential (denoted as y_5), as defined by Takeuchi and Saito [1950]. The simplified formulation of Saito [1974] relying on the radial function, y_5 is thus employed. This method is derived from the classical theory of elastic body deformation and the energy density integrals commonly used in the seismological community. The system of six differential equations (from which the radial function y_5) is solved by integrating the three independent solutions using a fifth-order Runge-Kutta method. A number of 10 models with different density ρ and rigidity μ profiles of Venus have been constructed [Dumoulin et al., 2017]. They all assume a fluid core, 5 are based on a cold temperature profile [Steinberger and Werner, 2010] and the other 5 on a hot temperature profile [Armann and Tackley, 2012]. They are constructed from composition and hydrostatic pressure from PREM extrapolation [Dziewonski and Anderson, 1981]. The model that we use is the number 5 from the hot temperature models denoted in their work as V5-T_{hot} (see Dumoulin et al. [2017]) therefore referred to as **V**.

The model **V** is characterized by a lower Fe content than the other models. This difference in composition is supposed to explain the 1.9% observed lower density of Venus compared to the density Venus would have if it was made of the same material as the Earth [Bas, 1981]. Model **V** was also chosen [Dumoulin et al., 2017] to explore different scenarii for the state of the core other than a fluid one, assuming a solid and partially fluid and partially solid core. The model has 500 layers excluding the atmosphere, hence a radial discretization with a step slightly larger than 12 km. To compare with their method and results, each major layer (core, lower mantle, upper mantle and crust) is averaged to be as one homogeneous layer. Figs. 3.1 and 3.2 show the model **V**. For the comparison with Dumoulin et al. [2017] with a mantle following the Andrade rheology, we use a wide range for the Andrade empirical parameter α. As for the other layers the model **V** is composed by an elastic crust ($\eta \to \infty$) and an inviscid fluid core ($\eta = 0$ Pa $\cdot$ s and $\mu = 0$ Pa). The values of α range from 0.1 to 0.5. Fig. 3.3 (a) and (b) show respectively the real part (i.e. k_2^r) and imaginary part (i.e. k_2^i) of k_2. Their associated quality factor Q is calculated as $Q^{-1} = \dfrac{k_2^i}{\|k_2\|}$ such that $\|k_2\| = \sqrt{k_2^{r\,2} + k_2^{i\,2}}$ and is shown in Fig. 3.3 (c) and (d). For olivine-rich rocks

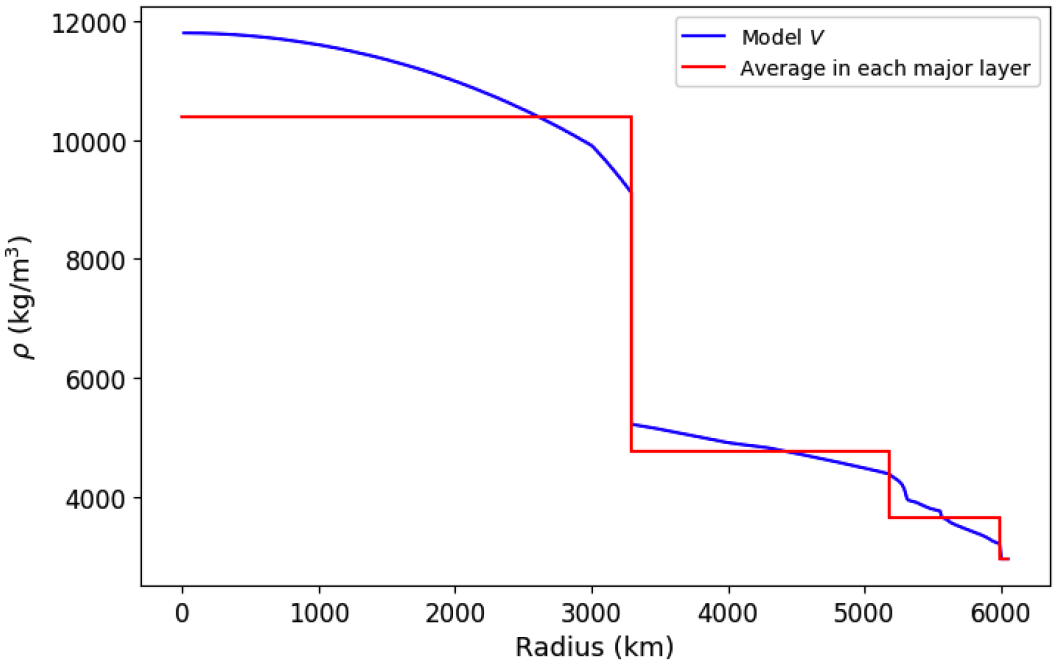

Figure 3.1: Density ρ (kg/m^3) for the model **V** from Dumoulin et al. [2017] and our 4-layer model derived by averaging each major layer.

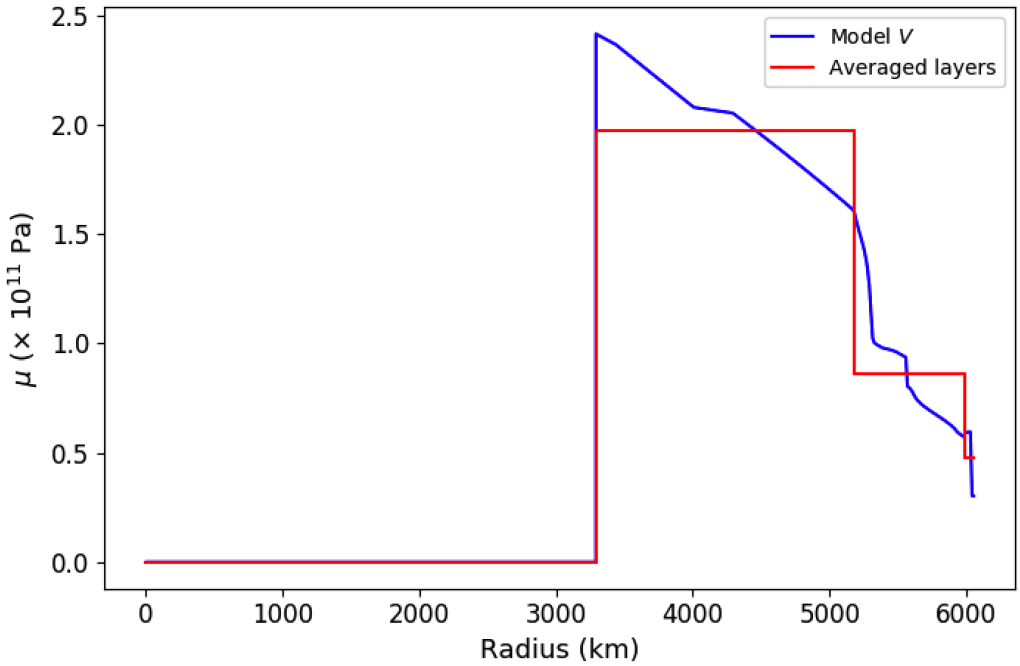

Figure 3.2: Rigidity μ (10^{11} Pa) for the model **V** from Dumoulin et al. [2017] and our 4-layer model derived by averaging each major layer.

α is between 0.2 and 0.4 [Jackson et al., 2002]. The variation of α in Dumoulin et al. [2017] is from 0.2 to 0.3 which is included in the olivine-rich rocks range. The range of values obtained in their work is represented as vertical lines in Fig. 3.3. For the real part k_2^r (Fig. 3.3 (a)) and for α between 0.2 and 0.3, the maximum difference between our results and those of Dumoulin et al. [2017] are between 1.8% to 2% depending on the mantle viscosity. These values translate into a difference of 5×10^{-3} and 7×10^{-3} in k_2^r, respectively. It is the same magnitude obtained (see also Figs 6 and 7 in Spada et al. [2011]) by comparing different methods to calculate the LLN (loading Love number) for a Heaviside step function as mentioned previously in section 2.3. Furthermore, the results

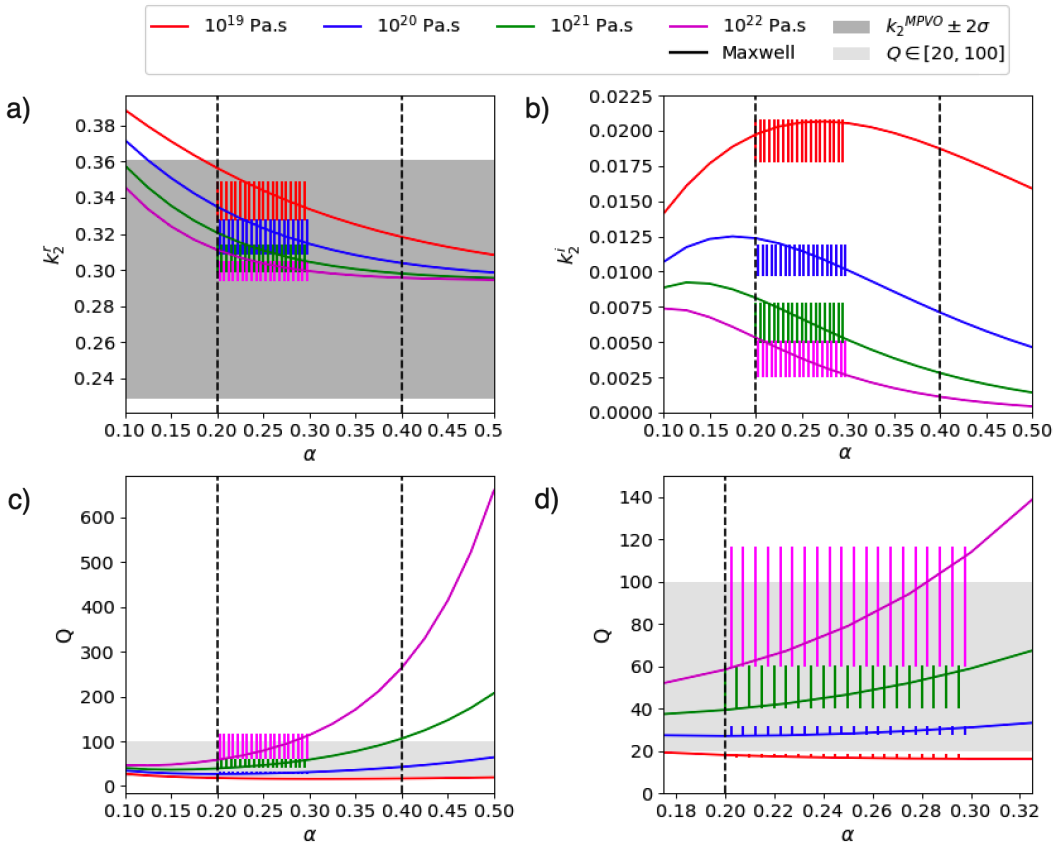

Figure 3.3: Real tidal Love number k_2^r (a), imaginary tidal Love number k_2 (b), quality factor Q (c) and its zoom into the area of interest (d) as functions of α for a mantle with an Andrade rheology and different viscosities for model **V**. The vertical bars represent the range obtained by Dumoulin et al. [2017] for $\alpha \in [0.2, 0.3]$. The vertical dashed lines correspond to α of 0.2 and 0.4. The dark grey area corresponds to the estimated value of $k_2^{\text{MPVO}} \pm 2\sigma$ [Konopliv and Yoder, 1996]. The light grey area corresponds to the Q range from 20 to 100 [Correia et al., 2003].

for k_2^r for $\alpha \in [0.2, 0.4]$, corresponding for olivine-rich rocks, fall into the range of the most recently estimated value k_2^{MPVO}, with a $\pm 2\sigma$ uncertainty [Konopliv and Yoder, 1996]. The values of k_2^r for this range of α vary maximum from 0.015 to 0.04 depending on the mantle viscosity, equivalently 7.5 to 20 times the uncertainty 2σ of EnVision which is 0.002 for k_2^r. The values of k_2^i for the same range of α vary from 0.002 to 0.005, equivalently 1 to 2.5 times the uncertainty 2σ of EnVision which is also 0.002 for the imaginary part.

The imaginary part k_2^i (Fig. 3.3 (b)), for $\eta \geq 10^{20}$ Pa $\cdot$ s, is different between 1% and 2.16% from our estimations and the ones of Dumoulin et al. [2017] depending on the value of α. For α between 0.2 and 0.3, the only non monotonous variation of k_2^i is obtained for $\eta = 10^{19}$ Pa $\cdot$ s. This is the main difference between the two results, since the range of variations between the minimum and maximum for the considered α range values is smaller than that of Dumoulin et al. [2017]. More specifically, the upper boundary is higher of 2.5% and the lower boundary is lower of approximately 6%. Finally the quality factor Q is illustrated in Fig. 3.3 (c) and zoomed in Fig. 3.3 (d) on the area of interest, one can see on these figures that its span (upper and lower boundaries) for $\alpha \in [0.2, 0.3]$ is almost the same for each viscosity. A different method was used Dumoulin et al. [2017] for the calculation of the TLN as well as the number of layers and initial conditions. Despite that, our results are similar and show the same tendencies for each of the mantle viscosities and values of α which define the transition phase of the Andrade law.

3.1.2 Effect of the rheology on the TLN k_2

In this subsection we compare the Maxwell and Andrade rheologies. Fig. 3.4 (a) shows the results of k_2^r, k_2^i and Q for mantle viscosities η and α between 0.1 and 0.5. Fig. 3.4 (a) shows that k_2^r is decreasing with increasing α, for each of the explored mantle viscosities. The k_2^r and k_2^i for an Andrade mantle gets closer to the results for a Maxwell mantle with higher α values (Fig. 3.4 (a) and (b)). This fact is expected from equation 2.26 which approaches the Maxwell creep equation with these higher α values. Fig. 3.4 (c) shows that the quality factor is more sensitive to the mantle viscosity for a Maxwell rheology than it is for Andrade rheology. Correia et al. [2003] shows that Q is between 20 and 100. Fig. 3.4 (c) and (d) show that Q has a magnitude less than 10^3 for the Andrade

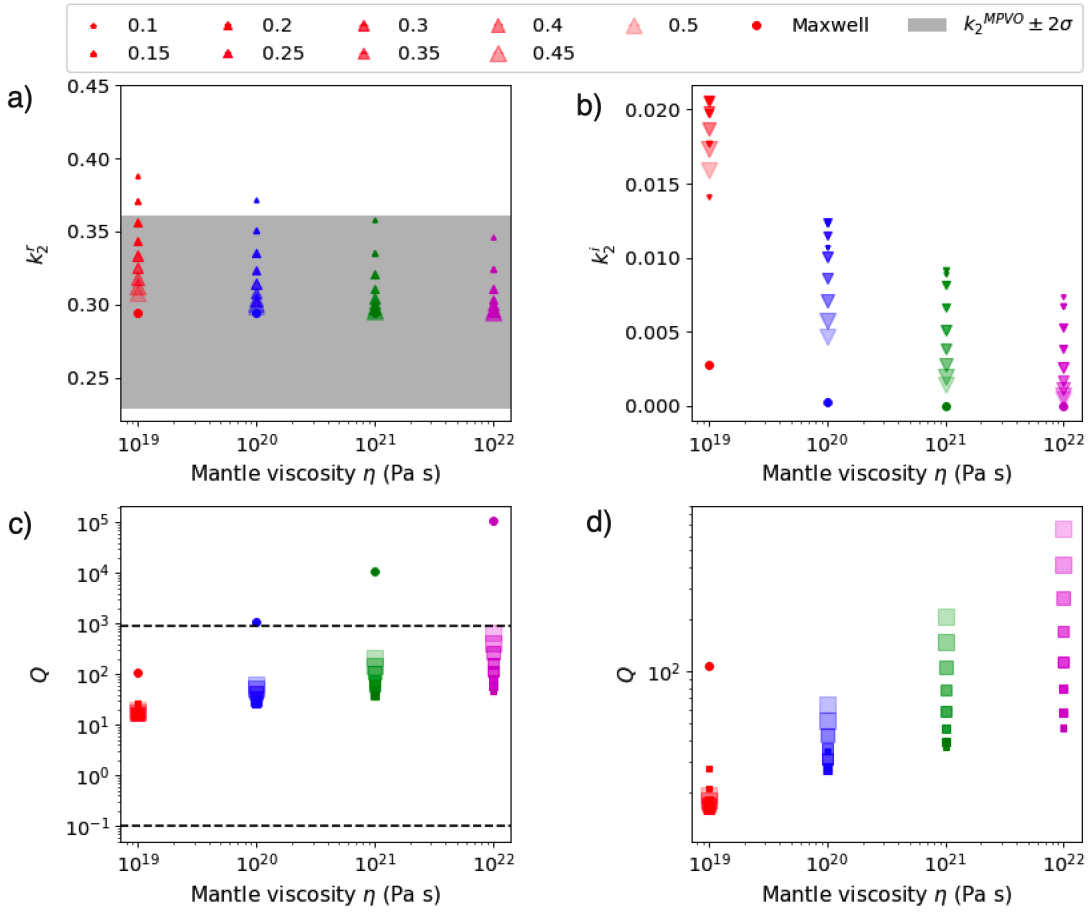

Figure 3.4: Real tidal Love number k_2^r (a), imaginary tidal Love number k_2 (b), quality factor Q (c) and its zoom into the area of interest (d) as functions of α for a mantle with Maxwell and Andrade rheologies and different viscosities for model **V**. The vertical dashed lines in (c) correspond to the zoomed area in (d). The dark grey area corresponds to the estimated value of $k_2^{\mathrm{MPVO}} \pm 2\sigma$ [Konopliv and Yoder, 1996]. The light grey area corresponds to the Q range of 60 ± 40 [Correia et al., 2003].

mantle rheology for the explored range of α. Which leads to the same conclusion as the other studies (see [Dumoulin et al., 2017; Castillo-Rogez et al., 2011]) that Andrade's rheological law is a better choice to mimic the attenuation behavior of rocks in the tidal period.

3.1.3 Effect of the atmosphere on the TLN k_2

The atmosphere of Venus is 92 times more massive than that of the Earth. The effect of the thick and dense atmosphere on k_2 is tested. The model of the atmosphere is taken from the Venus International Reference Atmosphere (i.e.

VIRA) [Seiff et al., 1985]. The atmosphere has a thickness of 100 km, a density $\rho_{\text{atm}} = 36.5$ kg/m^3 and a rigidity $\mu_{\text{atm}} = 0$ Pa (i. e. fluid). The viscosity of the atmosphere is set to 10^{-5} Pa $\cdot$ s [Schiffer et al., 1968] for each computation.

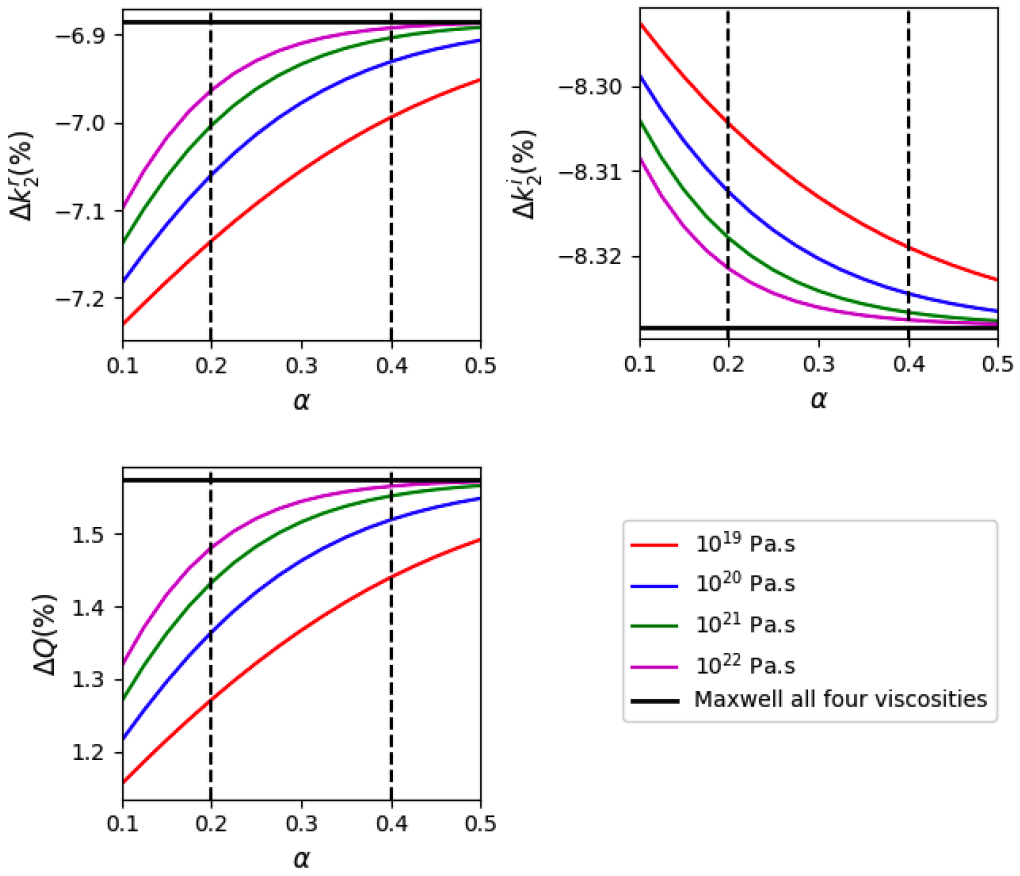

Figure 3.5: Difference in percentage (%) of k_2^r, k_2^i and Q of Venus without and with an atmosphere as a function of $\alpha \in [0.1, 0.5]$ for model **V**. The lines correspond to a mantle with either Andrade or Maxwell rheologies for different mantle viscosities η (Pa $\cdot$ s). The vertical dashed lines correspond to α of 0.2 and 0.4.

Fig. 3.5 represents the variations in % of the k_2^r, k_2^i and Q after we include the atmosphere. The atmosphere induces a decrease of the real and imaginary parts of k_2 at a maximum level of respectively 7.2% and 8.34% (Fig. 3.5). The former percentage of 7.2% is equivalent to a decrease in k_2^r of a maximum of 0.026 which is lower than the formal uncertainty (1σ). The variation depends slightly on the value of α and the mantle viscosity. This effect on quality factor Q, is only of a maximum of 1.65%. We conclude that the atmosphere does not significantly affect the studied parameters despite its high density and low viscosity.

3.1.4 Conclusions of the benchmarking

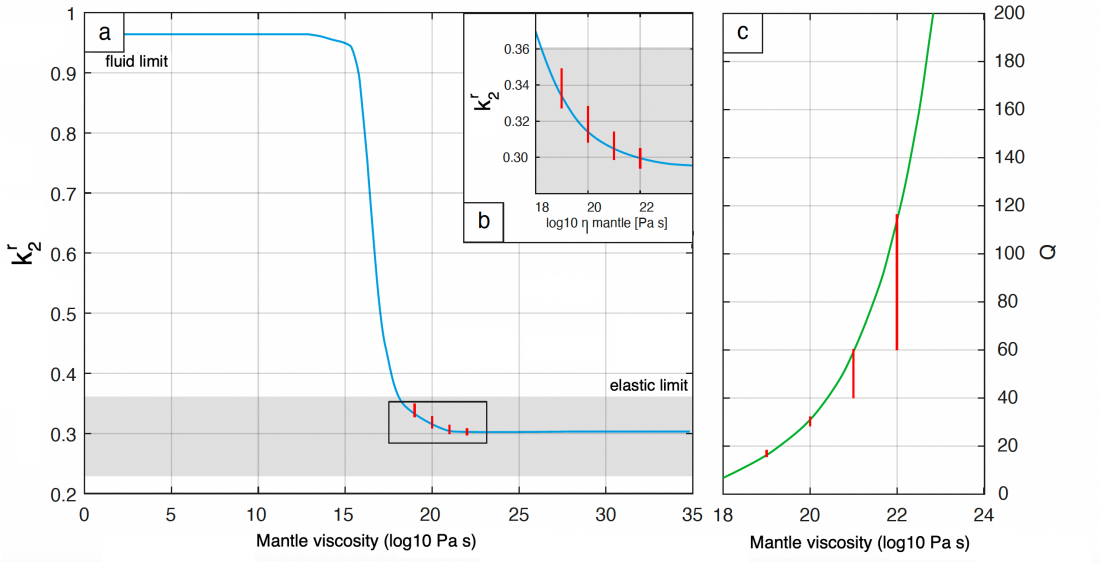

Figure 3.6: Real tidal Love number k_2^r (a), its zoom into the area of interest (b) and quality factor Q (c) as functions of the mantle viscosity for model **V**. The red vertical lines show the range of the results of Dumoulin et al. [2017] for α from 0.2 to 0.3. The dark grey area corresponds to the estimated value of $k_2^{\mathrm{MPVO}} \pm 2\sigma$ [Konopliv and Yoder, 1996].

A generalization of the study is made by expanding the viscosity range of the mantle from the previous range of 10^{19}, 10^{20}, 10^{21} and 10^{22} Pa · s to a complete variation from the fluid limit ($\eta \to 0$ Pa · s) to the elastic one ($\eta \to 10^{35}$ Pa · s) for $\alpha = 0.3$. Fig. 3.6 shows k_2^r and Q as a function of the mantle viscosity. The red vertical lines show the range of the results of Dumoulin et al. [2017] for α from 0.2 to 0.3 as in Fig. 3.3. The grey area represents the range of the estimated $k_2^{\mathrm{MPVO}} \pm 2\sigma$. The plot shows that for $\eta \geq 10^{19}$ Pa · s the k_2 fits well into the estimated range, this confirms the choice of the mantle viscosity range of Dumoulin et al. [2017]. The quality factor Q falls between 10 to 120 for both results which is in the same magnitude as the range found in Correia et al. [2003] of 20 to 100. The results of this work are in good agreement with that of Dumoulin et al. [2017] for model **V** in the context of the present accuracy in the Love number determinations (Fig. 3.3). Differences in both approaches stand in the number of layers and the conjecture of an incompressible planet, in opposition to Dumoulin et al. [2017] where a compressible planet is assumed. The comparison between Maxwell and Andrade for the mantle rheology (Fig. 3.4) shows that the results depend on the value of α. For α most likely between

0.2 and 0.4 (olivine-rich rocks), our results for k_2^r is in the range of the estimated Magellan and PVO k_2 with an uncertainty of 2σ range [Konopliv et al., 1999]. In what follows, `ALMA` is applied to calculate the TLN k_2 for different assumptions of the internal structure of Venus. The results are then used to filter the possible models using present observational and geophysical constraints.

3.2 Constraints on the Venusian internal structure

Since the internal structure of Venus is yet poorly constrained, we apply a Monte-Carlo simulation to randomly select several internal parameters of some of its layers within a certain range. This selection paves the way for the exploration of wide ranges of each parameter. We use the moment of inertia and mass to filter the possible models before calculating the TLN. After applying the remaining models to `ALMA`, k_2 and Q are calculated and used as an additional filters. Finally, constraints on the internal structure of Venus are made.

3.2.1 Statistical approach

Three types of profiles are considered in our Monte-Carlo approach: the presence of a fluid core (**Class 1**), a solid core (**Class 2**) and a fluid outer core with a solid inner core (**Class 3**). We denote by L the number of layers therefore $L = 4$ for **Classes 1** and **2** and $L = 5$ for **Class 3**. For each class, the crustal thickness and density are set to 60 km and 2950 kg/m^3 respectively [Steinberger and Werner, 2010]. The upper mantle radius is then fixed to 5991.8 km. The viscoelastic layers, namely the lower mantle, the upper mantle and the solid core/inner core follow the Andrade law $\alpha = 0.3$. The crust is elastic $\eta \to \infty$ and the viscosity of the inviscid fluid layers are set to be 10^{-5} Pa $\cdot$ s (Table 3.1). The density of each layer is denoted by ρ_i with $i \in \{1, \cdots, L\}$ and its radius (also called radial boundary) by r_i with $r_0 = 0$ being the center of the planet. The volume of each layer is:

$$V_i = \frac{4}{3}\pi(r_i^3 - r_{i-1}^3) \tag{3.1}$$

and its mass is $M_i = \rho_i \times V_i$. For each class we apply a random Monte-Carlo selection of parameters within a certain range. These parameters are the thickness,

density and viscosity of several layers defined in Table 3.1. After the random selection of models we accept only the ones such that $r_1 < \cdots < r_L$. In order to keep models consistent with the mass M_V (Table 1.1), the density of one layer for each class is deduced from the others. The compensation is done with the layer corresponding to $i = 1$, which is the core for **Classes 1** and **2** and the inner core for **Class 3** as:

$$\rho_1 = \frac{M_V - \sum_{i=2}^{L} M_i}{V_1}. \tag{3.2}$$

The compensated parameters are denoted by "compensation" in Table 3.1. The compensated core density of **Classes 1** and **2** are only accepted if $0 < \rho_{\text{Core}} < 22000$ kg/m^3 and the compensated inner core density is only accepted if $0 < \rho_{\text{IC}} < 30000$ kg/m^3. These are theoretical and relatively high upper boundaries for a terrestrial planet taking into account the Earth [Dziewonski and Anderson, 1981], terrestrial planets [Trønnes et al., 2019] and Venus [Shah et al., 2021]. In a second time, we accept the models with no density inversions ($\rho_1 > \cdots > \rho_L$). Finally we select models that fall within the limits and uncertainties of the total mass (since the density ρ_1 has been estimated to do so) and of the moment of inertia C as given by:

$$M_V = \sum_{i=1}^{L} M_i. \tag{3.3}$$

and

$$C = \frac{8\pi}{15} \sum_{i=1}^{L} \rho_i \left(r_i^5 - r_{i-1}^5 \right), \tag{3.4}$$

such that $r_0 = 0$ is the center of the planet. Thus, the normalized moment of inertia, MoI, for each model is obtained from Eqs. 3.3 and 3.4 as:

$$\text{MoI} = \frac{C}{M_V R_V^2}. \tag{3.5}$$

After filtering out the hypothetical models that do not match M_V and MoI, we use `ALMA` to compute k_2. The TLN k_2 from Table 1.1 is used as an additional filter. The last filter is the quality factor Q taken to be between 20 and 100 [Correia et al., 2003]. The rigidity is assumed to be constant for each layer and to be the same than model **V** of Dumoulin et al. [2017].

Table 3.1: Venus internal parameters, both fixed and simulated with random Monte-Carlo within their respective ranges

	r (km)	ρ (kg/m^3)	η (log10 Pa $\cdot$ s)	μ (GPa)
Crust	6052.8	2950	$+\infty$	47.65
Upper mantle	5991.8	$1000-15000$	$15-25$	85.7
Lower mantle	$2000-5900$	$3000-15000$	$15-25$	196.94
Fluid core (**Class 1**)	$1000-5000$	compensation	-5	0
Solid core (**Class 2**)	$1000-5000$	compensation	$11-22$	125.63
Outer core (**Class 3**)	$1000-5000$	$1000-15000$	-5	0
Inner core (**Class 3**)	$1-5000$	compensation	$10-20$	273.91

3.2.2 Results

For each layer we denote by $r_{\mathcal{L}}$, $th_{\mathcal{L}}$, $\rho_{\mathcal{L}}$ and $\eta_{\mathcal{L}}$, the radius (km), thickness (km), density (kg/m^3) and viscosity (Pa $\cdot$ s) respectively with $\mathcal{L}$ = UM, LM, Core, IC or OC representing the upper mantle, lower mantle, core, inner core and outer core respectively. We performed 3979402, 3357033 and 4364142 Monte-Carlo simulations respectively for **Classes 1**, **2** and **3**. It was done until we obtained for each class 65000 models with no density inversions. Both the fluid core of **Class 1** and the fluid outer core of **Class 3** are assumed to be inviscid fluids, equivalently $\mu \to 0$ Pa and $\eta \to 0$ Pa $\cdot$ s. The solid core of **Class 2** and the inner solid core of **Class 3** have a viscosity ranging between 10^{10} and 10^{22} Pa $\cdot$ s. This is a wide range that includes the Earth inner core viscosity derived from experiments [Gleason and Mao, 2013] and found to be between 10^{15} and 10^{18} Pa $\cdot$ s. MoI estimated by Margot et al. [2021] from the Earth-based observations radar data (also in Table 1.1) is 0.337 ± 0.024 (1σ). This uncertainty of 7% is too large to make any filtering of the original 65000 models with MoI $\pm\, 3\sigma$. Consequently, we use a filtering with MoI $\pm\, 1\sigma$. It then retains between 54.5 and 68% of the 65000 models, more precisely 35472, 35443 and 44390 models for **Class 1**, **Class 2** and **Class 3** respectively. Table 3.2 is obtained from Monte-Carlo statistical filtering, using the values of the MoI $\pm\, 1\sigma$ and estimated $k_2 \pm 2\sigma$, both in Table 1.1, and a range of $Q = 60 \pm 40$ [Correia et al., 2003]. Finally what remains from the latter filters are 6870, 7026 and 4160 models for **Class 1**, **Class 2** and **Class**

3 respectively. Table A.1 in Appendices represents the quartiles of the randomly selected and compensated internal structure parameters (th, ρ and η) after the filtering with the MoI, k_2 and Q. The core density ρ_{Core} distribution of **Classes 1** and **2** have both an upper boundary of 21999 kg/m^3 and the lower mantle density ρ_{LM} an upper boundary of 14999 kg/m^3 (Fig. A.1). The density upper boundaries of **Class 2** are respectively 21992 kg/m^3 and 14995 kg/m^3 (Fig. A.3). The inner core density ρ_{IC} of **Class 3** has an upper boundary of 30000 kg/m^3 and the one for the lower mantle ρ_{LM} is 14980 kg/m^3 (Fig. A.5). These result from the lower mantle density upper boundary (Table 3.1) set to $\rho_{\text{LM}} < 15000$ kg/m^3 for each class. In addition to the core density upper boundary for both **Class 1** and **2** set to $\rho_{\text{Core}} < 22000$ kg/m^3. And finally the inner core upper boundary for **Class 3** set to be $\rho_{\text{IC}} < 30000$ kg/m^3 after the compensation.

The 1D histograms distribution (Figs. A.1, A.3 and A.5) illustrate the first and third quantiles with black lines. The upper boundaries ($> 75\%$) for the $\rho_{\text{Core/IC}}$ and ρ_{LM} are high and almost evenly distributed. This results in a wide and high $25\% - 75\%$ percentile range of $11024 - 16684$ kg/m^3 and $5312 - 9259$ kg/m^3 (Table A.1) respectively for the core and lower mantle for **Class 1**. As for **Class 2** they are respectively of $9628 - 16342$ kg/m^3 and $5393 - 9196$ kg/m^3. Finally for **Class 3** they are $14300 - 22840$ kg/m^3 and $4984 - 7953$ kg/m^{3}for the inner core and lower mantle for **Class 3** respectively. This indicates that the MoI, estimated k_2 and Q filters do not constrain the upper boundaries of the lower mantle and core/inner core densities. This is the motivation for the density filtering for the lower mantle ($\rho_{\text{LM}} < 6000$ kg/m^3) and core/inner core ($\rho_{\text{Core/IC}} < 13000$ kg/m^3) [Trønnes et al., 2019; Shah et al., 2021]. These filters will be referred to as the additional density filters in Appendices and they are applied to the 3 classes of models. The histograms before the additional density filters are in Appendices. This additional filter reduces the number of models to 962, 1076 and 417 that fit the observations for **Class 1**, **Class 2** and **Class 3** respectively. Table 3.2 represents the first and third quartiles resulting from the Monte-Carlo simulation after all the filters applied.

Results for **Class 1** corresponding to an entirely inviscid fluid core, are plotted on Fig. 3.7, 3.8 and 3.9. The core thicknesses (Fig. 3.7 (e)) show that the core is the best constrained with a $25\% - 75\%$ percentile range of $2898 - 3372$ km. As for the lower and upper part of the mantle, their ranges are $1418 - 2232$ km and $600 - 1417$ km respectively. The 2D histogram of Fig. 3.9 (a) shows an

Table 3.2: Results of the Monte-Carlo sampling: the mean (50%) and first and third quartiles (25% and 75%) given as $50\%^{75\%}_{25\%}$ of the layer thicknesses th (km), their densities ρ (kg/m^3) and their viscosities η (log10 Pa·s).

Models	Layers	thickness (km)	density (kg.m^{-3})	viscosity (log10 Pa · s)
Fluid (**Class 1**)	upper mantle	963^{1417}_{600}	3765^{4123}_{3446}	$19.9^{22.3}_{18.3}$
	lower mantle	1839^{2232}_{1418}	4890^{5360}_{4484}	$20.78^{21.85}_{19.85}$
	core	3166^{3372}_{2898}	10899^{11909}_{9892}	-5
Solid (**Class 2A**)	upper mantle	1432^{2000}_{886}	3993^{4307}_{3622}	$20.95^{23.48}_{19}$
	lower mantle	1313^{2011}_{719}	5057^{5561}_{4616}	$21^{22.85}_{19.95}$
	core	3235^{3453}_{2940}	10533^{11723}_{9376}	$14.95^{19.44}_{13.35}$
Solid (**Class 2B**)	upper mantle	1053^{1295}_{771}	3562^{3842}_{3275}	$20.85^{22.9}_{18.95}$
	lower mantle	408^{689}_{220}	4718^{5277}_{4174}	$20.9^{23.48}_{18.97}$
	core	4499^{4699}_{4244}	7215^{7611}_{6924}	$20.7^{21}_{19.85}$
Fluid/Solid (**Class 3**)	upper mantle	931^{1357}_{593}	3722^{4009}_{3380}	$20^{22.6}_{18.3}$
	lower mantle	1717^{2088}_{1329}	4932^{5365}_{4434}	$21.48^{22.78}_{20.6}$
	outer core	386^{715}_{158}	8276^{9912}_{6723}	-5
	inner core	2823^{3148}_{2408}	11450^{12220}_{10450}	$15.6^{17.78}_{12.95}$

inverse relation between th_{LM} and th_{UM}. The models with $th_{\mathrm{UM}} < 600$ km, correspond to a relatively thick lower mantle with $th_{\mathrm{LM}} > 2232$ km as shown in Fig. 3.9 (a). As for the densities, the core and lower mantle are well constrained with the $25\% - 75\%$ percentile range of $9892 - 11909$ kg/m^3 (Fig. 3.7 (f)) and $4484 - 5360$ kg/m^3 (Fig. 3.7 (d)) respectively. As for the upper mantle, its 1D histogram (Fig. 3.7 (b)) is more distributed between its lower boundary of

2957 kg/m^3 and upper boundary of 4697 kg/m^3. Fig. 3.8 (c) shows that the lower mantle has a viscosity $\eta_{\mathrm{LM}} > 10^{18.5}$ Pa $\cdot$ s whereas the upper mantle viscosity is more evenly distributed through the explored range (Table 3.1) with $\eta_{\mathrm{UM}} > 10^{15.3}$ Pa $\cdot$ s. Models of Aitta [2012] and Dumoulin et al. [2017] are illustrated in Figs. 3.7 and 3.9 in red and green respectively for comparison to our study. They belong in the $25\% - 75\%$ quartiles of each th and ρ 1D histograms. Results for **Class 1** show the possibility of the existence of an entirely fluid core in Venus along ranges for the rheological parameters.

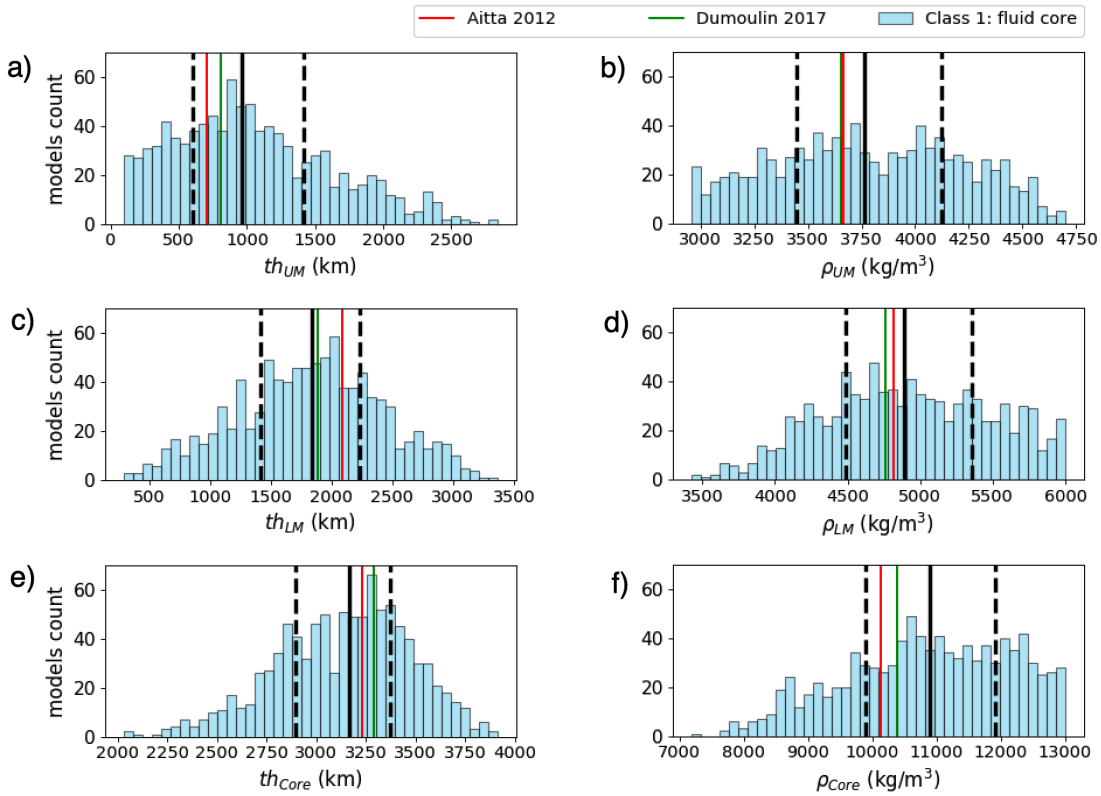

Figure 3.7: 1D histograms for each layer thicknesses th (km) (a), (c) and (e) and densities ρ (kg/m^3) (b), (d) and (f) for **Class 1** (the fluid core structure) for the upper mantle, the lower mantle, and the core respectively. The solid black lines correspond to the 50% quartile and the dashed black lines correspond from left to right to the 25% and 75% quartiles respectively. The red and green lines represent the Venus models of Aitta [2012] and Dumoulin et al. [2017] respectively.

Results for **Class 2** corresponding to an entirely solid core, are plotted on Fig. 3.10, 3.11 and 3.12. The distribution of the core thicknesses (Fig. 3.10 (c)) shows a bimodal tendency leading to the definition of two subclasses. The first

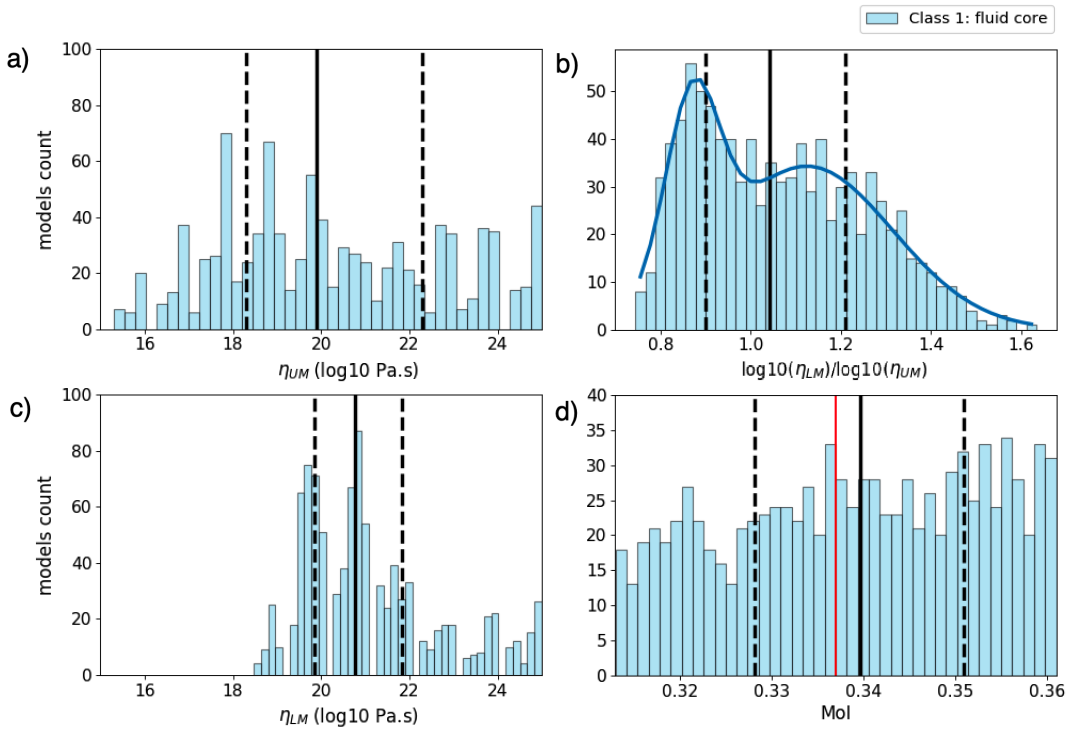

Figure 3.8: 1D histograms for the viscosities η (log10 Pa $\cdot$ s) of the upper mantle (a), the lower mantle (b), their viscosity ratio $\eta_{\mathrm{LM}}/\eta_{\mathrm{UM}}$ (c) and MoI (d) for **Class 1** (the fluid core structure). The solid black lines correspond to the 50% quartile and the dashed black lines correspond from left to right to the 25% and 75% quartiles respectively. The red line in (d) is the mean value of MoI (Table 1.1)

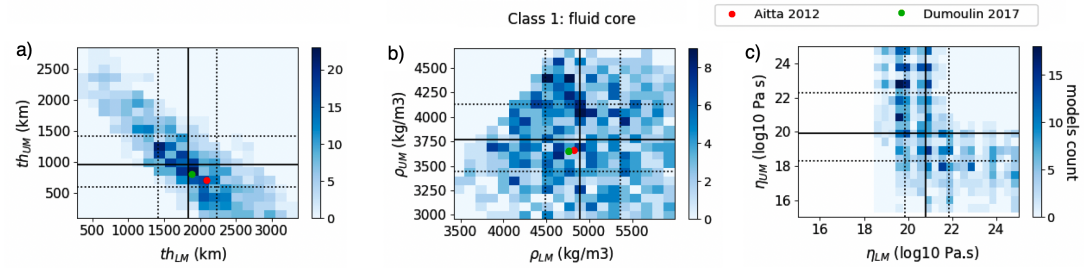

Figure 3.9: 2D histograms of the lower mantle and upper mantle thicknesses th (km) (a), densities ρ (kg/m^3) (b) and viscosities η (log10 Pa $\cdot$ s) (c) of **Class 1**: fluid core. The solid and dashed black lines represent the first, second and third quartiles as Figs. 3.7 and 3.8. The red and green circles represent the Venus models of Aitta [2012] and Dumoulin et al. [2017] respectively.

subclass **Class 2A** has a smaller core with $th_{\mathrm{Core}} \leq 3900$ km and the second subclass **Class 2B** has a larger core with $th_{\mathrm{Core}} > 3900$ km. The thickness and density histograms (Fig. 3.10 (c) and (f)) show that the two peaks of the core

thickness correspond to two different peaks in the core density: between 7153 and 12991 kg/m^3 and between 6473 and 10402 kg/m^3. **Class 2A** corresponds to a smaller core with $25\% - 75\%$ of $2940 - 3453$ km with a higher density of $9376 - 11723$ kg/m^3. It also has a larger lower mantle and a larger upper mantle than **Class 2B**. **Class 2B** corresponds to a larger core of $4244 - 4699$ km and a lower density of $6924 - 7611$ kg/m^3 with smaller and more constrained thicknesses for the lower mantle and upper mantle. The range of the th_{UM} for **Class 2A** is $886 - 2000$ km. The th_{LM} of **Class 2B** is smaller and better constrained with a range of $220 - 689$ km. The range of its th_{UM} is $771 - 1295$ km. Therefore the lower and upper part of the mantle are thinner and better constrained in for **Class 2B**. For both **Classes 2A** and **2B** the lower mantle viscosity η_{LM} does not show the same truncating as observed for **Class 1** from the originally explored range between 10^{15} to 10^{25} Pa $\cdot$ s (Table 3.1). The upper mantle viscosity for both classes shows a minor truncation with $\eta_{\mathrm{UM}} > 10^{15.3}$ Pa $\cdot$ s. The solid core viscosity η_{Core} is filtered from its originally explored range between 10^{11} to 10^{22} Pa $\cdot$ s (Table 3.1). In more details for **Class 2A** $\eta_{\mathrm{Core}} < 10^{16}$ Pa $\cdot$ s or $\eta_{\mathrm{Core}} > 10^{18.3}$ Pa $\cdot$ s. As for **Class 2B** 97% of the models have $\eta_{\mathrm{Core}} > 10^{18.8}$ Pa $\cdot$ s. From Table 3.2 which shows the $25\% - 75\%$ range for each studied parameter we conclude that **Class 2A** is closer to **Class 1**. On the contrary the **Class 2B** core has a larger radius and lower density, inconsistent to any terrestrial planets or previous work. This shows the possibility of the existence of an entirely solid core in Venus and the ranges of the internal structure parameters for this case. The most likely case of its existence is **Class 2A**.

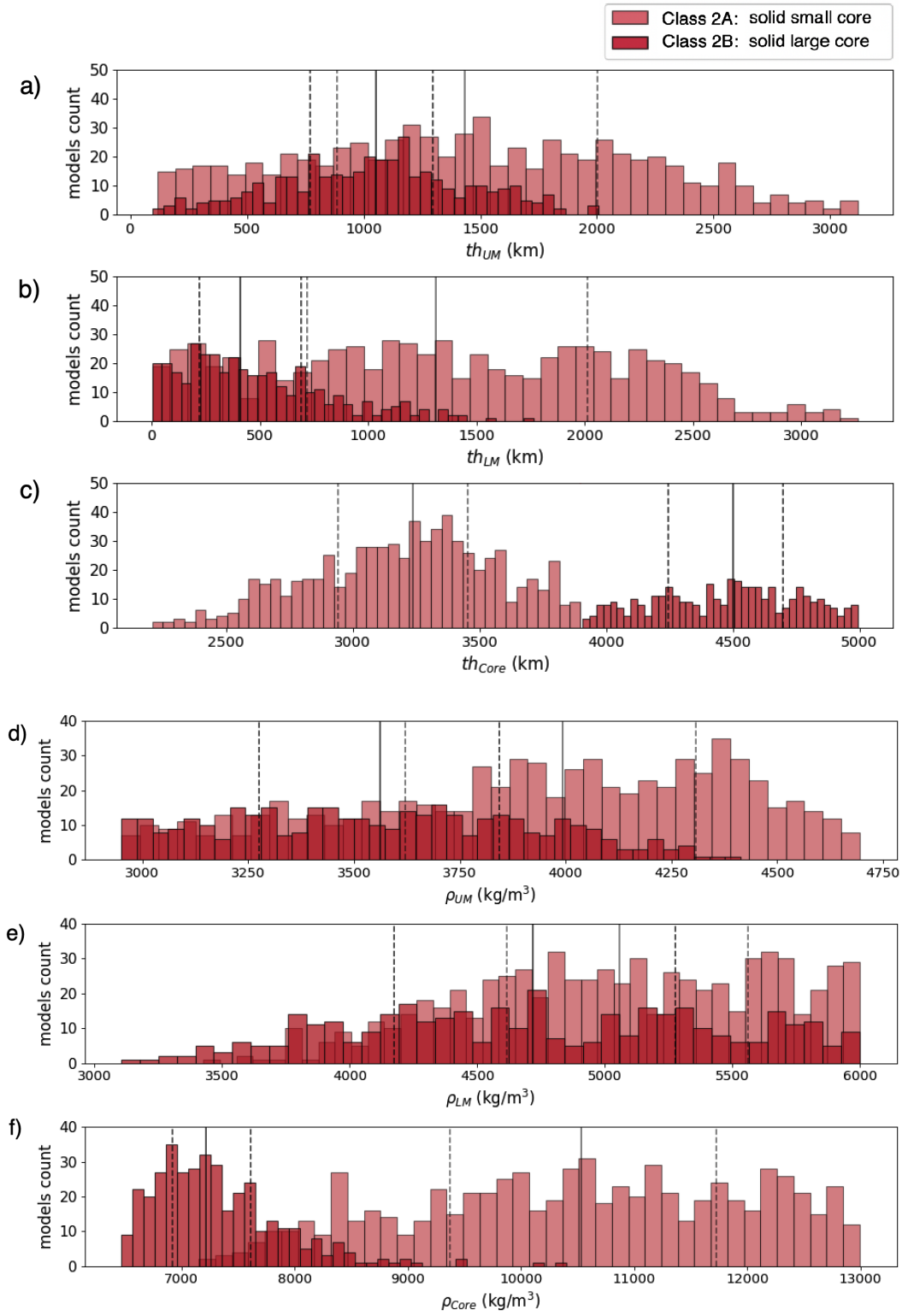

Figure 3.10: 1D histograms for each layer thicknesses th (km) (a), (b) and (c) and densities ρ (kg/m^3) (d), (e) and (f) for **Class 2** (the solid core structure) for the lower mantle, the upper mantle and the core respectively. The solid black lines correspond to the 50% quartile and the dashed black lines correspond from left to right to the 25% and 75% quartiles respectively.

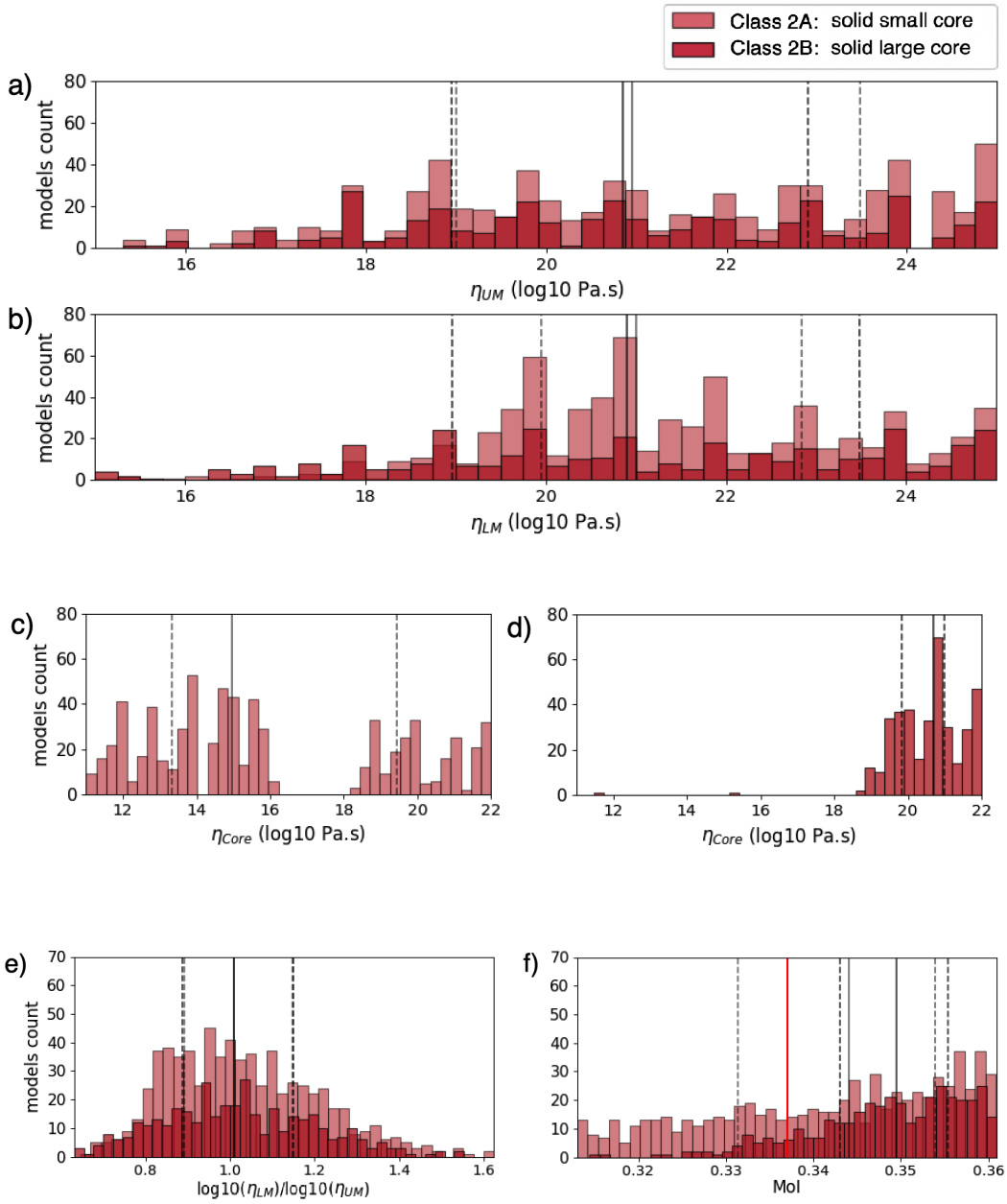

Figure 3.11: 1D histograms for the viscositites of the lower mantle (a), the upper mantle (b) and the core (c) and (d) η (log10 Pa $\cdot$ s) the viscosity ratio $\eta_{\mathrm{LM}}/\eta_{\mathrm{UM}}$ (e) and the MoI (f) for **Class 2** (the solid core structure). The solid black line corresponds to the 50% quartile and the dashed black lines correspond from left to right to the 25% and 75% quartiles respectively.

The 1D histograms for **Class 3** (the case of a solid inner core and a fluid outer core) are shown in Figs. 3.13 and 3.14, and the 2D histograms in Fig. 3.15. If a model of **Class 3** has a very thin or non existent outer core ($th_{\mathrm{OC}} = 0$) it converges to a model as in **Class 2** with only a solid core. If its inner core is very

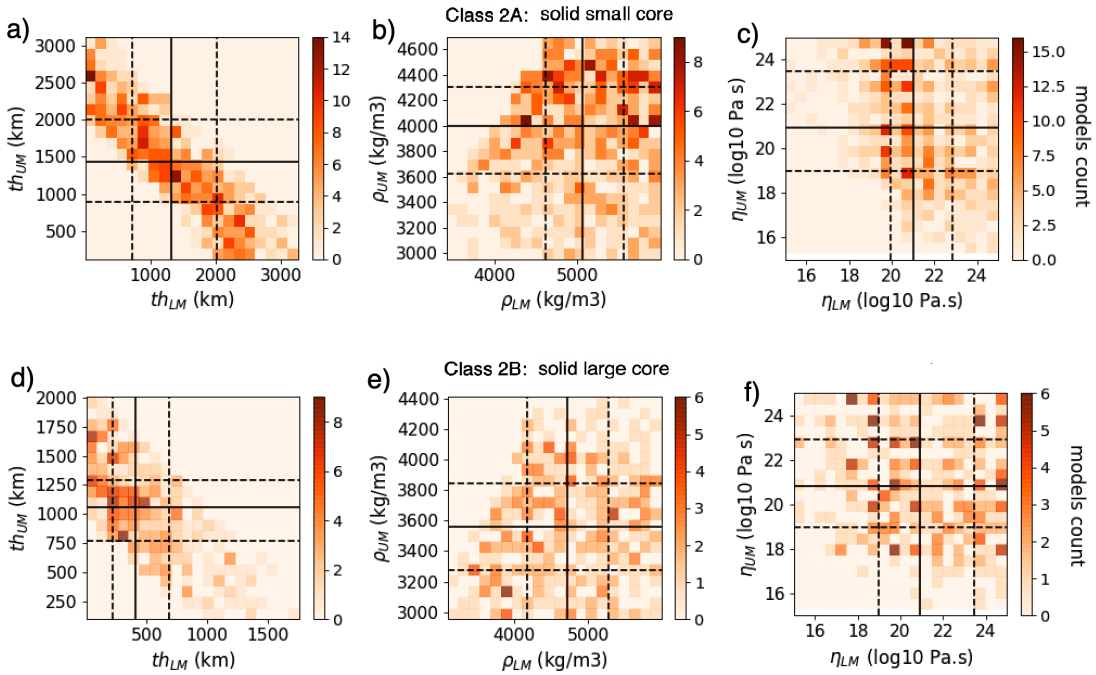

Figure 3.12: 2D histograms of the lower mantle and upper mantle thicknesses th (km) (a), densities ρ (kg/m^3) (b) and viscosities η (log10 Pa $\cdot$ s) (c) of **Classes 2A** and **2B**: solid core. The solid and dashed black lines represent the first, second and third quartiles as Figs. 3.10 and 3.11. The red line in (f) is the mean value of MoI (Table 1.1)

thin or non existent ($r_{\mathrm{IC}} = th_{\mathrm{IC}} = 0$) it converges to a model as in **Class 1** with only a fluid core. The Fig. 3.13 (e) shows that 25% of the models have an outer core less or equal to 158 km. Its percentile range is of $158-715$ km. Its density is not well constrained. It is fairly distributed between its 25% and 75% percentiles of respectively 6723 kg/m^3 and 9912 kg/m^3. The thickness of the inner core has a lower boundary of 571 km and an upper boundary of 4348 km. It is well constrained with a $25\%-75\%$ range of $2408-3148$ km. This indicates in **Class 3** the supposed existence of a thick inner core of almost the same magnitude of the fluid and solid cores of respectively **Classes 1** and **2**. Additionally its 25% percentile is 7% and 9% smaller than that of the core in **Classes 1** and **2A** respectively and 17% and 18% smaller than their respective 75% percentiles. Therefore it is smaller than the core **Classes 1** and **2A** with a higher density. The inner core density has a lower boundary of 8025 kg/m^3. Its upper boundary of 13000 kg/m^3 is a result of the applied density filters. More precisely the ρ_{IC} 25% is respectively 5.6% and 11.5% higher than that of **Classes 1** and **2A**. As

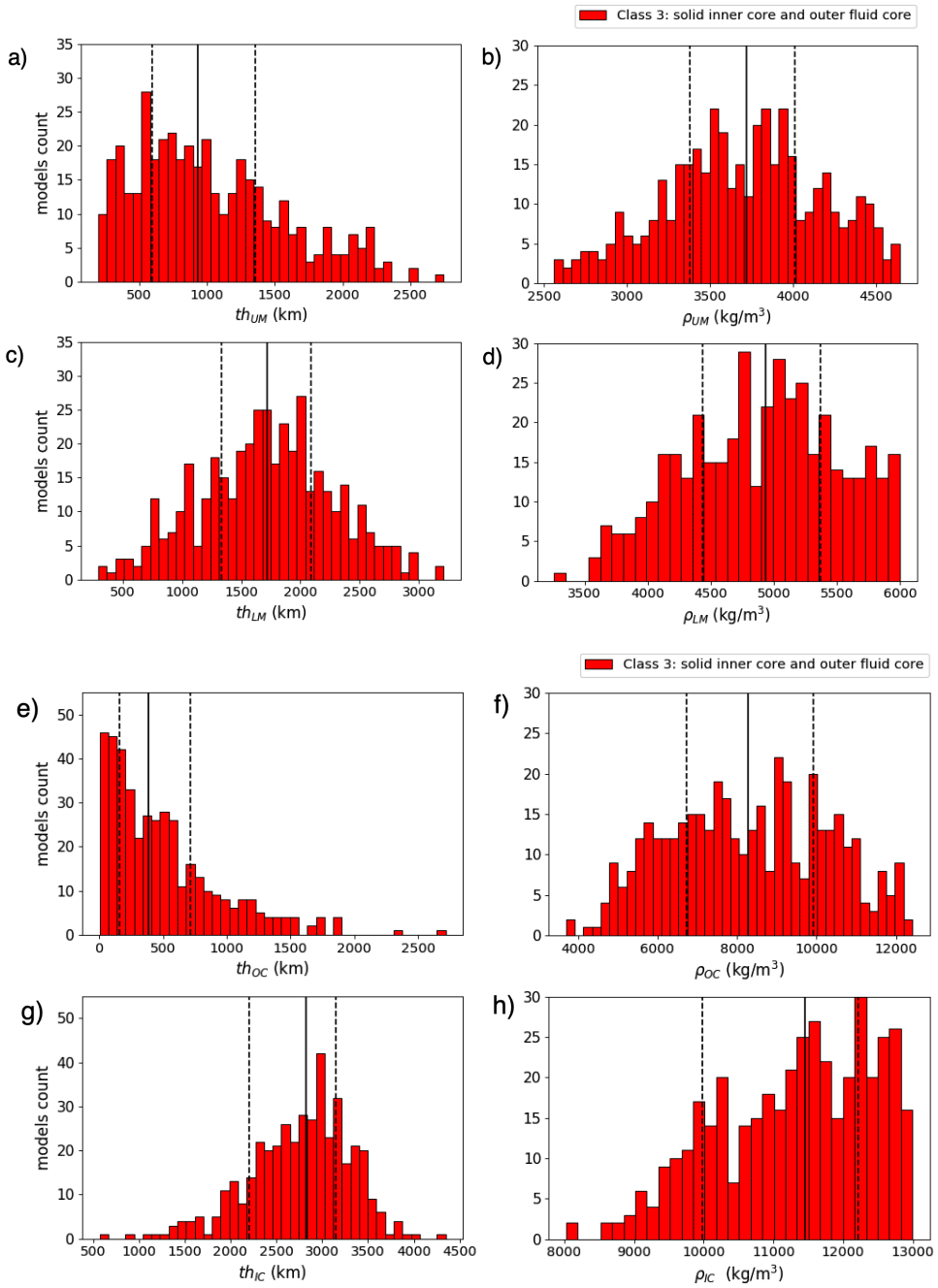

Figure 3.13: 1D histograms for each layer thicknesses th (km) (a), (c), (e) and (g) and densities ρ (kg/m^3) (b), (d), (f) and (h) for **Class 3** (the part solid part fluid core structure) for the upper mantle, the lower mantle, the outer core and the inner core respectively. The solid black lines correspond to the 50% quartile and the dashed black lines correspond from left to right to the 25% and 75% quartiles respectively.

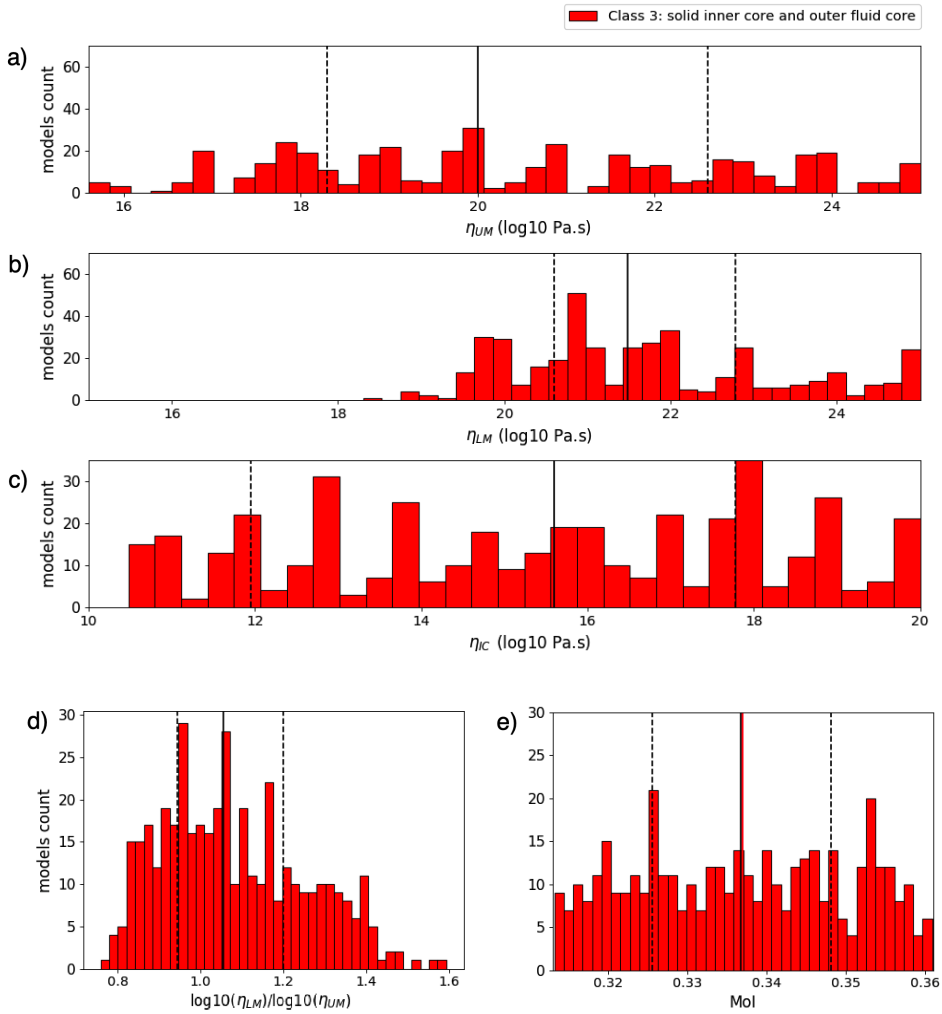

Figure 3.14: 1D histograms for the viscositites η (log10 Pa $\cdot$ s) of the upper mantle (a), the lower mantle (b), and the inner core (c), the viscosity ratio $\eta_{\rm LM}/\eta_{\rm UM}$ (d) and the MoI (e) for **Class 3**: solid inner core and fluid outer core. The solid black lines correspond to the 50% quartile and the dashed black lines correspond from left to right to the 25% and 75% quartiles respectively. The red line in (e) is the mean value of MoI (Table 1.1).

for the lower mantle it is well constrained and of the same magnitude of that of **Classes 1** and **2A** and larger. In comparison to the one of **Class 2B**, $th_{\rm LM}$ of **Class 3** has 6 times bigger 25% percentile. Its density $\rho_{\rm LM}$ has the same magnitude as the other classes. It is the same case for the upper mantle density $\rho_{\rm UM}$. The upper mantle density $\rho_{\rm UM}$ is similar to the better constrained ones as **2B** and specifically the closest to **Classes 1**. From Fig. 3.14 (c) the viscosity of the inner core is not truncated from its originally explored range between 10^{10} to 10^{20} Pa $\cdot$ s (Table 3.1). The lower mantle viscosity is truncated as in the case

of **Classes 1** and **2** with $\eta_{\mathrm{LM}} \geq 10^{18.3}$ Pa $\cdot$ s for all models. The upper mantle has a minor truncation with $\eta_{\mathrm{LM}} \geq 10^{15.6}$ Pa $\cdot$ s. Therefore **Class 3** shows the possibility of the existence of a part fluid part solid core in Venus as it is for the Earth and the ranges of the internal structure parameters for this case. The solid core part (inner core) exists in all models with a minimum radius of 571 km.

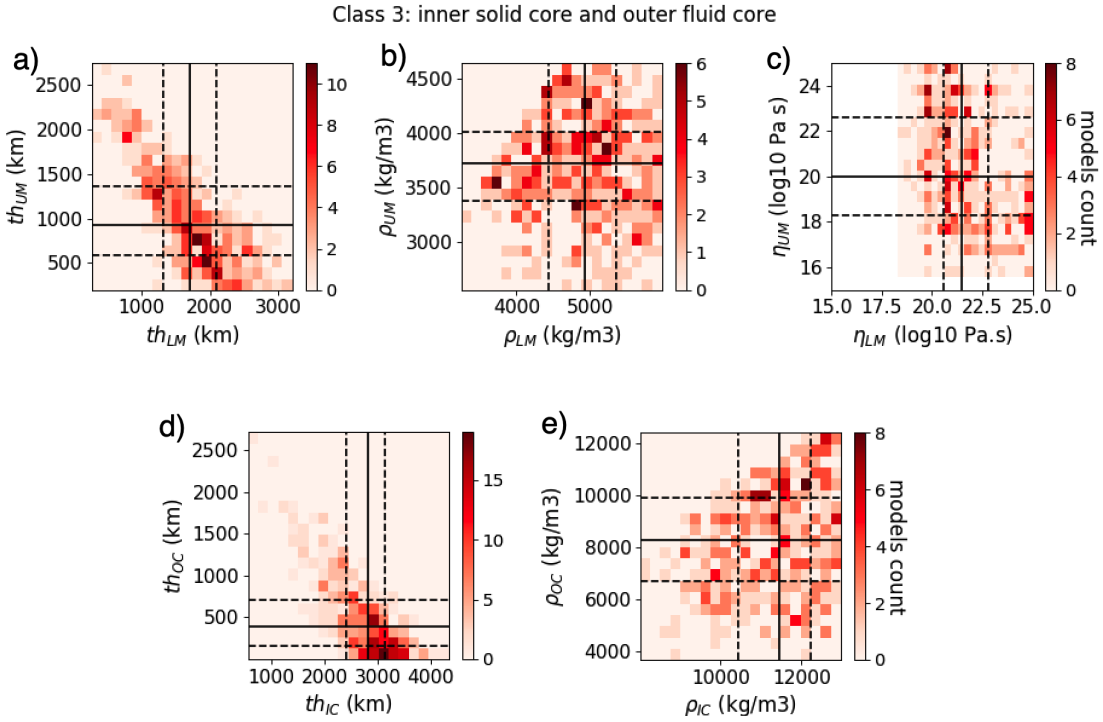

Figure 3.15: 2D histograms of the lower mantle and upper mantle thicknesses th (km) (a) and (d), densities ρ (kg/m^3) (b) and (e) and viscosities η (log10 Pa $\cdot$ s) (c) of **Class 3**: solid inner core and fluid outer core. The solid and dashed black lines represent the first, second and third quartiles as Fig. 3.13 and 3.14.

The Fig. 3.8 (b) illustrates the ratio $\eta_{\mathrm{LM}}/\eta_{\mathrm{UM}}$ of **Class 1**. Only 0.62% of the models (equivalently 6 models) have $\eta_{\mathrm{LM}}/\eta_{\mathrm{UM}} = 1$. These models fall in the range between $10^{19.7}$ and $10^{21.3}$ Pa $\cdot$ s. As for the models with different mantle viscosities the remaining models are split almost evenly with slightly more models having a more viscous lower mantle. It is similar for **Class 2A** (Fig. 3.11 (e)) where 1% of the models (equivalently 7 models) have an equal viscosity. These models fall in the range between $10^{19.8}$ and $10^{23.9}$ Pa $\cdot$ s. More specifically 56.44% for **Class 1** and 51.28% for **Class 2A** have a more viscous lower mantle. And 42.93% for **Class 1** and 47.72% for **Class 2A** have a more fluid lower mantle. The Fig. 3.14 (d) shows the ratio $\eta_{\mathrm{LM}}/\eta_{\mathrm{UM}}$ for **Class 3**. In this case 1.2% of

the models (equivalently 5 models) have $\eta_{LM}/\eta_{UM} = 1$. These models fall in the range between $10^{20.6}$ and 10^{22} Pa · s. In this case the remaining models are split between 60.7% and 38.1% with more models having a more viscous lower mantle.

The Figs. 3.9 (c), 3.12 (c) and 3.15 (c) illustrate the 2D histograms of η_{LM} and η_{UM} of these three classes. It is not the case for **Class 2B** where Fig. 3.12 (f) shows no signature relation between η_{LM} and η_{UM}. The models are more evenly distributed than the other 3 classes. Even though statistically also 0.27% of the models (equivalently 1 model) have $\eta_{LM}/\eta_{UM} = 1$. The remaining models are split between 52.14% and 47.59% with more models having a more viscous lower mantle which is similar to the previous classes. We fit both a Gaussian and a bimodal distribution to distinguish the possible existence of two different peaks in the viscosity ratio histograms for each of the classes (Table 3.3). A

Table 3.3: Mean $\mathtt{M}$, deviation σ and Chi-squared χ^2 fitting of the ratio viscosities η_{LM}/η_{UM} of each **Class**.

	Gaussian distribution			**Bimodal distribution**				
	$\mathtt{M}$	σ	χ^2	$\mathtt{M}_1$	σ_1	$\mathtt{M}_2$	σ_2	χ^2
Class 1	0.99	0.26	1.5	0.87	0.058	1.13	0.19	0.91
Class 2	1	0.19	1.42	0.9	0.11	1.1	0.16	0.97
Class 2A	1	0.18	1.7	0.88	0.09	1.07	0.17	1.22
Class 2B	1	0.2	1.2	0.97	0.16	1.26	0.09	2.58
Class 3	1.03	0.21	1.42	0.96	0.12	1.25	0.13	1.2

χ^2 value closer to 1 is a way to distinguish a better fit. **Classes 1**, **2A**, **3** and finally **2** which incorporates both **Classes 2A** and **2B** fit better with a bimodal distribution. Hence, for these cases, statistically more models have a mantle divided by 2 mantle layers with different viscosities. We illustrate in Fig. 3.8 (b) the bimodal distribution of the viscosity ratio η_{LM}/η_{UM} as an example. As for **Class 2B** it fits better with a Guassian distribution, hence has neither correlation nor inverse correlation between the mantle viscosities. The analysis for **Classes 1**, **2A** and **3** shows a generally inverse relation between the viscosity of lower and upper mantle with almost all the models concentrated in the zone

with a more viscous lower mantle and a more fluid upper mantle or vice versa. When the mantle viscosities are equal in both mantle layers, they fall within the range of the average viscosities ($10^{19} - 10^{23}$ Pa $\cdot$ s) from the explored range of $10^{15} - 10^{25}$ Pa $\cdot$ s (Table 3.1). It is not the case for **Class 2A** where no relation between the mantle viscosities is observed.

3.3 Discussion

For **Class 1** we compare our results with previous studies. Aitta [2012], as Dumoulin et al. [2017], constructed a model of Venus considered as a scaled Earth density model of the Earth, as a function of depth. They propose a Venus model with a fluid core and a mantle divided by two major parts, a lower and a upper mantle, as the Earth. They estimated the density and size at the core-mante boundary (CMB) assuming the core is molten iron and has enough light materials to reach an estimated density at its center and that the lower and upper mantle densities are similar to the Earth. The density estimation of each mantle part has been made using the Earth PREM as reference. The model of Aitta [2012] and the model **V** of Dumoulin et al. [2017] are encompassed in our first and third quartiles of the **Class 1** selected models (red and green lines in Fig. 3.7). Therefore the model of Aitta [2012] and the model **V** of [Dumoulin et al., 2017] are in agreement with our work.

The work of Shah et al. [2021] studies different structure models of Venus depending on the Si and Mg content in both the mantle and the crust and the S content in the core. They assumed that the segregation of the core of Venus happened as a single-stage event and set three different cases for the S content defined by the ratio of the number of moles of iron sulfide in the total amounts of moles in the core, the so-called mole fraction $X_{\mathrm{FeS}}^{\mathrm{Core}}$, from the Earth models as a reference. The three cases are a core having either a nominal S content ($X_{\mathrm{FeS}}^{\mathrm{Core}} = 0.08 - 0.15$), S-rich content ($X_{\mathrm{FeS}}^{\mathrm{Core}} = 0.2 - 0.5$) or S-free ($X_{\mathrm{FeS}}^{\mathrm{Core}} = 0$). Their allowed MoI range is as considered in our work the MoI $\pm 1\sigma$ estimated by [Margot et al., 2021], which is from 0.313 to 0.361. They find that not the whole range is possible, their total estimated MoI range is $0.317 - 0.351$. The MoI is calculated as our work (eq. 3.5) as a function of density, where the density ρ is calculated from the pressure P and temperature T, and for that an equation of

state for each material in the planet is required. More precisely a fourth order Runge Kutta is applied with the equations of state from the center to the surface to calculate P, T and consequently ρ as functions of the radius. Their results are divided by 3 ranges of MoI, the full MoI range $(0.317 - 0.351)$, a low range corresponding to the 1% of the lowest value $(0.317 - 0.326)$ and a high range corresponding to the 1% of the highest value $(0.323 - 0.351)$ in addition to the 3 cases for the core S content, hence 9 cases in total.

Table 3.4 shows the results of Shah et al. [2021] and our results with the MoI range corresponding to their estimations for different hypotheses. Their work permits the possibility to have an entirely fluid core ($r_{IC} = 0$) as our results for **Class 1**, an entirely solid core ($r_{IC} = r_{OC}$) as **Classes 2A** and **2B** and the possibility to have a partially fluid and partially solid core ($r_{IC} \leq r_{OC}$) as **Class 3**. More precisely in Shah et al. [2021] 6 of the 9 cases they consider might permit each of the three different core structures we propose (**Classes 1**, **2** and **3**). The other 3 cases require the existence of either the solid or the fluid part of the core. More precisely the only one case that the solid part is required, hence has an entirely or partially solid core is the one corresponding to a low MoI and an S-rich core. In this case $r_{IC} > 0$ and has a lower boundary of 1510 km. It is similar to our results for **Class 3** where the solid part of the core is required with the a radius lower boundary of the the set of models of 571 km. The only 2 cases where the fluid part is required, hence the existence of an entirely or partially fluid core, are when the upper boundary of the inner core radial boundary is smaller than the lower boundary of the outer core, equivalently $max\{r_{IC}\} < min\{r_{OC}\}$. They correspond to the high MoI cases and a nominal S or an S-rich core contents.

We filter our models for each class with the estimated low, high and total MoI ranges (Table 3.4). The Fig. 3.16 represents the radii ranges (r in km) as in 3.4. For a better comparison we represent for each parameter both the $25\% - 75\%$ (equivalently $\pm 50\%$) percentile range and the wider $\pm 2\sigma$ (equivalently $\pm 95.5\%$) range. **Classes 1**, **2A**, **2B** and **3** are denoted respectively by **C1**, **C2A**, **C2B** and **C3**. The same goes with the S-free, nominal S and S-rich core respectively denoted by SF, NS and SR. The Fig. 3.16 shows that for the low MoI models the inner core of **Class 3** is in agreement with each of the ranges for different S contents assumptions (S-free, nominal S and S-rich). The core/outer core ranges

fit with all the S contents for **Classes 1**, **2A** and **3**. It is not the case for **Class 2B** which fits with none of the results of Shah et al. [2021]. The lower mantle ranges for **Classes 1** and **3** fit with all the S contents ranges. This agreement persists with the smaller range of $25\% - 75\%$. As for the one of **Class 2A**, it fits only with the wider deviation of $\pm 2\sigma$. And **Class 2B** does not fit with any of the radii ranges from compared study. For the high MoI models the inner core of **Class 3** is not in agreement with the S-rich core content, it has an intersection with the nominal S with the wider deviation of $\pm 2\sigma$ and fits with the S-free range also for the $25\% - 75\%$ range. The core/outer core and lower mantle ranges follow the same analysis of the results for low MoI except for the lower mantle range for **Class 2B** which fits for the wider range of $\pm 2\sigma$ with each S content ranges. Finally we conclude that **Class 2B** which corresponds to a thick solid low density core does not fit with either of Shah et al. [2021] results.

Our results for the Earth like core size models, **Classes 1**, **Classes 2A**, **Classes 3**, are in agreements with the results of [Shah et al., 2021] with an S-free and in a lesser degree with a nominal S core. We previously mentioned that a low Fe content is a proposed explanation of the density deficit of Venus in contrast to the Earth. Lewis [1972] suggests that another explanation of this observation is the virtual absence of S in Venus. This proposition is compatible with our results of an S-free core. Nevertheless Ringwood and Anderson [1977] showed that this argument is insufficient to cause the density deficit in Venus. They also argued that the sulfur content in the atmosphere of Venus points to its presence in the planet and that the core was not the result of a catastrophic formation. Additionally during core formation S and Si are incompatible in the metal assuming the core formed in a low pressure single-stage formation [Kilburn and Wood, 1997] where Si becomes siderophile and S becomes lithophile. Therefore that might explain the existence of S in the mantle or the crust and the lack or poor existence of sulfur in the core. Suer et al. [2017] studied the behavior of S at specific pressures and temperatures corresponding to a terrestrial core formation in a deep magma ocean. They show experimentally that a core inferred from metal–silicate partitioning would result in a non continuous S accretion. This event might cause the core to be poor in its S content. [Bercovici et al., 2022] shows that in some cases where a molten core forms from chondrites, S forms immediately and rises to the mantle or erupt to space, therefore does not accrete abundantly in the core. This represents different hypotheses for the S

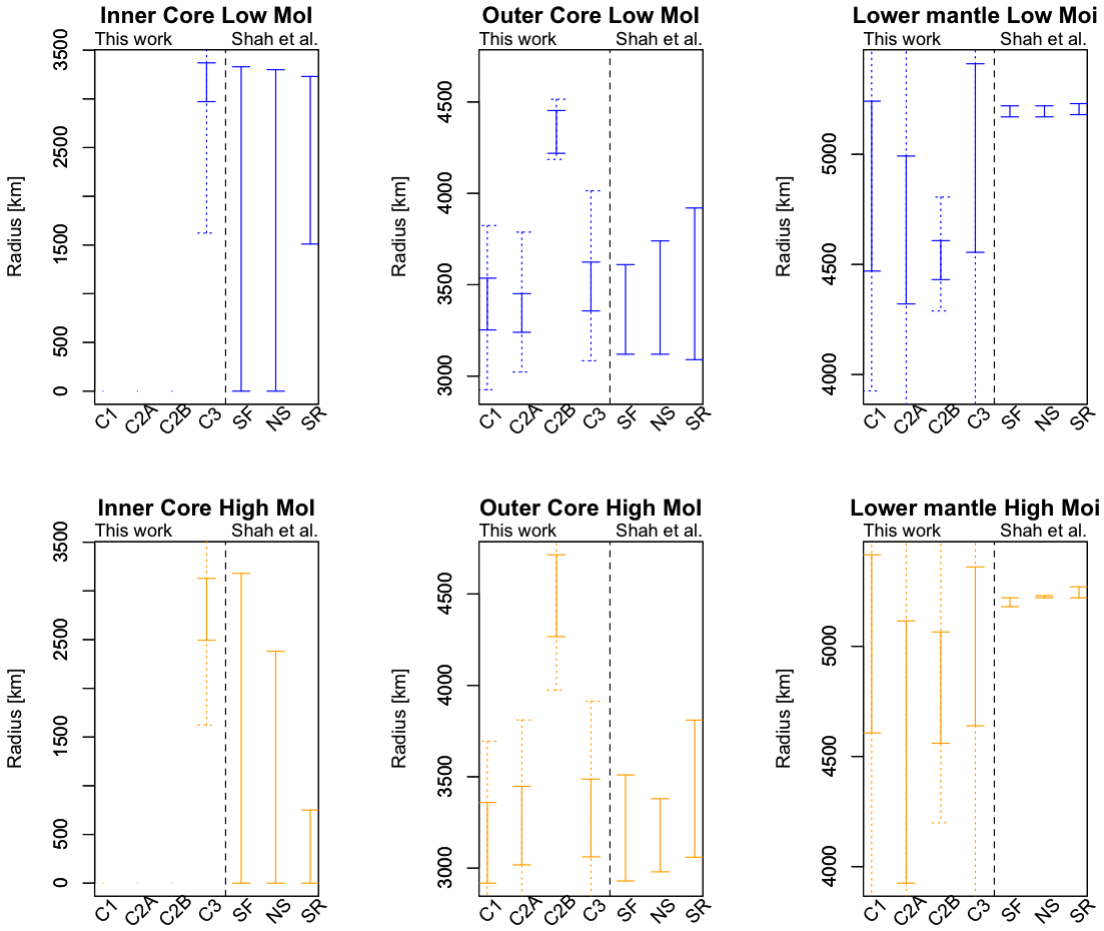

Figure 3.16: Comparisons between layer boundaries (radii) from Shah et al. [2021] and those obtained for the different classes considering MoI segregation as presented in Shah et al. [2021]. The denotations C1, C2A, C2B, C3 stand for **Class 1**, **Class 2A**, **Class 2B** and **Class 3**, respectively and SF, NS and SR stand for S-free, Nominal-S and S-rich core models as defined in Shah et al. [2021], respectively. The errorbars are given at 2σ (courtesy: A. Fienga).

content of Venus using experimental results and observation on Venus, the Earth and terrestrial planets generally.

3.4 Conclusion

In this work we explore randomly the space of parameters of Venus internal structure using a Monte-Carlo sampling. We consider three different classes for the core structure, an entirely fluid core (**Class 1**), an entirely solid core **Class 2** and a partially fluid and partially solid core (**Class 3**). The varying parameters are the radius, the density and the viscosity of each layer, they follow a uniform

distribution. We use all resulting models to calculate their MoI and filter out the models that do not match the most recent estimated range of the MoI of Venus. The TLN k_2 and quality factor Q are then calculated with `ALMA` and used to filter the models compatible with the most recent estimated value k_2^{MPVO} and the most likely estimated range for Q. Density filters for the lower mantle and core/inner core for each class is successively applied to select geophysically realistic models. We end up with two different classes for **Class 2**, one with a smaller core **Class 2A** and one with a larger core **Class 2B**. We deduce that for **Classes 1**, **2A** and **3** there is a contrast in the lower mantle and upper mantle viscosities and an inverse correlation. For **Class 3** the lower mantle tends to be more viscous than the upper mantle. After filtering with the geophysical parameters (MoI, k_2, Q) the **Class 3** inner core that is the viscid part of the core is required in this class. Hence it has a substantial contribution in the global gravity deformation of Venus.

Shah et al. [2021] built Venus models under different assumptions of chemical content. After the comparison of their results with ours we draw the conclusion that our admissible models of a fluid core **Class 1**, a solid core **Class 2A** and a partially fluid and partially solid core **Class 3** agree with their S-free core or nominal S core models. The S content in the core of Venus might help to understand the core formation. Different hypotheses can explain the core S content such as its accretion history (single-stage or multi-stage formation, continuous or catastrophic, $\cdots$) and the pressure-temperature conditions. The S accretion in the Earth core did not happen continuously during the planet accretion, which is why it would not be a major part of light elements in the core [Suer et al., 2017]. This might also be the case for Venus. According to Ringwood and Anderson [1977] the core of Venus formed continuously not catastrophically. Therefore S and Si became incompatible during this single-stage formation and the sulfur migrated out of the core [Kilburn and Wood, 1997]. This single-stage type of core formation is another possibility to consider for Venus which would result in S-poor/free core. Constructing different models of Venus based on its chemical content (as [Shah et al., 2021]) using geophysical constraints (as in our work) such as the TLN k_2, moment of inertia MoI and quality factor Q helps to constrain the mineralogy of the planet.

Table 3.4: Filtering our results for each class with the low and high MoI ranges [Shah et al., 2021] with their results.

	Layers	This work				Shah et al. [2021] results		
		Class 1	**Class 2A**	**Class 2B**	**Class 3**	S-free	Nominal S	S-rich
All MoI								
(0.317-0.351)								
	Lower mantle	5006^{5364}_{4588}	4576^{5098}_{3954}	4832^{5064}_{4557}	5068^{5384}_{4618}	5170-5220	5170-5250	5180-5280
r (km)	Outer core	3212^{3403}_{2980}	3266^{3450}_{3041}	4502^{4711}_{4267}	3318^{3522}_{3129}	2930-3610	2960-3890	3010-4350
	Inner core	-	-	-	2923^{3172}_{2527}	0-3330	0-3300	0-3230
Low MoI								
(0.317-0.326)								
	Lower mantle	4963^{5241}_{4470}	4638^{4992}_{4321}	4509^{4608}_{4431}	4910^{5411}_{4555}	5170-5220	5170-5220	5180-5230
r (km)	Outer core	3383^{3536}_{3253}	3340^{3451}_{3240}	4331^{4453}_{4219}	3506^{3624}_{3357}	3120-3610	3120-3740	3090-3920
	Inner core	-	-	-	3149^{3370}_{2972}	0-3330	0-3300	1510-3230
High MoI								
(0.323-0.351)								
	Lower mantle	5026^{5415}_{4607}	4547^{5115}_{3925}	4833^{5065}_{4560}	5095^{5360}_{4639}	5180-5220	5220-5230	5220-5270
r (km)	Outer core	3156^{3359}_{2918}	3252^{3448}_{3018}	4502^{4714}_{4267}	3266^{3487}_{3062}	2930-3510	2980-3380	3060-3810
	Inner core	-	-	-	2841^{3129}_{2494}	0-3180	0-2380	0-750

4. Coseismic and postseismic deformations

One way to explore the internal structure of a planet is, as done in section 3.2, by theoretically calculating parameters (such as the TLN) and comparing the results with geophysical observations. The same approach can be applied to learn more about the geological activity of a planet. The mantle plumes approaching the lithosphere cause seismic dislocations, rifts, volcanoes and other geological features as the novae, coronae and arachnoids. Aiming at discovering the geological activity of Venus, the BAT region is of interest (see chapter 1.1.1). It contains several plumes in the mantle approaching the surface and causing gravity anomalies, crustal uplift and surface deformations. The seismic rebound is a consequence of the seismic dislocation and causes deformations, such as displacement and gravity field variations that can be theoretically estimated. The purpose of this chapter is to use the analogies between Venus and the Earth done in previous studies [Phillips et al., 1981], [Mcgill et al., 1981], [Foster and Nimmo, 1996] and [Moores et al., 2013] and estimate the seismic rebound of hypothetical Venusquakes. Following Foster and Nimmo [1996] and Moores et al. [2013] we assume that Venusian rifting events in Beta Regio are similar to that of the East-African rift (see section 1.1.1). We use the `ASTRA` code [Melini et al., 2008] to calculate the seismic rebound both on the Earth and on Venus. We use as an example, the dip-slip dislocation that took place in the East-African rift in 2009. This approach aims at estimating the magnitude of such an event for a model of Venus and to see if it can be observed from its consequent surface deformation (observed by topography, altimetry, $\cdots$) or gravity field deformation.

4.1 Comparison between Beta Regio on Venus and the East-African rift

A triple junction is a spot on the surface of a planet where three different lithosphere plates meet. The Afar Triple Junction is the intersection of the divergent (i. e. extensional) plate boundaries of Nubian (sometimes called the African plate), Somalian and the Arabian plates. The Afar depression (also called Afar triangle, seen on Fig. 4.1 as the blue triangle in the North) is caused by the Afar Triple Junction also called the Afro-Arabian rift system. Fig. 4.2 zooms in the Afar depression (the triangular feature) in Fig. 4.1 and illustrates the three plate intersection and motion. The Afar triple junction formed the Red Sea Rift, the Aden Ridge and the EARS (Fig. 4.2) upon its intersection. The EARS span for 6500 km from the Afar depression to Mozambique. In the Afar Region, there is a 105 km^2 complex of basaltic shield volcanoes called Manda Hararo (MH in Fig. 4.2). Several authors [Malin and Saunders, 1977], [Mcgill et al., 1981] and [Phillips et al., 1981] made the analogy based on the radar imagery and altimetry between continental rifting on the Earth and rift systems on Venus. Mcgill et al. [1981] compared the topographic features on Venus to the one on the Earth based on the topographic maps from PVO altimetry data. They also suggested that the Beta Regio rift system is a consequence of a crustal uplift. Its elevation located at 27° N and 282° E caused the formation of a complex dome.
Mcgill et al. [1981] found it to be similar to domes in continental rift systems on the Earth (precisely the Kenyan and Ethiopian domes) in the EARS. This hypothesis that the Beta Regio elevation is a dome, not simply a volcano, suggested that Venus has a dynamic mantle.

The effective elastic thickness of the Beta Regio estimated by [Smrekar, 1994] ($\approx$ 30 km) is similar to that of the EARS. Both rifts then have the ability to withstand deformations. Foster and Nimmo [1996] found other similarities between the Beta Regio and the EARS using Magellan Synthetic-aperture radar (hereafter SAR). They measured the widths of the half grabens (rift basins), hence the distances between the rift faults of both features. Foster and Nimmo [1996] found that the rift systems have a maximum fault lengths of $\approx$ 100 km and that the half grabens are $\approx$ 50 km and $\approx$ 150 km wide respectively for the Beta Regio and the EARS.

Based on this conclusion and the one made about the effective elastic thick-

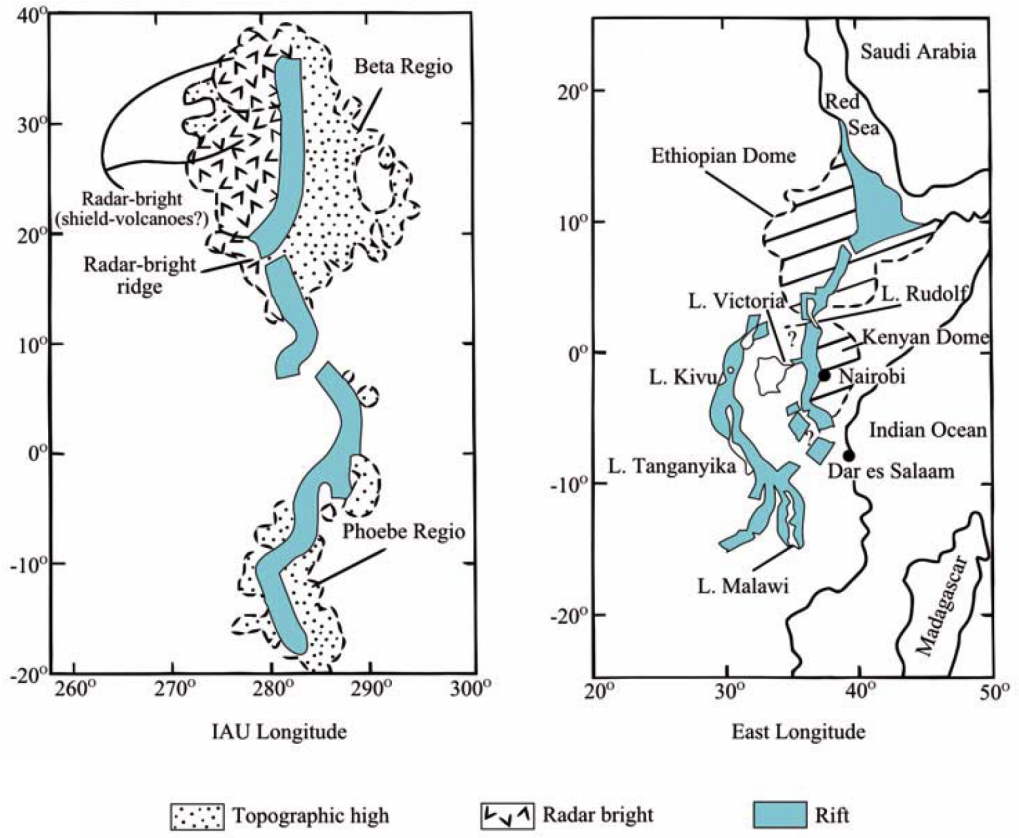

Figure 4.1: From Moores et al. [2013] rift system on Venus spanning from Beta Regio to Phoebe Regio (on the left) and the East-African rift region on the Earth (on the right). The figure is after Phillips and Malin [1984].

nesses of the two regions, Foster and Nimmo [1996] suggest that Venus in general and EARS have strong lithospheres. They further deduced that Venus requires higher shear stresses ($\approx$ 80 MPa) to act on the bounding faults of the rift to form half-graben in opposite to the EARS ($\approx 1-10$ MPa). The goal is to better understand the surface deformation of Venus and the tendency of the lithosphere to form rift systems, faults and fissures. We use `ASTRA` to reproduce the effect of the dip-slip fault of the rifting even of the 2005 EARS rifting event. However, we stress that the strength of the continental lithosphere depends largely on its thermal state [Karner et al., 1983]. The high surface temperature of Venus and its thick and dense atmosphere might cause the lithosphere to withstand deformations more than the Earth.

4.2 Manda Hararo-Dabbahu rifting of 2005

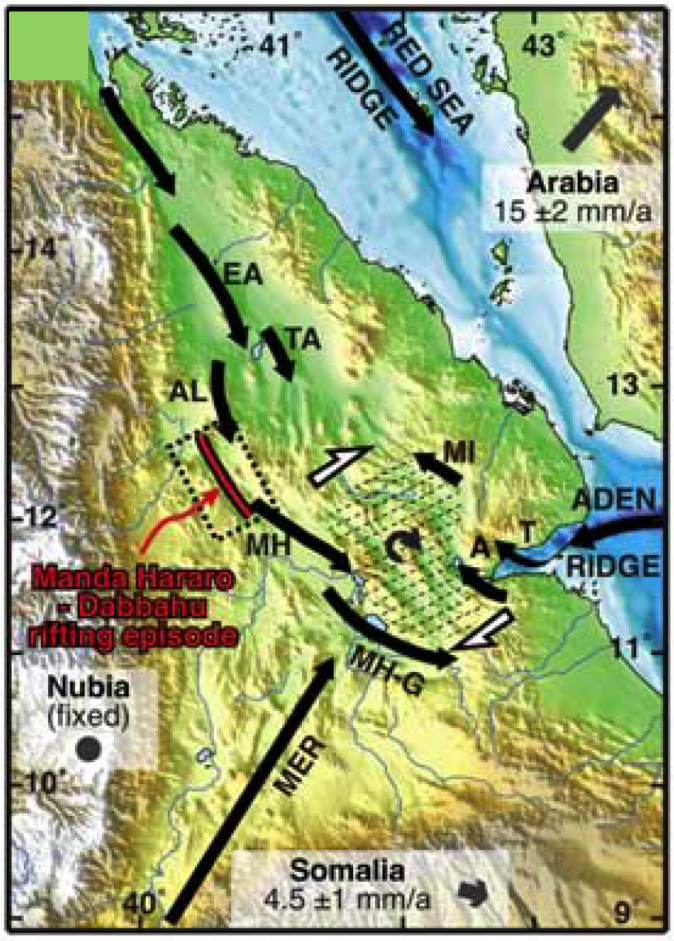

Figure 4.2: From Grandin et al. [2009] map of the Afar triple junction with rift segments (black arrows) overlap zone with bookshelf faulting (dashed black lines) and plate motion vectors (grey arrows). Asal-Ghoubbet (A), Alayta (AL), Erta'Ale (EA) Main Ethiopian Rift (MER), Manda Hararo (MH), Manda Hararo Goba'Ad (MH-G), Manda Inakir (MI), Tadjoura (T) and, Tat'Ali (TA).

A rifting event in September 2005 took place in Manda Hararo. It is called the Manda Hararo-Dabbahu rifting event since it is located near the Dabbahu volcano, a part of Manda Hararo. Grandin et al. [2009] used geodetic data such as INSAR (Interferometric synthetic aperture radar), SAR (synthetic aperture radar) and SPOT (satellite for observation of the Earth) images to construct the 3D displacement maps of the event. They suggest that the rifting event is a consequence of a volume of magma arriving from a mantle plume near the surface, causing the lithosphere to break and open a dike. This dike has a length of 65 km and a depth of 10 km. The dike opening consequently ruptured two faults in the

crust with a slip of 3 m on average. The estimated cumulative seismic moment of both faults rupture is 3.5×10^{19} N·m assuming a crustal rigidity of 3×10^{10} Pa. The resulting faults are two conjugate normal faults spanning from the surface to a depth of 3 km, a 2 m depression in between and uplifted shoulders of 2 m. After proposing the geometry and mechanism of the rifting event, Grandin et al. [2009] recreated the surface deformation using Okada [1985] analytic solutions for coseismic deformation, based on the Cagniard-de Hoop method. This method does not compute the postseismic response (the viscoelastic deformation), but the coseismic one (the elastic response). In addition to modeling seismic deformations, Okada [1985] solutions can also model a dike opening and a magma chamber deflation. The Earth model in this case is a homogeneous half space (flat model, not spherical as set in `ASTRA`), elastic, compressible and non-gravitating. In Okada [1985] only a model of the crust is needed, the coseismic response is observed and then computed by Grandin et al. [2009]. We will use the two conjugate normal faults geometry modeling as in Grandin et al. [2009] and calculate the coseismic response using `ASTRA`. We then compare our results of the surface deformation to theirs. We recreate the part of the dip-slip normal faults south of 12.55° N for an easier geometry for our test. This part of the rift is delimited by a red rectangle in Fig. 4.3.

4.3 ASTRA benchmarking on the 2005 Manda Hararo-Dabbahu rifting

4.3.1 The rift geometry

We use `ASTRA` on a model of the Earth to model the dip-slip seismic event which took place in Manda Hararo-Dabbahu in 2005. Since the seismic deformation is caused by relatively shallow faults (spanning from the surface to 3 km) the layers other than the crust, the lower mantle and upper mantle are expected to make negligible effect on the surface deformation. Nonetheless they are needed to be set for the computation of the code since `ASTRA` uses a model of the planet from the core to the surface as `ALMA`. Consequently some chosen parameters are set as a basic model of the Earth. The radius r, density ρ and V_S are from PREM [Dziewonski and Anderson, 1981]. The rigidity μ is calculated as $\mu = {V_S}^2 \rho$. The inner core and the outer core densities are averaged as one

homogeneous core. The transition zone is considered as a part of the upper mantle therefore averaging the upper mantle and the transition zone to be one homogeneous layer. As for the rheology and the viscosity η, the crust is set to be elastic ($\eta \to +\infty$ Pa $\cdot$ s). The core is set to be an inviscid fluid ($\mu = 0$ Pa and $\eta = 0$ Pa $\cdot$ s). Since only the coseismic (elastic) response is calculated, the mantle rheology and viscosity have no effect on the deformation. The lower mantle and upper mantle viscosities are set to 10^{20} Pa $\cdot$ s and with a Maxwell viscoelastic rheology. This rheology is chosen to be applied to the mantle since the source depth is shallow (in the crust) therefore the mantle rheology is assumed to have little effect on the outcome. This chapter is a preliminary work and it is mostly done for future perspectives. Therefore, since no comparison between the two rheologies have been done, a better known rheology (Maxwell) seems to be a better choice than Andrade's law for the extent of this work. The characteristics of the model are given in Table 4.1.

Table 4.1: The Earth model of four major layers: radius (r in km), density (ρ in kg/m^3), (S) seismic waves propagation velocity (V_S in km/s), rigidity (μ in Pa), viscosity (η in Pa $\cdot$ s) and rheology. Parameters r, ρ and V_S are from PREM [Dziewonski and Anderson, 1981], μ is calculated from V_S and ρ.

Layers	r (km)	ρ (kg/m^3)	V_S (km/s)	η (Pa $\cdot$ s)	μ (GPa)	rheology
Crust	6371	2520	3.074	$+\infty$	23.8	elastic
Upper mantle	6346.6	3604	4.858	10^{20}	85.8	Maxwell
Lower mantle	5701	4904	6.705	10^{20}	220.5	Maxwell
Core	3480	10987	0	0	0	inviscid fluid

A seismic rupture geometry has a shape and dimension (rupture point, segment (1D), rectangle (2D), $\cdots$). Its cumulative seismic moment M_0 is the sum of the seismic moment of each point rupture. The geometry and seismic moment in addition to its slip, rake and dip angle, model the rupture. These parameters are set in `ASTRA` as explained in section 2.3. The normal fault dip-slip motions of the Manda Hararo-Dabbahu rifting are modeled as two parallel faults with each $p = 28$ rupture points, the distance between the rupture points is set to be $L_p = 2$ km. We denote each rupture point from North to South by ${p_i}^w$ for the Western fault and ${p_i}^e$ for the Eastern fault such that $i \in \{1, \cdots, 28\}$. In `ASTRA` when a 1D fault is modeled the rupture points are assumed to have equal

seismic moments, precisely M_0/p each. The normal faults have rupture points with each different seismic moments. We compute each rupture point with its corresponding seismic moment and then add up the total deformation of the $2 \times p$ rupture points.

The seismic moment is defined as the product of the rigidity and geometric moment denoted by M_g, hence $M_0 = \mu M_g$. The geometric moment per unit of length of the rupture denoted by $M_{g/\text{km}}$ is given in Grandin et al. [2009] for each 2 km (which is equal to L_p). Therefore, the geometric moment for each rupture point is $M_g = L_p M_{g/\text{km}}$ since they are spaced, as our modeling, by 2 km. The cumulative geometric moment of the Western fault is the sum of its rupture points geometric moments, equal to ${M_g}^w = 0.66$ km^3. The cumulative geometric moment of the Eastern fault is the sum of its rupture points geometric moments, equal to ${M_g}^e = 0.37$ km^3. Therefore the cumulative geometric moment of the two slip-dip normal faults is the sum of the geometric moment of both fault equal to ${M_g}^{w+e} = {M_g}^e + {M_g}^w = 1.03$ km^3. Since M_0 is correlated to μ, a higher rigidity hence a higher resistance to deformation is equivalent to a higher seismic moment. We can either use the crustal rigidity (both for the Earth model and for calculating the seismic moment) of 30 GPa assumed in Grandin et al. [2009] or the one we derived from the Earth PREM (Table 4.1) of $\mu = 23.8$ GPa. These approaches are equivalent. The seismic moment of the fault ruptures (south of 12.55°N) is $M_0 = \mu {M_g}^{w+e}$, which is equal to 3.09×10^{19} N·m if we assume the crustal rigidity of 30 GPa. It is a coherent value for the fault rupture part that we recreate, since the total faulting event has a seismic moment of 3.5×10^{19} N·m. We set the rigidity values derived from the Earth PREM (Table 4.1). We then calculate the seismic moment M_0 for each rupture point p_i (Tables 4.2 and 4.3). The cumulative seismic moment of the eastern fault is then ${M_0}^w = 1.571 \times 10^{19}$ N·m. The one of the Western fault is then ${M_0}^e = 8.812 \times 10^{18}$ N·m. Finally the cumulative seismic moment of the faulting event is 2.452×10^{19} N·m.

From Grandin et al. [2009] we explore the geometry of the faults. At the surface the Western fault center is approximately at $(\theta_s^w, \varphi_s^w) = (40.585°\text{E}, 12.374°\text{N})$ and the Eastern one at $(\theta_s^e, \varphi_s^e) = (40.61°\text{E}, 12.384°\text{N})$. Both faults make an approximate angle of $\gamma = 22°$ with the North, inclined to the West. The distance between the two faults, which is the distance across the rift system, is denoted by L_s and given in Grandin et al. [2009] to be $L_s = 3$ km. The faults span from the surface to a depth $d = 3$ km [Grandin et al., 2009] where they intersect.

Table 4.2: The Eastern fault geometric moment per unit of length $M_{g/\mathrm{km}}$ for each rupture point p_i from Grandin et al. [2009]. The rupture points are spaced by L_p. Each point geometric moment is obtained by $M_{g/\mathrm{km}} = L_p M_g$ where L_p is in km and their seismic moment by $M_0 = \mu_{\mathrm{Crust}} M_g$.

	Eastern fault				
	$M_{g/\mathrm{km}}$ $(10^{-3}\mathrm{km}^3/\mathrm{km})$	M_g $(10^{-3}\mathrm{km}^3)$	M_0 $(10^{16}\mathrm{N{\cdot}m})$	θ $(^\circ)$	φ $(^\circ)$
p_1	0	0	0	40.517	12.597
p_2	0.86	1.72	4.093	40.523	12.581
p_3	2.6	5.2	12.376	40.530	12.564
p_4	3.4	6.8	16.184	40.537	12.547
p_5	2.6	5.2	12.376	40.544	12.531
p_6	3	6	14.280	40.55	12.514
p_7	2.2	4.4	10.472	40.557	12.497
p_8	2.6	5.2	12.376	40.564	12.481
p_9	4.3	8.6	20.468	40.57	12.464
p_{10}	5.6	11.2	26.656	40.577	12.447
p_{11}	6	12	28.560	40.584	12.431
p_{12}	8.2	16.4	39.032	40.591	12.414
p_{13}	9.5	19	45.220	40.597	12.397
p_{14}	10	20	47.600	40.604	12.381
p_{15}	9.5	19	45.220	40.611	12.364
p_{16}	12	24	57.120	40.618	12.347
p_{17}	14	28	66.640	40.624	12.331
p_{18}	15	30	71.400	40.631	12.314
p_{19}	14	28	66.640	40.638	12.297
p_{20}	13	26	61.880	40.645	12.281
p_{21}	11	22	52.360	40.651	12.264
p_{22}	9.9	19.8	47.124	40.658	12.247
p_{23}	8.6	17.2	40.936	40.665	12.230
p_{24}	7.8	15.6	37.128	40.672	12.214
p_{25}	5.6	11.2	26.656	40.678	12.197
p_{26}	3	6	14.280	40.685	12.18
p_{27}	0.43	0.86	2.046	40.692	12.164
p_{28}	0.43	0.86	2.046	40.698	12.147
cumulative	185.12	370.24	8.812×10^2	-	-

Table 4.3: The Western fault geometric moment per unit of length $M_{g/\mathrm{km}}$ for each rupture point p_i from Grandin et al. [2009]. The rupture points are spaced by L_p. Each point geometric moment is obtained by $M_{g/\mathrm{km}} = L_p M_g$ where L_p is in km and their seismic moment by $M_0 = \mu_{\mathrm{Crust}} M_g$.

	Western fault				
	$M_{g/\mathrm{km}}$ ($10^{-3}\mathrm{km}^3/\mathrm{km}$)	M_g ($10^{-3}\mathrm{km}^3$)	M_0 ($10^{16}\mathrm{N{\cdot}m}$)	θ (°)	φ (°)
p_1	6	12	28.560	40.504	12.592
p_2	9.9	19.8	47.124	40.51	12.576
p_3	16	32	76.160	40.517	12.559
p_4	17	34	80.920	40.524	12.542
p_5	18	36	85.680	40.531	12.525
p_6	16	32	76.160	40.537	12.509
p_7	16	32	76.160	40.544	12.492
p_8	14	28	66.640	40.55	12.476
p_9	22	44	104.720	40.557	12.459
p_{10}	22	44	104.720	40.564	12.442
p_{11}	21	42	99.960	40.571	12.425
p_{12}	16	32	76.160	40.578	12.409
p_{13}	12	24	57.120	40.584	12.392
p_{14}	11	22	52.360	40.591	12.376
p_{15}	12	24	57.120	40.598	12.359
p_{16}	15	30	71.400	40.604	12.342
p_{17}	13	26	61.880	40.611	12.326
p_{18}	9	18	43.316	40.618	12.309
p_{19}	10	20	47.600	40.625	12.292
p_{20}	11	22	52.360	40.632	12.276
p_{21}	9	19	47.124	40.638	12.259
p_{22}	10	20	47.600	40.645	12.242
p_{23}	7.3	14.6	34.748	40.652	12.225
p_{24}	4.7	9.4	22.372	40.659	12.209
p_{25}	1.7	3.4	8.092	40.665	12.192
p_{26}	4.7	9.4	22.372	40.672	12.175
p_{27}	3	6	14.280	40.679	12.159
p_{28}	1.7	3.4	8.092	40.685	12.142
cumulative	330	660	1.571×10^3	-	-

Therefore the point ruptures are modeled at the averaged center of depth of $d_p = 1.5$ km. Each fault dips at an angle of $\Lambda = \arctan[d/(L_s/2)]$ which is $\Lambda = 63.43°$. Since the two are normal faults, the strike of the Eastern fault is denoted by s^e and it is approximately $s^e = \pi - \gamma$, which in degrees is $s^e = 158°$. The strike of the Western fault is denoted by s^e and it is as $s^w = s^e + \pi$, which in degrees is $s^w = 338°$. Additionally the dip-slip fault rupture, which is a vertical downwards movement of its hanging wall, is modeled with a rake angle of $-90°$ in `ASTRA`, this is the value set for each rupture point. The coordinates of the centers of the faults at depth d_p have the same coordinates as their epicenters (projection at the surface). They are calculated from the coordinates of the centers faults at the surface $(\theta_s^w, \varphi_s^w)$ and $(\theta_s^e, \varphi^e{}_s)$. The fault centers at depth d_p are shifted from the fault centers at the surface by $\Delta\varphi = (L_s/4)\sin\Lambda = 0.671$ km in latitude and $\Delta\theta = (L_s/4)\cos\Lambda = 0.335$ km in longitude.

The Earth has a radius of $R_E = 6371$ km. To calculate $\Delta\varphi$ and $\Delta\theta$ in degrees, we multiply each by $\dfrac{360°}{2\pi R_E}$. Therefore, $\Delta\varphi \approx 0.006°$ and $\Delta\theta \approx 0.003°$. Finally, the fault centers at depth d_p have coordinates $(\theta^w, \varphi^w) = (\theta^w{}_s + \Delta\theta, \varphi^w{}_s + \Delta\varphi) = (40.591°, 12.376°)$ for the Western fault and $(\theta^e, \varphi^e) = (\theta_s^e - \Delta\theta, \varphi_s^e - \Delta\varphi) = (40.604°, 12.381°)$ for the Eastern fault. They correspond to the point ruptures number 14 out of $p = 28$, denoted by p_{14}^e and p_{14}^w in Tables 4.2 and 4.3 respectively. The distance in km of two point $p_A = (r, \theta_A, \varphi_A)$ and $p_B = (r, \theta_B, \varphi_B)$ at a certain radius r of a planet is calculated as:

$$D(p_A, p_B) = r \arccos[\sin\varphi_A \sin\varphi_B + \cos\varphi_A \cos\varphi_B * \cos(\theta_B - \theta_A)]. \tag{4.1}$$

The distance at the surface of the Earth is then calculated with Eq. 4.1 with $r = R_E$ and at the rupture points with $r = R_E - d_p$. We verify using Eq. 4.1 that the distance between (θ^w, φ^w) and (θ^e, φ^e) is equal to 1.5 km. We assume that the two fault are perfectly linear and we model each with a segment centered at these spherical coordinates ${p_{14}}^e = (d, \theta^e, \varphi^e)$ and ${p_{14}}^w = (d, \theta^w, \varphi^w)$. To calculate the coordinates of the other rupture points, we use trigonometry to map the linear distribution of p_i along the faults, similar to what is done to calculate the coordinates at depth of the faults centers. The faults span of a length of 56 km. Therefore the longitude and latitude variate between each rupture point by $\Delta\theta' = L_p \sin\gamma = 0.749$ km and $\Delta\varphi' = L_p \cos\gamma = 1.854$ km respectively. To calculate $\Delta\varphi'$ and $\Delta\theta'$ in degrees we multiply each by $\dfrac{360°}{2\pi(R_E - d_p)}$, therefore,

$\Delta\varphi' \approx 0.017°$ and $\Delta\theta' \approx 0.007°$. We set $p/2-1 = 13$ rupture points at the North of the centers and $p/2 = 14$ rupture points at the South of the centers. The Eastern fault rupture points to the North of its center (θ^e, φ^e) have coordinates of $(\theta^e - [p/2 - i]\Delta\theta', \varphi^e + [p/2 - i]\Delta\varphi')$ where $i \in \{1, \cdots, 14\})$. The rupture points of the Western fault to the North of its center (θ^w, φ^w) have coordinates of $(\theta^w - [p/2 - i]\Delta\theta', \varphi^w + [p/2 - i]\Delta\varphi')$ such that $i \in \{1, \cdots, p/2\})$. The eastern fault rupture points to the South of its center (θ^e, φ^e) have coordinates of $(\theta^e + [i - p/2]\Delta\theta', \varphi^e - [i - p/2]\Delta\varphi')$ such that $i \in \{p/2 + 1, \cdots, p\})$. The rupture points of the Western fault to the South of its center (θ^w, φ^w) have coordinates of $(\theta^w + [i - p/2]\Delta\theta', \varphi^w - [i - p/2]\Delta\varphi')$ such that $i \in \{p/2 + 1, \cdots, p\})$. The coordinates of the rupture points for the Eastern and Western faults are respectively in Tables 4.2 and 4.3. We observe the deformation at $t \to 0$ years, corresponding to the coseismic (elastic) deformation. The observations are set at the surface from 40.3°E to 40.8°E in longitude and from 11.9°E to 12.8°E in latitude. The distances in degrees between the observations are of 0.005° for both coordinates (longitude and latitude). We apply the fault geometry, the seismic moments (Tables 4.2 and 4.3), the strike, the rake and the dip angles as well as the observations time and space to `ASTRA`.

4.3.2 Results for the coseismic deformation

We compare our results with the one of Grandin et al. [2009]. The negative vertical (also called radial) displacement d_r correspond to a subsidence (sinking) of the surface below its original location. The positive vertical displacement d_r correspond to an uplift (elevation) of the surface above its original location. We obtain a maximum subsidence of 5.39 m and a maximum uplift of 1.36 m (Fig. 4.4 and Table 4.4). Grandin et al. [2009] found a maximum of 2 m uplift around the faults, caused by the uplift of the shoulders of the dip-slip faults and a 2 m subsidence in between (Fig. 4.3). Their uplift value is close to the 1.36 m we obtain. For the subsidence, our value (5.39 m) is more than 2 times bigger than theirs (2 m). We calculated the effect of each point and added the total deformation since each rupture point is modelled with a different seismic moment (Tables 4.2 and 4.3). Therefore in the areas where the rupture points are close and near each rupture point, there is an exaggeration of the deformation. In the case of this rifting event, the rupture points of the Western and Eastern sides

are close (distance of 3 km) and their effect of subsidence is exaggerated where they intersect, which is in the middle of the rift. Therefore a better comparison with the results of Grandin et al. [2009] is done with the resulting uplift than the subsidence. To avoid this exaggeration in future studies, solutions can be applied as removing the values calculated near each rupture point at a certain critical distance or as an attenuation of the results. This procedure is not done in this preliminary chapter and it can indeed be discussed for future work.

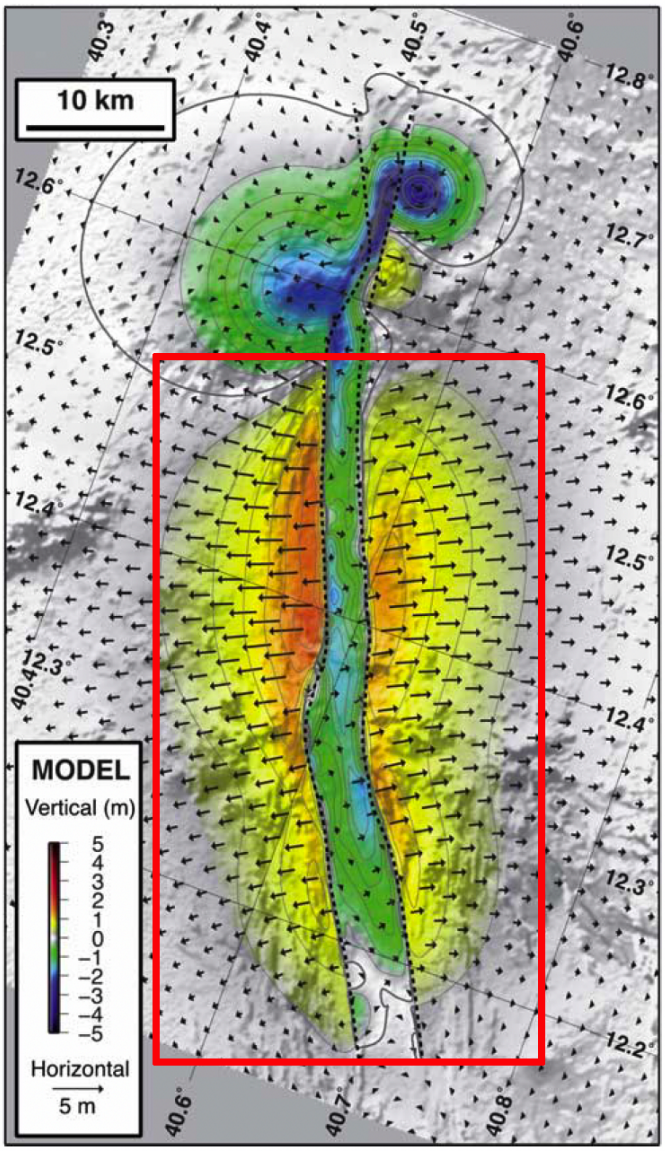

Figure 4.3: Modeled surface deformation from Grandin et al. [2009] of the slip-dip faults of the Manda Hararo-Dabbahu rifting of 2005 calculated with Okada [1985] solution. The red rectangle delimits the part of the rift that we recreate.

The surface deformations outputs from `ASTRA` are the vertical displacement

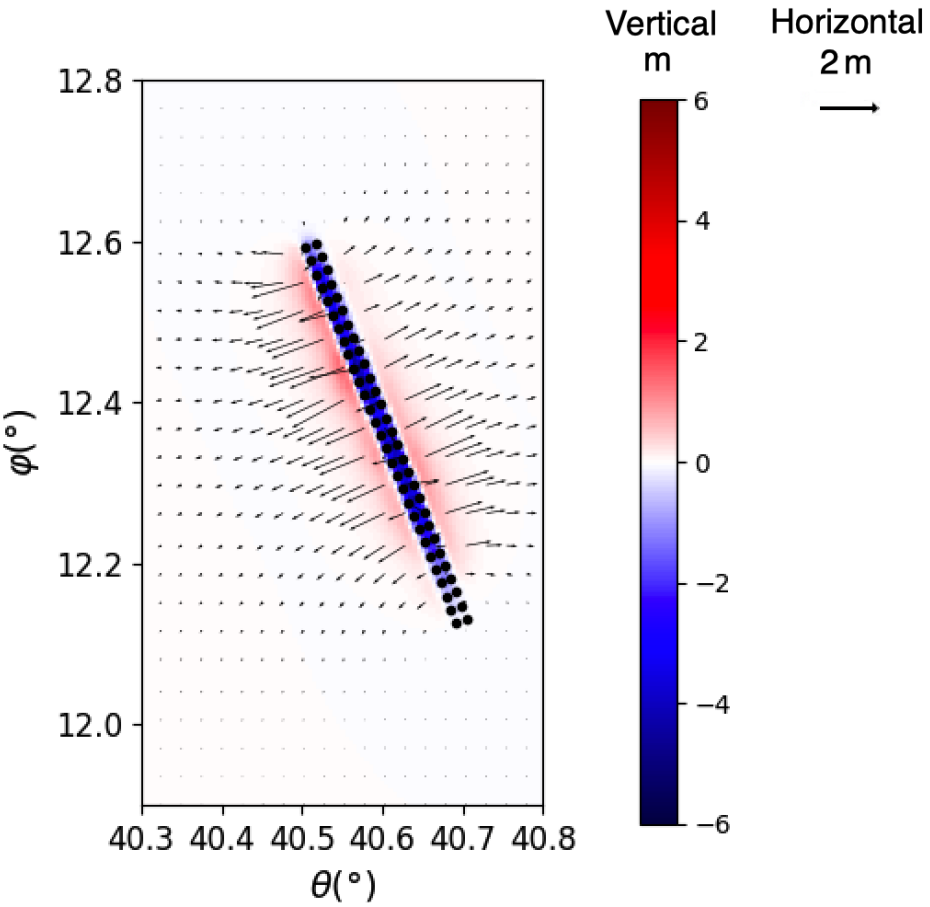

Figure 4.4: The Earth modeled Earth surface deformation of the slip-dip faults of the Manda Hararo-Dabbahu rifting of 2005 calculated with `ASTRA`. The black dots are each rupture point epicenter.

Table 4.4: Maximum coseismic surface displacement for the Earth after the Manda Hararo-Dabbahu normal faults dip-slip of 2005 calculated with `ASTRA`.

The Earth coseismic deformation		
	`ASTRA`	Grandin et al. [2009]
uplift (m)	1.36	2
subsidence (m)	5.39	2
tangential (m)	1.874	2.5

d_r and two components (d_θ and d_φ) for the tangential displacement (of perpendicular directions), from which we calculate the total tangential displacement $d_t = \sqrt{d_\theta^2 + d_\varphi^2}$. Fig. 4.4 shows this deformation as arrows pointing to the direction of the deformation, and the length of the arrow scaled to its norm d_t. The

values of d_t span from 0 m to 1.874 m (Fig. 4.4) which is in agreement with the value of Grandin et al. [2009] of ≈ 2.5 m (Fig. 4.3).

4.4 Application on Venus

Shalygin et al. [2015] first found proof of volcanic activity on the surface of Venus taking place in 2008 (section 1.1.2). No proof of activity was observed before, therefore next missions will focus on other possible proof of geological activity to dig deeper in this new discovery. One way to explore the geological activity of a planet is by observing its surface deformation from its topography. The Magellan mission collected radar altimetry data from the first 8 months (between September 1990 and May 1991) of its mission orbiting Venus. Two future missions, VERITAS [Freeman and Smrekar, 2015] and EnVision [Ghail et al., 2017] will be launched in 2027 and 2031, respectively (section 1.3). VERITAS will map the surface of Venus with Venus Interferometric Synthetic Aperture Radar (VISAR) instrument and EnVision with Venus Synthetic Aperture Radar (VenSAR). Comparing the past topography maps of Venus with future maps will give an outlook on its surface deformation. Magellan provided altimetry data of the surface with the vertical and tangential resolutions in Table 4.5. The future missions will provide an improved altimetry resolution, Table 4.5 shows the resolution of the past and future missions.

Table 4.5: Altimetry resolutions of past (Magellan) and future missions: VERITAS [Freeman and Smrekar, 2015] and EnVision [Ghail et al., 2017].

	vertical resolution (m)	along track (km)	cross track (km)
Magellan	$10 - 100$	$8 - 15$	$12 - 27$
VERITAS	5	0.25	0.25
EnVision	2.5	-	-

A radar (as VISAR and VenSAR) can also be used to achieve repeat-pass interferometry (RPI) which uses sub-wavelength precision to detect changes in the topography. The RPI can be done if the orbiter passes over the same location repeatedly within a specific path. It measures the differential altimetry between each observation with a better resolution than the global altimetry map.

Additionally to the high-resolution altimetry, VERITAS will perform RPI over at least 12 potentially active areas on the surface of Venus. Repeated cycles separated by 243 days are needed for the RPI. It will provide measurements of surface deformation with 2 mm precision [Smrekar et al., 2020].

We assume that Venus is subjected to a dip-slip event of the same geometry and magnitude of the 2005 EARS rifting event. We deduce, in addition to its coseismic effect, its resulting postseismic rebound for different time-scales. The difference between the postseismic rebound after some time t and the initial coseismic rebound is called the relaxation and it is due to the viscoelastic layers of the planet. We estimate the relaxation after $t = 3$ years which corresponds to the observations of VERITAS/EnVision (either each on its own or their combined data). Additionally we calculate the deformation after $t = 30$ years corresponding to the time difference between Magellan and VERITAS/EnVision and after $t = 100$ years as an exaggerated time-scale for testing.

4.4.1 The rift geometry

We apply the same normal fault dip-slip event rupture modeling described in section 4.3.1 on Venus. We use the model **V** of Dumoulin et al. [2017] detailed in section 3.1.1. In this section, the lower and upper mantle rheologies follow the Maxwell law instead of the Andrade law. The rupture point coordinates, geometric moments and seismic moments are in Tables 4.2 and 4.3. The same rupture depth and angles as in section 4.3.1 are applied. We recall having the dip angle equal to 63.43°, the rake angle equal to −90° (same dip and rake angles for both faults) and a strike angle $s^e = 158°$ and $s^w = 338°$ for the Eastern and Western faults respectively. The lower mantle and upper mantle are set to have equal viscosities ($\eta_{\text{LM}} = \eta_{\text{UM}} = 10^{20}$ Pa · s). The crust is first assumed to be elastic ($\eta \to +\infty$ Pa · s) as for the application on the Earth (section 4.3.1). The effect of the dense atmosphere is not considered. Neither is the effect of the atmosphere loading on the surface and the high surface temperature which affect the response of the faults in the lithosphere to seismic ruptures [Karner et al., 1983] as mentioned in section 4.1.

4.4.2 Results for the coseismic deformation

The resulting surface displacement (vertical and tangential) map for Venus is similar to the one obtained for the Earth (Fig. 4.4 and Table 4.4). The maximum subsidence is 5.5 m and the maximum uplift is 1.5 m. The tangential displacement has a maximum of 2.0 m. Since the Venus model **V** is based on PREM (section 3.1) and the atmosphere is not considered, these similar results are expected. The faults are not scaled down taking into consideration the slightly smaller size of Venus, therefore the same faults have a bigger effect on Venus than on the Earth. Hence the relatively minor differences in the results between the Earth and Venus (Table 4.6) is caused by the smaller size of Venus (by 5%). The incremental gravitational potential ϕ spans from 0 to 10.104 mJ/kg in the total deformed surface. The variation of gravity acceleration Δg has a minimum of -0.18 mGal and a maximum of 0.68 mGal (Figs. 4.5 and 4.6). These values are calculated on the surface and can not be done for an elevation above the surface with `ASTRA`. EnVision will have a significant improvement on the detection of the gravity field of Venus. Rosenblatt et al. [2021] estimated the gravity error that will be observed in the future by the EnVision orbiter mission. They cumulated the error up to 110 in degree and order and estimated that the observation error spans from 2 to 20 mGal depending on the location. Dampening the gravity acceleration variation Δg (Fig. 4.6) taking into account the elevation of a satellite (250 km for VERITAS and $220 - 470$ km for EnVision) around Venus gives an estimation of the observation of the orbiter. This approach approximates what a satellite would observe in terms of gravity acceleration variation as a response to a seismic dislocation. The deformation is exaggerated (section 4.3.2) between the faults and we did not take into account its dampening relatively to the satellite elevation. Even with these two facts, the future error of EnVision ($2 - 20$ mGal) is too large to observe the maximum gravity acceleration variation ($|\Delta g| = 0.68$ mGal) calculated by `ASTRA` for this particular dip-slip faults rupture.

We test the effect of a contrast in between the lower mantle and the upper mantle viscosities. From Fig. 3.7 (b) in section 3.2, representing $\eta_{\mathrm{LM}}/\eta_{\mathrm{UM}}$, we assume two different viscosity ratios: $\eta_{\mathrm{LM}}/\eta_{\mathrm{UM}} = 10$ and $\eta_{\mathrm{LM}}/\eta_{\mathrm{UM}} = 0.1$ corresponding to one higher and one lower order of magnitudes, respectively. We fix $\eta_{\mathrm{UM}} = 10^{20}$ Pa $\cdot$ s, hence $\eta_{\mathrm{LM}} = 10^{21}$ Pa $\cdot$ s and $\eta_{\mathrm{LM}} = 10^{19}$ Pa $\cdot$ s respectively

for each case. The coseismic rebound (both surface and gravity deformations) are the same for the three different mantle viscosity cases (Table 4.6). These results are expected since, with the coseismic deformation, it is the elastic response and not the relaxation (also called flow) that is involved. The overall coseismic surface displacement (Table 4.6): uplift (1.475 m), subsidence (5.504 m) and tangential displacement (1.954 m) are of the same magnitude of the future EnVision and VERITAS altimetry resolutions (Table 4.6). Therefore, the sizes of the rifts will be visualized with the future Venus exploration missions. The new data will provide more information about the geometry of the rift systems which will constrain the magnitude and depth of the seismic dislocation that formed them.

4.4.3 Results for the postseismic deformation

We calculate the postseismic rebound for $t = 3$ years, $t = 30$ years and $t = 100$ years to estimate the magnitude of the surface and gravity deformations in these time scales. Table 4.6 represents the Venusian coseismic and postseismic rebounds for the same normal faults rupture as previously and for the different mantle viscosity assumptions. Having equal or different lower mantle and upper mantle viscosities does not affect the surface displacement significantly, neither on the short term (3 years) nor on the long term (30 years and 100 years). More specifically the three different mantle viscosities contrast tested (Table 4.6) each cause a relaxation of almost 18 cm after 100 years. As the difference between having a mantle viscosity contrast by $\eta_{\mathrm{LM}} = 10 \times \eta_{\mathrm{UM}}$ and $\eta_{\mathrm{LM}} = \eta_{\mathrm{UM}}/10$ only affects the relaxation by a magnitude of 10^{-3} cm after 100 years. Therefore, the viscosity contrast of this magnitude is not strong enough to have an effect on the displacement after a dip-slip event of that model, neither on the coseismic nor on the postseismic rebounds. It also affects the incremental gravitational potential ϕ negligibly by a maximum of 0.2%. As for the gravity acceleration variation Δg, it is the same for different mantle viscosity cases and variates negligibly from the coseismic rebound ($t \to 0$ years) and the postseismic rebound ($t = 3$ years, $t = 30$ years and $t = 100$ years). Therefore, the postseismic gravity acceleration variation for this event is too small to be observed by EnVision in the future.

The tangential displacement (Table 4.6) does not change after 3 and 30 years and it increases by less than 1 mm after 100 years. The uplift and subsidence change each by 6 mm after 30 years from the elastic response and by 18 mm after

Table 4.6: Surface deformation for Venus after an event similar to the Manda Hararo-Dabbahu normal faults dip-slip of 2005, modeled with `ASTRA`. The relaxation is the difference between the postseismic rebound after certain time t and the initial coseismic rebound.

	Venus coseismic and postseismic deformation					
	uplift (m)	subsidence (m)	tangential (m)	ϕ (mJ/kg)	positive Δg (mGal)	negative Δg (mGal)
Coseismic	1.475	5.504	1.954	10.104	0.680	0.182
Relaxation	(mm)	(mm)	(mm)	(mJ/kg)	(mGal)	(mGal)
$\eta_{\rm LM} = \eta_{\rm UM}$						
3 years:	0.6	-0.6	0	-0.029	0	0
30 years:	5.96	-5.91	0	-0.281	0	0.001
100 years:	17.85	-17.7	0.7	-0.866	-0.002	0.003
$\eta_{\rm LM} = 10 \times \eta_{\rm UM}$						
3 years:	0.6	−0.6	0	−0.028	0	0
30 years	5.96	−5.90	0	−0.275	0	0.001
100 years	17.82	−17.68	0.7	−0.851	−0.002	0.003
$\eta_{\rm LM} = \eta_{\rm UM}/10$						
3 years:	0.6	−0.6	0	−0.029	0	0
30 years	5.97	−5.92	0	−0.285	0	0.001
100 years	17.86	−17.71	0.7	−0.875	−0.002	0.003

100 years. The altimetry map resolution of Magellan has errors that are too large (Table 4.5) to be compared with the future missions for the viscoelastic relaxation effect. We make conclusions based on the effect of an event of the magnitude of the 2005 Manda Hararo-Dabbahu rifting. Magellan topography map resolution is too low (Table 4.5) to observe the rifting event occurring between Magellan and the future missions (EnVision and VERITAS). Consequently, the vertical relaxation of 6 mm (Table 4.6) after $t = 30$ years will also not be observed, hence the time scale of the rupture can not be estimated from comparison between Magellan and the next generation altimetry. After an event of the magnitude of the EARS event, the future altimetry experiments will not be able to localize or

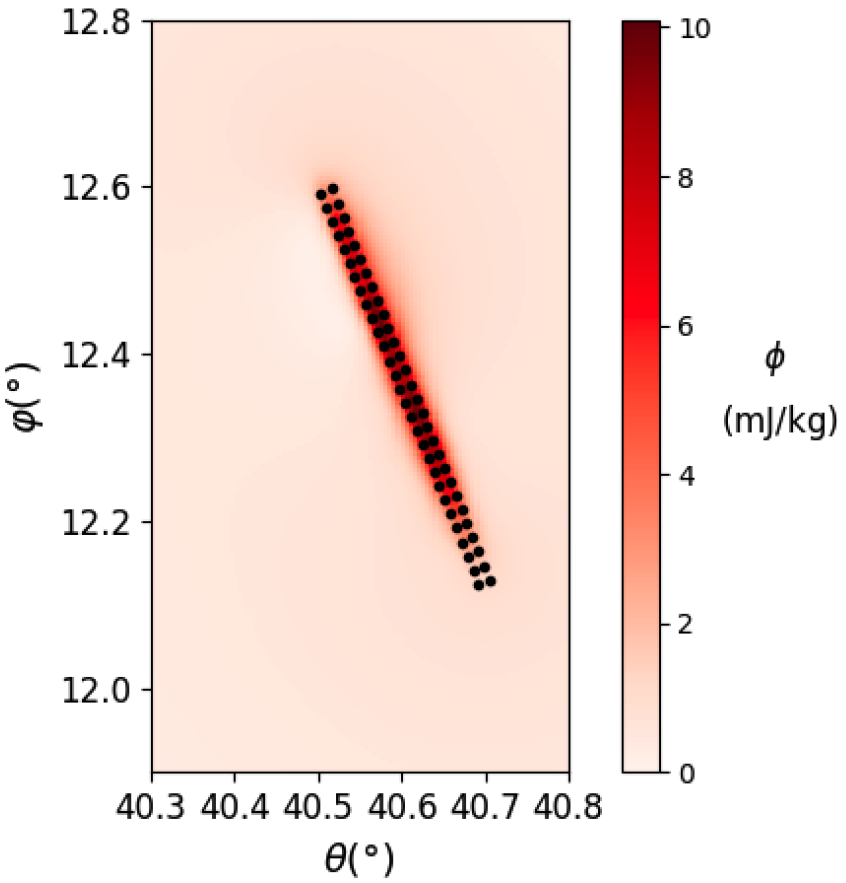

Figure 4.5: Modeled Venus coseismic incremental gravitational potential ϕ after an event similar to the Manda Hararo-Dabbahu normal faults dip-slip of 2005 calculated with `ASTRA`. The black dots are each rupture point epicenter.

date such a past rifting event from comparisons between past and present maps Table 4.6).

As for a same scale event occurring after 2027 when VERITAS and/or EnVision will be orbiting Venus, the coseismic deformation is big enough (Table 4.6) to be observed by the altimetry (Table 4.5) resolution that will be achieved by both missions. The RPI experiment will be done on more than 12 locations on Venus that have not been disclosed yet. This will correspond to the deformation differential resolution of 2 mm after each 243 days cycle. The relaxation of the surface deformation induced by an event such as the one of the 2005 EARS, will be 6 mm after 3 years for the vertical components (uplift and subsidence). Therefore it has a magnitude comparable with the surface differential achieved by the RPI after each cycle. Finally, with the RPI on these locations of interest on Venus the relaxation of the rifts should be detected. It will mostly depend on

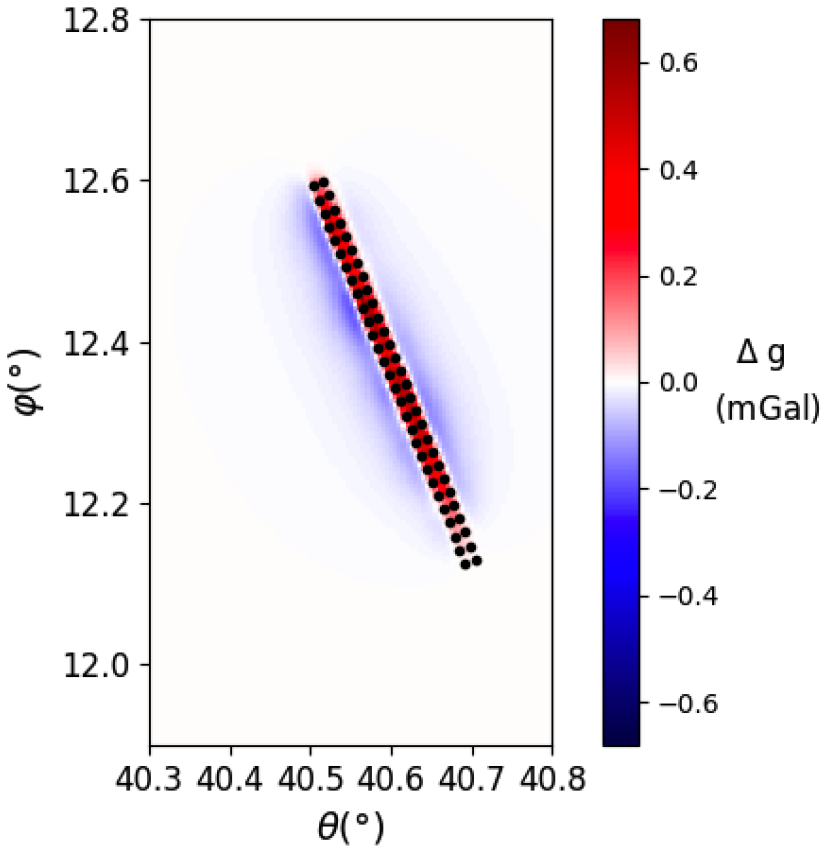

Figure 4.6: Modeled Venus variation of gravity acceleration Δg after an event similar to the Manda Hararo-Dabbahu normal faults dip-slip of 2005, calculated with `ASTRA`. The black dots are each rupture point epicenter.

the depth and the magnitude of the event and on the observation time t after its release.

4.4.4 Sensitivity of the viscosity of the crust

The lithosphere strength to withstand fractures and rift formation is shown to depend on its thermal state [Karner et al., 1983]. The high surface temperature of Venus of 737 K and massive atmosphere might cause the crust to behave more as a viscoelastic layer instead of an elastic layer. We set the mantle viscosity to be homogeneous and equal to 10^{20} Pa $\cdot$ s. The goal here is to test the impact of the crustal viscosity (η_{Crust}) on the vertical and tangential deformation for the coseismic and postseismic ($t = 30$ years) deformation and whether in this case the relaxation might be observed by comparing the Magellan altimetry map with the future VERITAS/EnVision maps.

We assume different crustal viscosities spanning from one equal to the mantle viscosity (10^{20} Pa · s) to the elastic limit as ($> 10^{30}$ Pa · s). We calculate the coseismic deformation and the postseismic deformation at $t = 30$ years. In Fig. 4.7, one can see that the vertical and tangential surface deformations tend to $+\infty$ m for a low crustal viscosity ($\eta_{\text{Crust}} \to 0$ Pa · s). This result is expected since the very low viscosity for the crust is equivalent to assuming a fluid crust which will enhance the deformation. The surface deformations are almost constant and of the order of a few meters for a crust of equal or higher viscosity as the mantle ($\eta_{\text{Crust}} > 10^{20}$ Pa · s). Therefore, the surface deformation is barely affected by

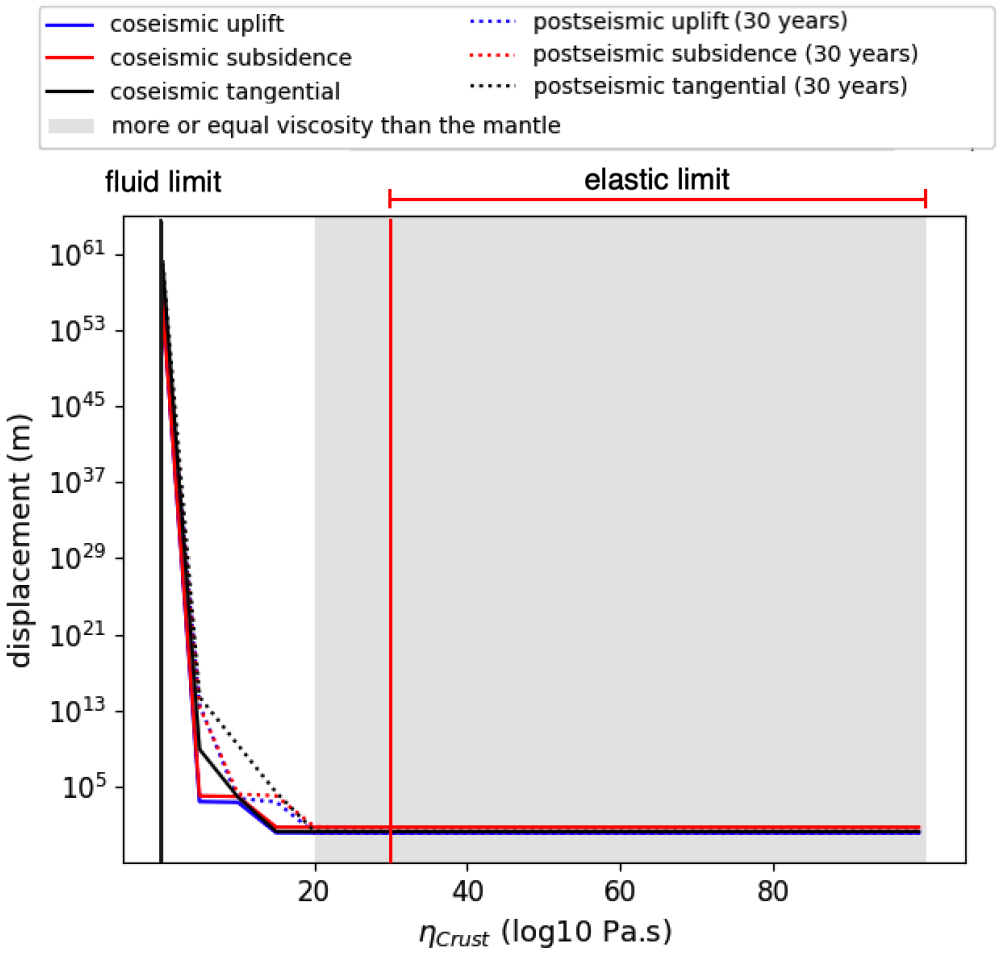

Figure 4.7: Vertical (uplift and subsidence) and tangential deformations for the cosesimic and the postseismic ($t = 30$ years) rebounds for Venus after a dip-slip dislocation of the same geometry and magnitude of the 2005 EARS event.

if the crust is elastic $\eta_{\text{Crust}} \to +\infty$ Pa · s or if it has equal or similar viscosity than the mantle ($\eta_{\text{Crust}} = 10^{20}$ Pa · s). This little effect might be due to the

shallow depth of only 1.5 km of this rift geometry. Taking this study further to the different crustal rigidity, the effect of a higher seismic moment and different seismic dislocation depths can be tested. Changing the seismic moment M_0 will consist of either fixing the rigidity and changing the geometric moment M_g or fixing the geometric moment and changing the crustal rigidity.

4.5 Conclusion

Venus is active in the present day as it has been observed from past missions. The NASA VERITAS and Davinci+ missions and the ESA EnVision missions are orbiters and an atmospheric probe that will be sent to Venus in the near future. They will be equipped with instruments to observe the geological activity of the planet. These deformations can be observed by orbiters. We suggest the possibility to observe a present seismic dislocation, or the signature of a seismic dislocation by studying the elastic (coseismic) and viscoelastic (postseismic) deformation. In this chapter we test the results obtained with `ASTRA` from Melini et al. [2008] on a model of the Earth and a model of Venus of the coseismic rebound from a dip-slip event. The applied seismic dislocation model is of the 2005 Manda Hararo-Dabbahu rifting. For the case of the Earth we compare our results with an other study [Grandin et al., 2009]. We show the accuracy of `ASTRA` despite the simple planetary model used and the approximate approach for the fault geometry. Afterwards the same fault geometry is applied to a model of Venus. An event of the magnitude of the 2005 Manda Hararo-Dabbahu rifting is not big enough to be observed by EnVision with the gravity field variation. The effect of deeper rupture centers and bigger fault lengths should be considered in future studies. As well as the satellite altitude from the planet from where the gravity acceleration will be dampened. Furthermore the history of Venus should also be taken into account, more specifically the evolution of the BAT region, assuming several events taking place in different timescales and their cumulative effect on the present day gravity field of Venus.

EnVision and VERITAS will be an improvement on previous radar maps of Venus from Magellan and VEx. This global view will give for the first time a new map of possible active regions. An area of interest is the BAT region detailed in section 1.1.2. Several seismic dislocations can be implemented at different locations on Venus with different timescales in order to compute its present and

future effects on the planet. The resulting deformations are both surface and gravity field deformations which will be observed by EnVision and VERITAS in the future. The overall deformation for such an event is of the same order of magnitude of the future altimetry errors ($2.5 - 5$ m from Table 4.5). Therefore, rift zones will be better mapped with the future missions. The coseismic deformation is of the same magnitude of the future VERITAS/EnVision altimetry maps. The uplift and subsidence of the rift mapped with such a resolution will be an indication for the possible magnitude and depth of the which caused the event. The relaxation (postseismic deformation) of such a rift is not big enough (6 mm after 30 years) to be observed by comparison between past and future altimetry maps. This is due to the low resolution of the Magellan altimetry map despite the high resolution of future VERITAS/EnVision altimetry maps. The future RPI measurements of VERITAS (2 mm) will be obtained for specific locations on Venus for each 243 days. Therefore the relaxation is of similar magnitude (0.6 mm after 3 years) of the RPI resolution which will play a significant role in the constraint of a potential seismic activity (location, depth and magnitude).

5. Conclusions and perspectives

In this work (chapter 3) we first adapt the `ALMA3` open-source fortran code [Melini et al., 2022] to the study of Venus. We apply a model of Venus with a fluid core from a pevious study [Dumoulin et al., 2017]. The mantle is assumed to have a Maxwell rheology or an Andrade rheology with different mantle viscosities (10^{19},10^{20},10^{21} and 10^{21} Pa·s) and different values of the Andrade experimental parameter α. We calculate the tidal Love number k_2 with `ALMA3` for each of these models and compare them with the results of Dumoulin et al. [2017]. We found that the real and imaginary parts of the TLN k_2, k_2^r and k_2^i, differ maximum from the results of Dumoulin et al. [2017] by 2% and 6% respectively depending on the mantle viscosity and value of α. The effect of the atmosphere on k_2 and Q depends on the rheology, mantle viscosity and parameter α. The difference between the lack and the presence of the atmosphere is maximum of 7.2%, 8.34%, 1.65% on the k_2^r, k_2^i and Q respectively. Therefore assuming that the mantle viscosity of Venus is homogeneous we tested `ALMA3` on a model of Venus and our results are consistent with the results of Dumoulin et al. [2017]. Afterwards we use geophysical constraints of Venus (mass, normalized moment of inertia, tidal Love number k_2 and quality factor Q) to explore possible scenarios of its internal structure. We explore a wide range of internal structure parameters of Venus, the thickness, density and viscosity of each major layer. We suppose the possibility of three different core structures: fluid core (**Class 1**), solid core (**Class 2**) and a solid inner core with a fluid outer core (**Class 3**). The random selection of each layer parameter is done with Monte-Carlo sampling before using the mass and moment of inertia to select the approved models. Then with `ALMA3` we calculate the TLN k_2 and quality factor Q and we use their estimated values for Venus to filter once again the models consistent with these parameters. We also add a density filter for the inner core/core and lower mantle for the three classes. We end up with 65000 models that fit with the moment of inertia of Margot et al. [2021] with $\pm 1\sigma$ for each class. The remaining models after the rest of the

filters are applied are 962, 1076 and 417 models for **Class 1**, **Class 2** and **Class 3**, respectively. We show that the possibility of having an entirely fluid core, a solid core and a partially fluid and partially solid core cannot be ruled out by only considering geophysical constraints. We also observe a contrast between the viscosities of the lower mantle and the upper mantle. Only 1% of each class have a homogeneous mantle viscosity. The difference between the lower mantle and the upper mantle densities and thicknesses also point out the non-homogeneity of the mantle. Our study which is based on geophysical constrains is compared to the work of Shah et al. [2021] which is based on the chemical assessment of the interior of Venus. We deduce that our models fit with their S-free models by comparing the radii and densities of the layers. It is in agreement with past studies which support the suggestion that the core of Venus is poor or free of sulfur [Lewis, 1972; Trønnes et al., 2019]. The radio-science experiment of EnVision and VERITAS will provide a global mapping of its gravity field which will estimate k_2. For example, for EnVision both the real and imaginary parts, with an uncertainty of $\sigma = 0.002$. This will be an improvement of the past estimation ($\sigma = 0.033$) of the real part of k_2 from Magellan and PVO gravity field. In the future this study can be expended by additionally randomly selecting the rigidity of each layer. This will take this study further with the improvement of the uncertainty of k_2 (real and imaginary parts) consequently of the quality factor Q. This better estimation of these two parameters will better filter the possible models.

In the second part of this work (chapter 4) we use a fixed model of Venus with a fluid core from Dumoulin et al. [2017] to calculate the seismic rebound of a fault dislocation. The seismic rebound is calculated by the fortran code `ASTRA` [Melini et al., 2008]. We assess the effect it has on the gravity field and surface displacement in the goal to conceive possible future detection of seismic activity from orbiters. We apply the same geometry, depth and moment of the 2005 Manda-Hararo Dabbahu rifting event on Venus. It consists of two conjugate normal faults dip-slip movement with a geodetic moment of 3.5×10^{19} Nm for a crustal rigidity of 3×10^{10} Pa and 1.5 km depth. We found that its instantaneous coseismic effect on the surface displacement is of 1.4 m shoulders uplift and 5.5 m subsidence between the faults. This vertical deformation is of interest since it is of the same magnitude of future altimetry measurements (2.5 m and 5 m for EnVision and VERITAS, respectively). Therefore a similar event that caused a

rift opening on the surface of Venus will be better mapped and constraints on the depth, geometry and geodetic moment of the seismic dislocation. Several regions rich in rift systems and have been already shown to be similar to locations on the Earth are of interest such as Beta Regio and Parga and Hecate chasmata. The postseismic rebound have been also calculated in the goal of comparing it with the coseismic rebound in the frame of past and future Venus exploration missions. Additionally to altimetry measurements, RPI experiments will be performed by VERITAS on several locations of interest on the surface of Venus. It will provide an estimation of the surface deformation for each 243 days cycle which will be an indication on the surface relaxation between each measurement. The relaxation, which is the difference between the postseismic and coseismic deformations, is due to the viscoelastic nature of the planet. The relaxation we calculated is after 3 years of the seismic dislocation taking into consideration the RPI experiments time-scales. Another one is after 30 years taking into account the difference between Magellan and future VERITAS/EnVision altimetry acquisition. We found that the Magellan topography resolution $10 - 100$ m is too big to detect any coseismic or postseismic deformations difference between the past and future missions. We also found that the contrast in the mantle viscosity does not affect the coseismic or the postseismic deformations significantly. The vertical relaxation after 3 years of an event as the 2005 Manda-Hararo Dabbahu rifting is of 0.6 mm. It is close to the future RPI differential resolution (2 mm) after each cycle. Therefore depending on the depth, size and magnitude of a rift, its relaxation might be detected by future RPI measurements. This will make it possible to compare theoretical estimation of the relaxation from codes as `ASTRA` with geophysical experiments. And therefore constrain the geometry and magnitude of the surface dislocation which formed a rift on Venus. The effect of deeper rupture centers and bigger fault lengths will be considered in future studies. I will continue working with the same team for the next few months in the goal of exploring more future observations of seismic activity of Venus. One way to explore the effect of one or more Venus-quakes is to use a random Monte-Carlo sampling of different locations, magnitudes, depths and geometries of several seismic dislocations. The history of Venus and more specifically of the BAT region should be taken into account. The goal is to gather the known facts about several major rifts (for example Parga, Devana and Hecate chasmata) as their approximate age, length and depth. We will vary these parameters as

well as the random trigger time of several major seismic dislocations on different locations. We will estimate the total surface displacement of the surface and assess its the potential past scenarios causing their formation by comparing our calculation with their present topography.

Bibliography

Basaltic volcanism on the terrestrial planets. Pergamon Press, 1981.

Aitta, A. The identity and quantity of the light matter on each side of the earth's inner core boundary. phys. earth planet. *Inter. 181, 132–140*, 2010a.

Aitta, A. Tricritical points and liquid-solid critical lines. in: Hobbs, c., paycha, s. (eds.). *European Women in Mathematics: Proceedings of the 13th General Meeting. World Scientific, 93–102*, 2010b.

Aitta, A. Venus' internal structure, temperature and core composition. *Icarus 218, 967-974, doi: 10.1016/j.icarus.2012.01.007*, 2012.

Alterman, Z., Jarosch, H., Pekeris, C. L., and Jeffreys, H. Oscillations of the earth. *Proceedings of the Royal Society of London. Series A. Mathematical and Physical Sciences*, 252(1268):80–95, 1959. doi: 10.1098/rspa.1959.0138. URL https://royalsocietypublishing.org/doi/abs/10.1098/rspa.1959.0138.

Alterman, Z., Eyal, Y., and Merzer, A. M. On free oscillations of the earth. *Geophysical surveys*, 1(1268):409–428, 1974. doi: 10.1007/BF01452247. URL https://doi.org/10.1007/BF01452247.

Andrade, E. N. D. C. On the viscous flow in metals, and allied phenomena. *B. Se., Physics Research Scholar, University College, London*, 1911.

Armann, M. and Tackley, P. J. Simulating the thermochemical magmatic and tectonic evolution of venus's mantle and lithosphere: Two-dimensional models. *J. Geophys. Res., 117, E12003*, 2012. doi: 10.1029/2012JE004231.

Basilevsky, A. Geologic map of the beta regio quadrangle (v-17), venus. 2008.

Bercovici, D. and Ricard, Y. Plate tectonics, damage and inheritance. *Nature*, 508(7497):513–516, 2014. doi: 10.1038/nature13072. URL https://doi.org/10.1038/nature13072.

Bercovici, H. L., Elkins-Tanton, L. T., O'Rourke, J. G., and Schaefer, L. The effects of bulk composition on planetesimal core sulfur content and size. *Icarus*, 380:114976, 2022. ISSN 0019-1035. doi: https://doi.org/10.1016/j.icarus.2022.114976. URL https://www.sciencedirect.com/science/article/pii/S0019103522000938.

Briaud, A., Fienga, A., Melini, D., Rambaux, N., Mémin, A., Spada, G., Saliby, C., Hussmann, H., and Stark, A. Constraints on the moon's deep interior from tidal deformation. 2022.

Bullen, K. E. The Variation of Density and the Ellipticities of Strata of Equal Density Within the Earth. *Geophysical Supplements to the Monthly Notices of the Royal Astronomical Society*, 3(9):395–401, 04 1936. ISSN 2051-1965. doi: 10.1111/j.1365-246X.1936.tb01747.x. URL https://doi.org/10.1111/j.1365-246X.1936.tb01747.x.

Bullen, K. E. The problem of the earth's density variation*. *Bulletin of the Seismological Society of America*, 30(3):235–250, 07 1940. ISSN 0037-1106. doi: 10.1785/BSSA0300030235. URL https://doi.org/10.1785/BSSA0300030235.

Bullen, K. E. The density variation of the earth's central core*. *Bulletin of the Seismological Society of America*, 32(1):19–29, 01 1942. ISSN 0037-1106. doi: 10.1785/BSSA0320010019. URL https://doi.org/10.1785/BSSA0320010019.

Cascioli, G., Hensley, S., DE MARCHI, F., Breuer, D., Durante, D., Racioppa, P., Iess, L., Mazarico, E., and Smrekar, S. E. The determination of the rotational state and interior structure of venus with veritas. *Earth and Space Science Open Archive*, page 15, 2021. doi: 10.1002/essoar.10506298.1. URL https://doi.org/10.1002/essoar.10506298.1.

Castillo-Rogez, J. C., Efroimsky, M., and Lainey, V. The tidal history of iapetus: Spin dynamics in the light of a refined dissipation model. *Journal of Geophysical Research: Planets*, 116(E9), 2011. doi: 10.1029/2010JE003664. URL https://agupubs.onlinelibrary.wiley.com/doi/abs/10.1029/2010JE003664.

Correia, A. C., Laskar, J., and de Surgy, O. N. Long-term evolution of the spin of venus: I. theory. *Icarus*, 163(1):1–23, 2003. ISSN 0019-1035. doi: https://doi.org/10.1016/S0019-1035(03)00042-3. URL https://www.sciencedirect.com/science/article/pii/S0019103503000423.

Cottereau, L., Rambaux, N., Lebonnois, S., and Souchay, J. The various contributions in venus rotation rate and lod. *A&A*, 531:A45, 2011. doi: 10.1051/0004-6361/201116606. URL https://doi.org/10.1051/0004-6361/201116606.

Crameri, F. and Kaus, B. Parameters that control lithospheric-scale thermal localization on terrestrial planets. *Geophysical Research Letters - GEOPHYS RES LETT*, 37, 05 2010. doi: 10.1029/2010GL042921.

Crumpler, L. and Aubele, J. Volcanism on venus. *Encyclopedia of volcanoes*, pages 727–770, 2000.

Davaille, A., Smrekar, S. E., and Tomlinson, S. Experimental and observational evidence for plume-induced subduction on venus. *Nature Geoscience*, 10:349–355, 2017. doi: 10.1051/0004-6361/201116606. URL https://doi.org/10.1038/ngeo2928.

Dumoulin, C., Tobie, G., Verhoeven, O., Rosenblatt, P., and Rambaux, N. Tidal constraints on the interior of venus: Tidal constraints on venus' interior. *J. Geophys. Res. Planets, 122, 1338-1352, doi: 10.1002/2016JE005249*, 2017.

Dziewonski, A. M. and Anderson, D. L. Preliminary reference earth model. *Phys. Earth Plan. Int. 25:297-356. doi: 10.17611/DP/9991844*, 1981.

Ebinger, C., Bechtel, T., Forsyth, D., and Bowin, C. Effective elastic plate thickness beneath the east african and afar plateaus and dynamic compensation of the uplifts. *Journal of Geophysical Research*, 94:2883–2901, 03 1989. doi: 10.1029/JB094iB03p02883.

Fegley, B. Venus. *In: Davis, A. M. (Ed.), Meteorites, Comets and Planets. Elsevier–Pergamon, pp. 487–507*, 2004.

Foster, A. and Nimmo, F. Comparisons between the rift systems of east africa, earth and beta regio, venus. *Earth and Planetary Science Letters*, 143(1):183–195, 1996. ISSN 0012-821X. doi: https://doi.org/10.1016/0012-821X(96)00146-X. URL https://www.sciencedirect.com/science/article/pii/0012821X9600146X.

Freeman, A. and Smrekar, S. Veritas – a discovery-class venus surface geology and geophysics mission. 06 2015.

Ghail, R., Wilson, C., Widemann, T., Bruzzone, L., Dumoulin, C., Helbert, J., Herrick, R., Marcq, E., Mason, P., Rosenblatt, P., Vandaele, A. C., and Burtz, L. J. Envision: understanding why our most earth-like neighbour is so different. *arXiv:1703.09010v1 [astro-ph.EP]*, 2017.

Gillmann, C. and Tackley, P. Atmosphere/mantle coupling and feedbacks on venus. *Journal of Geophysical Research: Planets*, 119(6):1189–1217, 2014. doi: https://doi.org/10.1002/2013JE004505. URL https://agupubs.onlinelibrary.wiley.com/doi/abs/10.1002/2013JE004505.

Gleason, A. and Mao, W. Strength of iron at core pressures and evidence for a weak earth/'s inner core. *Nature Geoscience*, 6:571–574, 05 2013. doi: 10.1038/ngeo1808.

Goetze, C. and Brace, W. Laboratory observations of high-temperature rheology of rocks. *Tectonophysics, vol. 13, pp. 583–600.*, 1972.

Goldreich, P. and Soter, S. Q in the solar system. *Icarus*, 5(1):375–389, 1966. ISSN 0019-1035. doi: https://doi.org/10.1016/0019-1035(66)90051-0. URL https://www.sciencedirect.com/science/article/pii/0019103566900510.

Goossens, S., Renaud, J. P., Henning, W. G., Mazarico, E., Bertone, S., and Genova, A. Evaluation of Recent Measurements of Mercury's Moments of Inertia and Tides Using a Comprehensive Markov Chain Monte Carlo Method. *psj*, 3(2):37, feb 2022. doi: 10.3847/PSJ/ac4bb8.

Graff, J., Ernst, R., and Samson, C. Evidence for triple-junction rifting focussed on local magmatic centres along parga chasma, venus. *Icarus*, 306:122–138, 2018. ISSN 0019-1035. doi: https://doi.org/10.1016/j.icarus.2018.02.010. URL https://www.sciencedirect.com/science/article/pii/S001910351730355X.

Grandin, R., Socquet, A., Binet, R., Klinger, Y., Jacques, E., de Chabalier, J. B., King, G. C. P., Lasserre, C., Tait, S., Tapponnier, P. E., Delorme, A., and Pinzuti, P. September 2005 manda hararo-dabbahu rifting event, afar (ethiopia): Constraints provided by geodetic data. *Journal of Geophysical Research*, 114, 2009.

Greff-Lefftz, M. and Legros, H. Core rotational dynamics and geological events. *Science*, 286(5445):1707–1709, 1999. ISSN 00368075, 10959203. URL http://www.jstor.org/stable/2900091.

Gülcher, A. J. P., Gerya, T. V., Montési, L. G. J., and Munch, J. Corona structures driven by plume-lithosphere interactions and evidence for ongoing plume activity on venus. *Nature Geoscience*, 13:547–554, 2020. URL https://doi.org/10.1038/s41561-020-0606-1.

Head, J. W., Crumpler, L. S., Aubele, J., Guest, J. E., and Saunders, R. S. Venus volcanism: Classification of volcanic features and structures, associations, and global distribution from magellan data. *Journal of Geophysical Research*, 97: 13153–13197, 1992.

Jackson, I., Fitz Gerald, J. D., Faul, U. H., and Tan, B. H. Grain-size-sensitive seismic wave attenuation in polycrystalline olivine. *Journal of Geophysical Research: Solid Earth*, 107(B12):ECV 5–1–ECV 5–16, 2002. doi: 10.1029/2001JB001225. URL https://agupubs.onlinelibrary.wiley.com/doi/abs/10.1029/2001JB001225.

James, P. B., Zuber, M. T., and Phillips, R. J. High temperature rheology of westerly granite. *J. Geophys. Res, vol. 76, pp. 1223–1230.*, 1971.

James, P. B., Zuber, M. T., and Phillips, R. J. Geoid to topography ratios on venus and implications for crustal thickness. *Lunar Planet. Sci. 41. Abstracts 2663. doi:10.17611/DP/9991844*, 2010.

Karner, G. D., Steckler, M. S., and Thorne, J. A. Long-term thermo-mechanical properties of the continental lithosphere. *Nature*, 304(5923):250–253, 1983. doi: 10.1038/304250a0. URL https://doi.org/10.1038/304250a0.

Kilburn, M. and Wood, B. Metal–silicate partitioning and the incompatibility of s and si during core formation. *Earth and Planetary Science Letters*, 152(1):139–148, 1997. ISSN 0012-821X. doi: https://doi.org/10.1016/S0012-821X(97)00125-8. URL https://www.sciencedirect.com/science/article/pii/S0012821X97001258.

Konopliv, A. S. and Yoder, C. F. Venusian k2 tidal love number from magellan and pvo tracking data. *Geophys. Res. Lett. 23, 1857–1860*, 1996.

Konopliv, A. S., Bnerdt, W. B., and Sjogren, W. L. Venus gravity: 180th degree and order model. *Icarus 138: 3-18, doi: 10.1006/icar.1999.60860*, 1999.

Krassilnikov, A. S. Tectonic structure, classification, and evolution of arachnoids on venus: Preliminary results. *Solar System Research*, 36:374–402, 2002a. URL https://doi.org/10.1023/A:1020411404593.

Krassilnikov, A. S. Tectonics and evolution of novae and coronae on venus: Tectonophysical modeling based on gravitational models. *Solar System Research*, 36:293–321, 2002b. URL https://doi.org/10.1023/A:1019524405537.

Lambeck, K. *The Earth's variable rotation: Geophysical causes and consequences*. Cambridge University Press, 1980. ISBN 9780511569579, doi: 10.1017/CBO9780511569579.

Lewis, J. S. Metal/silicate fractionation in the solar system. *Earth and Planetary Science Letters*, 15:286–290, 1972.

Louchet, F. and Duval, P. Andrade creep revisited. *International Journal of Materials Research - INT J MATER RES*, 100:1433–1439, 10 2009. doi: 10.3139/146.110189.

Love, A. E. H. The yielding of the earth to disturbing forces. *Proceedings of the Royal Society of London. Series A, Containing Papers of a Mathematical and Physical Character*, 82(551):73–88, 1909.

Malin, M. C. and Saunders, R. S. Surface of venus: Evidence of diverse landforms from radar observations. *Science*, 196(4293):987–990, 1977. doi: 10.1126/science.196.4293.987. URL https://www.science.org/doi/abs/10.1126/science.196.4293.987.

Margot, J.-L., Campbell, D. B., Giorgini, J. D., Jao, J. S., Snedeker, L. G., Ghigo, F. D., and Bonsall, A. Spin state and moment of inertia of venus. *Nature Astronomy*, 5:676–683, 2021. doi: 10.1038/s41550-021-01339-7.

Martinec, Z. Spectral–finite element approach to three-dimensional viscoelastic relaxation in a spherical earth. *Geophysical Journal International*, 142(1):117–141, 07 2000. ISSN 0956-540X. doi: 10.1046/j.1365-246x.2000.00138.x. URL https://doi.org/10.1046/j.1365-246x.2000.00138.x.

Mcgill, G. E., Steenstrup, S. J., Barton, C. A., and Ford, P. G. Continental rifting and the origin of beta regio, venus. *Geophysical Research Letters*, 8:737–740, 1981.

Melini, D., Cannelli, V., Piersanti, A., and Spada, G. Post-seismic rebound of a spherical Earth: new insights from the application of the Post-Widder inversion formula. *Geophysical Journal International*, 174(2):672–695, 08 2008. ISSN 0956-540X. doi: 10.1111/j.1365-246X.2008.03847.x. URL https://doi.org/10.1111/j.1365-246X.2008.03847.x.

Melini, D., Saliby, C., and Spada, G. On computing viscoelastic Love numbers for general planetary models: the ALMA3 code. *Geophysical Journal International*, 07 2022. ISSN 0956-540X. doi: 10.1093/gji/ggac263. URL https://doi.org/10.1093/gji/ggac263.

Mocquet, A., Rosenblatt, P., Dehant, V., and Verhoeven, O. The deep interior of venus, mars, and the earth: A brief review and the need for planetary surface-based measurements. *Planetary and Space Science*, 59(10):1048–1061, 2011. ISSN 0032-0633. doi: https://doi.org/10.1016/j.pss.2010.02.002. URL https://www.sciencedirect.com/science/article/pii/S0032063310000437. Comparative Planetology: Venus-Earth-Mars.

Molodensky, S. On the relation between the love numbers and the load coefficients. *Fizika Zemli*, 3:3–7, 1977.

Montesi, L. Morphology of bottom-driven rifts: Implications for venusian tectonics. pages 2861–, 03 2013.

Moores, E. M., Yıkılmaz, M. B., and Kellogg, L. H. Tectonics: 50 years after the Revolution. In *The Web of Geological Sciences: Advances, Impacts, and Interactions*. Geological Society of America, 09 2013. ISBN 9780813725000. doi: 10.1130/2013.2500(10). URL https://doi.org/10.1130/2013.2500(10).

Moresi, L. and Solomatov, V. Mantle convection with a brittle lithosphere: thoughts on the global tectonic styles of the earth and venus. *Geophysical Journal International*, 133(3):669–682, 06 1998. ISSN 0956-540X. doi: 10.1046/j.1365-246X.1998.00521.x. URL https://doi.org/10.1046/j.1365-246X.1998.00521.x.

Morgan, J. W. and Anders, E. Chemical composition of earth, venus, and mercury. *Proceedings of the National Academy of Sciences of the United States of America*, 77(12):6973–6977, 1980. doi: 10.1073/pnas.77.12.6973.

Murray, C. D. and Dermott, S. F. *Solar System Dynamics*. Cambridge University Press, 2000. doi: 10.1017/CBO9781139174817.

Nimmo, F. and McKenzie, D. Volcanism and tectonics on venus. *Annual Review of Earth and Planetary Sciences*, 26(1):23–51, 1998. doi: 10.1146/annurev.earth.26.1.23.

Noack, L., Breuer, D., and Spohn, T. Coupling the atmosphere with interior dynamics: Implications for the resurfacing of venus. *Icarus*, 217(2):484–498, 2012. ISSN 0019-1035. doi: https://doi.org/10.1016/j.icarus.2011.08.026. URL https://www.sciencedirect.com/science/article/pii/S0019103511003435. Advances in Venus Science.

Okada, Y. Surface deformation to shear and tensile faults in a half space. *Bull. Seismol. Soc. Am.*, 75:1135–1154, 1985.

Patrick Wu, W. R. P. Viscous gravitational relaxation. *Geophysical Journal International*, 70:435–485, 1982. URL https://doi.org/10.1111/j.1365-246X.1982.tb04976.x.

Peltier, W. R. The impulse response of a maxwell earth. *Reviews of Geophysics*, 12(4):649–669, 1974. doi: https://doi.org/10.1029/RG012i004p00649. URL https://agupubs.onlinelibrary.wiley.com/doi/abs/10.1029/RG012i004p00649.

Phillips, R. J. and Malin, M. C. Tectonics of venus. *Annual Review of Earth and Planetary Sciences*, 12(1):411–443, 1984. doi: 10.1146/annurev.ea.12.050184.002211. URL https://doi.org/10.1146/annurev.ea.12.050184.002211.

Phillips, R. J., Kaula, W. M., McGill, G. E., and Malin, M. C. Tectonics and evolution of venus. *Science*, 212(4497):879–887, 1981. doi: 10.1126/science.212.4497.879. URL https://www.science.org/doi/abs/10.1126/science.212.4497.879.

Phillips, R. J., Bullock, M. A., and Hauck II, S. A. Climate and interior coupled evolution on venus. *Geophysical Research Letters*, 28(9):1779–1782, 2001. doi: https://doi.org/10.1029/2000GL011821. URL https://agupubs.onlinelibrary.wiley.com/doi/abs/10.1029/2000GL011821.

Piersanti, A., Spada, G., Sabadini, R., and Bonafede, M. Global post-seismic deformation. *Geophysical Journal International*, 120(3):544–566,

1995. doi: https://doi.org/10.1111/j.1365-246X.1995.tb01838.x. URL https://onlinelibrary.wiley.com/doi/abs/10.1111/j.1365-246X.1995.tb01838.x.

Post, E. L. Generalized differentiation. *Transactions of the American Mathematical Society*, 32(4):723–781, 1930.

Ranalli, G. *Rheology of the Earth*. Springer Netrlands, 1995.

Renaud, J. P. and Henning, W. G. Increased tidal dissipation using advanced rheological models: Implications for io and tidally active exoplanets. *apj*, 857 (2):98, Apr. 2018. doi: 10.3847/1538-4357/aab784.

Ringwood, A. and Anderson, D. L. Earth and venus: A comparative study. *Icarus*, 30(2):243–253, 1977. ISSN 0019-1035. doi: https://doi.org/10.1016/0019-1035(77)90156-7. URL https://www.sciencedirect.com/science/article/pii/0019103577901567.

Romeo, I. and Turcotte, D. Resurfacing on venus. *Planetary and Space Science*, 58:1374–1380, 08 2010. doi: 10.1016/j.pss.2010.05.022.

Rosenblatt, Pinet, and Thouvenot. Comparative hypsometric analysis of earth and venus. *Geophys.Res.Lett.21,465–468.*, 1994.

Rosenblatt, P., Bruinsma, S., Müller-Wodarg, I., Häusler, B., Svedhem, H., and Marty, J. First ever in situ observations of venus' polar upper atmosphere density using the tracking data of the venus express atmospheric drag experiment (vexade). *Icarus*, 217(2):831–838, 2012. ISSN 0019-1035. doi: https://doi.org/10.1016/j.icarus.2011.06.019. URL https://www.sciencedirect.com/science/article/pii/S0019103511002363. Advances in Venus Science.

Rosenblatt, P., Dumoulin, C., Marty, J.-C., and Genova, A. Determination of venus' interior structure with envision. *Remote Sensing*, 13(9), 2021. ISSN 2072-4292. doi: 10.3390/rs13091624. URL https://www.mdpi.com/2072-4292/13/9/1624.

Sabadini, R., Yuen, D. A., and Boschi, E. Polar wandering and the forced responses of a rotating, multilayered, viscoelastic planet. *Journal of Geophysical Research: Solid Earth*, 87(B4):2885–2903, 1982.

Sabadini, R., Yuen, D. A., and Boschi, E. The effects of post-seismic motions on the moment of inertia of a stratified viscoelastic earth with an asthenosphere. *Geophysical Journal International*, 79(3):727–745, 12 1984. ISSN 0956-540X. doi: 10.1111/j.1365-246X.1984.tb02865.x. URL https://doi.org/10.1111/j.1365-246X.1984.tb02865.x.

Saito, M. Some problems of static deformation of the earth. *Journal of Physics of the Earth*, 22(1):123–140, 1974. doi: 10.4294/jpe1952.22.123.

Saito, M. Relationship between tidal and load love numbers. *Journal of Physics of the Earth*, 26(1):13–16, 1978. doi: 10.4294/jpe1952.26.13.

Saunders, R. S. and Malin, M. C. Geologic interpretation of new observations of the surface of venus. *Geophysical Research Letters*, 4(11):547–550, 1977. doi: https://doi.org/10.1029/GL004i011p00547. URL https://agupubs.onlinelibrary.wiley.com/doi/abs/10.1029/GL004i011p00547.

Schiffer, R., Beck, A., Aeronautics, U. S. N., and Administration, S. *Models of Venus Atmosphere (1968)*. NASA SP. National Aeronautics and Space Administration, 1968. URL https://books.google.fr/books?id=V8xAAQAAMAAJ.

Schubert, G., Turcotte, D. L., and Olson, P. *Mantle Temperatures and Thermodynamic Properties*. Cambridge University Press, 2001. doi: 10.1017/CBO9780511612879.005.

Seiff, A., Schofield, J. T., Kliore, A. J., Taylor, F. W., Limaye, S. S., Revercomb, H. E., Sromovsky, L. A., Kerzhanovich, V. V., Moroz, V. I., and Marov, M. Y. Models of the structure of the atmosphere of Venus from the surface to 100 kilometers altitude. *Advances in Space Research*, 5(11):3–58, Jan. 1985. doi: 10.1016/0273-1177(85)90197-8.

Shah, O., Helled, R., Alibert, Y., and Mezger, K. Interior structure models of venus. 2021.

Shalygin, E. V., Markiewicz, W. J., Basilevsky, A. T., Titov, D. V., Ignatiev, N. I., and Head, J. W. Active volcanism on venus in the ganiki chasma rift zone. *Geophysical Research Letters*, 42(12):4762–4769, 2015. doi: https://doi.org/10.1002/2015GL064088. URL https://agupubs.onlinelibrary.wiley.com/doi/abs/10.1002/2015GL064088.

Shida, T. On the elasticity of the earth and the earth's crust. *Kyoto Imperial University*, 1912.

Smrekar, S., Dyar, M., Helbert, J., Nunes, D., and Whitten, J. Veritas (venus emissivity, radio science, insar, topography and spectroscopy): A proposed discovery mission. 01 2020.

Smrekar, S. E. Evidence for active hotspots on venus from analysis of magellan gravity data. *Icarus*, 112:2–26, 1994.

Smrekar, S. E. and Sotin, C. Constraints on mantle plumes on venus: Implications for volatile history. *Icarus*, 217(2):510–523, 2012. ISSN 0019-1035. doi: https://doi.org/10.1016/j.icarus.2011.09.011. URL https://www.sciencedirect.com/science/article/pii/S0019103511003563. Advances in Venus Science.

Smrekar, S. E., Stofan, E. R., Mueller, N., Treiman, A., Elkins-Tanton, L., Helbert, J., Piccioni, G., and Drossart, P. Recent hotspot volcanism on venus from virtis emissivity data. *Science*, 328(5978):605–608, 2010. doi: 10.1126/science.1186785. URL https://www.science.org/doi/abs/10.1126/science.1186785.

Soldati, G., Piersanti, A., and Boschi, E. Global postseismic gravity changes of a viscoelastic earth. *Journal of Geophysical Research: Solid Earth*, 103(B12):29867–29885, 1998. doi: https://doi.org/10.1029/98JB02793. URL https://agupubs.onlinelibrary.wiley.com/doi/abs/10.1029/98JB02793.

Spada, G. Alma, a fortran program for computing the viscoelastic love numbers of a spherically symmetric planet. *Comput. Geosci.*, 34:667–687, 2008.

Spada, G. and Boschi, L. Using the Post—Widder formula to compute the Earth's viscoelastic Love numbers. *Geophysical Journal International*, 166(1):309–321, 07 2006. ISSN 0956-540X. doi: 10.1111/j.1365-246X.2006.02995.x. URL https://doi.org/10.1111/j.1365-246X.2006.02995.x.

Spada, G., Sabadini, R., Yuen, D. A., and Ricard, Y. Effects on post-glacial rebound from the hard rheology in the transition zone. *Geophysical Journal International*, 109(3):683–700, 06 1992. ISSN 0956-540X. doi: 10.1111/j.1365-246X.1992.tb00125.x. URL https://doi.org/10.1111/j.1365-246X.1992.tb00125.x.

Spada, G., Antonioli, A., Boschi, L., Boschi, L., Brandi, V., Cianetti, S., Galvani, G., Giunchi, C., Perniola, B., Agostinetti, N. P., Piersanti, A., and Stocchi, P. Modeling earth's post-glacial rebound. *Eos, Transactions American Geophysical Union*, 85(6):62–64, 2004. doi: https://doi.org/10.1029/2004EO060007. URL https://agupubs.onlinelibrary.wiley.com/doi/abs/10.1029/2004EO060007.

Spada, G., Barletta, V. R., Klemann, V., Riva, R. E. M., Martinec, Z., Gasperini, P., Lund, B., Wolf, D., Vermeersen, L. L. A., and King, M. A. A benchmark study for glacial isostatic adjustment codes. *Geophysical Journal International*, 185(1):106–132, 04 2011. ISSN 0956-540X. doi: 10.1111/j.1365-246X.2011.04952.x. URL https://doi.org/10.1111/j.1365-246X.2011.04952.x.

Steinberger, B. and Werner, S. Deep versus shallow origin of gravity anomalies, topography and volcanism on earth, venus and mars. *Icarus*, 207:564–577, 06 2010. doi: 10.1016/j.icarus.2009.12.025.

Stevenson, D. J. Planetary magnetic fields. *Earth and Planetary Science Letters*, 208(1):1–11, 2003. ISSN 0012-821X. doi: https://doi.org/10.1016/S0012-821X(02)01126-3. URL https://www.sciencedirect.com/science/article/pii/S0012821X02011263.

Stofan, E. R., Smrekar, S. E., Mueller, N., and Helbert, J. Themis regio, venus: Evidence for recent (?) volcanism from virtis data. *Icarus*, 271:375–386, 2016. ISSN 0019-1035. doi: https://doi.org/10.1016/j.icarus.2016.01.034. URL https://www.sciencedirect.com/science/article/pii/S0019103516000567.

Strom, R. G., Schaber, G. G., and Dawson, D. D. The global resurfacing of venus. *Journal of Geophysical Research: Planets*, 99(E5):10899–10926, 1994. doi: https://doi.org/10.1029/94JE00388. URL https://agupubs.onlinelibrary.wiley.com/doi/abs/10.1029/94JE00388.

Suer, T.-A., Siebert, J., Remusat, L., Menguy, N., and Fiquet, G. A sulfur-poor terrestrial core inferred from metal–silicate partitioning experiments. *Earth and Planetary Science Letters*, 469:84–97, 2017. ISSN 0012-821X. doi: https://doi.org/10.1016/j.epsl.2017.04.016. URL https://www.sciencedirect.com/science/article/pii/S0012821X17301954.

Sundberg, M. and Cooper, R. F. A composite viscoelastic model for incorporating grain boundary sliding and transient diffusion creep; correlating creep and attenuation responses for materials with a fine grain size. *Philosophical Magazine*, 90(20):2817–2840, 2010. doi: 10.1080/14786431003746656. URL https://doi.org/10.1080/14786431003746656.

Surkov, Y. A., Kirnozov, F. F., Glazov, V. N., Dunchenko, A. G., and Tatsij, L. P. *Content of natural radioactive elements into the Venus rocks by data the Venera 9 and Venera 10 automatic interplanetary stations*, volume 14 (5), 704-709. 1976. URL http://inis.iaea.org/search/search.aspx?orig_q=RN:09409863.

Takeuchi, H. On the earth tide of the compressible earth of variable density and elasticity. *American Geophysical Union Transactions 31, 651-689*, 1950.

Takeuchi, H. and Saito, M. Seismic surfaces waves. *In: Bolt, B.A. (Ed.), Methods in Computational Physics, vol. 1. Academic Press, New York, pp. 217–295.*, 1950.

Taylor, F. W. The atmospheres of terrestrial planets. *Geophys. Surv. 7, 385–408.*, 1985.

Thomson, W. Dynamical problems regarding elastic spheroidal shells. *Phil. Trans. R. Soc., London, vol 153*, 1863.

Tiesinga, E., Mohr, P. J., Newell, D. B., and Taylor, B. N. Codata recommended values of the fundamental physical constants: 2018. *Rev. Mod. Phys.*, 93: 025010, Jun 2021. doi: 10.1103/RevModPhys.93.025010. URL https://link.aps.org/doi/10.1103/RevModPhys.93.025010.

Touma, J. and Wisdom, J. Resonances in the early evolution of the earth-moon system. *The Astronomical Journal*, 115(4):1653, apr 1998. doi: 10.1086/300312. URL https://dx.doi.org/10.1086/300312.

Trønnes, R., Baron, M., Eigenmann, K., Guren, M., Heyn, B., Løken, A., and Mohn, C. Core formation, mantle differentiation and core-mantle interaction within earth and the terrestrial planets. *Tectonophysics*, 760:165–198, 2019. ISSN 0040-1951. doi: https://doi.org/10.1016/j.tecto.2018.10.021. URL https://www.sciencedirect.com/science/article/pii/S0040195118303494. Linking Plate Tectonics and Volcanism to Deep Earth Dynamics – a tribute to Trond H. Torsvik.

Turcotte, D., Morein, G., Roberts, D., and Malamud, B. Catastrophic resurfacing and episodic subduction on venus. *Icarus*, 139(1):49–54, 1999. ISSN 0019-1035. doi: https://doi.org/10.1006/icar.1999.6084. URL https://www.sciencedirect.com/science/article/pii/S0019103599960840.

Upcott, N. M., Mukasa, R. K., Ebinger, C. J., and Karner, G. D. Along-axis segmentation and isostasy in the western rift, east africa. *jgr*, 101(B2):3247–3268, feb 1996. doi: 10.1029/95JB01480.

Vermeersen, L. A., Sabadini, R., and Spada, G. Analytical visco-elastic relaxation models. *Geophysical research letters*, 23(7):697–700, 1996.

Weertman, J., White, S., and Cook, A. H. Creep laws for the mantle of the earth [and discussion]. *Philosophical Transactions of the Royal Society of London. Series A, Mathematical and Physical Sciences*, 288(1350):9–26, 1978. ISSN 00804614. URL http://www.jstor.org/stable/74973.

Widder, D. V. The inversion of the laplace integral and the related moment problem. *Transactions of the American Mathematical Society*, 36(1):107–200, 1934.

Yoder, C. F. Venus' free obliquity. *Icarus, Volume 117, Issue 2, p. 250-286, doi: 10.1006/icar.1995.1156*, 1995.

Zharkov, V. N. Models of the internal structure of venus. *The moon and the planets*, 29(2):139–175, 1983. doi: 10.1007/BF00928322.

Appendices

Appendix A: Scientific Communications

You will find a comprehensive list of the scientific communications done with my supervisor.

Peer-reviewed journal articles

- Daniele Melini, Christelle Saliby, Giorgio Spada. On computing viscoelastic Love numbers for general planetary models: the ALMA3 code. Geophysical Journal International, 2022.

- **Submitted:** Arthur Briaud, Agnès Fienga, Daniele Melini, Nicolas Rambaux, Anthony Mémin, Giorgio Spada, Christelle Saliby, Hauke Hussmann, Alexander Stark, and Vishnu Viswanathan. Icarus, 2022.

- **Submitted:** Christelle Saliby, Agnès Fienga, Arthur Briaud, Anthony Mémin, Carianna. Viscosity contrasts in the Venus mantle from tidal deformations Herrera. Planetary and Space Science, 2022.

Geophysical Journal International

Geophys. J. Int. (2022) **231,** 1502–1517
Advance Access publication 2022 July 7
GJI Gravity, Geodesy and Tides

https://doi.org/10.1093/gji/ggac263

On computing viscoelastic Love numbers for general planetary models: the ALMA^3 code

D. Melini [1], C. Saliby[2] and G. Spada [3]

[1] *Istituto Nazionale di Geofisica e Vulcanologia,* 00143 *Roma RM, Italy. E-mail: daniele.melini@ingv.it*
[2] *Géoazur, CNRS, Observatoire de la Côte d'Azur, Université Côte d'Azur,* 06560 *Valbonne, France*
[3] *Dipartimento di Fisica e Astronomia Augusto Righi (DIFA), Alma Mater Studiorum Università di Bologna,* 40127 *Bologna BO, Italy*

Accepted 2022 July 5. Received 2022 June 30; in original form 2021 November 2

SUMMARY

The computation of the Love numbers (LNs) for a spherically symmetric self-gravitating viscoelastic Earth is a classical problem in global geodynamics. Here we revisit the problem of the numerical evaluation of loading and tidal LNs in the static limit for an incompressible planetary body, adopting a Laplace inversion scheme based upon the Post-Widder formula as an alternative to the traditional viscoelastic normal modes method. We also consider, within the same framework, complex-valued, frequency-dependent LNs that describe the response to a periodic forcing, which are paramount in the study of the tidal deformation of planets. Furthermore, we numerically obtain the time-derivatives of LNs, suitable for modelling geodetic signals in response to surface loads variations. A number of examples are shown, in which time and frequency-dependent LNs are evaluated for the Earth and planets adopting realistic rheological profiles. The numerical solution scheme is implemented in ALMA^3 (the plAnetary Love nuMbers cAlculator, version 3), an upgraded open-source Fortran 90 program that computes the LNs for radially layered planetary bodies with a wide range of rheologies, including transient laws like Andrade or Burgers.

Key words: Loading of the Earth; Tides and planetary waves; Transient deformation; Planetary interiors.

1 INTRODUCTION

Love numbers (LNs), first introduced by A.E.H. Love in 1911, provide a complete description of the response of a planetary body to external, surface or internal perturbations. In his seminal work, Love (1911) defined the LNs in the context of computing the radial deformation and the perturbation of gravity potential for an elastic, self-gravitating, homogeneous sphere that is subject to the gravitational pull of a tide-raising body. This definition has been subsequently extended by Shida (1912) to include also horizontal displacements. In order to describe the response to surface loads, an additional set of LNs, dubbed *loading Love numbers*, has been introduced in order to describe the Earth's response to surface loads (see e.g. Munk & MacDonald 1960; Farrell 1972) and today they are routinely used in the context of the Post Glacial Rebound problem (Spada *et al.* 2011). In a similar way, *shear Love numbers* represent the response to a shear stress acting on the surface (Saito 1978) while *dislocation Love numbers* describe deformations induced by internal point dislocations (see e.g. Sun & Okubo 1993).

The LN formalism has been originally defined in the realm of purely elastic deformations, for spherically symmetric Earth models consistent with global seismological observations. However, invoking the Correspondence Principle in linear viscoelasticity (see e.g. Christensen 1982), the LNs can be generalized to anelastic models in a straightforward way. Currently, viscoelastic LNs are a key ingredient of several geophysical applications involving the time-dependent response of a spherically symmetric Earth model to surface loads or endogenous perturbations. For example, they are essential to the solution of the sea level equation (Farrell & Clark 1976) and are exploited in current numerical implementations of the Glacial Isostatic Adjustment (GIA) problem, either on millennial (see e.g. Spada & Melini 2019) or on decadal time scale (see e.g. Melini *et al.* 2015).

Since LNs depend on the internal structure of a planet and on its constitution, they can provide a means of establishing constraints on some physical parameters of the planet interior on the basis of geodetic measurements or astronomic observations (see e.g. Zhang 1992; Kellermann *et al.* 2018). For tidal periodic perturbations, complex LNs can be defined in the frequency domain, accounting for both the amplitude and phase lag of the response to a given tidal frequency (Williams & Boggs 2015). Frequency-domain LNs are widely used to constrain the interior structure of planetary bodies on the basis of observations of tidal amplitude and phase lag (see e.g. Sohl *et al.* 2003; Dumoulin *et al.* 2017; Tobie *et al.* 2019), to study the state of stress of satellites induced by tidal forcings (see

e.g. Wahr *et al.* 2009) or to investigate the tidal response of the giant planets (see e.g. Gavrilov & Zharkov 1977).

Viscoelastic LNs for a spherically symmetric, radially layered, self-gravitating planet are traditionally computed within the framework of the 'viscoelastic normal modes' method introduced by Peltier (1974), which relies upon the solution of Laplace-transformed equilibrium equations using the formalism of elastic propagators. As discussed for example by Spada & Boschi (2006) and Melini *et al.* (2008), this approach becomes progressively less feasible as the detail of the rheological model is increased or if complex constitutive laws are considered. Several workarounds have been proposed in the literature to avoid these shortcomings (see, e.g. Rundle 1982; Friederich & Dalkolmo 1995; Riva & Vermeersen 2002; Tanaka *et al.* 2006). Among these, the Post-Widder Laplace inversion formula (Post 1930; Widder 1934), first applied by Spada & Boschi (2006) to the evaluation of viscoelastic LNs for the Earth, has the advantage of maintaining unaltered the formal structure of the viscoelastic normal modes and of allowing for a straightforward implementation of complex rheological laws. For periodic loads, alternative numerical integration schemes similar to those developed by Takeuchi & Saito (1972) for the elastic problem (Na & Baek 2011; Wang *et al.* 2012) have been applied to the viscoelastic case by integrating Fourier-transformed solutions (Tobie *et al.* 2005, 2019).

In this work, we revisit the Post-Widder approach to the evaluation of LNs with the aim of extending it to more general planetary models, relaxing some of the assumptions originally made by Spada & Boschi (2006). In particular, we introduce a layered core in the Post-Widder formalism and obtain analytical expressions for the time derivatives of LNs, needed to model geodetic velocities in response to the variation of surface loads. In this respect, our approach is complementary to that of Padovan *et al.* (2018), who derived a semi-analytical solution for the fluid LNs using the propagator formalism. We implement our results in `ALMA`^{3} (the plAnetary Love nuMbers cAlculator, version 3), an open-source code which extends and generalizes the program originally released by Spada (2008). `ALMA`^{3} introduces a range of new capabilities, including the evaluation of frequency-domain LNs describing the response to periodic forcings, suitable for studying tidal dissipation in the Earth and planets.

This paper is organized as follows. In Section 2, we give a brief outline of the theory underlying the computation of viscoelastic LNs and of the application of the Post-Widder Laplace inversion formula. In Section 3 we discuss some general aspects of `ALMA`^{3}, leaving the technical details to a User Manual. In Section 4, we validate `ALMA`^{3} through some benchmarks between our numerical results and available reference solutions In Section 5, we discuss some numerical examples before drawing our conclusions in Section 6.

2 MATHEMATICAL BACKGROUND

The details of the Post-Widder approach to numerical Laplace inversion have been extensively discussed in previous works (see Spada & Boschi 2006; Melini *et al.* 2008; Spada 2008). In what follows, we only give a brief account of the Post-Widder Laplace inversion method for the sake of illustrating how the new features of `ALMA`^{3} have been implemented within its context.

2.1 Viscoelastic normal modes

Closed-form analytical expressions for the LNs exist only for a few extremely simplified planetary models. The first is the homogeneous, self-gravitating sphere, often referred to as the 'Kelvin sphere' (Thomson 1863). The second is the two-layer, incompressible, non self-gravitating model that has been solved analytically by Wu & Ni (1996). For more complex models, LNs shall be computed either through fully numerical integration of the equilibrium equations, or by invoking semi-analytical schemes. Among the latter, the viscoelastic normal modes method, introduced by Peltier (1974), relies upon the solution of the equilibrium equations in the Laplace-transformed domain. Invoking the Correspondence Principle (e.g. Christensen 1982) the equilibrium equations can be cast in a formally elastic form by defining a complex rigidity $\mu(s)$ that depends on the rheology adopted and is a function of the Laplace variable s.

Following Spada & Boschi (2006), at a given harmonic degree n, the Laplace-transformed equations can be solved with standard propagator methods, and their solution at the planet surface ($r = a$) can be written in vector form as

$$\tilde{\mathbf{x}}(s) = \tilde{f}(s)\Big(P_1\Lambda(s)J\Big)\Big(P_2\Lambda(s)J\Big)^{-1}\mathbf{b}\,, \tag{1}$$

where the tilde denotes Laplace-transformed quantities, vector $\tilde{\mathbf{x}}(s) = (\tilde{u}, \tilde{v}, \tilde{\varphi})^T$ contains the nth degree harmonic coefficients of the vertical ($\tilde{u}$) and horizontal ($\tilde{v}$) components of the displacement field and the incremental potential ($\tilde{\varphi}$), $\tilde{f}(s)$ is the Laplace-transformed time-history of the forcing term, P_1 and P_2 are appropriate 3×6 projection operators, J is a 6×3 array that accounts for the boundary conditions at the core interface, and $\mathbf{b}$ is a three-component vector expressing the surface boundary conditions (either of loading or of tidal type). In eq. (1), $\Lambda(s)$ is a 6×6 array that propagates the solution from the core radius ($r = c$) to the planet surface ($r = a$), which has the form:

$$\Lambda(s) = \prod_{k=N}^{1} Y_k(r_{k+1}, s)Y_k^{-1}(r_k, s)\,, \tag{2}$$

where N is the number of homogeneous layers outside the planet core, r_k is the radius of the interface between the $(k-1)$th and kth layer, with $r_1 \leq ... \leq r_N$, $r_1 = c$ and $r_{N+1} = a$. In eq. (2), $Y_k(r, s)$ is the fundamental matrix that contains the six linearly independent solutions of the equilibrium equations valid in the kth layer, whose expressions are given analytically in Sabadini *et al.* (1982). When incompressibility is assumed, the matrix $Y_k(r, s)$ depends upon the rheological constitutive law through the functional form of the complex rigidity $\mu(s)$, which replaces the elastic rigidity μ of the elastic propagator (Wu & Peltier 1982). Table 1 lists expressions of $\mu(s)$ for some rheological laws. For a fluid inviscid (i.e. zero viscosity) core, the array J in eq. (1) is a 6×3 interface matrix whose components are explicitly given by Sabadini *et al.* (1982); conversely, for a solid core, J corresponds to the 6×3 portion of the fundamental matrix for the core $Y_c(c, s)$ that contains the three solutions behaving regularly for $r \mapsto 0$.

From the solution $\tilde{\mathbf{x}}(s)$ obtained in eq. (1), the Laplace-transformed LNs are defined as:

$$\tilde{h}_n(s) = \frac{m}{a}\tilde{u}_n(s) \tag{3}$$

$$\tilde{l}_n(s) = \frac{m}{a}\tilde{v}_n(s) \tag{4}$$

$$\tilde{k}_n(s) = -1 - \frac{m}{ag}\tilde{\varphi}_n(s)\,, \tag{5}$$

Table 1. Complex rigidities $\mu(s)$ for the linear viscoelastic rheologies implemented in ALMA[3]. Here, μ is the elastic rigidity, η is the Newtonian viscosity, μ_2 and η_2 are the rigidity and viscosity of the transient element in the bi-viscous Burgers rheology, respectively. In the Andrade rheological law, α is the creep parameter while $\Gamma(x)$ is the Gamma function.

Rheological law	Complex rigidity $\mu(s)$
Hooke	μ
Maxwell	$\dfrac{\mu s}{s+\mu/\eta}$
Newton	ηs
Kelvin	$\mu+\eta s$
Burgers	$\dfrac{\mu s\left(s+\dfrac{\mu_2}{\eta_2}\right)}{s^2+s\left(\dfrac{\mu}{\eta}+\dfrac{\mu+\mu_2}{\eta_2}\right)+\dfrac{\mu\,\mu_2}{\eta\,\eta_2}}$
Andrade	$\left[\dfrac{1}{\mu}+\dfrac{1}{\eta s}+\Gamma(\alpha+1)\dfrac{1}{\mu}\left(\dfrac{\eta s}{\mu}\right)^{-\alpha}\right]^{-1}$

where we have made the n-dependence explicit, m is the mass of the planet and g is the unperturbed surface gravitational acceleration (Farrell 1972; Wu & Peltier 1982). Using Cauchy's residue theorem, for Maxwell or generalized Maxwell rheologies eqs (3)–(5) can be cast in the standard normal modes form, which for an impulsive load ($\tilde{f}(s)=1$) reads

$$\tilde{L}_n(s) = L_n^e + \sum_{k=1}^{N_M} \frac{L_n^k}{s-s_n^k}\,, \tag{6}$$

where $\tilde{L}_n(s)$ denotes any of the three LNs, L_n^e is the elastic component of the LN (i.e. the limit for $s\mapsto\infty$), L_n^k are the viscoelastic components (residues), s_n^k are the (real and negative) roots of the secular equation $\mathrm{Det}(P_2\Lambda(s)J)=0$, and where N_M is the number of viscoelastic normal modes, each corresponding to one root of the secular equation (Spada & Boschi 2006). However, such standard form is not always available, since for some particular rheologies the complex rigidity $\mu(s)$ cannot be cast in the form of a rational fraction (this occurs, for example, for the Andrade's rheology, see Table 1). This is one of the motivations for adopting non-conventional Laplace inversion formulas like the one discussed in next section.

2.2 LNs in the time domain

To obtain the time-domain LNs $h_n(t)$, $l_n(t)$ and $k_n(t)$, it is necessary to perform the inverse Laplace transform of eqs (3)–(5). Within the viscoelastic normal-mode approach, this is usually accomplished through an integration over a (modified) Bromwich path in the complex plane, by invoking the residue theorem. In this case, the inversion of eq. (6) yields the time-domain LN in the form:

$$L_n(t) = L_n^e\delta(t) + H(t)\sum_{k=1}^{N_M} L_n^k \mathrm{e}^{s_n^k t}\,, \tag{7}$$

where $\delta(t)$ is the Dirac delta and $H(t)$ is the Heaviside step function defined by eq. (14) below, and an impulsive time history is assumed ($\tilde{f}(s)=1$). As discussed by Spada & Boschi (2006), the traditional scheme of the viscoelastic normal modes suffers from a few but significant shortcomings that, with models of increasing complexity, effectively hinders a reliable numerical inverse transformation. Indeed, the application of the residue theorem demands the identification of the poles of the Laplace-transformed solutions (see eqs 3–5), which are the roots of the secular polynomial equation whose algebraic degree increases with the number of rheologically distinct layers. In addition, its algebraic complexity may be unpractical to handle, particularly for constitutive laws characterized by many material parameters.

As shown by Spada & Boschi (2006) and Spada (2008), a possible way to circumvent these difficulties is to compute the inverse Laplace transform through the Post-Widder (PW) formula (Post 1930; Widder 1934). We note, however, that other viable possibilities exist, as the one recently discussed by Michel & Boy (2021), who have used Fourier techniques to avoid some of the problems inherent in the Laplace transform method. While Fourier techniques may be more appropriate to take complex rheologies into account, and are clearly more relevant to address LNs at tidal frequencies, the motivation of our approach is to address in a unified framework the computation of LNs describing both tidal and surface loads. If $\tilde{F}(s)=\mathcal{L}(F(t))$ is the Laplace transform of $F(t)$, the PW formula gives an asymptotic approximation of the inverse Laplace transform $\mathcal{L}^{-1}(\tilde{F}(s))$ as a function of the nth derivatives of $\tilde{F}(s)$ evaluated along the real positive axis:

$$F(t) = \lim_{n\to\infty} \frac{(-1)^n}{n!}\left(\frac{n}{t}\right)^{n+1}\left[\frac{d^n}{ds^n}\tilde{F}(s)\right]_{s=\frac{n}{t}}\,. \tag{8}$$

In general, an analytical expression for the nth derivative of $\tilde{F}(s)$ required in eq. (8) is not available. By using a recursive discrete approximation of the derivative and rearranging the corresponding terms, Gaver (1966) has shown that an equivalent expression is

$$F(t) = \lim_{n\to\infty} \frac{n\ln 2}{t}\binom{2n}{n}\sum_{j=0}^{n}(-1)^j\binom{n}{j}\tilde{F}\left(\frac{(n+j)\ln 2}{t}\right)\,, \tag{9}$$

where the inverse transform $F(t)$ is expressed in terms of samples of the Laplace transform $\tilde{F}(s)$ on the real positive axis of the complex plane. Since for a stably stratified incompressible planet all the singularities of $\tilde{\mathbf{x}}(s)$ (eq. 1) are expected to be located along the real negative axis that ensures the long-term gravitational stability (Vermeersen & Mitrovica 2000), eq. (9) provides a strategy for evaluating the time-dependent LNs without the numerical complexities associated with the traditional contour integration. However, as discussed by Valkó & Abate (2004), the numerical convergence of (9) is logarithmically slow, and the oscillating terms can lead to catastrophic loss of numerical precision. Stehfest (1970) has shown that, for practical applications, the convergence of eq. (9) can be accelerated by rewriting it in the form

$$F(t) = \lim_{M\to\infty} \frac{\ln 2}{t}\sum_{j=1}^{2M}\zeta_{j,M}\tilde{F}\left(\frac{j\ln 2}{t}\right)\,, \tag{10}$$

where M is the order of the Gaver sequence and where the ζ constants are

$$\zeta_{k,M} = (-1)^{M+k}\sum_{j=\mathrm{floor}\left(\frac{k+1}{2}\right)}^{\min(M,k)}\frac{j^{M+1}}{M!}\binom{M}{j}\binom{2j}{j}\binom{j}{k-j}\,, \tag{11}$$

with floor(x) being the greatest integer less or equal to x. Eq. (10) can be applied to (1) to obtain an Mth order approximation of the time-domain solution vector:

$$\mathbf{x}^{(M)}(t) = \frac{\ln 2}{t}\sum_{j=1}^{2M}\zeta_{j,M}\,\tilde{\mathbf{x}}\left(\frac{j\ln 2}{t}\right)\,, \tag{12}$$

from which the time-domain LNs can be readily obtained according to eqs (3)–(5).

Recalling that the Laplace transform of $F(t)$ and that of its time derivative $\dot{F}(t)$ are related by $\mathcal{L}(\dot{F}(t)) = s\mathcal{L}(F(t)) - F(0^-)$ and being $\mathbf{x}(t) = 0$ for $t < 0$, it is also possible to write an asymptotic approximation for the time derivative of the solution:

$$\dot{\mathbf{x}}^{(M)}(t) = \left(\frac{\ln 2}{t}\right)^2 \sum_{j=1}^{2M} j\, \zeta_{j,M}\, \tilde{\mathbf{x}}\left(\frac{j \ln 2}{t}\right), \tag{13}$$

from which the time derivative of the LNs $\dot{h}_n(t)$, $\dot{l}_n(t)$ and $\dot{k}_n(t)$ can be obtained according to eqs (3)–(5). The numerical computation of the time-derivatives of the LNs according to eq. (13) is one of the new features introduced in ALMA^3.

The time dependence of the solution vector obtained through eqs (12)–(13) is also determined by the time history of the forcing term (either of loading or tidal type), whose Laplace transform $\tilde{f}(s)$ appears in eq. (1). If the loading is instantaneously switched on at $t = 0$, its time history is represented by the Heaviside (left-continuous) step function

$$H(t) = \begin{cases} 0, & t \le 0 \\ 1, & t > 0\,, \end{cases} \tag{14}$$

whose Laplace transform is

$$\tilde{H}(s) = \mathcal{L}(H(t)) = \frac{1}{s}\,. \tag{15}$$

Since any piecewise constant function can be expressed as a linear combination of shifted Heaviside step functions (see, e.g. Spada & Melini 2019), LNs obtained assuming the loading time history in eq. (14) can be used to compute the response to arbitrary piecewise constant loads. However, for some applications, it may be more convenient to represent the load time history as a piecewise linear function. It is easy to show that any such function can be written as a linear combination of shifted *elementary ramp functions* of length t_r, of the type

$$R(t) = \begin{cases} 0, & t \le 0 \\ \dfrac{t}{t_r}, & 0 < t \le t_r \\ 1, & t > t_r\,, \end{cases} \tag{16}$$

whose Laplace transform is

$$\tilde{R}(s) = \mathcal{L}(R(t)) = \frac{1}{s} \cdot \frac{1 - e^{-s t_r}}{s\, t_r}\,. \tag{17}$$

Laplace-transformed LNs corresponding to a stepwise or rampwise forcing time history can be obtained by setting $\tilde{f}(s) = \tilde{H}(s)$ or $\tilde{f}(s) = \tilde{R}(s)$ in eq. (1). The rampwise forcing function defined by eq. (16) is one of the new features introduced in ALMA^3.

2.3 Frequency dependent LNs

In the context of planetary tidal deformation, it is important to determine the response to an external periodic tidal potential. The previous version of ALMA was limited to the case of an instantaneously applied forcing. For periodic potentials, the time dependence of the forcing term has the oscillating form $e^{i\omega t}$, where

$$\omega = \frac{2\pi}{T} \tag{18}$$

is the angular frequency of the forcing term, T is the period of the oscillation and $i = \sqrt{-1}$ is the imaginary unit. In the time domain, the solution vector can be cast in the form

$$\mathbf{x}_\omega(t) = \mathbf{x}_\delta(t) * e^{i\omega t}\,, \tag{19}$$

where $\mathbf{x}_\delta(t)$ is the time-domain response to an impulsive (δ-like) load and the asterisk indicates the time convolution. Since the impulsive load is a causal function, $\mathbf{x}_\delta(t) = 0$ for $t < 0$ and eq. (19) can be expressed as

$$\mathbf{x}_\omega(t) = e^{i\omega t} \int_0^\infty \mathbf{x}_\delta(t') e^{-i\omega t'} dt' = \mathbf{x}_0(\omega) e^{i\omega t}\,, \tag{20}$$

where $\mathbf{x}_0(\omega)$ is the Laplace transform of $\mathbf{x}_\delta(t)$ evaluated at $s = i\omega$. By setting $\tilde{f}(s) = \mathcal{L}(\delta(t)) = 1$ and $s = i\omega$ in eq. (1), we obtain

$$\mathbf{x}_0(\omega) = \Big(P_1 \Lambda(i\omega) J\Big)\Big(P_2 \Lambda(i\omega) J\Big)^{-1}\, \mathbf{b}\,. \tag{21}$$

Hence, in analogy with eqs (3)–(5), the frequency-domain LNs $h_n(\omega)$, $l_n(\omega)$ and $k_n(\omega)$ are defined as

$$h_n(\omega) = \frac{m}{a} u_n(\omega) \tag{22}$$

$$l_n(\omega) = \frac{m}{a} v_n(\omega) \tag{23}$$

$$k_n(\omega) = -1 - \frac{m}{ag} \varphi_n(\omega)\,, \tag{24}$$

where $u_n(\omega)$, $v_n(\omega)$ and $\varphi_n(\omega)$ are the three components of vector $\mathbf{x}_0(\omega) = (u_n, v_n, \varphi_n)^T$.

Since the frequency-domain LNs are complex numbers, in general a phase difference exists between the variation of the external periodic potential and the planet response, due to the energy dissipation within the planetary mantle. If $L_n(\omega)$ is any of the three frequency-dependent LNs, the corresponding time-domain LNs are:

$$L_n(t) = L_n(\omega) e^{i\omega t} = |L_n(\omega)| e^{i(\omega t - \phi)}\,, \tag{25}$$

where the *phase lag* ϕ is

$$\tan\phi = -\frac{\mathrm{Im}(L_n(\omega))}{\mathrm{Re}(L_n(\omega))}\,, \tag{26}$$

and $\mathrm{Re}(z)$ and $\mathrm{Im}(z)$ denote the real and the imaginary parts of z, respectively. A vanishing phase lag ($\phi = 0$) is only expected for elastic planetary models (i.e. for $\mathrm{Im}(L_n(\omega)) = 0$), for which no dissipation occurs. We remark that the evaluation of the frequency-dependent LNs (eqs 22–24) does not require the application of the Post-Widder method outlined in Section 2.2, since in this case no inverse transform is to be evaluated.

Tidal dissipation is phenomenologically expressed in term of the quality factor, Q (Kaula 1964; Goldreich & Soter 1966), which according to for example Efroimsky & Lainey (2007) and Clausen & Tilgner (2015) is related to the phase lag ϕ through

$$Q(\omega) = \frac{1}{\sin\phi} = -\frac{|L_2(\omega)|}{\mathrm{Im}\,(L_2(\omega))}\,, \tag{27}$$

thus implying $Q = \infty$ in the case of no dissipation. Tidal dissipation is often measured in terms of the ratio

$$\frac{|k_2|}{Q} = |k_2| \sin\phi = -\mathrm{Im}\, k_2\,. \tag{28}$$

For terrestrial bodies, the quality factor Q usually lies in a range between 10 and 500 (Goldreich & Soter 1966; Murray & Dermott 2000). We remark that the quality factor Q is a phenomenological parameter used when the internal rheology is unknown; if LNs are computed by means of a viscoelastic model, it may be more convenient to consider the imaginary part of k_2, which is directly proportional to dissipation (Segatz *et al.* 1988).

3 AN OVERVIEW OF ALMA^3

Here we briefly outline how the solution scheme described in previous section is implemented in ALMA^3, leaving the technical details and practical considerations to the accompanying User Manual. ALMA^3 evaluates, for any given harmonic degree n, the time-domain LNs ($h_n(t)$, $l_n(t)$, $k_n(t)$), their time derivatives ($\dot{h}_n(t)$, $\dot{l}_n(t)$, $\dot{k}_n(t)$) and the frequency-domain LNs ($h_n(\omega)$, $l_n(\omega)$, $k_n(\omega)$), either corresponding to surface loading or to tidal boundary conditions. While the original version of the code was limited to time-domain LNs, the other two outputs represent new capabilities introduced by ALMA^3. The planetary model can include, in principle, any number of layers in addition to a central core. Each of the layers can be characterized by any of the rheological laws listed in Table 1, while the core can also have a fluid inviscid rheology. As we show in Section 5, numerical solutions obtained with ALMA^3 are stable even with models including a large number of layers, providing a way to approximate rheologies whose parameters are varying continuously with radius.

Time-domain LNs are computed by evaluating numerically eqs (12) and (13), assuming a time history of the forcing that can be either a step function (eq. 14) or an elementary ramp function (eq. 16). In the latter case, the duration t_r of the loading phase can be configured by the user. Since eqs (12) and (13) are singular for $t = 0$, ALMA^3 can compute time-domain LNs only for $t > 0$. In the "elastic limit", the LNs can be obtained either by sampling them at a time t that is much smaller than the characteristic relaxation times of the model, or by configuring the Hooke's elastic rheology for all the layers in the model. In the second case, the LNs will follow the same time history of the forcing. As discussed in Section 2, the sums in eqs (12) and (13) contain oscillating terms that can lead to loss of precision due to catastrophic cancellation (Spada & Boschi 2006). To avoid the consequent numerical degeneration of the LNs, ALMA^3 performs all computations in arbitrary-precision floating point arithmetic, using the Fortran FMLIB library (Smith 1991, 2003).

When running ALMA^3, the user shall configure both the number D of significant digits used by the FMLIB library and the order M of the Gaver sequence in eqs (12) and (13). As discussed by Spada & Boschi (2006) and Spada (2008), higher values of D and M ensure a better numerical stability and accuracy of the results, but come at the cost of rapidly increasing computation time. All the examples discussed in the next section have been obtained with parameters $D = 128$ and $M = 8$. While these values ensure a good stability in relatively simple models, a special care shall be devoted to numerical convergence in case of models with a large number of layers and/or when computing LNs to high harmonic degrees; in that case, higher values of D and M may be needed to attain stable results.

Complex-valued LNs are obtained by ALMA^3 by directly sampling eq. (21) at the requested frequencies ω, and therefore no numerical Laplace antitransform is performed. While for frequency-domain LNs the numerical instabilities associated with the Post-Widder formula are avoided, the use of high-precision arithmetic may still be appropriate, especially in case of models including a large number of layers. ALMA^3 does not directly compute the tidal phase lag ϕ, the quality factor Q nor the k_2/Q ratio, which can be readily obtained from tabulated output values of the real and imaginary parts of LNs through eqs (26)–(28).

Although ALMA^3 is still limited to spherically symmetric and elastically incompressible models, with respect to the version originally released by Spada (2008) now the program includes some new significant features aimed at increasing its versatility. These are: (i) the evaluation of frequency-dependent loading and tidal LNs in response to periodic forcings, (ii) the possibility of dealing with a layered core that includes fluid and solid portions, (iii) the introduction of a ramp-shaped forcing function to facilitate the implementation of loading histories varying in a linear piecewise manner, (iv) the implementation of the Andrade transient viscoelastic rheology often used in the study of planetary deformations, (v) the explicit evaluation of the derivatives of the LNs in the time domain to facilitate the computation of geodetic variations in deglaciated areas, (vi) a short but exhaustive User Guide and (vii) a facilitated computation of frequency-dependent loading and tidal planetary LNs, with pre-defined and easily customizable rheological profiles for some terrestrial planets and moons.

4 BENCHMARKING ALMA^3

In the following we discuss a suite of numerical benchmarks for LNs computed by ALMA^3. First, we consider a uniform, incompressible, self-gravitating sphere with Maxwell rheology (the so-called 'Kelvin sphere') and compare tidal LNs computed numerically by ALMA^3 with well known analytical results. Then, we test numerical results from ALMA^3 by reproducing the viscoelastic LNs for an incompressible Earth model computed within the benchmark exercise by Spada *et al.* (2011). Finally, we discuss the impact of the incompressibility approximation assumed in ALMA^3 by comparing elastic and viscoeastic LNs for a realistic Earth model with recent numerical results by Michel & Boy (2021), who use a compressible model.

4.1 The viscoelastic Kelvin sphere

Simplified planetary models for which closed-form expressions for the LNs are available are of particular relevance here, since they allow an analytical benchmarking of the numerical solutions discussed in Section 2 and provided by ALMA^3.

In what follows, we consider a spherical, homogeneous, self-gravitating model, often referred to as the 'Kelvin sphere' (Thomson 1863), which can be extended to a viscoelastic rheology in a straightforward manner. For example, adopting the complex modulus $\mu(s)$ appropriate for the Maxwell rheology (see Table 1), for a Kelvin sphere of radius a, density ρ and surface gravity g, in the Laplace domain the harmonic degree $n = 2$ LNs take the form

$$\tilde{L}_2(s) = \frac{L_f}{1 + \gamma^2 \dfrac{s}{s + 1/\tau}}, \tag{29}$$

where L_2 stands for any of (h_2, l_2, k_2), L_f is the 'fluid limit' of $\tilde{L}_2(s)$ (i.e. the value attained for $s \to 0$), the Maxwell relaxation time is

$$\tau = \frac{\eta}{\mu} \tag{30}$$

and

$$\gamma^2 = \frac{19}{2} \frac{\mu}{\rho g a} \tag{31}$$

is a positive non-dimensional constant. Note that g is a function of a and ρ, since for the homogeneous sphere $g = \frac{4}{3}\pi G \rho a$, where G is the universal gravitational constant.

After some algebra, (29) can be cast in the form

$$\tilde{L}_2(s) = \frac{L_f}{1 + \gamma^2} \left(1 + \frac{1/\tau - 1/\tau'}{s + 1/\tau'} \right), \tag{32}$$

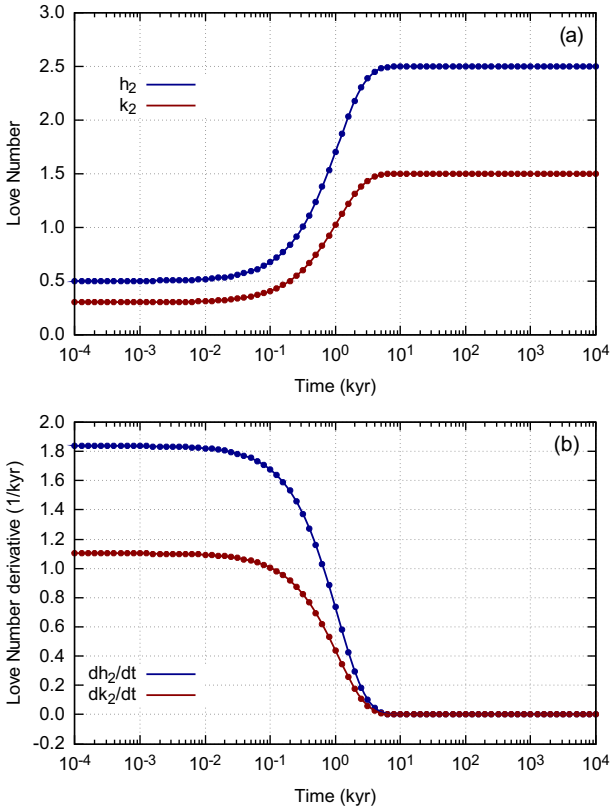

Figure 1. (a) Comparison between numerical (dotted) and analytical solutions (solid) for the h_2 and k_2 tidal LNs of a Kelvin sphere with Maxwell rheology having radius $a = 6371$ km, density $\rho = 5.514 \times 10^3$ kg·m^{-3}, rigidity $\mu = 1.46 \times 10^{11}$ Pa and viscosity $\eta = 10^{21}$ Pa·s. (b) The same, for the time derivatives of the LNs. Note that the time axis is logarithmic.

where for a tidal forcing, the fluid limits for degree $n = 2$ are $h_f = \frac{5}{2}, l_f = \frac{3}{4}$ and $k_f = \frac{3}{2}$ (see e.g. Lambeck 1988) and where we have defined

$$\tau' = (1 + \gamma^2)\tau \,. \tag{33}$$

From eq. (32), the LNs in the time domain can be immediately computed analytically through an inverse Laplace transformation:

$$L_2(t) = \frac{L_f}{1+\gamma^2}\left[\delta(t) + H(t)\left(\frac{1}{\tau} - \frac{1}{\tau'}\right)e^{-t/\tau'}\right], \tag{34}$$

while for an external forcing characterized by a step-wise time-history, the LNs $L_2^{(H)}(t)$ are obtained by a time convolution with the Heaviside function:

$$L_2^{(H)}(t) = L_2(t) * H(t)\,, \tag{35}$$

that yields

$$L_2^{(H)}(t) = \frac{L_f}{1+\gamma^2}\left[1 + \gamma^2\left(1 - e^{-t/\tau'}\right)\right], \quad t \geq 0\,, \tag{36}$$

from which the time derivative of $L_2^{(H)}(t)$ is readily obtained:

$$\dot{L}_2^{(H)}(t) = \frac{L_f}{1+\gamma^2}\left(\frac{1}{\tau} - \frac{1}{\tau'}\right)e^{-t/\tau'}, \quad t > 0\,. \tag{37}$$

In Fig. 1(a), the dotted curves show the h_2 (blue) and the k_2 (red) tidal LN of harmonic degree $n = 2$ obtained by a configuration of ALMA^3 that reproduces the Kelvin sphere (the parameters are given in the Figure caption). The LNs, shown as a function of time, are characterized by two asymptotes corresponding to the elastic and fluid limits, respectively, and by a smooth transition in between. The solid curves, obtained by the analytical expression given by eq. (36), show an excellent agreement with the ALMA^3 numerical solutions. The same holds for the time-derivatives of these LNs, considered in Fig. 1(b), where the analytical LNs (solid lines) are computed according to eq. (37).

The frequency response of the Kelvin sphere for a periodic tidal potential can be obtained by setting $s = i\omega$ in eq. (29), which after rearranging gives:

$$L_2(\omega) = \frac{L_f}{1+\gamma^2}\left[1 + \frac{\gamma^2}{1+(\omega\tau')^2} - i\gamma^2\frac{\omega\tau'}{1+(\omega\tau')^2}\right], \tag{38}$$

which remarkably depends upon ω and τ only through the $\omega\tau$ product. Therefore, a change in the relaxation time τ shall result in a shift of the frequency response of the Kelvin sphere, leaving its shape unaltered.

Using eq. (38) in (26), the phase lag turns out to be:

$$\tan\phi = \frac{\gamma^2\omega\tau}{1+\omega^2\tau\tau'}\,, \tag{39}$$

where it is easy to show that for frequency

$$\omega_0 = \frac{1}{\sqrt{\tau\tau'}} \tag{40}$$

the maximum phase lag $\phi = \phi_{\max}$ is attained, with

$$\tan\phi_{max} = \frac{\gamma^2}{2\sqrt{1+\gamma^2}}\,. \tag{41}$$

By using eq. (38) into (27), for the Kelvin sphere the quality factor is

$$Q_K(\omega) = \sqrt{1 + \frac{1}{\gamma^4}\left(\omega\tau' + \frac{1}{\omega\tau}\right)^2}\,, \tag{42}$$

which at $\omega = \omega_0$ attains its minimum value

$$Q_{\min} = 1 + \frac{2}{\gamma^2}\,. \tag{43}$$

In Fig. 2(a), the dotted curve shows the phase lag ϕ as a function of the tidal period $T = 2\pi/\omega$, obtained by the same configuration of ALMA^3 described in the caption of Fig. 1. The solid line corresponds to the analytical expression of $\phi(T)$ which can be obtained from eq. (39), showing once again an excellent agreement with the numerical results (dotted). Fig. 2(b) compares numerical results obtained from ALMA^3 for Q with the analytical expression for $Q_K(T)$ obtained from (42). By using in eq. (40) the numerical values of ρ, a and μ assumed in Figs 1 and 2, the period $T_0 = 2\pi/\omega_0$ is found to scale with viscosity η as

$$T_0 = (3.06\,\text{kyr})\left(\frac{\eta}{10^{21}\,\text{Pa}\cdot\text{s}}\right), \tag{44}$$

so that for $\eta = 10^{21}$ Pa · s, representative of the Earth's mantle bulk viscosity (see e.g. Mitrovica 1996; Turcotte & Schubert 2014), the maximum phase lag $\phi_{\max} \simeq 41.9°$ and the minimum quality factor $Q_{\min} \simeq 1.5$ are attained for $T_0 \simeq 3$ kyr, consistent with the results shown in Fig. 2.

4.2 Community-agreed LNs for an incompressible Earth model

Due to the relevance of viscoelastic LNs in a wide range of applications in Earth science, several numerical approaches for their

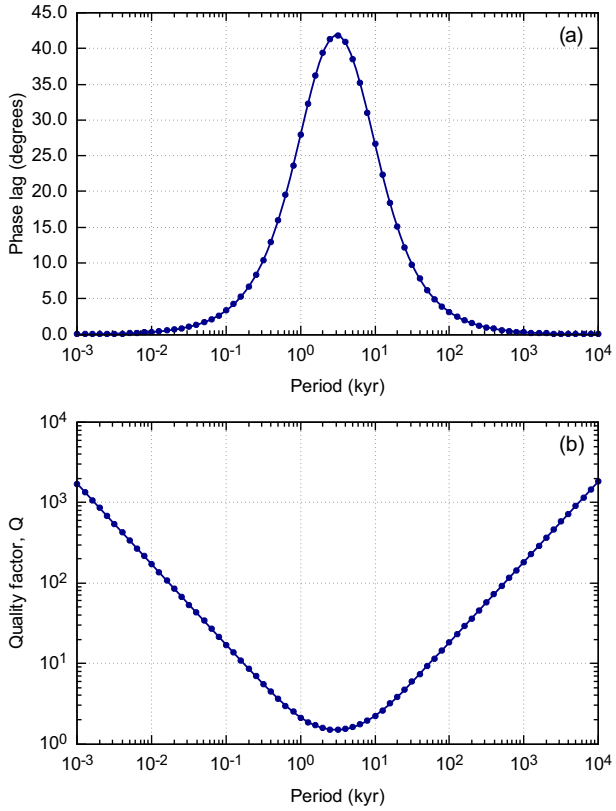

Figure 2. Comparison between numerical (dotted) and analytical solutions (solid) for the tidal phase lag ϕ (a) and quality factor Q (b) for the $n = 2$ tidal LNs of a Kelvin sphere with Maxwell rheology, using the same parameters detailed in the caption of Fig. 1.

evaluation have been independently developed and proposed in literature. This ignited the interest on benchmark exercises, in which a set of agreed numerical results can be obtained and different approaches and methods can be cross-validated. Here we consider a benchmark effort that has taken place in the framework of the Glacial-Isostatic Adjustment community (Spada *et al.* 2011), in which a set of reference viscoelastic LNs for an incompressible, spherically symmetric Earth model has been derived through different numerical approaches, including viscoelastic normal modes, spectral-finite elements and finite elements. This allows us to validate our numerical results by implementing in ALMA^3 the M3-L70-V01 Earth model described in table 3 of Spada *et al.* (2011), which includes a fluid inviscid core, three mantle layers with Maxwell viscoelastic rheology and an elastic lithosphere, and comparing the set of LNs from ALMA^3 with reference results from the benchmark exercise.

Fig. 3 shows elastic ($h_n^{(e)}$, $l_n^{(e)}$, $k_n^{(e)}$) and fluid LNs ($h_n^{(f)}$, $l_n^{(f)}$, $k_n^{(f)}$), both for the loading and tidal cases, computed by ALMA^3 for the M3-L70-V01 Earth model in the range of harmonic degrees $2 \leq n \leq 250$. The elastic and fluid limits have been simulated in ALMA^3 by sampling the time-dependent LNs at $t_e = 10^{-5}$ kyr and $t_f = 10^{10}$ kyr, respectively. Reference results from Spada *et al.* (2011), represented by solid lines in Fig. 3, are practically indistinguishable from results obtained with ALMA^3 over the whole range of harmonic degrees, demonstrating the reliability of the numerical approach used in ALMA^3.

Fig. 4 shows time-dependent LNs $h_n(t)$, $l_n(t)$ and $k_n(t)$, for both the loading and tidal cases, computed by ALMA^3 for harmonic degrees $2 \leq n \leq 5$ and for t between 10^{-3} and 10^5 kyr, a time range that encompasses the complete transition between the elastic and fluid limits. Also in this case, numerical results obtained by ALMA^3 (shown by symbols) are coincident with the reference LNs from Spada *et al.* (2011), represented by solid lines.

4.3 Viscoleastic LNs for a PREM-layered Earth model

In this last benchmark, we compare numerical results from ALMA^3 with reference viscoelastic LNs for a realistic Earth model which accounts for an elastically compressible rheology, in order to assess its importance when modelling the tidal and loading response of a large planetary body. In the context of Earth rotation, the role of compressibility has been addressed by Vermeersen *et al.* (1996); the reader is also referred to Sabadini *et al.* (2016) for a broader presentation of the problem and to Renaud & Henning (2018) for a discussion of the effects of compressibility in the realm of planetary modelling.

Here we focus on numerical results recently obtained by Michel & Boy (2021), who used Fourier techniques to compute frequency-dependent viscoelastic LNs for periodic forcings both of loading and tidal types. They have adopted an Earth model with the elastic structure of PREM (Preliminary Reference Earth Model, Dziewonski & Anderson 1981) and a fully liquid core, and replaced the outer oceanic layer with a solid crust layer, adjusting crustal density in such a way to keep the total Earth mass unchanged. Following Michel & Boy (2021), we have built a discretized realization of PREM suitable for ALMA^3 with a fluid core and 28 homogeneous mantle layers, which has been used to obtain the numerical results discussed later.

Fig. 5 compares elastic LNs obtained by Michel & Boy (2021) in the range of harmonic degrees between $n = 2$ and $n = 10{,}000$ with those computed with ALMA^3 . The largest difference between the two sets of LNs can be seen for h_n in the loading case (Fig. 5a), where the assumption of incompressibility leads to a significant underestimation of deformation across the whole range of harmonic degrees. Incompressible elasticity leads to an underestimation also of the k_n loading LN (Fig. 5b), although the differences are much smaller and limited to the lowest harmonic degrees. Conversely, for the tidal response (Figs 5c and d) the two sets of LNs turn out to be almost overlapping, suggesting a minor impact of elastic compressibility on tidal deformations.

In Fig. 6 we consider a periodic load and compare viscoelastic tidal LNs h_2 and k_2 computed with ALMA^3 with corresponding results from Michel & Boy (2021). Consistently with the elastic case, we see that the incompressibility approximation used in ALMA^3 generally results in smaller modelled deformations across the whole range of forcing periods. The largest differences are found on $|h_2|$ (Fig. 6a) and reach the ∼20 per cent level in the range of periods between 10^5 and 10^6 d, while on $|k_2|$ (6b) the differences are much smaller, reaching the ∼10 per cent level in the same range of periods. Similarly, for the phase lags (Figs 6c and d) we find a larger difference for h_2 than for k_2, with the phase lag being remarkably insensitive to compressibility up to forcing periods of the order of 10^4–10^5 d.

5 EXAMPLES OF ALMA^3 APPLICATIONS

In this Section we consider four applications showing the potential of ALMA^3 in different contexts. First, we will discuss the k_2 tidal Love number of Venus, based upon a realistic layering for the interior of this planet. Second, we shall evaluate the tidal LNs for a simple

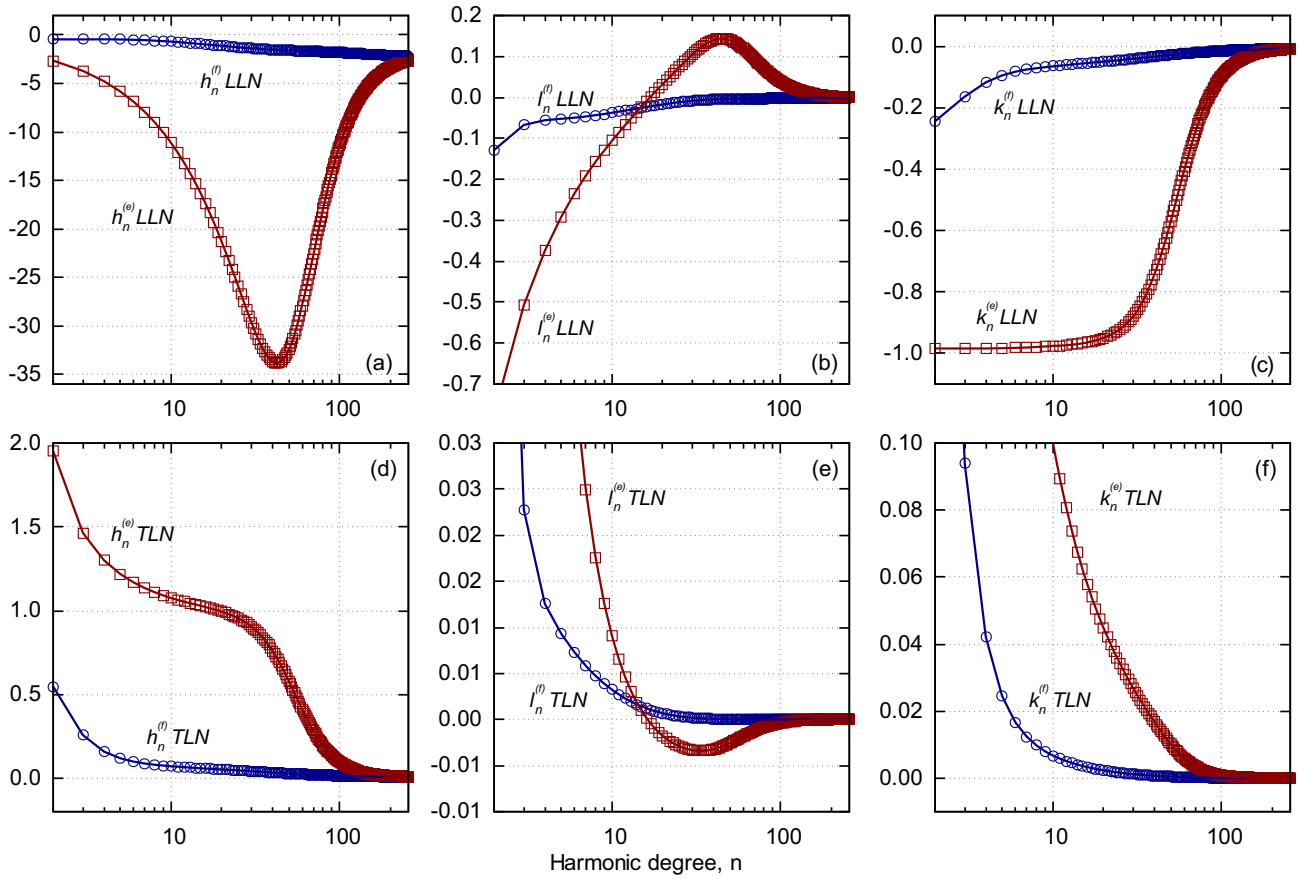

Figure 3. Elastic (red) and fluid (blue) Love numbers as a function of the harmonic degree for the Earth model M3-L70-V01 defined in Spada *et al.* (2011). Top (a–c) and bottom frames (d–f) show Love numbers for loading and tidal forcing, respectively. Symbols show numerical results obtained with ALMA^3 while solid lines represent reference results from the benchmark exercise by Spada *et al.* (2011).

model of the Saturn's moon Enceladus, in order to show how an internal fluid layer can be simulated as a low-viscosity Newtonian fluid rheology and how a depth-dependent viscosity in a conductive shell may be approximated using a sequence of thin homogeneous layers. Third, we will evaluate a set of loading LNs suitable for describing the transient response of the Earth to the melting of large continental ice sheets. As a last example, we will demonstrate how ALMA^3 can simulate the tidal dissipation on the Moon using two recent interior models based on seismological data. While these numerical experiments are put in the context of state-of-the-art planetary interior modelling, we remark that they are aimed only at illustrating the modelling capabilities of ALMA^3 .

5.1 Tidal deformation of Venus

The planet Venus is often referred to as 'Earth's twin planet', since its size and density differ only by ∼5 per cent from those of the Earth. These similarities lead to the expectation that the chemical composition of the Earth and Venus may be similar, with an iron-rich core, a magnesium silicate mantle and a silicate crust (Kovach & Anderson 1965; Lewis 1972; Anderson 1980). Despite these similarities, there is a lack of constraints on the internal structure of Venus. Therefore, its density and rigidity profiles are often assumed to be a rescaled version of the Preliminary Reference Earth Model (PREM) of Dziewonski & Anderson (1981), accounting for the difference in the planet's radius and mass, as in Aitta (2012). One of the main observational constraints on the planet's interior, along its mass and moment of inertia, is its k_2 tidal LN. The current observational estimate of k_2 for Venus is 0.295 ± 0.066 ($2 \times$ formal σ), and it has been inferred from Magellan and Pioneer Venus orbiter spacecraft data (Konopliv & Yoder 1996). However, due to uncertainties on k_2, it is not possible to discriminate between a liquid and a solid core (Dumoulin *et al.* 2017).

Here we use ALMA^3 to reproduce results obtained by means of the Venus model referred to as $T_5^{\rm hot}$ by Dumoulin *et al.* (2017), based on the 'hot temperature profile' from Armann & Tackley (2012), having a composition and hydrostatic pressure from the PREM model of Dziewonski & Anderson (1981). The viscosity η of the mantle of Venus is fixed and homogeneous; the crust is elastic ($\eta \to \infty$), the core is assumed to be inviscid ($\eta = 0$) and the rheology of the mantle follows Andrade's law (see Table 1). The parameters of the $T_5^{\rm hot}$ model have been volume-averaged into the core, the lower mantle, the upper mantle and the crust. The calculation of k_2 is performed at the tidal period of 58.4 d (Cottereau *et al.* 2011). In the work of Dumoulin *et al.* (2017), k_2 is computed by integrating the radial functions associated with the gravitational potential, as defined by Takeuchi & Saito (1972), hence the simplified formulation of Saito (1974) relying on the radial function is used. The method is derived from the classical theory of elastic body deformation and the energy density integrals commonly used in the seismological community. One of the main differences between their computation and the results presented here is the assumption about compressibility, since Dumoulin *et al.* (2017) use a compressible planetary model, while in ALMA^3 an incompressible rheology is always assumed. In Fig. 7,

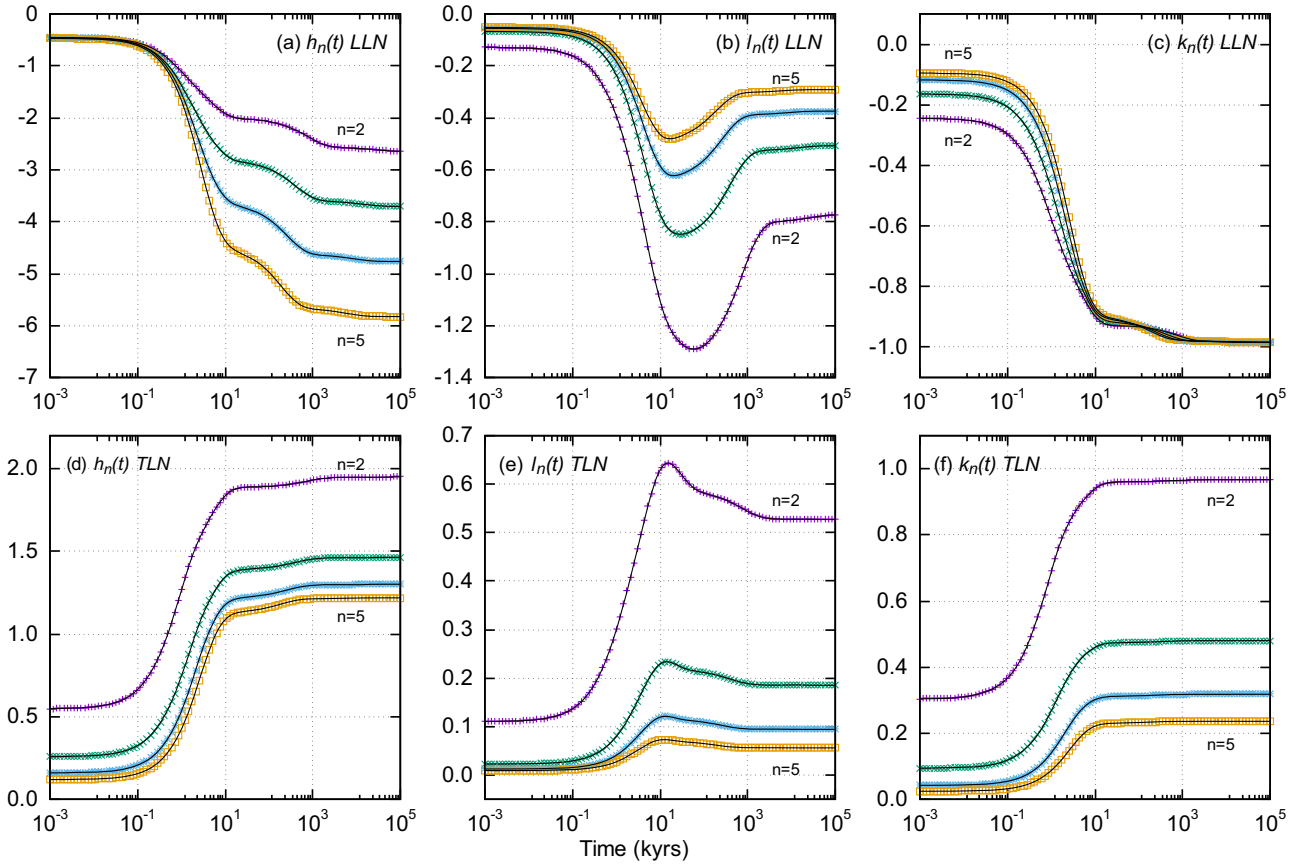

Figure 4. Time-dependent viscoelastic Love numbers for the M3-L70-V01 Earth model at long spatial wavelengths (harmonic degrees $2 \leq n \leq 5$). Top panels (frames a–c) and bottom ones (d–f) show Love numbers for a loading and tidal forcing, respectively. The time history of the load is an Heaviside unit step function. Symbols show numerical results obtained with ALMA^3 while solid lines represent reference results from the benchmark exercise by Spada *et al.* (2011).

the two curves show the k_2 tidal LN corresponding to Andrade creep parameters $\alpha = 0.2$ and $\alpha = 0.3$ as a function of mantle viscosity for the tidal period of 58.4 d. Each of the vertical red segments corresponds to the interval of k_2 values obtained by Dumoulin *et al.* (2017) for discrete mantle viscosity values $\eta = 10^{19}$, 10^{20}, 10^{21} and 10^{22} Pa·s, respectively, and for a range of the Andrade creep parameter α in the interval between 0.2 and 0.3. The grey shaded area illustrates the most recent observed value of k_2 according to Konopliv & Yoder (1996) to an uncertainty of $2 \times$ formal σ. Fig. 7 shows that the k_2 values obtained with ALMA^3 for the $T_5^{\rm hot}$ Venus model fit well with the lower boundary of the compared study for each of the discrete mantle viscosity values if an Andrade creep parameter $\alpha = 0.3$ is assumed, while for $\alpha = 0.2$ the modelled k_2 slightly exceeds the upper boundary of Dumoulin *et al.* (2017).

5.2 The tidal response of Enceladus

The scientific interest on Enceladus has gained considerable momentum after the 2005 Cassini flybys, which confirmed the icy nature of its surface and evidenced the existence of water-rich plumes emerging from the southern polar regions (Porco *et al.* 2006; Ivins *et al.* 2020). These hint to the existence of a subsurface ocean, heated by tidal dissipation in the core, where physical conditions allowing life could be possible, in principle (for a review, see Hemingway *et al.* 2018). The interior structure of Enceladus has been thoroughly investigated in literature on the basis of observations of its gravity field (Iess *et al.* 2014), tidal deformation and physical librations (see, e.g. Čadek *et al.* 2016), setting constraints on the possible structure of the ice shell and of the underlying liquid ocean (Roberts & Nimmo 2008), and on the composition of its core (Roberts 2015). Lateral variations in the crustal thickness of Enceladus have been inferred in studies about the isostatic response of the satellite using gravity and topography data as constraints (see Beuthe *et al.* 2016; Čadek *et al.* 2016, 2019) and in works dealing with the computation of deformation and dissipation (see Souček *et al.* 2016, 2019; Beuthe 2018, 2019). Indeed, from all the above studies, it clearly emerges that a full insight into the tidal dynamics of Enceladus could be only gained adopting 3-D models of its internal structure.

While a thorough investigation of the signature of the interior structure of Enceladus on its tidal response is far beyond the scope of this work, here we set up a simple spherically symmetric model with the purpose of illustrating how the LNs for a planetary body including a fluid internal layer like Enceladus can be computed with ALMA^3, and how a radially-dependent viscosity structure can be approximated with homogeneous layers. We define a spherically symmetric model including an homogeneous inner solid core of radius $c = 192$ km (Hemingway *et al.* 2018), surrounded by a liquid water layer and an outer icy shell, and investigate the sensitivity of the tidal LNs to the thickness of the ice layer, along the lines of Roberts & Nimmo (2008) and Beuthe (2018). In our setup, the core is modelled as a homogeneous elastic body with rigidity $\mu_c = 4 \times 10^{10}$ Pa and whose density is adjusted to ensure that, when varying

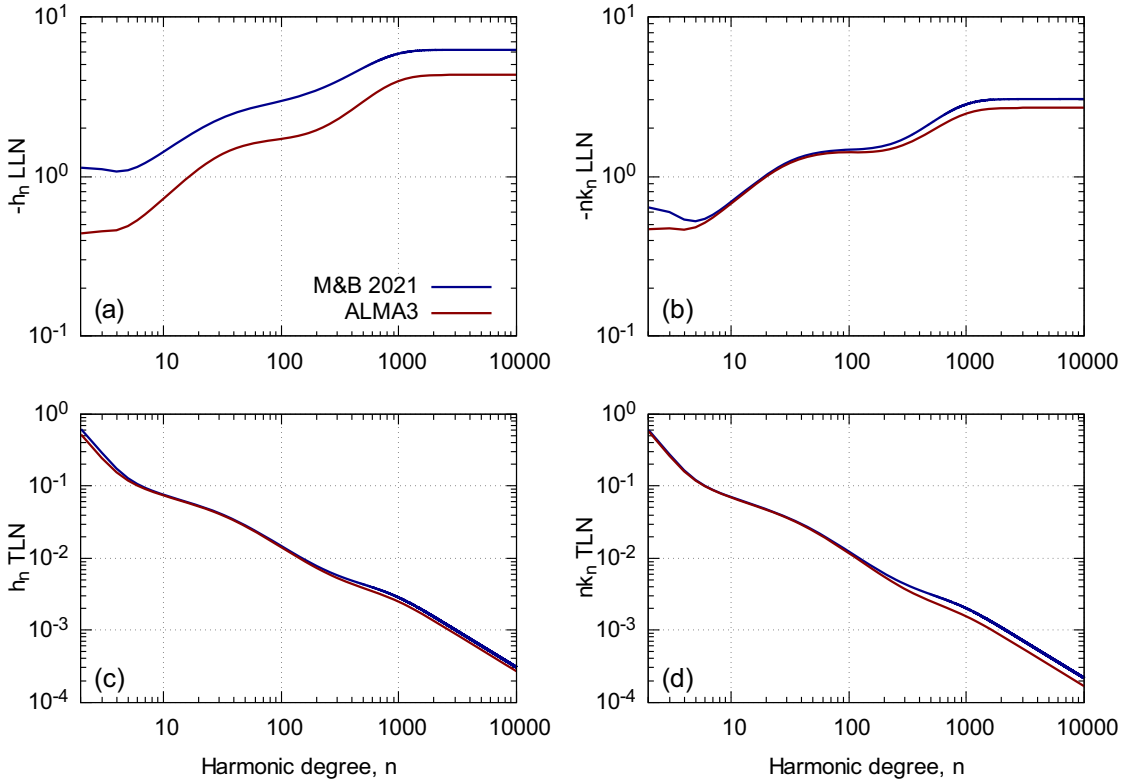

Figure 5. Comparison between elastic Love numbers h_n (left-hand panels) and k_n (right-hand panels) obtained by Michel & Boy (2021) with numerical results from `ALMA`^{3}. In both cases, the Earth model has the elastic structure of PREM in the crust and in the mantle, while the core is modelled as an uniform, inviscid fluid. Top and bottom panels show loading and tidal Love numbers, respectively.

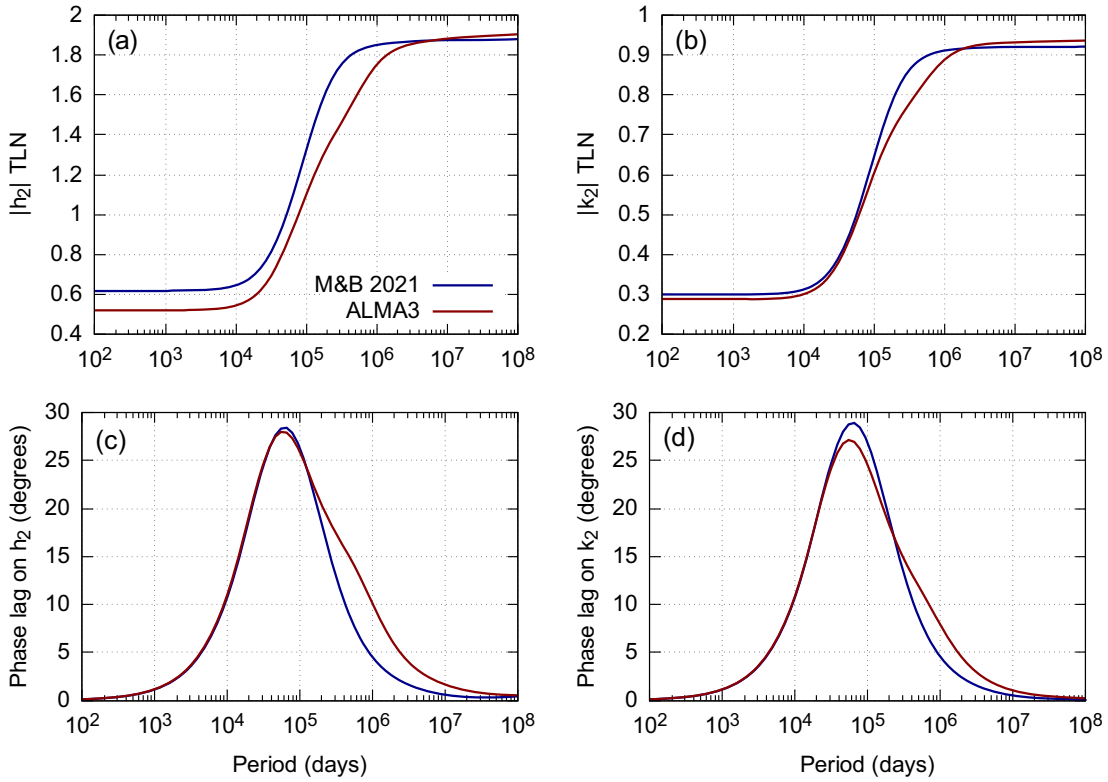

Figure 6. Comparison between the modulus of tidal Love numbers $|h_2|$ and $|k_2|$ (top panels) and corresponding phase lags (bottom panels) obtained by Michel & Boy (2021) for a periodic forcing with numerical results from `ALMA`^{3}. The Earth model has the elastic structure of PREM and a Maxwell rheology with viscosity $\eta = 10^{21}$ Pa·s is assumed in the mantle.

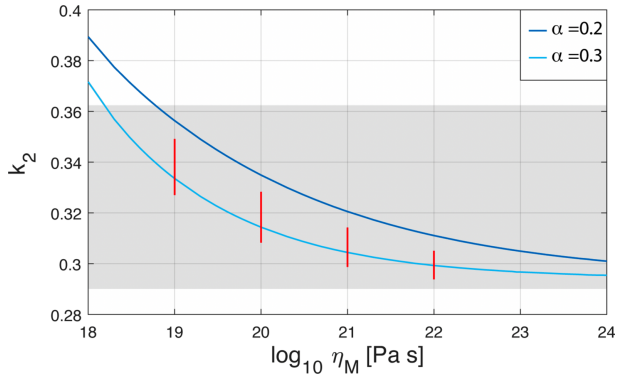

Figure 7. Tidal Love number k_2 as a function of the mantle viscosity η_M for the internal model $T_5^{\rm hot}$ of Dumoulin *et al.* (2017). The two curves correspond to numerical results from ALMA^3 assuming Andrade creep parameters $\alpha = 0.2$ and $\alpha = 0.3$, respectively. Red vertical segments represent the range of the estimates obtained by Dumoulin *et al.* (2017), while the grey shaded area represents the most recent observed value of k_2 and its 2σ uncertainty according to Konopliv & Yoder (1996).

the thickness of the ice shell, the average bulk density of the model is kept constant at $\rho_b = 1610\ \mathrm{kg{\cdot}m^{-3}}$. Since in ALMA^3 a fluid inviscid rheology can be prescribed only for the core, we approximate the ocean layer as a low viscosity Newtonian fluid ($\eta_w = 10^4$ Pa·s). The ice shell is modelled as a conductive Maxwell body whose viscosity profile depends on the temperature T according to the Arrhenius law:

$$\eta(T) = \eta_m \exp\left[\frac{E_a}{R_g T_m}\left(\frac{T_m}{T} - 1\right)\right], \tag{45}$$

where E_a is the activation energy, R_g is the gas constant, T_m is the temperature at the base if the ice shell and η_m is the ice viscosity at $T = T_m$. Following Beuthe (2018), we use $E_a = 59.4\ \mathrm{J\,(mol \cdot K)^{-1}}$, $\eta_m = 10^{13}$ Pa·s and $T_m = 273$ K, and assume that the temperature inside the ice shell varies with radius r according to

$$T(r) = T_m^{\frac{r-a}{r_b-a}}\, T_s^{\frac{r_b-r}{r_b-a}}, \tag{46}$$

where r_b is the bottom radius of the ice shell and $T_s = 59$ K is the average surface temperature. Since in ALMA^3 the rheological parameters must be constant inside each layer, we discretize the radial viscosity profile given by eq. (45) using a onion-like structure of homogeneous spherical shells. To assess the sensitivity of results to the choice of discretization resolution, we perform three numerical experiments in which the thickness of ice layers is set to 0.25, 0.5 and 1 km. The ice and water densities are set to $\rho_i = 930\ \mathrm{kg{\cdot}m^{-3}}$ and $\rho_w = 1020\ \mathrm{kg{\cdot}m^{-3}}$, respectively, while the ice rigidity is set to $\mu_i = 3.5 \times 10^9$ Pa, a value consistent with evidence from tidal flexure of marine ice (Vaughan 1995) and laboratory experiments (Cole & Durell 1995).

Fig. 8(a) shows the elastic tidal LNs h_2, l_2 and k_2 for the Enceladus model discussed above as a function of the thickness of the ice shell. The elastic tidal response is strongly dependent on the ice thickness, with the h_2 LN decreasing from ∼0.090 for a 10-km-thick shell to ∼0.015 for a 50-km-thick shell. It is of interest to compare these results with elastic LNs obtained by Beuthe (2018) in the uniform-shell approximation. It turns out that the h_2 LN shown in Fig. 8(a) is slightly smaller than corresponding results from Beuthe (2018), with relative differences between the 5 and 10 per cent level, consistently with their estimate of the effect of incompressibility. Fig. 8(b) shows the real and imaginary parts of

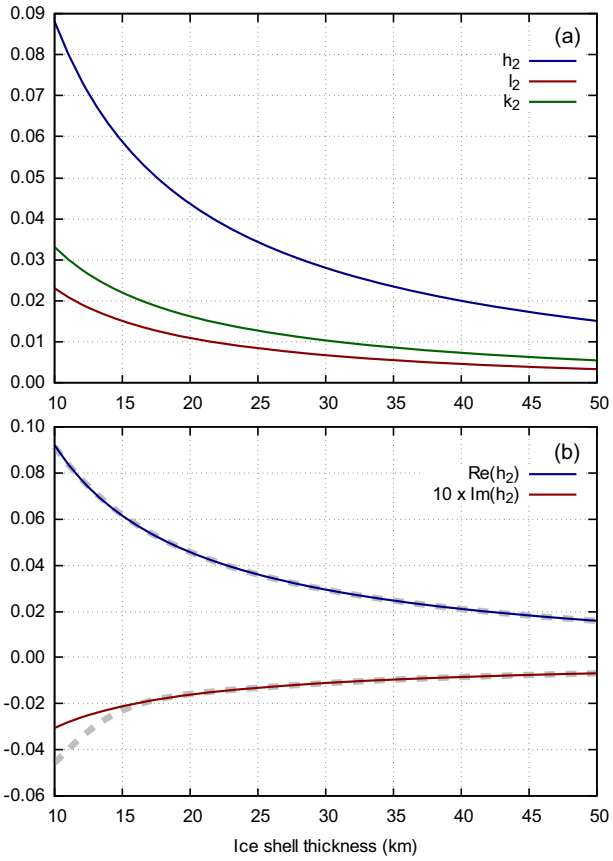

Figure 8. Elastic harmonic degree 2 tidal Love numbers for Enceladus (a) as a function of the thickness of the ice shell. In (b), real and imaginary parts of the viscoelastic tidal Love number h_2 for a forcing period of 1.73 d are shown. Solid lines and dashed lines correspond to discretization steps for the ice shell of 0.50 and 1.00 km, respectively. Please note that Im(k_2) has been multiplied by a factor of 10 to improve readability.

the h_2 tidal LN as a function of the thickness of the ice layer for a periodic load of period $T = 1.37$ d, which corresponds to the shortest librational oscillation of Enceladus (Rambaux *et al.* 2010). As discussed above, for this numerical experiment we implemented in ALMA^3 a radially variable viscosity profile by discretizing eq. (45) into a series of uniform layers. Solid and dashed lines in Fig. 8(b) show results obtained with a discretization step of 0.5 and 1.0 km, respectively; we verified that with a step of 0.25 km the results are virtually identical to those obtained with a step of 0.5 km. The effect of the discretization is evident only on the imaginary part of h_2, where a coarse layer size of 1 km leads to a significant overestimation of Im(k_2) if the ice shell is thinner than ∼15 km. By a visual comparison of the results of Fig. 8(b) with fig. 4 of Beuthe (2018), we can see that the imaginary part of h_2 is well reproduced, while the real part is underestimated by the same level we found for the elastic LNs; this difference is likely to be attributed to the incompressibility approximation adopted in ALMA^3.

5.3 Loading LNs for transient rheologies in the Earth's mantle

Loading LNs are key components in models of the response of the Earth to the spatio-temporal variation of surface loads, including the ongoing deformation due to the melting of the late Pleistocene

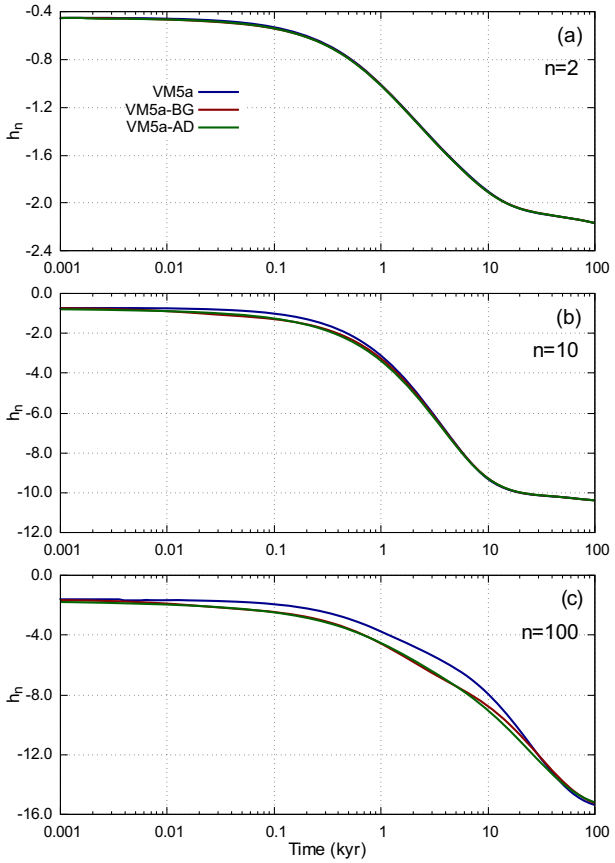

Figure 9. Loading Love number $h_n(t)$ for $n = 2$ (frame a), $n = 10$ (b) and $n = 100$ (c), obtained with the VM5a viscosity model by Peltier & Drummond (2008) and with two variants that assume Burgers (VM5a-BG) or Andrade (VM5a-AD) rheologies in the upper mantle layers.

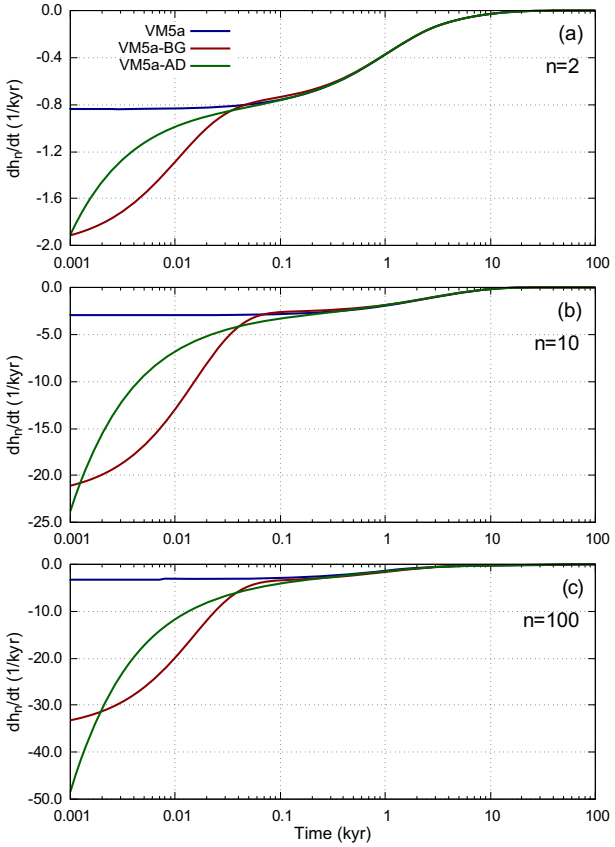

Figure 10. Time-derivative of the loading Love number $\dot{h}_n(t)$ for harmonic degrees $n = 2$, 10 and 100, adopting the rheological models described in the caption of Fig. 9.

ice complexes (see e.g. Peltier & Drummond 2008; Purcell *et al.* 2016), the present-day and future response to climate-driven melting of ice sheets and glaciers (Bamber & Riva 2010; Slangen 2012), and deformations induced by the variation of hydrological loads (Bevis *et al.* 2016; Silverii *et al.* 2016). Evidence from Global Navigation Satellite System measurements of the time-dependent surface deformation point to a possible transient nature of the mantle in response to the regional-scale melting of ice sheets and to large earthquakes (see, e.g. Pollitz 2003, 2005; Nield *et al.* 2014; Qiu *et al.* 2018). Here, it is therefore of interest to present the outcomes of some numerical experiments in which `ALMA`^{3} is configured to compute the time-dependent h loading Love number assuming a transient rheology in the mantle. Numerical estimates of $h_n(t)$ and of its time derivative $\dot{h}_n(t)$ would be needed, for instance, to model the response to the thickness variation of a disc-shaped surface load, as discussed by Bevis *et al.* (2016).

In Fig. 9 we show the time evolution of the $h_n(t)$ loading LN for $n = 2$, 10 and 100, comparing the response obtained assuming the VM5a viscosity model of Peltier & Drummond (2008), which is fully based on a Maxwell rheology, with those expected if VM5a is modified introducing a transient rheology in the upper mantle layers. An Heaviside time history for the load is adopted throughout. In model VM5a-BG we assumed a Burgers bi-viscous rheological law in the upper mantle, with $\mu_2 = \mu_1$ and $\eta_2/\eta_1 = 0.1$ (see Table 1), while in model VM5a-AD an Andrade rheology (Cottrell 1996) with creep parameter $\alpha = 0.3$ has been assumed for the upper mantle. For $n = 2$ (Fig. 9a) the responses obtained with the three models almost overlap. Indeed, for long wavelengths (by Jean's rule, the wavelength corresponding to harmonic degree n is $\lambda = \frac{2\pi a}{n+\frac{1}{2}}$, where a is Earth's radius) the response to surface loads is mostly sensitive to the structure of the lower mantle, where the three variants of VM5a considered here have the same rheological properties. Conversely, for $n = 10$ (Fig. 9b) we see a slightly faster response to the loading for both transient models in the time range between 0.01 and 1 kyr. For $n = 100$, the transient response of VM5a-BG and VM5a-AD becomes even more enhanced between 0.01 and 10 kyr. It is worth to note that, for times less than ∼10 kyr, the two transient versions of VM5a almost yield identical responses, suggesting that an Andrade rheology in the Earth's upper mantle might explain the observed vertical transient deformations in the same way as a Burgers rheology. The differences between the three models are more evident in Fig. 10, where we use `ALMA`^{3} for computing the time derivatives $\dot{h}_n(t)$ (this option was not available in previous versions of the program). Compared with the Maxwell model, the transient ones show a significantly larger initial rate of vertical displacement, that differ significantly for Burgers and Andrade. The three rheologies provide comparable responses only ∼0.1 kyr after loading. We shall remark, however, that the incompressiblity approximation used in `ALMA`^{3} has a significant impact on the h_n Love number, as we discussed in Section 4.3, so the results shown above must be taken with caution, and a more detailed analysis of the impact of compressibility on the time evolution of LNs would be in order.

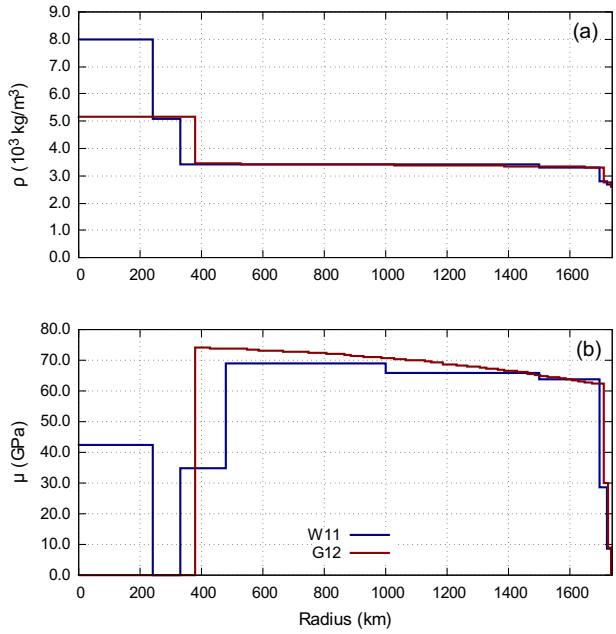

Figure 11. Radial profiles of density (a) and rigidity (b) for the Moon models by Weber *et al.* (2011) (W11, blue) and Garcia *et al.* (2011, 2012) (G12, red). Models W11 and G12 include 10 and 71 homogeneous layers, respectively.

5.4 Tidal dissipation on the Moon

The Moon is the extraterrestrial body for which the most detailed information about the internal structure is available. In addition to physical constraints from observations of tidal deformation (Williams *et al.* 2014), seismic experiments deployed during the Apollo missions (Nunn *et al.* 2020) provided instrumental recordings of moonquakes which allowed the formulation of a set of progressively refined interior models (see, e.g. Heffels *et al.* 2021).

In this last numerical experiment, we configured `ALMA`^{3} to compute tidal LNs for the Moon according to the two interior models proposed by Weber *et al.* (2011,W11 hereafter) and Garcia *et al.* (2011, 2012, G12 hereafter). Profiles of density ρ and rigidity μ for models W11 and G12 are shown in Fig. 11, with the most notable difference being that the former assumes an inner solid core and a fluid outer core, while the latter contains an undifferentiated fluid core. We emphasize that model G12 includes 70 rheological layers in the mantle and crust, demonstrating the stability of `ALMA`^{3} with densely layered planetary models. For both models, we assumed a Maxwell rheology in the crust and the mantle, with a viscosity of 10^{20} Pa·s. A more realistic approach has been followed by Nimmo *et al.* (2012), who have modelled the Moon's LNs and dissipation adopting an extended Burgers model for the mantle, which also accounts for transient tidal deformations (Faul & Jackson 2015). Such rheological model is not incorporated in the current release of `ALMA`^{3}, but it can be implemented by the user modifying the source code in order to compute the corresponding complex rigidity modulus $\mu(s)$. The fluid core has been modelled as a Newtonian fluid with viscosity 10^4 Pa·s while in the inner core, for model W11, we used a Maxwell rheology with a viscosity of 10^{16} Pa·s, a value within the estimated ranges for the viscosity of the Earth inner core (Buffett 1997; Dumberry & Mound 2010; Koot & Dumberry 2011). Following the lines of Harada *et al.* (2014, 2016) and Organowski & Dumberry (2020), we defined a 150-km-thick low-viscosity zone (LVZ) at the base of the mantle and computed the k_2 tidal LNs as a function of the LVZ viscosity for a forcing period $T = 27.212$ d.

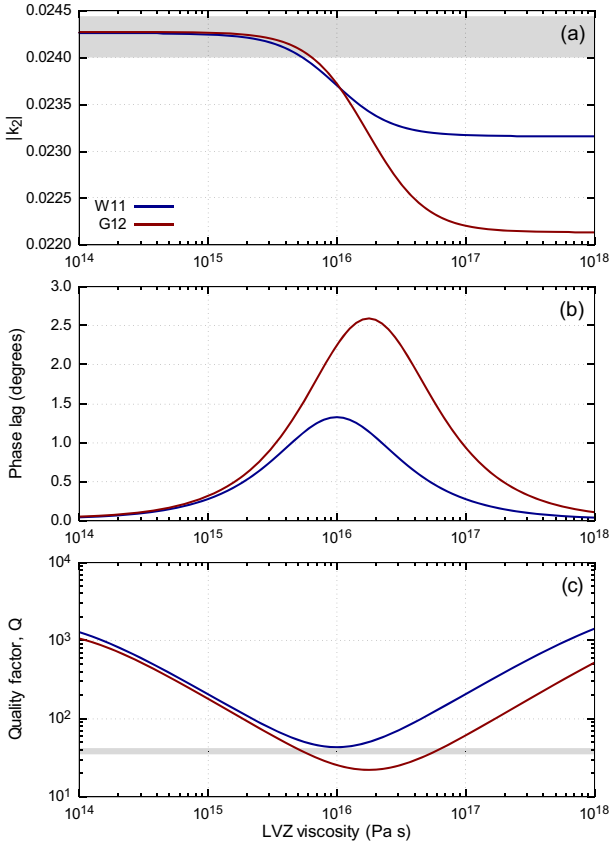

Figure 12. Modulus of the tidal Love number $|k_2|$ for the Moon (frame a), phase lag (b) and quality factor (c) as a function of the LVZ viscosity, for a forcing period $T = 27.212$ d. Blue and red curves correspond to the Moon models by Weber *et al.* (2011) and Garcia *et al.* (2011, 2012) shown in Fig. 11. Shaded areas in frames (a) and (c) correspond to the 1σ confidence intervals for measured values of k_2 and Q according to Williams & Boggs (2015).

For both W11 and G12 models, Fig. 12 shows the dependence on the LVZ viscosity of the k_2 tidal LN (Fig. 12a), of its phase lag angle (Fig. 12b) and of the quality factor Q (Fig. 12c). With the considered setup, for a LVZ viscosity smaller than 10^{15} Pa·s the tidal response of the two models is almost coincident, while for higher viscosities model G12 predicts a stronger tidal dissipation. Shaded grey areas in frames (Figs 12a and c) show 1σ confidence intervals for experimental estimates of k_2 (Williams *et al.* 2014) and Q (Williams & Boggs 2015). With both models we obtain values of k_2 within the 1σ interval for an LVZ viscosity smaller than about 5×10^{15} Pa·s; interestingly, for that LVZ viscosity the G12 model predicts a quality factor Q within the measured range, while model W11 would require a slightly higher LVZ viscosity (10^{16} Pa·s). Of course, a detailed assessment of the ability of the two models to reproduce the observed tidal LNs would be well beyond the scope of this work, and several additional parameters potentially affecting the tidal response (as e.g. the LVZ thickness or the core radius) would need to be considered.

6 CONCLUSIONS

We have revisited the Post-Widder approach in the context of evaluating viscoelastic LN and their time derivatives for arbitrary planetary models. Our results are the basis of a new version of ALMA^3, a user friendly Fortran program that computes the LNs of a multilayered, self-gravitating, spherically symmetric, incompressible planetary model characterized by a linear viscoelastic rheology. ALMA^3 can be suitably used to solve a wide range of problems, either involving the surface loading or the tidal response of a rheologically layered planet. By taking advantage of the Post-Widder Laplace inversion method, the evaluation of the time-domain LNs is simplified, avoiding some of the limitations of the traditional viscoelastic normal mode approach. Differently from previous implementations (Spada 2008), ALMA^3 can evaluate both time-domain and frequency-domain LNs, for an extended set of linear viscoelastic constitutive equations that also include a transient response, like Burgers or Andrade rheologies. Generalized linear rheologies that until now have been utilized in flat geometry like the one characterizing the extended Burgers model (Ivins *et al.* 2020) could be possibly implemented as well modifying the source code, if the corresponding analytical expression of the complex rigidity modulus is available. Furthermore, ALMA^3 can compute the time-derivatives of the LNs, and can deal with step-like and ramp-shaped forcing functions. The resulting LNs can be linearly superposed to obtain the planet response to arbitrary time evolving loads. Numerical results from ALMA^3 have been benchmarked with analytical expressions for a uniform sphere and with a reference set of viscoelastic LNs for an incompressible Earth model (Spada *et al.* 2011). The well-known limitations of the incompressibility approximation in modelling deformations of large terrestrial bodies have been quantitatively assessed by a comparison between numerical outputs of ALMA^3 and viscoelastic LNs recently obtained by Michel & Boy (2021) for a realistic, compressible Earth model. The versatility of ALMA^3 has then been demonstrated by a few examples, in which the LNs and some associated quantities like the quality factor Q, have been evaluated for some multilayered models of planetary interiors characterized by complex rheological profiles and by densely layered internal structures.

ACKNOWLEDGMENTS

We thank the Associate Editor Gael Choblet and two anonymous reviewers for their very constructive comments that considerably helped improving our manuscript. We have benefited from discussion with all scientists involved in the project 'LDLR – Lunar tidal Deformation from Earth-based and orbital Laser Ranging', funded by the French ANR and the German agency DGF. We are indebted to Steve Vance, Saikiran Tharimena, Marshall Styczinski and Bruce Bills for encouragement and advice. DM is funded by a INGV (Istituto Nazionale di Geofisica e Vulcanologia) 2020-2023 'ricerca libera' research grant and partly supported by the INGV project Pianeta Dinamico 2021-22 Tema 4 KINDLE (grant no. CUP D53J19000170001), funded by the Italian Ministry of University and Research 'Fondo finalizzato al rilancio degli investimenti delle amministrazioni centrali dello Stato e allo sviluppo del Paese, Legge 145/2018'. CS is funded by a PhD grant of the French Ministry of Research and Innovation. CS also acknowledges the ANR, project number ANR-19-CE31-0026 project LDLR (Lunar tidal Deformation from Earth-based and orbital Laser Ranging). GS is funded by a FFABR (Finanziamento delle Attività Base di Ricerca) grant of MIUR (Ministero dell'Istruzione, dell'Università e della Ricerca) and by a RFO research grant of DIFA (Dipartimento di Fisica e Astronomia 'Augusto Righi') of the Alma Mater Studiorum Università di Bologna.

Conflicts of Interest

The authors declare no conflicts of interest with respect to the research presented in this article.

DATA AVAILABILITY

Source code of the ALMA^3 version used to obtain numerical results presented in this work is available as a supplementary material. The latest version of ALMA^3 can be downloaded from https://github.com/danielemelini/ALMA3. The data underlying plots shown in this paper are available upon request to the corresponding author.

REFERENCES

Aitta, A., 2012. Venus' internal structure, temperature and core composition, *Icarus,* **218**(2), 967–974.

Anderson, D.L., 1980. Tectonics and composition of Venus, *Geophys. Res. Lett.,* **7**(1), 101–102.

Armann, M. & Tackley, P.J., 2012. Simulating the thermochemical magmatic and tectonic evolution of Venus's mantle and lithosphere: Two-dimensional models, *J. geophys. Res.,* **117,** E12003, doi:10.1029/2012JE004231.

Bamber, J. & Riva, R., 2010. The sea level fingerprint of recent ice mass fluxes, *Cryosphere,* **4**(4), 621–627.

Beuthe, M., 2018. Enceladus's crust as a non-uniform thin shell: I. Tidal deformations, *Icarus,* **302,** 145–174.

Beuthe, M., 2019. Enceladus's crust as a non-uniform thin shell: II. Tidal dissipation, *Icarus,* **332,** 66–91.

Beuthe, M., Rivoldini, A. & Trinh, A., 2016. Enceladus's and Dione's floating ice shells supported by minimum stress isostasy, *Geophys. Res. Lett.,* **43**(19), 10–088.

Bevis, M., Melini, D. & Spada, G., 2016. On computing the geoelastic response to a disk load, *J. geophys. Int.,* **205**(1), 1804–1812.

Buffett, B.A., 1997. Geodynamic estimates of the viscosity of the Earth's inner core, *Nature,* **388,** 1476–4687.

Čadek, O., *et al.*, 2016. Enceladus's internal ocean and ice shell constrained from Cassini gravity, shape, and libration data, *Geophys. Res. Lett.,* **43**(11), 5653–5660.

Čadek, O., Souček, O., Běhounkovà, M., Choblet, G., Tobie, G. & Hron, J., 2019. Long-term stability of Enceladus' uneven ice shell, *Icarus,* **319,** 476–484.

Christensen, R., 1982. *Theory of Viscoelasticity,* Dover.

Clausen, N. & Tilgner, A., 2015. Dissipation in rocky planets for strong tidal forcing, *Astron. Astrophys.,* **584,** A60, doi:10.1051/0004-6361/201526082.

Cole, D.M. & Durell, G.D., 1995. The cyclic loading of saline ice, *Philos. Mag. A,* **72**(1), 209–229.

Cottereau, L., Rambaux, N., Lebonnois, S. & Souchay, J., 2011. The various contributions in Venus rotation rate and LOD, *Astron. Astrophys.,* **531,** A45, doi:10.1051/0004-6361/201116606.

Cottrell, A.H., 1996. Andrade creep, *Philos. Mag. Lett.,* **73**(1), 35–36.

Dumberry, M. & Mound, J., 2010. Inner core–mantle gravitational locking and the super-rotation of the inner core, *J. geophys. Int.,* **181**(2), 806–817.

Dumoulin, C., Tobie, G., Verhoeven, O., Rosenblatt, P. & Rambaux, N., 2017. Tidal constraints on the interior of Venus, *J. geophys. Res.,* **122**(6), 1338–1352.

Dziewonski, A.M. & Anderson, D.L., 1981. Preliminary reference Earth model, *Phys. Earth planet. Inter.,* **25**(4), 297–356.

Efroimsky, M. & Lainey, V., 2007. Physics of bodily tides in terrestrial planets and the appropriate scales of dynamical evolution, *J. geophys. Res.,* **112,** E12003, doi:10.1029/2007JE002908.

Farrell, W., 1972. Deformation of the Earth by surface loads, *Rev. Geophys.,* **10**(3), 761–797.
Farrell, W. & Clark, J., 1976. On postglacial sea level, *J. geophys. Int.,* **46,** 647–667.
Faul, U. & Jackson, I., 2015. Transient creep and strain energy dissipation: an experimental perspective, *Ann. Rev. Earth planet. Sci.,* **43,** 541–569.
Friederich, W. & Dalkolmo, J., 1995. Complete synthetic seismograms for a spherically symmetric earth by a numerical computation of the Green's function in the frequency domain, *J. geophys. Int.,* **122**(2), 537–550.
Garcia, R.F., Gagnepain-Beyneix, J., Chevrot, S. & Lognonné, P., 2011. Very preliminary reference Moon model, *Phys. Earth planet. Inter.,* **188**(1), 96–113.
Garcia, R.F., Gagnepain-Beyneix, J., Chevrot, S. & Lognonné, P., 2012. Erratum to "Very Preliminary Reference Moon Model", by R.F. Garcia, J. Gagnepain-Beyneix, S. Chevrot, P. Lognonné [Phys. Earth Planet. Inter. 188 (2011) 96–113], *Phys. Earth planet. Inter.,* **202–203,** 89–91.
Gaver, D.P., 1966. Observing stochastic processes, and approximate transform inversion, *Operat. Res.,* **14**(3), 444–459.
Gavrilov, S. & Zharkov, V., 1977. Love numbers of the giant planets, *Icarus,* **32**(4), 443–449.
Goldreich, P. & Soter, S., 1966. Q in the solar system, *Icarus,* **5**(1), 375–389.
Harada, Y., Goossens, S., Matsumoto, K., Yan, J., Ping, J., Noda, H. & Haruyama, J., 2014. Strong tidal heating in an ultralow-viscosity zone at the core–mantle boundary of the Moon, *Nat. Geosci.,* **7,** 569–572.
Harada, Y., Goossens, S., Matsumoto, K., Yan, J., Ping, J., Noda, H. & Haruyama, J., 2016. The deep lunar interior with a low-viscosity zone: Revised constraints from recent geodetic parameters on the tidal response of the Moon, *Icarus,* **276,** 96–101.
Heffels, A., Knapmeyer, M., Oberst, J. & Haase, I., 2021. Re-evaluation of Apollo 17 Lunar Seismic Profiling Experiment data including new LROC-derived coordinates for explosive packages 1 and 7, at Taurus-Littrow, Moon, *Planet. Space Sci.,* **206,** 105307.
Hemingway, D., Iess, L., Tajeddine, R. & G. Tobie, G., 2018. The interior of Enceladus, in *Enceladus and the Icy Moons of Saturn,* pp. 57–77, eds Schenk, P.M., Clark, R.N., Howett, C.J.A., Verbiscer, A.J. & Waite, J.H., University of Arizona.
Iess, L., *et al.*, 2014. The gravity field and interior structure of Enceladus, *Science,* **344**(6179), 78–80.
Ivins, E.R., Caron, L., Adhikari, S., Larour, E. & Scheinert, M., 2020. A linear viscoelasticity for decadal to centennial time scale mantle deformation, *Rep. Prog. Phys.,* **83**(10), 106801.
Kaula, W.M., 1964. Tidal dissipation by solid friction and the resulting orbital evolution, *Rev. Geophys.,* **2**(4), 661–685.
Kellermann, C., Becker, A. & Redmer, R., 2018. Interior structure models and fluid Love numbers of exoplanets in the super-Earth regime, *Astron. Astrophys.,* **615,** A39.
Konopliv, A. & Yoder, C., 1996. Venusian k2 tidal Love number from Magellan and PVO tracking data, *Geophys. Res. Lett.,* **23**(14), 1857–1860.
Koot, L. & Dumberry, M., 2011. Viscosity of the Earth's inner core: constraints from nutation observations, *Earth planet. Sci. Lett.,* **308**(3), 343–349.
Kovach, R.L. & Anderson, D.L., 1965. The interiors of the terrestrial planets, *J. geophys. Res.,* **70**(12), 2873–2882.
Lambeck, K., 1988. The earth's variable rotation: some geophysical causes, in *Symposium-International Astronomical Union,* Vol. **128,** pp. 1–20, Cambridge Univ. Press.
Lewis, J.S., 1972. Metal/silicate fractionation in the solar system, *Earth planet. Sci. Lett.,* **15**(3), 286–290.
Love, A.E.H., 1911. *Some Problems of Geodynamics: Being an Essay to which the Adams Prize in the University of Cambridge was Adjudged in 1911,* CUP Archive.
Melini, D., Cannelli, V., Piersanti, A. & Spada, G., 2008. Post-seismic rebound of a spherical Earth: new insights from the application of the Post-Widder inversion formula, *J. geophys. Int.,* **174**(2), 672–695.
Melini, D., Gegout, P., King, M., Marzeion, B. & Spada, G., 2015. On the rebound: Modeling Earth's ever-changing shape, *EOS,* **96**(15), 14–17.
Michel, A. & Boy, J.-P., 2021. Viscoelastic Love numbers and long-period geophysical effects, *J. geophys. Int.,* **228**(2), 1191–1212.
Mitrovica, J.X., 1996. Haskell [1935] revisited, *J. geophys. Res.: Solid Earth,* **101**(B1), 555–569.
Munk, W.H. & MacDonald, G.J., 1960. *The Rotation of the Earth: A Geophysical Discussion,* Cambridge Univ. Press.
Murray, C.D. & Dermott, S.F., 2000. *Solar System Dynamics,* Cambridge Univ. Press.
Na, S.-H. & Baek, J., 2011. Computation of the Load Love number and the Load Green's function for an elastic and spherically symmetric earth, *J. Korean Phys. Soc.,* **58**(5), 1195–1205.
Nield, G., *et al.*, 2014. Rapid bedrock uplift in the Antarctic Peninsula explained by viscoelastic response to recent ice unloading, *Earth planet. Sci. Lett.,* **397,** 32–41.
Nimmo, F., Faul, U. & Garnero, E., 2012. Dissipation at tidal and seismic frequencies in a melt-free Moon, *J. geophys. Res.,* **117**(E9), doi:10.1029/2012JE004160.
Nunn, C., *et al.*, 2020. Lunar seismology: a data and instrumentation review, *Space Sci. Rev.,* **216**(89), doi:10.1007/s11214-020-00709-3.
Organowski, O. & Dumberry, M., 2020. Viscoelastic relaxation within the Moon and the phase lead of its Cassini state, *J. geophys. Res.,* **125**(7), e2020JE006386, doi:10.1029/2020JE006386.
Padovan, S., Spohn, T., Baumeister, P., Tosi, N., Breuer, D., Csizmadia, S., Hellard, H. & Sohl, F., 2018. Matrix-propagator approach to compute fluid Love numbers and applicability to extrasolar planets, *Astron. Astrophys.,* **620,** A178, doi:10.1051/0004-6361/201834181.
Peltier, W. & Drummond, R., 2008. Rheological stratification of the lithosphere: a direct inference based upon the geodetically observed pattern of the glacial isostatic adjustment of the North American continent, *Geophys. Res. Lett.,* **35**(16), doi:10.1029/2008GL034586.
Peltier, W.R., 1974. The impulse response of a Maxwell Earth, *Rev. Geophys. Space Phys.,* **12**(4), 649–669.
Pollitz, F.F., 2003. Transient rheology of the uppermost mantle beneath the Mojave Desert, California, *Earth planet. Sci. Lett.,* **215**(1–2), 89–104.
Pollitz, F.F., 2005. Transient rheology of the upper mantle beneath central Alaska inferred from the crustal velocity field following the 2002 Denali earthquake, *J. geophys. Res.,* **110**(B8), doi:10.1029/2005JB003672.
Porco, C.C., *et al.*, 2006. Cassini observes the active south pole of Enceladus, *Science,* **311**(5766), 1393–1401.
Post, E.L., 1930. Generalized differentiation, *Trans. Am. Math. Soc.,* **32**(4), 723–781.
Purcell, A., Tregoning, P. & Dehecq, A., 2016. An assessment of the ICE6G_C (VM5a) glacial isostatic adjustment model, *J. geophys. Res.,* **121**(5), 3939–3950.
Qiu, Q., Moore, J.D.P., Barbot, S., Feng, L. & Hill, E.M., 2018. Transient rheology of the Sumatran mantle wedge revealed by a decade of great earthquakes, *Nat. Commun.,* **9**(1), 995.
Rambaux, N., Castillo-Rogez, J.C., Williams, J.G. & Karatekin, Ö., 2010. Librational response of Enceladus, *Geophys. Res. Lett.,* **37**(4), doi:10.1029/2009GL041465.
Renaud, J.P. & Henning, W.G., 2018. Increased tidal dissipation using advanced rheological models: Implications for Io and tidally active exoplanets, *Astrophys. J.,* **857**(2), 98.
Riva, R.E.M. & Vermeersen, L.L.A., 2002. Approximation method for high-degree harmonics in normal mode modelling, *J. geophys. Int.,* **151**(1), 309–313.
Roberts, J.H., 2015. The fluffy core of Enceladus, *Icarus,* **258,** 54–66.
Roberts, J.H. & Nimmo, F., 2008. Tidal heating and the long-term stability of a subsurface ocean on Enceladus, *Icarus,* **194**(2), 675–689.
Rundle, J.B., 1982. Viscoelastic-gravitational deformation by a rectangular thrust fault in a layered Earth, *J. geophys. Res.,* **87**(B9), 7787–7796.
Sabadini, R., Yuen, D.A. & Boschi, E., 1982. Polar wandering and the forced responses of a rotating, multilayered, viscoelastic planet, *J. geophys. Res.,* **87**(B4), 2885–2903.
Sabadini, R., Vermeersen, B. & Cambiotti, G., 2016. *Global dynamics of the Earth,* Springer.
Saito, M., 1974. Some problems of static deformation of the Earth, *J. Phys. Earth,* **22**(1), 123–140.
Saito, M., 1978. Relationship between tidal and load Love numbers, *J. Phys. Earth,* **26**(1), 13–16.

Segatz, M., Spohn, T., Ross, M. & Schubert, G., 1988. Tidal dissipation, surface heat flow, and figure of viscoelastic models of Io, *Icarus,* **75**(2), 187–206.

Shida, T., 1912. *On the elasticity of the Earth and the Earth's crust,* Kyoto Imperial University.

Silverii, F., D'Agostino, N., Métois, M., Fiorillo, F. & Ventafridda, G., 2016. Transient deformation of karst aquifers due to seasonal and multiyear groundwater variations observed by GPS in southern Apennines (Italy), *J. geophys. Res.,* **121**(11), 8315–8337.

Slangen, A., 2012. Modelling regional sea–level changes in recent past and future, *PhD thesis*, Utrecht University, the Netherlands.

Smith, D., 2003. Using multiple-precision arithmetic, *Comput. Sci. Eng.,* **5**(4), 88–93.

Smith, D.M., 1991. Algorithm 693: a FORTRAN package for floating-point multiple-precision arithmetic, *ACM Trans. Math. Softw.,* **17**(2), 273–283.

Sohl, F., Hussmann, H., Schwentker, B., Spohn, T. & Lorenz, R.D., 2003. Interior structure models and tidal Love numbers of Titan, *J. geophys. Res.,* **108**(E12), doi:10.1029/2003JE002044.

Souček, O., Hron, J., Běhounková, M. & Čadek, O., 2016. Effect of the tiger stripes on the deformation of Saturn's moon Enceladus, *Geophys. Res. Lett.,* **43**(14), 7417–7423.

Souček, O., Běhounková, M., Čadek, O., Hron, J., Tobie, G. & Choblet, G., 2019. Tidal dissipation in Enceladus' uneven, fractured ice shell, *Icarus,* **328,** 218–231.

Spada, G., 2008. ALMA, a Fortran program for computing the viscoelastic Love numbers of a spherically symmetric planet, *Comp. Geosci.,* **34**(6), 667–687.

Spada, G. & Boschi, L., 2006. Using the Post-Widder formula to compute the Earth's viscoelastic Love numbers, *J. geophys. Int.,* **166**(1), 309–321.

Spada, G. & Melini, D., 2019. SELEN^4 (SELEN version 4.0): a Fortran program for solving the gravitationally and topographically self-consistent sea-level equation in glacial isostatic adjustment modeling, *Geoscient. Model Dev.,* **12**(12), 5055–5075.

Spada, G., *et al.*, 2011. A benchmark study for glacial isostatic adjustment codes, *J. geophys. Int.,* **185**(1), 106–132.

Stehfest, H., 1970. Algorithm 368: numerical inversion of Laplace transforms [D5], *Commun. ACM,* **13**(1), 47–49.

Sun, W. & Okubo, S., 1993. Surface potential and gravity changes due to internal dislocations in a spherical Earth'I. Theory for a point dislocation, *J. geophys. Int.,* **114**(3), 569–592.

Takeuchi, H. & Saito, M., 1972. Seismic surface waves, *Methods Comput. Phys.,* **11,** 217–295.

Tanaka, Y., Okuno, J. & Okubo, S., 2006. A new method for the computation of global viscoelastic post-seismic deformation in a realistic earth model (I)'vertical displacement and gravity variation, *J. geophys. Int.,* **164**(2), 273–289.

Thomson, W., 1863. XXVII. On the rigidity of the earth, *Phil. Trans. R. Soc. Lond.,* **153,** 573–582.

Tobie, G., Mocquet, A. & Sotin, C., 2005. Tidal dissipation within large icy satellites: applications to Europa and Titan, *Icarus,* **177**(2), 534–549.

Tobie, G., Grasset, O., Dumoulin, C. & Mocquet, A., 2019. Tidal response of rocky and ice-rich exoplanets, *Astron. Astrophys.,* **630,** A70.

Turcotte, D.L. & Schubert, G., 2014. *Geodynamics - Applications of Continuum Physics to Geological Problems,* Cambridge Univ. Press.

Valkó, P.P. & Abate, J., 2004. Comparison of sequence accelerators for the Gaver method of numerical Laplace transform inversion, *Comp. Math. Appl.,* **48**(3), 629–636.

Vaughan, D.G., 1995. Tidal flexure at ice shelf margins, *J. geophys. Res.,* **100**(B4), 6213–6224.

Vermeersen, L. & Mitrovica, J., 2000. Gravitational stability of spherical self-gravitating relaxation models, *J. geophys. Int.,* **142**(2), 351–360.

Vermeersen, L.L.A., Sabadini, R. & Spada, G., 1996. Compressible rotational deformation, *J. geophys. Int.,* **126,** 735–761.

Wahr, J., Selvans, Z.A., Mullen, M.E., Barr, A.C., Collins, G.C., Selvans, M.M. & Pappalardo, R.T., 2009. Modeling stresses on satellites due to nonsynchronous rotation and orbital eccentricity using gravitational potential theory, *Icarus,* **200**(1), 188–206.

Wang, H., Xiang, L., Jia, L., Jiang, L., Wang, Z., Hu, B. & Gao, P., 2012. Load Love numbers and Green's functions for elastic Earth models PREM, iasp91, ak135, and modified models with refined crustal structure from Crust 2.0, *Comp. Geosci.,* **49,** 190–199.

Weber, R.C., Lin, P.-Y., Garnero, E.J., Williams, Q. & Lognonné, P., 2011. Seismic detection of the lunar core, *Science,* **331**(6015), 309–312.

Widder, D.V., 1934. The inversion of the Laplace integral and the related moment problem, *Trans. Am. Math. Soc.,* **36**(1), 107–200.

Williams, J.G. & Boggs, D.H., 2015. Tides on the Moon: Theory and determination of dissipation, *J. geophys. Res.,* **120**(4), 689–724.

Williams, J.G., *et al.*, 2014. Lunar interior properties from the GRAIL mission, *J. geophys. Res.,* **119**(7), 1546–1578.

Wu, P. & Ni, Z., 1996. Some analytical solutions for the viscoelastic gravitational relaxation of a two-layer non-self-gravitating incompressible spherical earth, *J. geophys. Int.,* **126**(2), 413–436.

Wu, P. & Peltier, W., 1982. Viscous gravitational relaxation, *J. geophys. Int.,* **70**(2), 435–485.

Zhang, C., 1992. Love numbers of the Moon and of the terrestrial planets, *Earth, Moon, Planets,* **56**(3), 193–207.

SUPPORTING INFORMATION

Supplementary data are available at *GJI* online.

alma-sources-20211026.zip

Please note: Oxford University Press is not responsible for the content or functionality of any supporting materials supplied by the authors. Any queries (other than missing material) should be directed to the corresponding author for the paper.

Viscosity contrasts in the Venus mantle from tidal deformations

Christelle Saliby[a], Agnès Fienga[a,b], Arthur Briaud[a], Anthony Mémin[a], Carianna Herrera[a]

[a] *Geoazur, CNRS, Observatoire de la Cote d'Azur, Universite Cote d'Azur, 250 av. A. Einstein, Valbonne, 06560, France*
[b] *IMCCE, Observatoire de Paris, PSL University, CNRS, Sorbonne Universite, 77 av. Denfert-Rochereau, Paris, 75014, France*

Abstract

The tidal deformations of a planet are often considered as markers of its inner structure. In this work, we use the tide excitations induced by the Sun on Venus for deciphering the nature of its internal layers. In using a Monte Carlo Random Exploration of the space of parameters describing the thickness, density and viscosity of 4 or 5 layer profiles, we were able to select models that can reproduce the observed mass, total moment of inertia, k_2 Love number and expected quality factor Q. Each model is assumed to have homogeneous layers with constant density, viscosity and rigidity. These models show significant contrasts in the viscosity for the upper mantle and the lower mantle. They also favor a S-free core and a lower mantle slightly hotter, but still consistent, than the expected limits.

Keywords: Venus, Internal structure, Geophysics, Celestial Mechanics

PACS: 0000, 1111

2000 MSC: 0000, 1111

1. Introduction

The terrestrial planet Venus is a reminiscent of the Earth, its twin planet in size and density, Venus being only 5% smaller than the Earth but also 2% less dense. Despite the similarities between Venus and the Earth, these two neighbors have evolved differently as witnessed by the lack of plate tectonics and of magnetic field on Venus. In addition it has a CO_2-rich atmosphere 92 times more massive than the Earth atmosphere. These discrepancies reflect differences in the internal structure, which can be constrained by Venus global properties (mass, radius and distance to the Sun) and geophysical experiments such as topography and gravity field. Most prominently is the latter and its global deformation due to tidal forces from the Sun.

The presence of hot spots on the surface of Venus has been clearly demonstrated in 2008 with the measurements obtained by the mission Venus Express (VEX) [1, 2]. The question is then not if Venus is active but more about the extent of its activity. As there is no indication of plate tectonics on Venus surface [3, 4], its volcanic activity should be driven by plumes emitted from the planet inner part to the crust. The high temperature and pressure at its surface (about 740 K for 93 bars respectively) can favor a more ductile crust than on the Earth. But how are the plumes produced ? From which layer of the planet do they come from ? These are some of the open questions that will be addressed by the future ESA and NASA missions to Venus [5, 6].

In this paper, we use tidal deformations as a tool for exploring the internal structure of the planet and more specifically its mantle and its core.

Tidal forces on a planet cause deformations and mass redistributions in its interior leading to surface motions and variations of its gravity field that can be observed with geophysical and geophysical experiments. [7] studied a compressible homogeneous Earth model and showed that the resulting effects could be represented by a set of dimensionless numbers, so-called Love numbers (hereafter LNs). These Love numbers reflect the internal structure of the planet as they describe the capability of the planet to resist or enhance a forcing excitation. In particular, the change in the gravitational field of a planet due to the influence of an external gravity field, more specifically its degree 2, is primarily described by the tidal Love number (hereafter TLN) k of degree 2, denoted by k_2. This number can be estimated from the analysis of spacecraft radio tracking data. Indeed, Venus TLN k_2 has been estimated by [8] from Doppler tracking of Magellan and Pioneer Venus orbiters (PVO) to $k_2 = 0.295 \pm 0.066$ at 2-σ. Due to these uncertainties, the distinction between liquid and solid core cannot be done [9, 10]. Therefore constraining the internal structure of Venus is still limited for now [11]. The absence of a present internal magnetic field is not a constraint since both a liquid and a solid core are compatible with this observation [12]. However, from the TLNs, it is possible to estimate the energy loss of the planet induced by its visco-elastic deformation at tidal frequencies. It is quantified by the quality factor, Q (as defined i.e. by [13]), and can be derived by considering the real and the imaginary parts of the TLNs. Generic studies about the energy loss of the solar system planets [14] as well as works on the long term spin evolution of Venus [15] provide an interval of possible values for Q for Venus

ranging from 20 to 100.

In this paper we compute the TLN k_2 and the quality factor Q of Venus using the Fortran program, ALMA[3] [16] which calculates the TLNs of a planet under a periodic forcing. In the first part of the paper, we present the basics of the tidal deformation modeling and the internal model of Venus. We explore the effect of two different rheologies (Andrade and Maxwell) and the influence of the thick and dense Venusian atmosphere on k_2 and Q. In the second part of the paper, we randomly explore the space of the internal structure parameters of Venus (densities, viscosities and thicknesses) for 4- and 5-layer models. We use the mass, the total moment of inertia, the value of k_2 derived from observations and the expected limits for the quality factor Q to filter out models that are not consistent with these constraints. We end up with new scenarii for the internal structure of Venus. In particular, we demonstrate that the mantle of Venus presents a clear gradient of viscosities that exists whatever the state of the deeper layers: with or without solid inner core.

2. Model of Venus tidal deformation

2.1. Tidal modeling

The LNs describe how a planetary body deforms in response to a surface load or an external potential and how consequently the equipotential surfaces are modified [7, 17, 16]. The open-source Fortran 90 program ALMA [18, 17, 16] computes LNs using a semi-analytical approach and for a spherically symmetric (1 dimensional), incompressible, visco-elastic model

of planet. The method used in ALMA is similar to the Visco-elastic Normal-Modes method (hereafter VNM) introduced by [19] and is based on finding the solution of the equilibrium equations in the Laplace domain.

This method invokes the correspondence principal of linear viscoleasticity [19] which states that the time dependent viscoelastic response can be simplified to be solved as the elastic problem. The LNs in ALMA^3 are therefore calculated in the Laplace domain (dependent on the Lalpace variable s) and the Post-Widder formula serves to transform them to the time domain [16]. The planet is assumed to be incompressible therefore the six linearly independent solutions of the equilibrium equations depend on the complex rigidity (also called shear modulus) $\tilde{\mu}(s)$ of each layer rheology [20] . In this case the elastic rigidity μ is replaced by the complex rigidity $\tilde{\mu}$ [21]. In Sect. 2.2 we discuss more the assumption of incompressibility and its effect on the calculation of the TLN k_2. The so called Post-Widder method [22, 23] is a non-conventional technique for the Laplace inversion introduced and benchmarked in [18], which allows to overcome most of the intrinsic limitations of VNMs. The original version of ALMA aimed at evaluating time-dependent LNs for a forcing term following a Heaviside time-history. In the case of the tidal excitation, the forcing is periodic and in the case of Venus, the main tides are induced by the Sun with a period of 58 days [24]. We then use a modified version of the code, called ALMA^3, to estimate the TLNs for a periodic forcing acting on the planet [25, 16]. The difference between ALMA and ALMA^3 is that the latter accommodates the periodic perturbations which are used in this study to constrain the internal structure of Venus. This version

ALMA^3 calculates the complex LNs for a given tidal frequency ω where the real and imaginary parts account for the amplitude and phase lag of the tidal response, respectively. The quality factor Q can then be estimated [14, 13], it is calculated as the ratio between the module of k_2 and its imaginary part, see Eq. 2. The theory behind ALMA^3 is explained in details in [25] and [16].

To compute the LNs, it is required as inputs a multi-layered discretization of seismological 1D profiles (i.e., radius, density, rigidity and viscosity) such as the PREM (Preliminary reference Earth model) model [26].

The models tested in this work have 4 or 5 layers excluding the atmosphere. A first family of models is constituted by 4 homogeneous layers : the core, the lower mantle, the upper mantle and the crust. The core could be either fluid (with a viscosity up to 10^{-5} Pa.s) or solid (with a viscosity up to 10^{31} Pa.s). The models with 5 layers are constituted as the models of 4 layer with an additional solid inner core. The layers for the lower and the upper mantle are visco-elastic and are described with an Andrade rheology. Finally the crust is supposed to be elastic. Fig. 1 shows the profiles in densities (top figure) and viscosities (bottom figure) used for the initial benchmark of the model. They will be one of the possible profiles explored with the Monte Carlo exploration (see Sect. 3.2).

The Andrade's creep function used in this work was deduced from the work of both [28] and [29] on the olivine mineral, a magnesium iron silicate, the primary component of the Earth upper mantle. The creep function $J(\omega)$

defining the complex rigidity is given by

$$J(\omega) = \frac{1}{\mu} + \beta \frac{\Gamma(\alpha+1)}{(i\omega)^{\alpha}} - \frac{i}{\eta\omega} \tag{1}$$

with Γ is the Gamma function, μ is the rigidity, η the viscosity, α and β respectively determine the transient response duration in the primary creep and its amplitude. More precisely β, characterizes the intensity of anelastic friction in the material. [29] approximated β which is affixed to the density of the defects, to be $\beta = \mu^{\alpha-1}/\eta^{\alpha}$. The value of α has been determined for olivine-rich rocks to be within $[0.1, 0.5]$, most often within $[0.2, 0.4]$ (see [29]). The transient creep of this law translates in the second addend of Eq. 1.

2.2. Validation: Comparisons to [10]

In [10], the TLN k_2 is computed by integrating the radial functions associated with the gravitational potential (denoted as y_5), as defined by [30], for 10 models with different profiles for the density ρ and the rigidity μ but all with a fluid core. These 10 models are based on either hot or cold temperature profiles, as well as composition and hydrostatic pressure from PREM [26] extrapolation. For comparison with our estimates, we select the model 5 from the hot temperature models in [10], denoted in their work as V5-T_{hot}, referred hereafter as **V**. If the composition of Venus was the same as the Earth, its density would have been 1.9% higher than that of the currently observed one [31, 32, 33]. One reasonable explanation is that Venus and the Earth have different internal structures, and for example, Venus could have a lower Fe content than that of the Earth [27]. This is the basis of the model

V which was constructed in [10] using possible Earth-like chemical content with a lower Fe from [27], specifically 8.1 wt%, i. e. percentage by weight, FeO in the mantle and the crust.

The density and rigidity profiles corresponding to the model **V** are shown on Fig. 1. The model **V** was also chosen by [10] to explore different scenarii for the state of the core other than a fluid one, assuming a solid or a partially fluid and partially solid core. The model has 500 layers excluding the atmosphere, hence a radial discretization with a step a slightly larger than 12 km. The model **V** was also used by [34] to test the effect of incompressibility. Since their code can be applied to both an incompressible and a compressible model, the TLN k_2 has been calculated for model **V** for both cases. For this test the mantle is assumed to follow an Andrade rheology with $\alpha = 0.3$ with an homogeneous viscosity of 10^{20} Pa.s. The real part of k_2 was found to be equal to 0.2948 (4.6% smaller than the compressible case). The imaginary part of k_2 was found to be the same for both cases with a value of 0.0087. In what follows the models are assumed to be incompressible resulting from the limitations of ALMA[3].

We average sub-layers corresponding to each major Venus layer as a single homogeneous layer, reducing our initial 500 layers to 4 layers without the atmosphere. To compare with model **V**, we used for the mantle the Andrade rheology and four viscosities η from 10^{19} to 10^{22} Pa.s. Fig. 2 (a) and Fig. 2 (b) show the real part (i.e. k_2^r) and the imaginary part (i.e. k_2^i) of k_2, respectively. Their associated quality factor Q is calculated as

$$Q^{-1} = \frac{k_2^i}{\|k_2\|}, \tag{2}$$

with $\|k_2\| = \sqrt{{k_2^r}^2 + {k_2^i}^2}$ and is shown on Fig. 2 (c) and (d). The variation of α in [10] is between 0.2 and 0.3. The range of values obtained in their work is represented as vertical lines on Fig. 2. For the real part k_2^r and for α between 0.2 and 0.3, the maximum difference between our results and those of [10] are between 1.8% to 2% depending on the mantle viscosity. These differences are consistent with the one obtained by [35] when comparing different methods to calculate the LN for a Heaviside step function.

Furthermore, as one can see on Fig. 2 (a), the results for k_2^r for $\alpha \in [0.2, 0.4]$ [29] (corresponding to olivine-rich rocks) fall into the range of the most recently estimated value from the data of Magellan and PVO, therefore denoted by k_2^{MPVO}, with a ± 2-σ uncertainty. For each mantle viscosity, the maximum difference in the values of k_2^r we obtain for this range of α is decreasing with increasing mantle viscosity.

The imaginary part k_2^i (see Fig. 2 (b)), for $\eta \geq 10^{20}$ Pa.s, is different between 1% and 2.16% from our estimates and the ones of [10] depending on α. Nonetheless, for $\eta = 10^{19}$ Pa.s, the peak of the curve falls in the range of $\alpha \in [0.2, 0.3]$. This is the main difference between the two results, since the range of variations between the minimum and maximum for the considered α range values is smaller than that of [10]. The quality factor Q is illustrated on Fig. 2 (c) and (d). One can see on these figures that its span (upper and lower boundaries) for $\alpha \in [0.2, 0.3]$ is almost the same for each viscosity.

Finally, we expand the viscosity range of the mantle from the previous range of 10^{19}, 10^{20}, 10^{21} and 10^{22} Pa.s to a complete variation from the elastic limit ($\eta \to 10^{31}$ Pa.s) to the fluid one ($\eta \to 0$ Pa.s) for $\alpha = 0.3$. Fig. 3 shows the real k_2 as a function of the mantle viscosity. The red dashed line illustrates the range of the observed k_2 with the Magellan and PVO 2-σ uncertainty. One can see that for $\eta > 10^{18}$ Pa.s the value of k_2 fits well into the observed range. This is consistent with the choice of the mantle viscosity range of [10], also used in our study for the comparison.

2.3. Sensitivity to rheologies

A comparison between the Andrade and the Maxwell rheologies is performed in order to assess the model (and more specifically the quality factor) sensitivity to the rheologies. Fig. 4 shows the results of k_2^r, k_2^i and Q for different mantle viscosities η in Pa.s.

On Fig. 4 (a), one can see that k_2^r is decreasing with increasing α, for each of the explored mantle viscosities. They also approach the results for a Maxwell mantle with higher α values, which is also the case for k_2^i (see Fig. 4 (b)). The quality factor, plotted on Fig. 4 (c) and (d), is sensitive to the mantle viscosity η for both Maxwell and Andrade rheologies. However, when Q computed with the Andrade rheology remains in the expected interval of $20 < Q < 100$ [15], the value of Q obtained with the Maxwell rheology reaches far bigger values (from 100 with a low viscosity of 10^{19} Pa.s to 100 000 for a viscosity of 10^{22} Pa.s). Moreover, regarding the Andrade rheology, only Q estimated with $\alpha < 0.3$ are smaller than 100 for all considered viscosities.

These results are in agreement with the other studies [10, 29] which suggest that an Andrade rheological law is a better choice to mimic the attenuation behavior of planetary rocks at tidal periods [10, 36].

2.4. Influence of the atmosphere

Finally, we test the effect of the dense Venus atmosphere on the global tidal deformation of the planet. A model of the atmosphere is added as a viscous layer on top of the surface. The TLN k_2 with the atmosphere is calculated with ALMA[3] on top of the shallowest layer, which is the atmosphere. The model of the atmosphere is taken from the Venus International Reference Atmosphere [37]. The atmosphere has a thickness of 100 km, a density $\rho_{atmo} = 36.5$ kg.m^{-3} and no rigidity ($\mu_{atmo} = 0$ Pa) . The viscosity of the atmosphere is fixed to 10^{-5} Pa.s for each computation. Fig. 5 shows the variations (in %) of the k_2^r, k_2^i and Q when we include the effect of the atmosphere. We can see that the atmosphere induces a decrease of the real and imaginary parts of k_2 at a maximum level of respectively 7.2% and 8.34% (Fig. 5 (a) and (b)). The former percentage of 7.2% is equivalent to a decrease in k_2^r of a maximum of 0.026 which is lower than the 1-σ uncertainty of PVO. The variation depends slightly on the value of α and the mantle viscosity. The effect on quality factor Q (see Fig. 5 (c)) is only of a maximum of +1.65%. We then conclude that the atmosphere does affect the studied parameters but not outside the $\pm$2-σ of the observed k_2, despite its high density and low viscosity.

3. Monte Carlo exploration

Based on the previous comparisons, we extend the space of parameters to explore (thicknesses of the layers but also their densities and viscosities) in order to build profiles for the internal structure of Venus that match with the present geophysical constraints. These constraints are the total mass of Venus, its moment of inertia, the TLN k_2 and the planet quality factor Q.

3.1. geophysical constraints

The mean surface radius of Venus is set to $R_V = 6051.8 \pm 1$ km [38]. The total mass with its atmosphere is denoted by M_{V+a}. It is determined with its uncertainty from the gravitational constants G and GM_{V+a}. Using $G = (6.67430 \pm 0.00015) \times 10^{-11} \mathrm{m^3 kg^{-1} s^{-2}}$ [39] and $GM_{V+a} = 324858.592 \pm 0.006$ $\mathrm{km^3 s^{-2}}$ [40] we deduce M_{V+a}. The mass of the atmosphere equals to 4.77×10^{20} kg [41] is therefore subtracted to obtain the mass M_V without the atmosphere as given on Table 1. Several parameters of Venus are used to constrain its interior in addition to its mass without the atmosphere. These parameters are the normalized moment of inertia $\tilde{C} = C/M_V R_V^2$ (hereafter MoI) [42], such that C is its polar moment of inertia and its observed TLN k_2 shown on Table 1. Finally we also consider the possible values for the quality factor Q at 58 days as given by [15]. Table 1 gathers these state-of-the-art constants that are used as constraints for this work.

3.2. Method

As explained in Sect. 2.1, to compute the tidal deformation of the planet and then to compare the TLN and quality factor to the state-of-the-art val-

Table 1: Venus state-of-the-art geophysical constraints. The mass M_V is without the atmosphere.

Constant	Value	± 1-σ	References
R_V (km)	6051.8	1	[38]
M_V ($\times 10^{24}$kg)	4.8673	1.1×10^{-4}	-
MoI	0.337	0.024	[42]
k_2	0.295	0.033	[8]
Q	$20 < Q < 100$		[15]

ues, a discretized description of the Venus internal structure in terms of profiles of density, rigidity and viscosity is requested, considering different possible rheologies (Newton, Andrade or Maxwell). The aim of this work is to explore the space of these internal structure parameters (ISP) by using the geophysical constraints given in Sect. 3.1 as references for filtering acceptable combinations of ISP.

Three types of profiles are considered: the **Class 1** is constituted with an elastic crust, two visco-elastic layers for the mantle and an inviscid fluid core, the **Class 2** has a solid core instead of an inviscid fluid core and the **Class 3** has both a solid inner core and a fluid outer core. We also impose no density inversion in the profiles but we allow equal densities for successive layers. This leaves the algorithm free to propose 3-layer models with either the same characteristics for the upper and the lower mantle or for the crust and upper mantle layer. But as one can see on Table 3, the probability of

3-layer models with the same upper and lower mantle is very weak and the probability of having an upper mantle with the same characteristics as the crust is ruled out by non negligeable upper mantle viscosities for all classes.

Finally the total mass of the planet is conserved in each model. To do so, the density of the innermost layer of each class is not randomly selected, but instead calculated from its random thickness and random densities and thicknesses of the other layers. Consequently, the densities of the fluid core for **Class 1**, of the solid core for **Class 2** and of the solid inner core for **Class 3** are not randomly sampled but deduced from the other layers.

For each class, the crustal thickness and density are both fixed to 60 km and 2950 kg.m^{-3} [43], respectively. As a consequence the upper mantle boundary is fixed to 5991.8 km. The thicknesses that vary are the ones of the lower mantle and the core. In contrast, the third class gets three layer radial boundaries that vary. The crustal thickness is constrained in [44] to be from 8 to 25 km. Testing the effect of the crustal thickness, we replace the original crustal thickness of 60 km in model V to 8 km. The effect on the real and imaginary parts of k_2 are 0.6% and 0.7%, respectively. In this work we uniformly explore the structural and rheological parameters in intervals given by Table 2. The fluid core of **Class 1** is assumed to be an inviscid fluid therefore its viscosity is fixed to $\eta = 0$ Pa.s. The viscosity of the fluid outer core of **Class 3** can not be set to be an inviscid fluid (zero viscosity), therefore it is set to be a fluid with an arbitrary low viscosity (here 10^{-5} Pa.s). For the solid layers (the mantle layers for all classes, the core for **Class 2** and the inner core for **Class 3**), we consider an Andrade rheology

with $\alpha = 1/3$ [45]. The rigidities are fixed for each layer and are equal to the values corresponding to the rigidity profile given on Fig. 1 and on Table 2. Ultimately, we select models according to the constraints mentioned in Sect. 3.1 considering a 3-σ interval for the mass and TLN k_2, a 1-σ interval for the MoI and the range specified in Tab. 1 for the 58-day quality factor Q.

Table 2: Venus internal parameters, both fixed and simulated with random Monte-Carlo within their respective range.Values indicated with a star are fixed values and values marked with a dagger are deduced as explained in Sect. 3.2.

	R (km)	ρ (kg.m^{-3})	η (log10 (Pa.s))	μ (GPa)
Crust	6051.8*	2950*	∞	47.65*
Upper mantle	5991.9*	1000-15000	15-25	85.7
Lower mantle	2000-5900	3000-15000	15-25	196.94
Fluid core (**Class 1**)	1000-5000	7000-22000†	$-\infty$*	0*
Solid core (**Class 2**)	1000-5000	6000-22000†	11-22	125.63
Outer core (**Class 3**)	1000-5000	1000-15000	-5*	0*
Inner core (**Class 3**)	1-5000	5000-30000†	10-20	273.91

4. Results

65000 models have been produced by varying the thickness, density and viscosity for the different layers. After a first filtering with MoI $\pm$ 1-σ, we retain between 54.5 and 68% of the 65000 models which correspond to 35472, 35443 and 44390 models for **Class 1**, **Class 2** and **Class 3**, respectively. A second filtering considering the TLN results in 13077, 16172 and 9944 models for **Class 1**, **Class 2** and **Class 3**, respectively. Finally the quality factor Q filter is performed resulting in 4703, 4536 and 4160 selected models. To test whether the number of models simulated are enough, we tested subsets of the original 65000 models. The randomly chosen subsets of models consist increasingly of 650 to 65000 models. After filtering with the MoI, k_2 and Q filters we illustrate (see Fig. B1) in Appendix B the percentage of selected models after several filters for **Class 1** as an example. In Appendix A, are given the results when the quality factor Q is not used as a constraint. Table 3 gives the statistics of the selected models namely the mean and the first and third quartiles of the parameters that have been randomly sampled and selected according to our method.

4.1. ***Class 1****: only a fluid core*

The models of **Class 1** include a mantle with two separated layers (upper and lower), to reproduce the Earth structure, and an inviscid fluid core. From our simulations, it appears that when only a fluid core is present, the lower mantle (1839^{2232}_{1418} km) is significantly thicker than the upper mantle (963^{1417}_{600} km) with a higher density (4890^{5360}_{4484} versus 3765^{4123}_{3446} kg.m^{-3}) and a

Table 3: Results of the selection process over 65000 randomly sampled profiles. Are given in Column 1, the type of models considered and on Column 2 the layers. Column 3 gives the mean and first and third quartiles (25% and 75%) of the layer thicknesses (km), Column 4 the densities (kg.m^{-3}) and Column 5 the viscosities in log10(Pa.s).

Models	Layers	thickness (km)	density (kg.m^{-3})	viscosity log10 (Pa.s)
Fluid (**Class 1**)	upper mantle	963^{1417}_{600}	3765^{4123}_{3446}	$19.9^{22.3}_{18.3}$
	lower mantle	1839^{2232}_{1418}	4890^{5360}_{4484}	$20.78^{21.85}_{19.85}$
	core	3166^{3372}_{2898}	10899^{11909}_{9892}	-5
Solid (**Class 2A**)	upper mantle	1432^{1996}_{883}	3987^{4306}_{3619}	$20.95^{23.48}_{19}$
	lower mantle	1313^{2007}_{715}	5057^{5561}_{4612}	$21^{22.85}_{19.95}$
	core	3240^{3460}_{2944}	10527^{11713}_{9373}	$14.95^{19.48}_{13.4}$
Solid (**Class 2B**)	upper mantle	1052^{1275}_{773}	3562^{3844}_{3275}	$20.85^{22.9}_{18.95}$
	lower mantle	410^{689}_{220}	4719^{5277}_{4188}	$20.9^{23.48}_{18.95}$
	core	4502^{4702}_{4257}	7209^{7597}_{6917}	$20.7^{21}_{19.85}$
Fluid/Solid (**Class 3**)	upper mantle	925^{2099}_{585}	3722^{4010}_{3377}	$20^{22.6}_{18.3}$
	lower mantle	1718^{2099}_{1330}	4932^{5369}_{4431}	$21.48^{22.78}_{20.54}$
	outer core[17]	381^{712}_{159}	8204^{9900}_{6723}	-5
	inner core	2825^{3141}_{2402}	11450^{12220}_{10425}	$15.7^{17.81}_{12.95}$

significantly higher viscosity ($20.78^{21.85}_{19.85}$ and $19.9^{22.3}_{18.3}$ log10(Pa.s)). The higher lower mantle density is a result of the assumption of no density inversion in each model. This assumption is also driven by the fact that an increased density from the surface to the center of the planet can be obtained by integrating its pressure equations. These significant differences between the lower and the upper mantles stress the dichotomy of state and nature of these two layers. Furthermore, the distribution of the ratio between the lower and the upper mantle viscosities (Table 4 and Fig. 6) show two trends of models: the first trend has a peak of distribution for $\eta_{\rm LM}/\eta_{\rm UM} \approx 0.9$ and the second trend has a peak of distribution for $\eta_{\rm LM}/\eta_{\rm UM} \approx 1.1$. Fig. 6 also shows that we have slightly more models with a more viscous lower mantle since the mean (second quartile) of the histogram is for $\eta_{\rm LM}/\eta_{\rm UM} > 1$. It is unexpected since the lower mantle is expected to be less viscous than the upper mantle by the Arrhenius law [46]. The result is based on the selection of models with geophysical constraints and statistical study with minimal initial assumptions on the chemical content or temperature profile of Venus. Table 4 gives the results in terms of χ^2 for two adjustments of the viscosity ratio distribution considering a bi-modal and a Gaussian profiles. The bi-modal model gives a better χ^2 than the Gaussian profile (0.91 versus 1.5), favoring a double distribution of the upper and lower viscosity ratios: one centered around 0.87 ± 0.058 (with a more viscous upper mantle) and one around 1.13 ± 0.19 (with a more viscous lower mantle). The possible entanglement of the lower and upper mantle viscosities is even more visible on the 2-D histograms shown on Fig. 7. On this Figure, one can see that a more viscous

lower mantle relates to a more fluid upper mantle and vice versa, unless the two layers have similar viscosities. Models with the same viscosity (between 10^{19} and 10^{21} Pa.s) for both the lower and the upper mantles represent about 1% of the models. Fig. 7 (c) also shows that the lower and upper mantles can not be both more fluid ($\eta_{\rm LM} < 10^{19.5}$ Pa.s and $\eta_{\rm UM} < 10^{19}$ Pa.s) or more viscous ($\eta_{\rm LM} > 10^{21.8}$ Pa.s and $\eta_{\rm UM} > 10^{21}$ Pa.s).

Finally, the distribution of the thicknesses of the lower and upper mantle (Fig. 7 (a)) shows a direct correlation, expected for a terrestrial planet as Venus. Moreover, the density of the fluid core that we obtain (10899^{11909}_{9892} kg.m^{-3}) is consistent with what is expected for a planet of the size of Venus composed by iron alloys [9].

4.2. ***Class 2:*** *only a solid core*

The models of **Class 2** include a mantle with two separated layers, as for the models of **Class 1**, and a solid visco-elastic core following an Andrade rheology, similar to the one of the mantle, with a rigidity of 125.63 GPa (see Appendix B for the impact of the fixed rigidity on the results).

Fig. 8 shows the histogram of the selected thicknesses for the solid inner core. Two families of models are distinguished: one with a large core of about 4500 km and one with a small core of about 3235 km. Fitting the thickness of the core with a Gaussian and with a bi-modal distributions gives values of χ^2 of 2.47 and 0.94, respectively. Therefore the two families have been defined in fitting a bi-modal distribution of the thicknesses and in separating the two distributions at 92% of the two populations. The

two families, labelled **Class 2A** and **Class 2B** on Table 3 and Fig. 8, are considered separately in the analysis. As expected, the bigger core (**Class 2B**) which is 4499^{4699}_{4244} km thick presents a lower density 7215^{7611}_{6924} kg.m^{-3}, favoring a scenario of a core enriched in light elements. This low density core is also associated with a significantly higher viscosity ($20.7^{21}_{19.85}$ log10(Pa.s)) in comparison with models of **Class 2A** that have a smaller core (3235^{3453}_{2940} km thick) and a lower viscosity ($14.95^{19.44}_{13.35}$ log10(Pa.s)).

Thicknesses and densities (10533^{11723}_{9376} kg.m^{-3}) of the core for models of **Class 2A** are consistent with those of **Class 1** and are in the expected range for a planet of the size of Venus. On Table 4, one can see that, also for **Class 2**, the bi-modal distribution of the upper and lower mantle viscosity contrast is also validated (χ^2 of 0.97 for bi-modal versus 1.42 for Gaussian).

However, it is not so clearly the case when we separately consider the two sub-classes **2A** and **2B**. In particular, for the family with the biggest core (**Class 2B**), the contrast of viscosities between the upper and the lower mantles as presented on Table 4 is not present and the single Gaussian distribution centered on the equal viscosity for upper and lower layers gives a better χ^2 (1.2) than the bi-modal distribution (2.58). At the opposite, as one can see on Table 4, the models of the **Class 2A** favor a bi-modal distributions of the viscosities (χ^2 bi-modal equals to 1.22 where χ^2 Gaussian is equal to 1.7).

*4.3. **Class 3**: fluid outer core and solid inner core*

On Table 4, **Class 3** also shows a bi-modal distribution of the viscosity

Table 4: Gaussian and bi-modal distributions of the ratio between viscosities of the lower mantle and the viscosities of the upper mantle (viscosity contrast) for the different classes of models. Are given in Columns 2, 5 and 7, the centroids M, M_1 and M_2, in Columns 3, 6 and 8, the uncertainties σ, σ_1 and σ_2 and in Columns 4 and 9, the χ^2 of the each fit.

	Gaussian distribution			**Bi-modal distribution**				
	M	σ	χ^2	M_1	σ_1	M_2	σ_2	χ^2
Class 1	0.99	0.26	1.5	0.87	0.058	1.13	0.19	0.91
Class 2	1	0.19	1.42	0.9	0.11	1.1	0.16	0.97
Class 2A	1	0.18	1.7	0.88	0.09	1.07	0.17	1.22
Class 2B	1	0.2	1.2	0.97	0.16	1.26	0.09	2.58
Class 3	1.03	0.21	1.42	0.96	0.12	1.25	0.13	1.2

ratio of upper and lower layers of the mantle (χ^2 for bi-modal distribution of 1.2 versus 1.42 for Gaussian) but with a shift of the centroids towards higher ratios. Indeed, where for **Class 1**, the modes were centered on 0.87± 0.058 and 1.13 ± 0.19 (marginally compatible with 1), the first mode of **Class 3** is marginally compatible with a center at 1 (0.96± 0.12) and the second mode is centered on 1.25 ± 0.13. In addition, Table 3 shows that the viscosities of the lower mantle increased in comparison to the viscosity of the same layer for models of **Class 1** ($20.78^{21.85}_{19.85}$ versus $21.48^{22.78}_{20.6}$ log10(Pa.s)) when

the viscosities of **Class 1** and **Class 3** remain identical for the upper layer. The densities of the two layers increase marginally for **Class 3** relatively to **Class 1** but not significantly. The mechanism of the increase of the lower mantle viscosity induced by the introduction of the solid inner core is then confirmed by the results presented on Tables 3 and 4. In terms of core densities, they are high both for the solid inner core (11450^{12220}_{10450} kg.m^{-3}) and for the fluid outer core (8276^{9912}_{6723} kg.m^{-3}). They are in average compatible with the densities of **Class 1** and **Class 2A**. Finally, when for the fluid core, the viscosity remains close to a low value, the viscosity of the inner core is obtained to be also quite small ($15.6^{17.78}_{12.95}$ log10(Pa.s)) for the **Class 3** but compatible with the value found for **Class 2A**.

5. Discussion

We compare our results with previous studies such as the one of [10] and [9] which constructed a scaled model of the density of Venus as a function of depth using the density profile of PREM [26]. Both studies consider a Venus model with a fluid core and a mantle divided into a lower and an upper layer, as the Earth. These profiles are then comparable with models of **Class 1** as defined in Sect. 4.1, except that there is no viscosity contrast in between the two mantle layers in [10]. As one can see from Fig. 9, our **Class 1** models are in good agreement with the limits extracted from [10] model V and [9] (illustrated respectively with red and green vertical lines). Moreover, we agree on the [10] conclusion that a solid core with a high density is mostly likely to be associated with a low viscosity. This case corresponds

to the models of our **Class 2A** with a density for the solid core not smaller than 9376 kg.m^{-3} and a viscosity not greater than $10^{19.5}$ Pa.s. We also agree that the probability of having a $k_2 < 0.25$ is of about 90 % with a solid core (**Class 2**) but only of 18 % and 6 % with a fluid core or a solid inner core and a fluid outer core, respectively (see Fig. 10). This result stresses that the k_2 value is indeed a good marker of the core state. Figs. 11, 12 and 13, obtained with [47], show the relation between the real part of k_2, MoI and mass for each of the **Classes 1**, **2** and **3**, respectively . The mean value of the geophysical constraints of k_2, MoI and mass are 0.295, 0.337 and 4.8673×10^{24} kg respectively (see Table 1) and are illustrated in red, black and green. These Figures show that the model distribution is centered around the mean mass. The models of **Class 1** are 55.8% higher and 44.17% lower than the MoI mean (see 13. These values are respectively 72.39% and 27.6% for **Class 2** (see Fig. 12) and 49.16% and 50.83% for **Class 3** (see Fig. 13). Additionally 59.57% of the models of **Class 2** have a MoI higher and a k_2 respectively higher and lower than the mean estimated value from Table 1 (see Fig. 12). Therefore a better estimation of the MoI of Venus, additionally to k_2, will better constrain the core structure between a totally solid state and a partially or totally fluid one as the conclusion made with k_2 (see Fig. 10).

We finally compare the density estimates from our classes of models with the end-members of the [10] density profiles for hot and cold temperature mantle hypothesis (Fig. 14). We obtain that the density of the lower and the upper mantles match with [10] profiles within the 2-σ error bars, except for

models of **Class 2B** which have a core density completely out the range from [10] profiles (green dot). Regarding the density of the cores, our estimates appear to be slightly higher than the one from [10], except for the fluid outer core of models of **Class 3** (including also a solid inner core), which seems to match well with the profiles of [10]. So despite the fact that our models favor a viscosity contrast between the two mantle layers (as discussed in Sect. 4), upper and lower mantle densities from all our models match well with that of [10]. It is not the case for the core densities which are significantly higher than the one of [10] for the solid inner core, the fluid core and the solid core. Beside, our densities agree with the [48] S-free density profiles (Fig. 14). Fig. 14 shows the densities obtained in this work as a function of the relative radius (R) with respect to the Earth radius (RE) and compared with the density profiles from [48] for the three core compositions (S-free, Nominal-S and S-rich).

[48] studied also different structure models of Venus based on the equations of state evolution for different hypothesis of core compositions: without sulfur (S-free, with 0 wt%), with the same amount of sulfur as the Earth (Nominal-S, with 4.6-7.6 wt%) and with more sulfur than the Earth (S-Rich, with 9.1-22 wt%). They also make the hypothesis of a core segregation happening as a single-stage event. Their estimated MoI values are encompassed in the 1-σ uncertainty of [42] and they considered two different patterns of model: those with low MoI values (generally smaller than 0.323) representing models within the 1% lowest possible values of MoI and those with high MoI (generally greater than 0.323) gathering models within the 1% highest

possible values of MoI. In their cases, low or high MoI could indicate different rates of oxygen fugacity in the Venus mantle. In order to make meaningful comparisons, we consider two subcategories of our models according to their MoI values using the same MoI intervals as in [48]. More than 57% of our models included in the [48] Low and High MoI intervals belong to the High MoI models when only 13% of our models belong to the Low MoI type of models. 30% of the rest of our results have either smaller or higher values for the MoI. From Fig. 14, we can see that there is a good consistency between our densities and [48] results for the three compositions, except for the **Class 2B** set of models which appears to be outside [48] ranges. The inner core, the outer core and the lower mantle densities obtained for 5 or 4 layers with solid or fluid cores are encompassed in the intervals proposed by [48] without considering MoI discrimination. For the upper mantle (above 0.8 Earth radius), our estimations appear to be slightly larger. However, [48] consider the upper mantle and the crust as a single layer while we consider two different layers.

The radius and density of the upper mantle obtained in this work are about 5968 km and 3765 kg.m^{-3}, respectively. The radius of the lower mantle is about 5005 km. In averaging the upper mantle with the crust which has a fixed density of 2950 kg.m^{-3}, we obtain a crust+upper mantle density of about 3688 kg.m^{-3}, closer to the value expected by [48]. We consider the same MoI subcategories as the one proposed in [48], and as one can see on Fig. 15 where the densities are plotted versus the relative depth for models presenting Low MoI at the bottom and models having High MoI at the top,

the same conclusions remain for the Low MoI case. For models with High MoIs (gathering more than 57% of our models), we see a better consistency between our estimates and the S-free and the Nominal S profiles. In particular, on the bottom side panel of Fig. 15, the **Class 3** inner core density and the **Class 1** and **Class 2A** core densities are significantly different from the one expected with a S-rich profile, whereas they are statistically consistent at 2-σ with the nominal-S profile and totally encompassed in the S-free profile.

One way to model the temperature dependence of the viscosity is to use the Arrhenius law. [46] shows that the viscosity of a material can be expressed as an exponential function of temperature, in other words as an Arrhenius-type function. Based on this fact, [49, 50] deduced an expression of the temperature which is highly dependent on the viscosity. Eq. 3 is reformulated from equation 2 of [51] which is deduced from the work of [49, 50]. As explained in [51], it is possible if one assumes the temperature T_u and the viscosity η_u of the upper mantle layer to deduce the temperature of the lower layer, T_l, by considering the following relation:

$$T_l = \frac{H_l^* T_u}{H_u^* + T_u R_g ln(\frac{\eta_l}{\eta_u})} \tag{3}$$

where η_l is the lower mantle viscosity, η_u is the upper mantle viscosity, H_l^* and H_u^* are the activation enthalpy for the lower and the upper mantle respectively and R_g is the gas constant. Therefore we calculate the temperature of the lower mantle from the deduced viscosities. From the mantle parameters (temperature, density thickness and viscosity) we obtain a Rayleigh number much higher than the critical value, therefore the mantle in convective. This

result justifies the use of Eq. 3 for convective layers [51]. Using Eq. 3, we estimate the temperature of the lower mantle from the viscosity contrast between the upper and the lower mantle layers for each class of models. They are shown on Fig. 16. We assume for this an upper mantle temperature of 1600 K as given by the [48] temperature profile reproduced on Fig. 16. The activation enthalpy values (H^*) are taken equivalent to those given for the Earth (240 kJ.mol^{-1} for the upper mantle and 430 kJ.mol^{-1} for the lower mantle) as in [52]. We consider values of the upper mantle viscosities given by Table 3 for the different models. We then obtain values plotted on Fig. 16. The errorbars in x-axis correspond to 2-σ uncertainties given in Table 3 and the errorbars in y-axis correspond to uncertainties deduced from Table 3 upper mantle viscosities. From these estimations, we see that our models seem to propose a slightly hotter, but still statistically consistent, lower mantle temperature in comparison with [48] with or without MoI subcategories (see Figs. 16 and 18). The lower mantle temperatures deduced from our approach are also consistent with the temperature profiles from [43] and [53] as one can see on Fig. 16. These two reference profiles give two possible extrema of temperature evolution with depth: a cold one from [43] (Venus scaled adiabatic profile) and a hot one from [53] (thermo-chemical Venus evolution). Our temperature for the lower mantle is compatible at 2-σ with the two hot and cold profiles but suggests an even hotter temperature than [53].

The radii of the different layers considered in this work and in [48] are shown on Fig. 17. As in [48], we consider two regimes of models according

to MoI values: high MoI (greater than 0.323) and with low MoI (smaller than 0.323). The upper mantle is not consider here as it is supposed to be fixed in [48]. With these comparisons, it appears that the **Class 2B** (models with a big core and a low density) is not consistent with [48]. This class was already pointed as an outlier of our selection (see discussion of Sect. 4.2) and gathers models with no viscosity contrast between the upper mantle and the lower mantle. For models with high MoI (lower row of Fig. 17), there is a clear trend from our models to be more consistent with S-free models from [48] than with Nominal-S or S-rich models, especially for the **Class 3**. It is particularly clear with the radius of the inner core for which **Class 3** value (2841^{3129}_{2494} km) is consistent with that of S-free (from 0 to 3180 km) but not with that of Nominal-S (from 0 to 2380 km) or S-rich (from 0 to 750 km). For the lower mantle and the outer core radii for models of **Class 3** but also of **Class 1** and **Class 2B**, our values match well with all the models of [48]. For models with low MoI (upper row of Fig. 17), all our models but those of **Class 2B** are consistent with the models of [48]. The comparisons between the densities estimated in this former work and ours, presented previously, also pointed out, especially for high MoI models (representing more than 57% of our results), the same trend of our models to be more consistent with S-free profiles than with S-rich.

Finally, regarding the core, the **Class 2B** models presenting a very big core (of about 73% of the total size of the planet) but with a low density (7215 kg.m^{-3}) and presenting no contrast in mantle layer viscosities, is not

compatible with [48] and [10].

6. Conclusion

In this work, we have used state-of-the-art geophysical constraints of Venus (mass, total MoI, Love number k_2 and quality factor Q) to infer possible internal structure of the planet. Therefore we aim at constraining the internal structure of Venus with minimal assumptions about its chemical content. We adapted the deformation semi-analytical modeling of the ALMA^3 open-source Fortran 90 program [16] originally designed for studying the loading deformations of the Earth [17], to the case of the tidal deformation of Venus.

For one given set of parameters extracted from [10] (model V), we first demonstrate that our model leads to similar results in terms of real and imaginary Love numbers, consistent values of the Andrade rheology α parameter of the Venus mantle and consistent intervals of the mantle viscosities when this latter is supposed to be homogeneous. We then randomly sample the parameter space of the possible internal structure profiles, in varying the thicknesses, the densities and the viscosities of 4 or 5 layer profiles. Each layer is assumed to be homogeneous therefore having averaged values of parameters (density, rigidity and viscosity). We only consider models that induce geophysical quantities consistent with the state-of-the-art constraints given on Table 1. Over 65000 models produced randomly, remain about 18000 models with 23% of them being 5 layer models (with a solid inner core and a fluid outer core) and 77% having either a fluid (38 %) or a solid core (39

%). We assume incompressible models, which is in the theoretical basis of ALMA[3], with layer-fixed rigidity. The existence of the Venus inner core is not clearly demonstrated from our results but we show that the existence of a solid core cannot be ruled out by only considering geophysical constraints. Moreover, an interesting pattern in our models is the contrast of viscosities in the mantle. Indeed as it has been discussed in Sect. 5, only 1 % of our 4 and 5-layer models have the same viscosity for the lower and the upper mantle, inducing significant viscosity contrasts between the two layers. Significant differences in densities and thicknesses for these two layers also stress the non-homogeneity of the Venus mantle.

Furthermore, as one can see on Fig. 16, the viscosity contrasts are also an indication of a change in the temperature profile in the Venus mantle, with a lower mantle hotter (with a minimum of 1800 K) than the upper mantle (fixed at 1600 K). These lower mantle temperatures are also hotter (but still in agreement at 2-σ) than the temperatures proposed by [48], [43] and [53].

The comparisons with [48] also indicate a trend of our models towards S-free Venus models (considering the density or the radius comparisons). Such types of models with a very low percentage of sulfur are in agreement with the past literature [32, 54]. They also ruled out the only class of models (**Class 2B**) proposing mantle layers without viscosity contrast.

The differences in viscosities are a marker of differences in temperatures for the planetary mantles. This type of indication of temperature differences can be used as a tool for understanding the thermal evolution of the body. With a stagnant lid, the core heat is not evacuated and maintains the mantle

into higher temperatures closer to the core. This could explain the non existence of plate tectonics on Venus and the existence of plumes from the hotter regions of the mantle towards the ductile crust crossing cooler mantle regions.

Finally, for the future missions towards Venus, we confirm that the determination of a very accurate k_2 TLN will be a key for deciphering the state of the Venus core with 90% probability that a low k_2 ($k_2 < 0.25$) will indicate a solid unique core with a density compatible with an iron alloy (not less than 9000 kg.m^{-3}) and a low viscosity (of about 10^{15} Pa.s). We stress, at last, that these results rely on an interval for the quality factor Q. The one used in this work is based on the range deduced from previous models and realistic assumptions as no direct measurement of the tidal dissipation has been done so far for Venus. Such an estimation will be an important outcome of future space missions.

Acknowledgments

The authors thank Giorgio Spada and Daniele Melini for providing the ALMA^3 program as well as many constructive discussions. The authors also gratefully acknowledge the cooperation of Caroline Dumoulin in this work and the engaging conversations with Nicolas Coltice. This work was supported by the "Programme National de Gravitation, Références, Astronomie, Métrologie" (PN-GRAM) of CNRS/INSU co-funded by CEA and CNES.

References

[1] S. E. Smrekar, E. R. Stofan, N. Mueller, A. Treiman, L. Elkins-Tanton, J. Helbert, G. Piccioni, P. Drossart, Recent Hotspot Volcanism on Venus from VIRTIS Emissivity Data, Science 328 (5978) (2010) 605. doi:10.1126/science.1186785.

[2] E. V. Shalygin, W. J. Markiewicz, A. T. Basilevsky, D. V. Titov, N. I. Ignatiev, J. W. Head, Active volcanism on Venus in the Ganiki Chasma rift zone, grl 42 (12) (2015) 4762–4769. doi:10.1002/2015GL064088.

[3] D. Bercovici, Y. Ricard, Plate tectonics, damage and inheritance, Nature 508 (7497) (2014) 513–516. doi:10.1038/nature13072.
URL `https://doi.org/10.1038/nature13072`

[4] F. Crameri, B. Kaus, Parameters that control lithospheric-scale thermal localization on terrestrial planets, Geophysical Research Letters - GEOPHYS RES LETT 37 (05 2010). doi:10.1029/2010GL042921.

[5] R. Ghail, C. Wilson, T. Widemann, L. Bruzzone, C. Dumoulin, J. Helbert, R. Herrick, E. Marcq, P. Mason, P. Rosenblatt, A. C. Vandaele, L. J. Burtz, Envision: understanding why our most earth-like neighbour is so different, arXiv:1703.09010v1 [astro-ph.EP] (2017).

[6] S. E. Smrekar, S. Hensley, M. Dyar, D. Nunes, J. Whitten, J. Helbert, L. Iess, M. Erwan, VERITAS (Venus Emissivity, Radio science, InSAR, Topography, And Spectroscopy): Discovering the Secrets of a Lost Hab-

itable World, in: AGU Fall Meeting Abstracts, Vol. 2021, 2021, pp. P34B–01.

[7] A. E. H. Love, The yielding of the earth to disturbing forces, Proceedings of the Royal Society of London. Series A, Containing Papers of a Mathematical and Physical Character 82 (551) (1909) 73–88.

[8] A. S. Konopliv, C. F. Yoder, Venusian k2 tidal love number from magellan and pvo tracking data, Geophys. Res. Lett. 23, 1857–1860 (1996).

[9] A. Aitta, Venus' internal structure, temperature and core composition, Icarus 218, 967-974, doi: 10.1016/j.icarus.2012.01.007 (2012).

[10] C. Dumoulin, G. Tobie, O. Verhoeven, P. Rosenblatt, N. Rambaux, Tidal constraints on the interior of venus: Tidal constraints on venus' interior, J. Geophys. Res. Planets, 122, 1338-1352, doi: 10.1002/2016JE005249 (2017).

[11] C. Xiao, F. Li, J. Yan, M. Gregoire, W. Hao, Y. Harada, M. Ye, J.-P. Barriot, Possible deep structure and composition of venus with respect to the current knowledge from geodetic data, Journal of Geophysical Research: Planets 126 (7) (2021) e2019JE006243, e2019JE006243 2019JE006243. arXiv:https://agupubs.onlinelibrary.wiley.com/doi/pdf/10.1029/2019JE006243, doi:https://doi.org/10.1029/2019JE006243.
URL https://agupubs.onlinelibrary.wiley.com/doi/abs/10.1029/2019JE006243

[12] D. J. Stevenson, Planetary magnetic fields, Earth and Planetary Science Letters 208 (1) (2003) 1–11. doi:https://doi.org/10.1016/S0012-821X(02)01126-3.
URL https://www.sciencedirect.com/science/article/pii/S0012821X02011263

[13] C. Murray, S. Dermott, Solar System Dynamics, Cambridge University Press, 2000.
URL https://books.google.fr/books?id=-9FoswEACAAJ

[14] P. Goldreich, S. Soter, Q in the Solar System, icarus 5 (1) (1966) 375–389. doi:10.1016/0019-1035(66)90051-0.

[15] A. C. Correia, J. Laskar, O. N. de Surgy, Long-term evolution of the spin of venus: I. theory, Icarus 163 (1) (2003) 1–23. doi:https://doi.org/10.1016/S0019-1035(03)00042-3.
URL https://www.sciencedirect.com/science/article/pii/S0019103503000423

[16] D. Melini, C. Saliby, G. Spada, On computing viscoelastic Love numbers for general planetary models: the ALMA3 code, Geophysical Journal InternationalGgac263 (07 2022). arXiv:https://academic.oup.com/gji/advance-article-pdf/doi/10.1093/gji/ggac263/44588975/ggac263.pdf, doi:10.1093/gji/ggac263.
URL https://doi.org/10.1093/gji/ggac263

[17] G. Spada, Alma, a fortran program for computing the viscoelastic love

numbers of a spherically symmetric planet, Comput. Geosci. 34 (2008) 667–687.

[18] G. Spada, L. Boschi, Using the Post—Widder formula to compute the Earth's viscoelastic Love numbers, Geophysical Journal International 166 (1) (2006) 309–321. arXiv:https://academic.oup.com/gji/article-pdf/166/1/309/5884019/166-1-309.pdf, doi:10.1111/j.1365-246X.2006.02995.x.
URL https://doi.org/10.1111/j.1365-246X.2006.02995.x

[19] W. R. Peltier, The impulse response of a maxwell earth, Reviews of Geophysics 12 (4) (1974) 649–669. arXiv:https://agupubs.onlinelibrary.wiley.com/doi/pdf/10.1029/RG012i004p00649, doi:https://doi.org/10.1029/RG012i004p00649.
URL https://agupubs.onlinelibrary.wiley.com/doi/abs/10.1029/RG012i004p00649

[20] R. Sabadini, D. A. Yuen, E. Boschi, Polar wandering and the forced responses of a rotating, multilayered, viscoelastic planet, Journal of Geophysical Research: Solid Earth 87 (B4) (1982) 2885–2903.

[21] W. R. P. Patrick Wu, Viscous gravitational relaxation., Geophysical Journal International 70 (1982) 435–485.
URL https://doi.org/10.1111/j.1365-246X.1982.tb04976.x

[22] E. L. Post, Generalized differentiation, Transactions of the American Mathematical Society 32 (4) (1930) 723–781.

[23] D. V. Widder, The inversion of the laplace integral and the related moment problem, Transactions of the American Mathematical Society 36 (1) (1934) 107–200.

[24] Cottereau, L., Rambaux, N., Lebonnois, S., Souchay, J., The various contributions in venus rotation rate and lod, A&A 531 (2011) A45. doi:10.1051/0004-6361/201116606.
URL https://doi.org/10.1051/0004-6361/201116606

[25] A. Briaud, A. Fienga, D. Melini, N. Rambaux, A. Mémin, G. Spada, C. Saliby, H. Hussmann, A. Stark, Constraints on the Moon's Deep Interior from Tidal Deformation, in: LPI Contributions, Vol. 2678 of LPI Contributions, 2022, p. 1349.

[26] A. M. Dziewonski, D. L. Anderson, Preliminary reference earth model, Phys. Earth Plan. Int. 25:297-356. doi: 10.17611/DP/9991844 (1981).

[27] B. V. S. Project, Basaltic Volcanism on the Terrestrial Planets, Pergamon Press, New York, 1981.

[28] I. Jackson, J. D. Fitz Gerald, U. H. Faul, B. H. Tan, Grain-size-sensitive seismic wave attenuation in polycrystalline olivine, Journal of Geophysical Research: Solid Earth 107 (B12) (2002) ECV 5–1–ECV 5–16. arXiv:https://agupubs.onlinelibrary.wiley.com/doi/pdf/10.1029/2001JB001225, doi:10.1029/2001JB001225.
URL https://agupubs.onlinelibrary.wiley.com/doi/abs/10.1029/2001JB001225

[29] J. C. Castillo-Rogez, M. Efroimsky, V. Lainey, The tidal history of iapetus: Spin dynamics in the light of a refined dissipation model, Journal of Geophysical Research: Planets 116 (E9) (2011). arXiv:https://agupubs.onlinelibrary.wiley.com/doi/pdf/10.1029/2010JE003664, doi:10.1029/2010JE003664.
URL https://agupubs.onlinelibrary.wiley.com/doi/abs/10.1029/2010JE003664

[30] H. Takeuchi, M. Saito, Seismic surfaces waves., In: Bolt, B.A. (Ed.), Methods in Computational Physics, vol. 1. Academic Press, New York, pp. 217–295. (1950).

[31] A. Ringwood, D. L. Anderson, Earth and venus: A comparative study, Icarus 30 (2) (1977) 243–253. doi:https://doi.org/10.1016/0019-1035(77)90156-7.
URL https://www.sciencedirect.com/science/article/pii/0019103577901567

[32] J. S. Lewis, Metal/silicate fractionation in the solar system, Earth and Planetary Science Letters 15 (1972) 286–290.

[33] K. A. Goettel, J. A. Shields, D. A. Decker, Density constraints on the composition of Venus., Lunar and Planetary Science Conference Proceedings 12 (1982) 1507–1516.

[34] C. Dumoulin, Compressibility for model v, private communication (2020).

[35] G. Spada, V. R. Barletta, V. Klemann, R. E. M. Riva,

Z. Martinec, P. Gasperini, B. Lund, D. Wolf, L. L. A. Vermeersen, M. A. King, A benchmark study for glacial isostatic adjustment codes, Geophysical Journal International 185 (1) (2011) 106–132. arXiv:https://academic.oup.com/gji/article-pdf/185/1/106/1636052/185-1-106.pdf, doi:10.1111/j.1365-246X.2011.04952.x.
URL https://doi.org/10.1111/j.1365-246X.2011.04952.x

[36] A. Bagheri, A. Khan, D. Al-Attar, O. Crawford, D. Giardini, Tidal response of mars constrained from laboratory-based viscoelastic dissipation models and geophysical data, Journal of Geophysical Research: Planets 124 (11) (2019) 2703–2727. arXiv:https://agupubs.onlinelibrary.wiley.com/doi/pdf/10.1029/2019JE006015, doi:https://doi.org/10.1029/2019JE006015.
URL https://agupubs.onlinelibrary.wiley.com/doi/abs/10.1029/2019JE006015

[37] A. Seiff, J. T. Schofield, A. J. Kliore, F. W. Taylor, S. S. Limaye, H. E. Revercomb, L. A. Sromovsky, V. V. Kerzhanovich, V. I. Moroz, M. Y. Marov, Models of the structure of the atmosphere of Venus from the surface to 100 kilometers altitude, Advances in Space Research 5 (11) (1985) 3–58. doi:10.1016/0273-1177(85)90197-8.

[38] P. Rosenblatt, P.and Pinet, E. Thouvenot, Comparative hypsometric analysis of earth and venus., Geophys.Res.Lett.21,465–468. (1994).

[39] E. Tiesinga, P. J. Mohr, D. B. Newell, B. N. Taylor, Codata recom-

mended values of the fundamental physical constants: 2018, Rev. Mod. Phys. 93 (2021) 025010. doi:10.1103/RevModPhys.93.025010.
URL https://link.aps.org/doi/10.1103/RevModPhys.93.025010

[40] A. S. Konopliv, W. B. Bnerdt, W. L. Sjogren, Venus gravity: 180th degree and order model, Icarus 138: 3-18, doi: 10.1006/icar.1999.60860 (1999).

[41] F. W. Taylor, The atmospheres of terrestrial planets., Geophys. Surv. 7, 385–408. (1985).

[42] J.-L. Margot, D. B. Campbell, J. D. Giorgini, J. S. Jao, L. G. Snedeker, F. D. Ghigo, A. Bonsall, Spin state and moment of inertia of venus, Nature Astronomy 5 (2021) 676–683. doi:10.1038/s41550-021-01339-7.

[43] B. Steinberger, S. Werner, Deep versus shallow origin of gravity anomalies, topography and volcanism on earth, venus and mars, Icarus 207 (2010) 564–577. doi:10.1016/j.icarus.2009.12.025.

[44] P. B. James, M. T. Zuber, R. J. Phillips, Crustal thickness and support of topography on venus, Journal of Geophysical Research: Planets 118 (4) (2013) 859–875. arXiv:https://agupubs.onlinelibrary.wiley.com/doi/pdf/10.1029/2012JE004237, doi:https://doi.org/10.1029/2012JE004237.
URL https://agupubs.onlinelibrary.wiley.com/doi/abs/10.1029/2012JE004237

[45] F. Louchet, P. Duval, Andrade creep revisited, International Journal

of Materials Research - INT J MATER RES 100 (2009) 1433–1439. doi:10.3139/146.110189.

[46] M. B. Roller, Rheology of curing thermosets: A review, Polymer Engineering & Science 26 (6) (1986) 432–440. arXiv:https://onlinelibrary.wiley.com/doi/pdf/10.1002/pen.760260610, doi:https://doi.org/10.1002/pen.760260610.
URL https://onlinelibrary.wiley.com/doi/abs/10.1002/pen.760260610

[47] D. Foreman-Mackey, corner.py: Scatterplot matrices in python, The Journal of Open Source Software 1 (2) (2016) 24. doi:10.21105/joss.00024.
URL https://doi.org/10.21105/joss.00024

[48] O. Shah, R. Helled, Y. Alibert, K. Mezger, Possible chemical composition and interior structure models of venus inferred from numerical modelling, The Astrophysical Journal 926 (2) (2022) 217. doi:10.3847/1538-4357/ac410d.
URL https://doi.org/10.3847/1538-4357/ac410d

[49] S. Karato, P. Wu, Rheology of the upper mantle: A synthesis, Science 260 (5109) (1993) 771–778. arXiv:https://www.science.org/doi/pdf/10.1126/science.260.5109.771, doi:10.1126/science.260.5109.771.
URL https://www.science.org/doi/abs/10.1126/science.260.5109.771

[50] S. Karato, Contents, Cambridge University Press, 2008, pp. v–viii.

[51] M. Nakada, C. Iriguchi, S. Karato, The viscosity structure of the d ”layer of the earth's mantle inferred from the analysis of chandler wobble and tidal deformation, Physics of the Earth and Planetary Interiors 208 (2012) 11–24.

[52] T. Nakakuki, M. Tagawa, Y. Iwase, Dynamical mechanisms controlling formation and avalanche of a stagnant slab, Physics of the Earth and Planetary Interiors 183 (1) (2010) 309–320, special Issue on Deep Slab and Mantle Dynamics. doi:https://doi.org/10.1016/j.pepi.2010.02.003.
URL https://www.sciencedirect.com/science/article/pii/S0031920110000294

[53] M. Armann, P. J. Tackley, Simulating the thermochemical magmatic and tectonic evolution of venus's mantle and lithosphere: Two-dimensional models, Journal of Geophysical Research: Planets 117 (E12) (2012). arXiv:https://agupubs.onlinelibrary.wiley.com/doi/pdf/10.1029/2012JE004231, doi:https://doi.org/10.1029/2012JE004231.
URL https://agupubs.onlinelibrary.wiley.com/doi/abs/10.1029/2012JE004231

[54] R. Trønnes, M. Baron, K. Eigenmann, M. Guren, B. Heyn, A. Løken, C. Mohn, Core formation, mantle differentiation and core-mantle interaction within earth and the terrestrial planets, Tectonophysics 760 (2019) 165–198, linking Plate Tectonics and Volcanism to Deep Earth Dynamics – a tribute to Trond H. Torsvik. doi:https://doi.org/10.1016/j.tecto.2018.10.021.
URL https://www.sciencedirect.com/science/article/pii/S0040195118303494

Appendix A. Sensitivity to the value of dissipation

The results obtained in this work are driven by the interval of possible values for the quality factor Q. In this section, we show the selection of models without considering the Q filter. The original 65000 models of each class have been filtered with the mass, MoI and observed k_2 as used in this work. Therefore the difference between the original results (Table 3) and this section is the lack of the Q filter. The following Table A1 presents the results with this filter. Fig A1 shows the histograms of Q for each class with and without this filter. Without the quality factor Q filter set between 20 and 100, the Q values for **Classes 1**, **2** and **3** range in 2-1987, 2-1707, 2-1017 respectively (see Fig A1).

Table A1 shows that for **Class 1** the thicknesses Th_{Core}, Th_{LM} and Th_{UM} quartiles (25%, 50% and 75%,) vary from -0.82% to -0.52%, 2.64% to 3.5% and -4.56% to -1.72% respectively. The three layers respective densities quartiles (ρ_{Core}, ρ_{LM} and ρ_{UM}) vary from -0.52% to 0.17%, 0.25% to 0.58% and -0.81% to -0.23%. As for the viscosities of the lower mantle η_{LM} and the upper mantle η_{UM} vary from 0% to 4.81% and 1.63% to 4.77 respectively. Table A1 also shows that for **Class 2** the thicknesses quartiles of the layers, Th_{Core}, Th_{LM} and Th_{UM} vary respectively from -2.32% to 2.7%, -0.46% to 27.39% and -3.79% to -4.27% respectively. The three layers respective densities (ρ_{Core}, ρ_{LM} and ρ_{UM}) quartiles vary from -1.1% to 3.35%, -1.63% to -0.56% and -2.36% to -1.6%. As for the viscosities of the core η_{Core}, the lower mantle η_{LM} and the upper mantle η_{UM} vary from -6.99% to 11.88%,

895 -9.25% to -0.43% and -5.78% to -0.65% respectively. The same table
896 (Table A1) shows that for **Class 3** the thicknesses Th_{IC}, Th_{OC}, Th_{LM} and
897 Th_{UM} quartiles (25%, 50% and 75%,) vary from -3.22% to -1.56%, 1.31%
898 to 8.8%, 3.15% to 5.3% and -2.32% to 3.15%. Their respective densities
899 (ρ_{IC}, ρ_{OC}, ρ_{LM} and ρ_{UM}) quartiles vary from -0.21% to 0.08%, -0.58% to
900 1.33%, 0.87% to 1.15% and -0.08% to 1.63%. The viscosities of the inner
901 core η_{IC}, the lower mantle η_{LM} and the upper mantle η_{UM} vary from -0.38%
902 to 0.5%, -2.62% to 3.07% and 1.32% to 4.25%.

Table A1: Results of the selection process over 65000 randomly sampled profiles. Are given in Column 1, the type of models considered and on Column 2 the layers. Column 3 gives the mean and first and third quartiles (25% and 75%) of the layer thicknesses (km), Column 4 the densities (kg.m^{-3}) and Column 5 the viscosities in log10(Pa.s).

Models	Layers	thickness (km)	density (kg.m^{-3})	viscosity log10 (Pa.s)
Fluid (**Class 1**)	upper mantle	919^{1392}_{576}	3749^{4114}_{3418}	$20.85^{22.9}_{18.6}$
	lower mantle	1904^{2295}_{1453}	4915^{5392}_{4496}	$21.78^{23.6}_{19.85}$
	core	3142^{3355}_{2874}	10956^{11938}_{9909}	-5
Solid (**Class 2**)	upper mantle	1166^{1645}_{777}	3739^{4100}_{3385}	$20.48^{22.85}_{17.9}$
	lower mantle	971^{1661}_{472}	4889^{5441}_{4402}	$20.48^{22.85}_{17.95}$
	core	3571^{4170}_{3157}	9278^{10939}_{7789}	$17.95^{19.9}_{16}$
Fluid/Solid (**Class 3**)	upper mantle	903^{2165}_{580}	3738^{4076}_{3374}	$20.85^{22.9}_{18.6}$
	lower mantle	1780^{2165}_{1400}	4975^{5431}_{4475}	$21.85^{23.48}_{20}$
	outer core	386^{740}_{173}	8313^{9843}_{6795}	-5
	inner core	2734^{3091}_{2344}	11425^{12230}_{10430}	$15.7^{17.9}_{12.9}$

Appendix B. Testing the effect of the number of simulated models and the sensitivity to the rigidity

The rigidities of the different layers have been fixed so far. In this appendix we consider the effects of changing these parameters on the models selection. We also show the fact that the 65000 originally simulated models are enough for the statistical analysis of this work. We take **Class 1** (fluid core) as an example.

We select random subsets of the original 65000 models of **Class 1** and filter them with the MoI, k_2 and Q filters used in this work. Fig. B2 illustrates the percentage of the filtered models with respect to the number of models in each random subset. Fig. B1 shows the percentage of filtered models (y-axis) as a function of the number of models (x-axis) of the subsets. Fig. B1 shows that for the 65000 originally simulated models, the MoI, k_2 and Q filters preserve 7.2% of the models (or 4703 models). This value is approached after 10000 simulated models. Therefore simulating more models does not provide a higher percentage of models after filtration. The same conclusion is valid for the other two filters: the MoI and k_2 filters applied together and the MoI filter solely applied.

We test the effect of the rigidity variation on a subset of 10000 models of the original 65000 original 4-layer models of **Class 1**. For each of the models from this subset we vary the rigidity of only one layer and then we calculate the TLN k_2 and quality factor Q for the new models. The core is considered to be an inviscid fluid therefore $\mu_{\text{Core}} = 0$ Pa and therefore it does not vary.

Therefore the layers rigidities that are tested are of the lower mantle, the upper mantle and the crust. The rigidity of each layer is varied each from the original values (see Table 2) either by $\pm 5\%$, $\pm 10\%$, $\pm 15\%$ or $\pm 20\%$.

We denote by O_X and N_X the original and new parameters respectively with $X = k_2$ or $X = Q$. Fig. B2 illustrates $\Delta k_2 = \dfrac{N_{k_2} - O_{k_2}}{O_{k_2}} \times 100$ and $\Delta Q = \dfrac{N_Q - O_Q}{O_Q} \times 100$ after we vary the rigidity of one layer. The y-axis and the legend indicate which layer rigidity has varied from the original models and the percentage of variation respectively. Fig. B2 shows that the rigidity of the crust has the least effect on k_2 and Q probably due to its smaller size. The effect of the rigidity of the other layers (lower mantle and upper mantle) has almost the same significance. The maximum effect caused by the variation of the lower mantle or the upper mantle rigidities by 20% increases Q by almost 30% and k_2 by less than 20%. The estimated k_2 from Table 1 has an uncertainty with 2-σ of 22.37%, therefore it is of the magnitude of the difference in percentage a different rigidity of one layer causes to the resulting k_2 and Q.

Appendix C. Sensitivity to creep parameter α

In this section we investigate which layer parameters are the most sensitive to the α parameter of the Andrade rheology. The experimental parameter α is still not very well constrained, the value used in this work is $\alpha = 1/3$ [45]. We test the effect of α on a subset of the 65000 original models. We randomly select 5000 models and fix α values between 0.1 and 0.5 [29] with a step of 0.1. For each value of α and for $\alpha = 1/3$, we calculate the TLN k_2 and quality factor Q for the subset of models. Afterwards we apply the same filters (mass, MoI, k_2 and Q) to each case. We obtain new results for the 5000 models subset for each class and different values of α. Finally we study the difference in the first, second and third quartiles obtained with the original and new α values. Figs. C1, C2 and C3 represent the difference in percentage for the quartiles of each layer parameters. The viscosities of each layer are studied with a unit of log10 Pa.s as in Table 3.

Fig. C1 shows that the variations between the original and new results of each of the three quartiles are between +33% and −30% for **Class 1**. These two furthermost values correspond respectively to the Th_{LM} and Th_{UM} and for $\alpha = 0.1$. For an approximate lower mantle and upper mantle thicknesses of 1800 km and 960 km (see Table 3), a change of +33% and −30% amounts to a variation of 594 km and of −288 km, respectively. The other parameters quartiles vary between ±10% depending on the value of α. For an approximate lower mantle viscosity of $10^{20.78}$ Pa.s, a ±10% variation results in new viscosity values of $10^{18.7}$ Pa.s and $10^{22.86}$ Pa.s. For an approximate value of

an upper mantle density of 3700 kg.m^{-3}, a change of $\pm 5\%$ amounts to a variation of ± 185 kg.m^{-3} of the density. **Classes 2** and **3** have the similar patterns as **Class 1**. Fig. C2 shows that the **Class 2** quartiles vary between -13% and 33% depending on the layer parameters and the values of α. The first quartile varies $\approx$ by maximum of -12.8% and 33.7% corresponding to $\alpha = 0.1$ for ρ_{Core} and Th_{UM} respectively. The other layer parameters first quartile vary between $\pm 10\%$ except Th_{LM} which varies by 26.9% and 17.5% for $\alpha = 0.1$ and $\alpha = 0.2$ respectively. The second (respectively third) quartile vary in between -13.4% and 12.36% (respectively -13% and 7.2%). These maximum variations correspond to Th_{LM}. The other layer parameters vary between $\pm 5\%$ except Th_{UM} for $\alpha = 0.1$ which varies by -13.2% and -7.5% for the second and third quartiles respectively. Fig. C3 shows that the maximum variation of the first and second quartiles of **Class 3** correspond to $\alpha = 0.1$ and to Th_{IC} and Th_{LM}. The first quartile of the parameters of these 2 layers varies by -19% and $+17\%$, respectively and their second quartile varies by -9.6% and 16%, respectively. The first quartile of the other parameters vary between $\pm 10\%$ except Th_{OC} and ρ_{OC} which vary by -16% and 11% for $\alpha = 1/3$ and $\alpha = 0.1$ respectively. The second quartile of the other parameters varies between $\pm 10\%$ except ρ_{OC} and Th_{LM} which vary by 13.6% and 16%, respectively, both for $\alpha = 0.1$. The third quartile of **Class 3** varies between -8% and 27.6% and these furthermost values correspond to $\alpha = 0.1$. The most affected parameters are Th_{OC} (between 18.8% and 27.6% for α of 0.1, 0.2 and 0.3) and Th_{LM} (14% for $\alpha = 0.1$). The other layer parameters vary between $\pm 10\%$. Therefore the α parameter affects k_2

and Q for each of the classes, hence it affects the distribution of the layer parameters after filtering with the ranges of k_2 and Q. Nonetheless the effect is not big enough to affect the original general study.

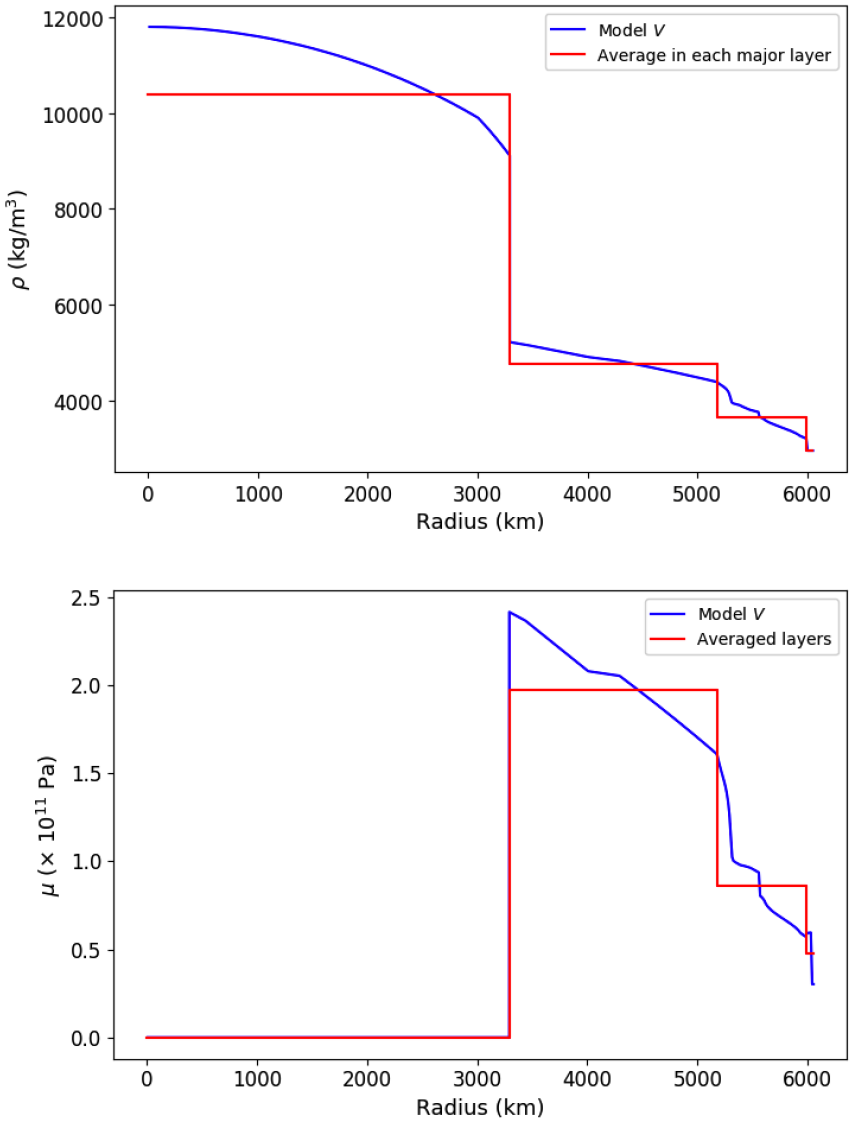

Figure 1: Density ρ in kg.m^{-3} (top) and rigidity μ in 10^{11} Pa (bottom). Each major layer has been averaged for the introduction in ALMA^3. The model **V** refers to the [10] reference profile. It is built as an Earth-like Venus model with a lower Fe content (8.1 wt%, FeO in the mantle and the crust) to explain the density deficit of Venus in comparison to the Earth [27].

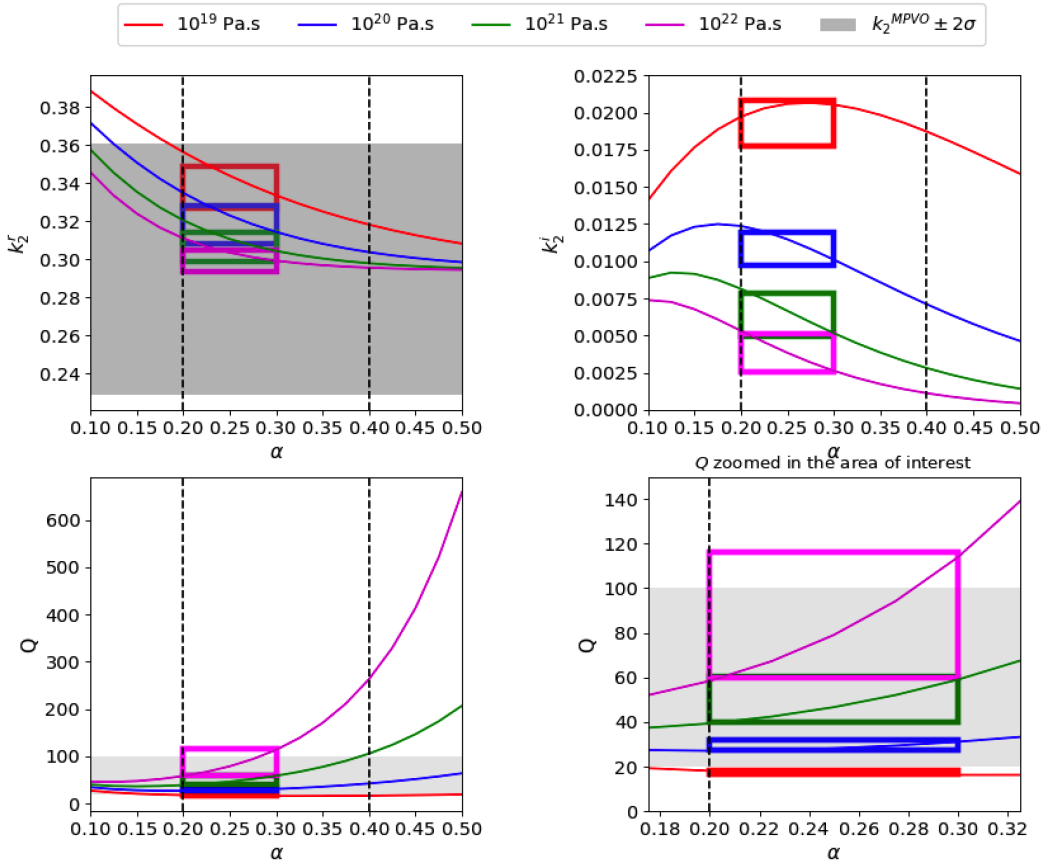

Figure 2: Real part of k_2 (a), Imaginary part of k_2 (b), Quality factor Q (c) and and its zoom (d) as a function of α (x-axis). The mantle follows an Andrade rheology with different viscosities specified in the legend, from 10^{19} Pa.s to 10^{22} Pa.s. The rectangles represent the intervals obtained by [10] for $\alpha \in [0.2, 0.3]$. The black dashed lines represent the range of α for olivine-rich rocks. The gray delimitation shows the most recently observed value range according to an uncertainty of 2-σ from [8].

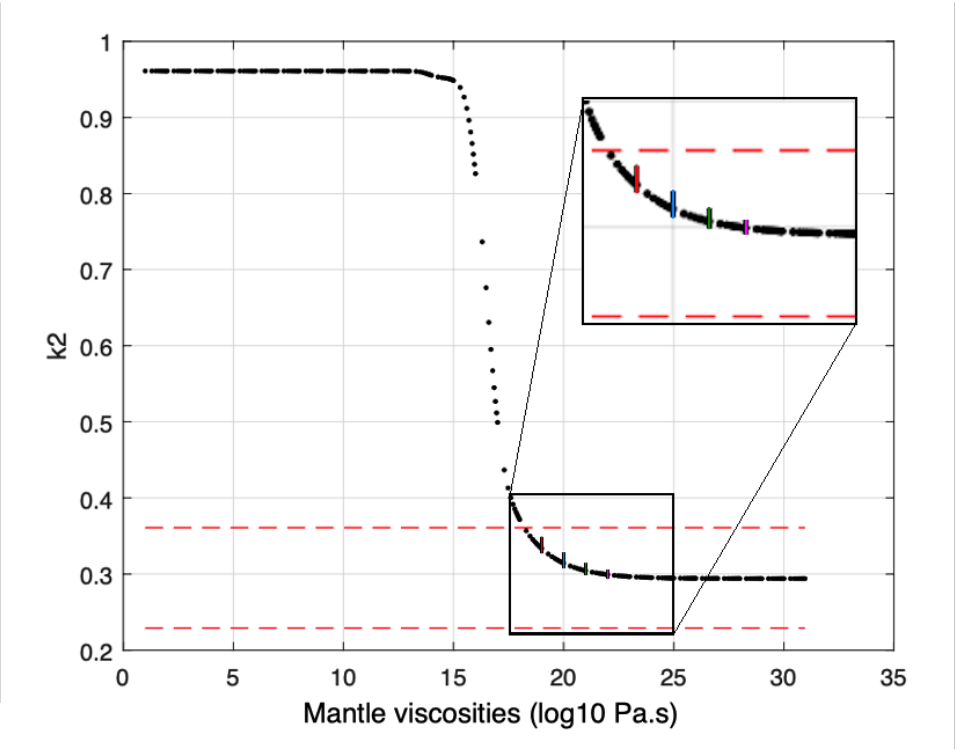

Figure 3: The real k_2 as a function of the mantle viscosity and for $\alpha = 0.3$. The model used is **V**. The dashed red lines indicate the interval of k_2 as observed by Magellan and PVO [8]. The colored vertical lines represent the intervals obtained by [10] for α between 0.2 and 0.3 for different mantle viscosities. The color code of the vertical lines is similar to Fig. 2 which indicate the four different mantle viscosities.

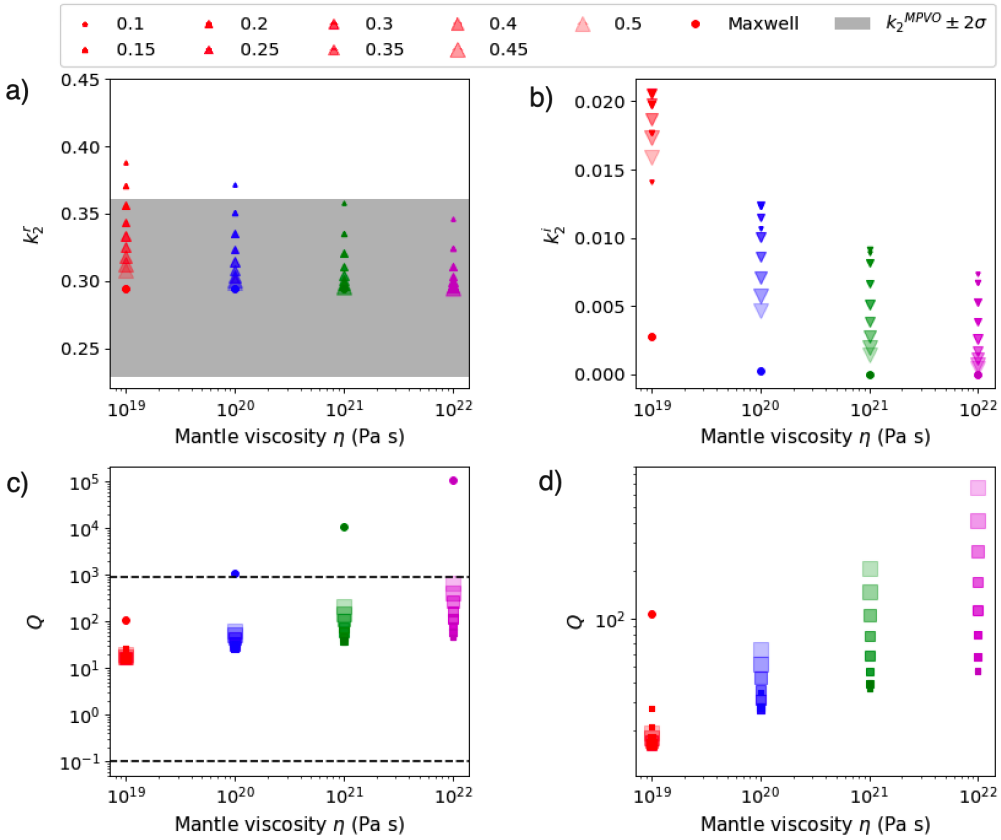

Figure 4: Real part of k_2 (a), Imaginary part (b), Quality factor Q (c) and its zoom (d) as a function of mantle viscosities η in Pa.s (x-axis) for a mantle with an Andrade rheology for different values of $\alpha \in [0.1, 0.5]$. The black dashed lines in (c) delimits the zoomed area in (d). The gray delimitation shows the most recently observed value range according to an uncertainty of 2-σ from [8].

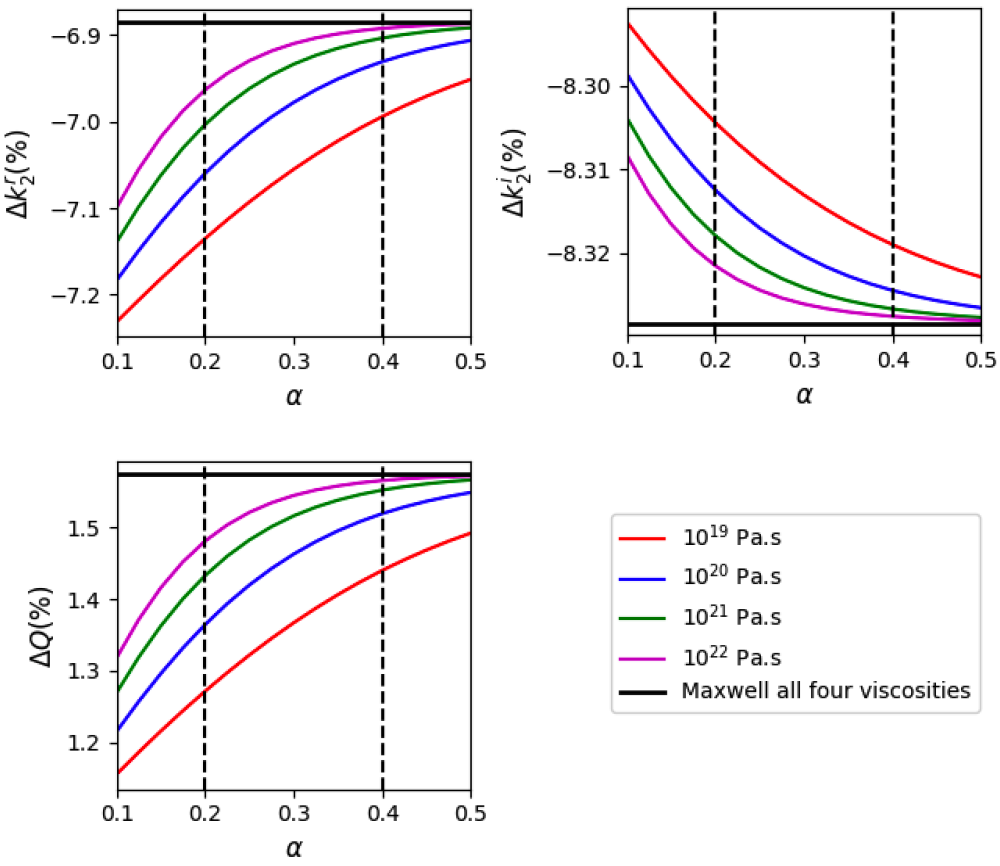

Figure 5: Representation of the percentage variation in (%) of k_2^r, k_2^i and Q (y-axis) of Venus without and with an atmosphere as a function of $\alpha \in [0.1, 0.5]$ (x-axis). The values correspond to a mantle with either an Andrade and Maxwell rheologies for different values of mantle viscosities η in Pa.s. The black dashed lines represent the range of α for olivine-rich rocks.

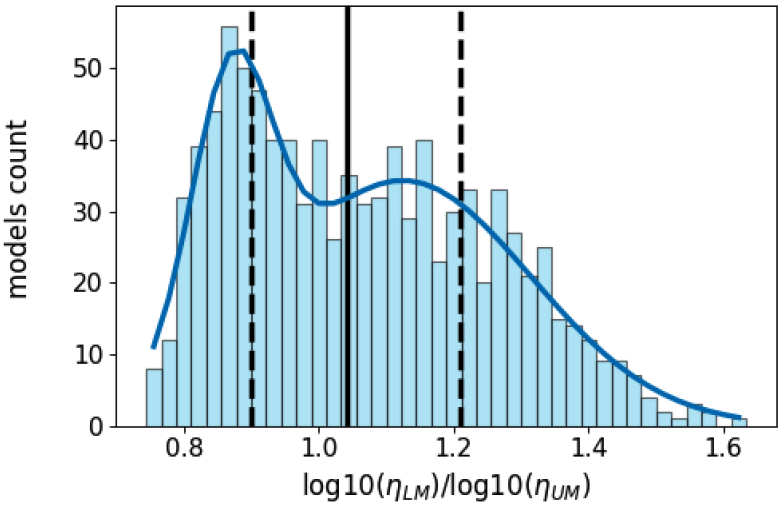

Figure 6: **Class 1**: Histogram of the ratio between the lower mantle viscosity versus the upper mantle viscosities. The black curve is the bi-modal fit of the ratio distribution. Black plain and dash lines correspond to the median and the first and third quartiles, respectively.

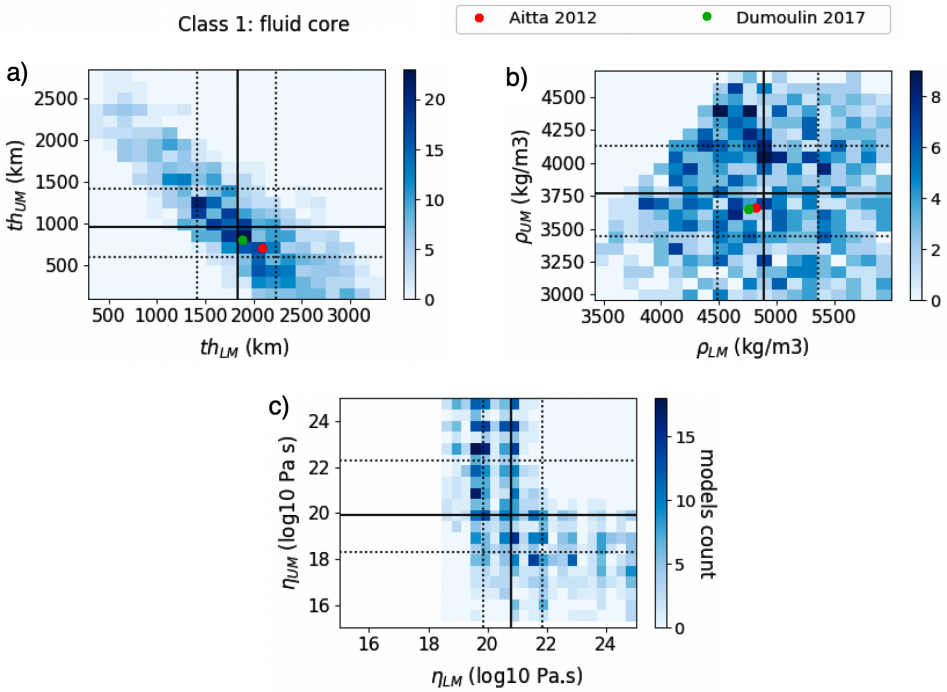

Figure 7: **Class 1**: 2-D Histograms for the thicknesses (top left-hand side), the densities (top right-hand side) and the viscosities (bottom side) of the lower mantle versus that of the upper mantle. The red and green dots show the values considered by [9] and [10], respectively.

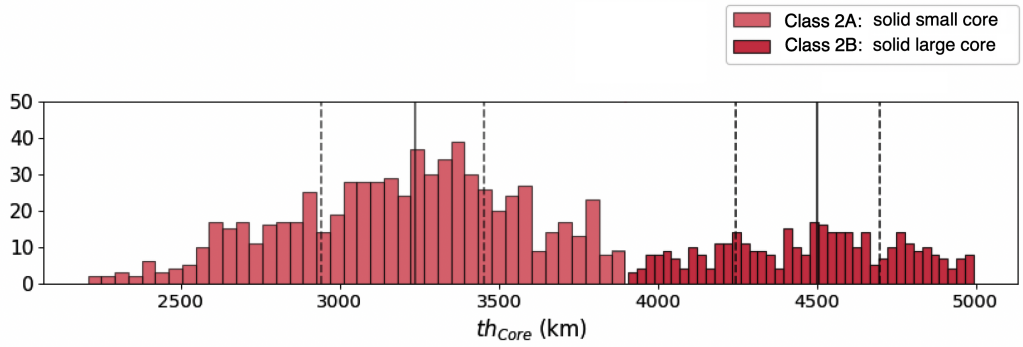

Figure 8: **Class 2**: Histograms of the thicknesses of the core. Black plain and dash lines correspond to the median and the first and third quartiles, respectively for each sub-class.

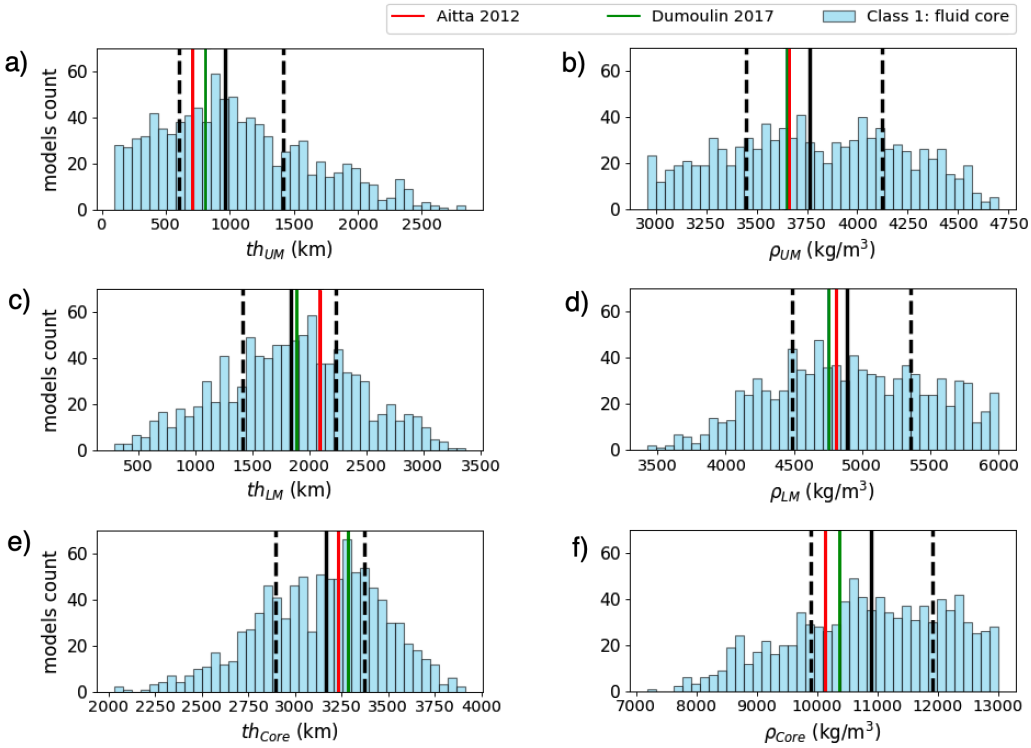

Figure 9: Comparisons between the models of **Class 1** and those from [10] and [9]: Histograms in thicknesses in (km) (left-hand side column) and densities in (kg.m^{-3}) (right-hand side column). The solid black line corresponds to the mean and the dashed black lines correspond respectively to the first and third quartiles. The red and green vertical lines indicate the limits of the models proposed by [10] and [9] respectively.

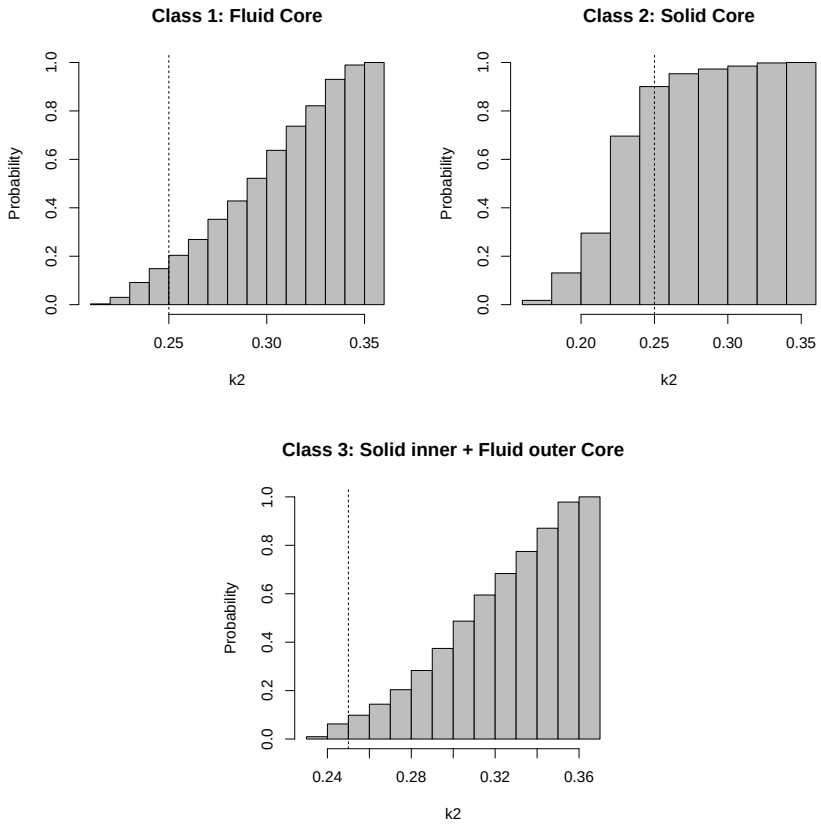

Figure 10: Cumulative histograms of the k_2 values obtained with the models of **Class 1** (fluid core), **Class 2** (solid core) and **Class 3** (solid inner and fluid outer core).

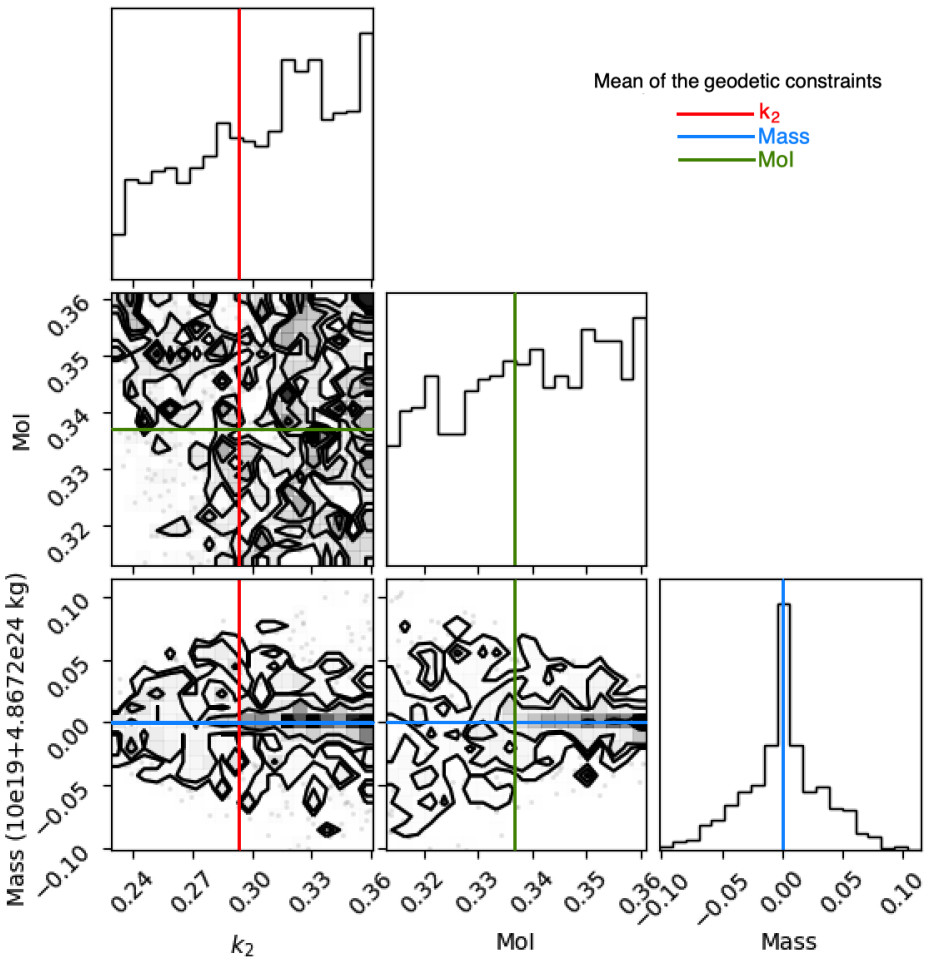

Figure 11: Histograms and corner plots of the real k_2, MoI and mass values obtained with the models of **Class 1** (fluid core). The solid red, black and green lines corresponds to the mean values of the geophysical constraints k_2, mass and MoI from Table 1.

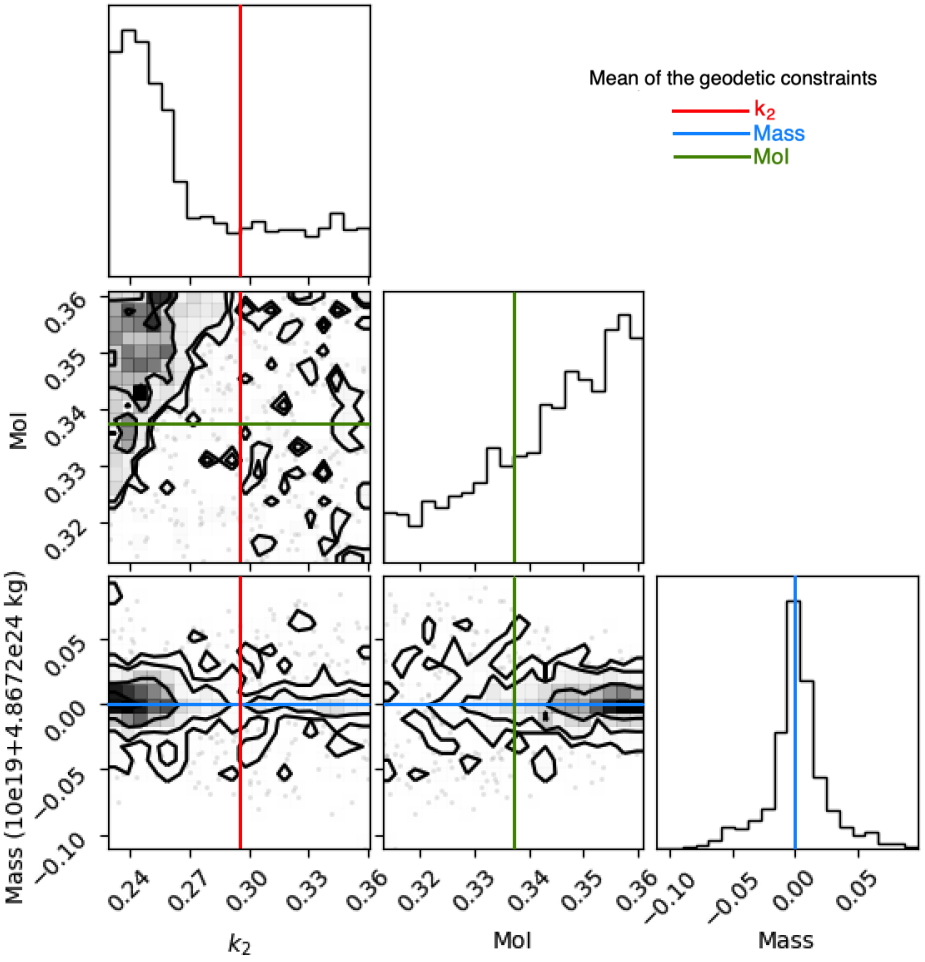

Figure 12: Histograms and corner plots of the real k_2, MoI and mass values obtained with the models of **Class 2** (fluid core). The solid red, black and green lines corresponds to the mean values of the geophysical constraints k_2, mass and MoI from Table 1.

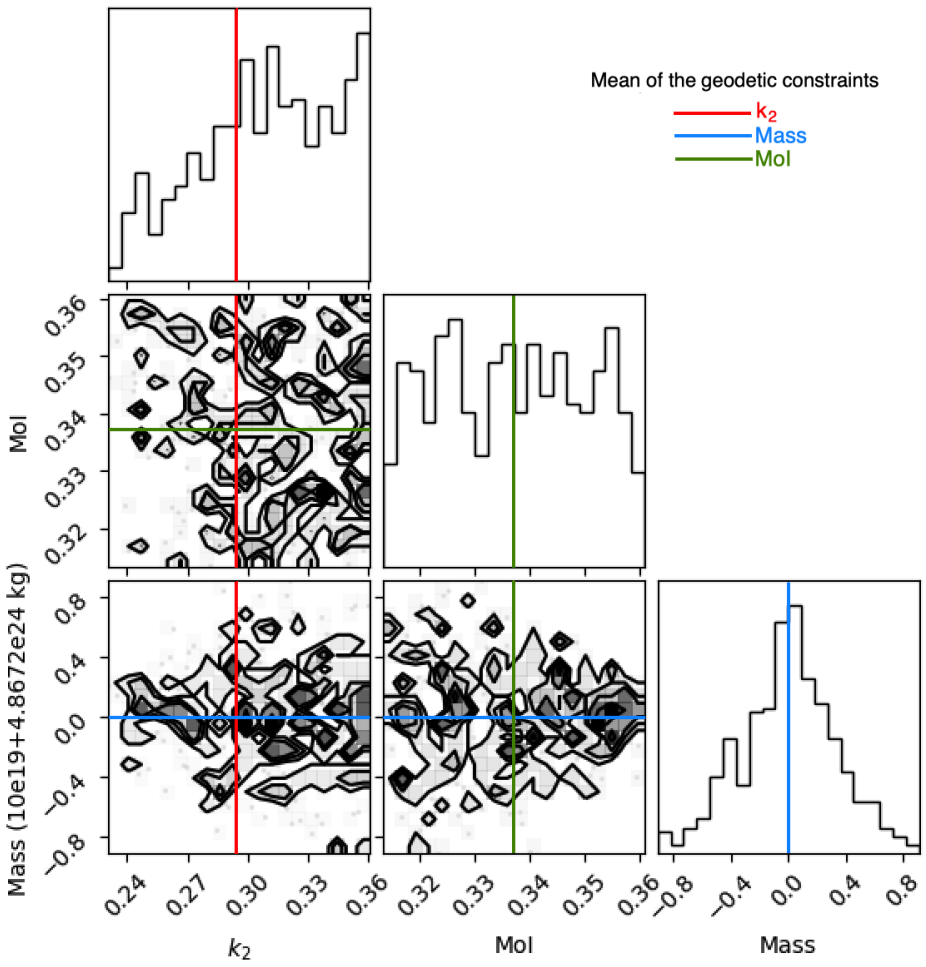

Figure 13: Histograms and corner plots of the real k_2, MoI and mass values obtained with the models of **Class 3** (fluid core). The solid red, black and green lines corresponds to the mean values of the geophysical constraints k_2, mass and MoI from Table 1.

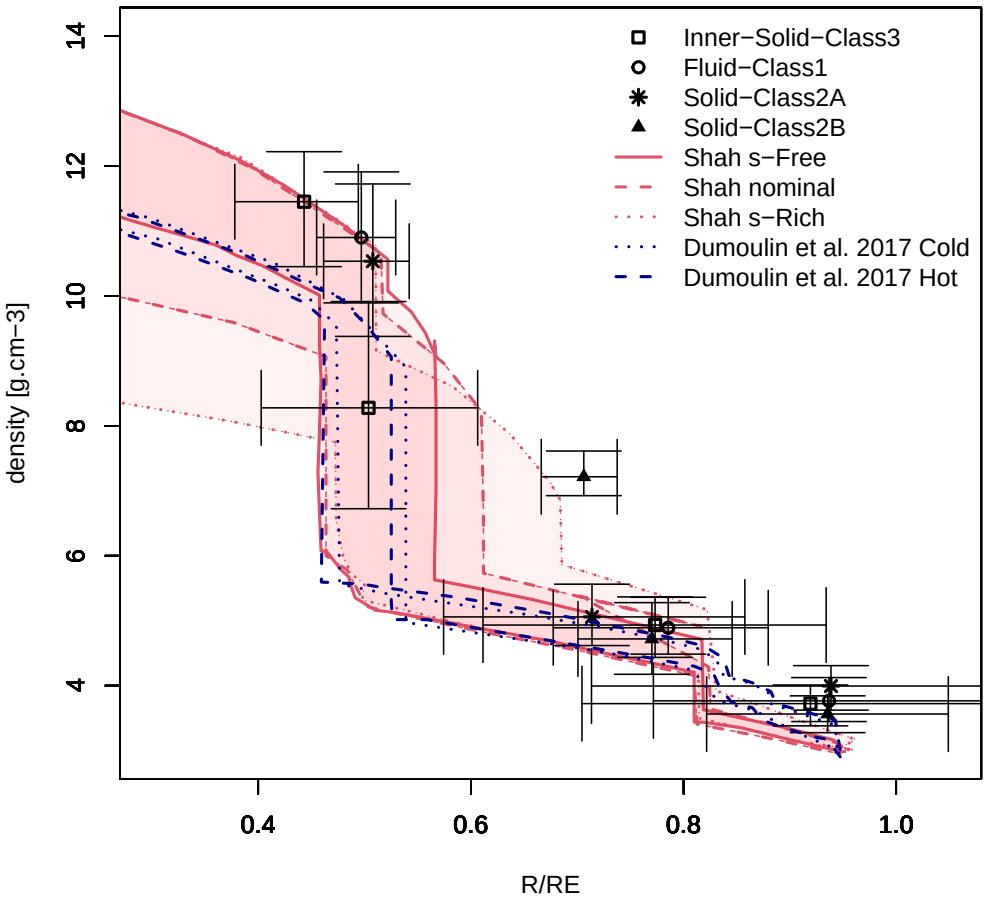

Figure 14: Comparison of the densities obtained with this work for the different classes of models with the profiles from [48] without subcategories according to the MoI values and [10] for the two temperature profiles considered in this study (hot and cold). The x-axis gives the ratio between the radius R of each layer and the Earth radius. The errorbars are given at 2-σ.

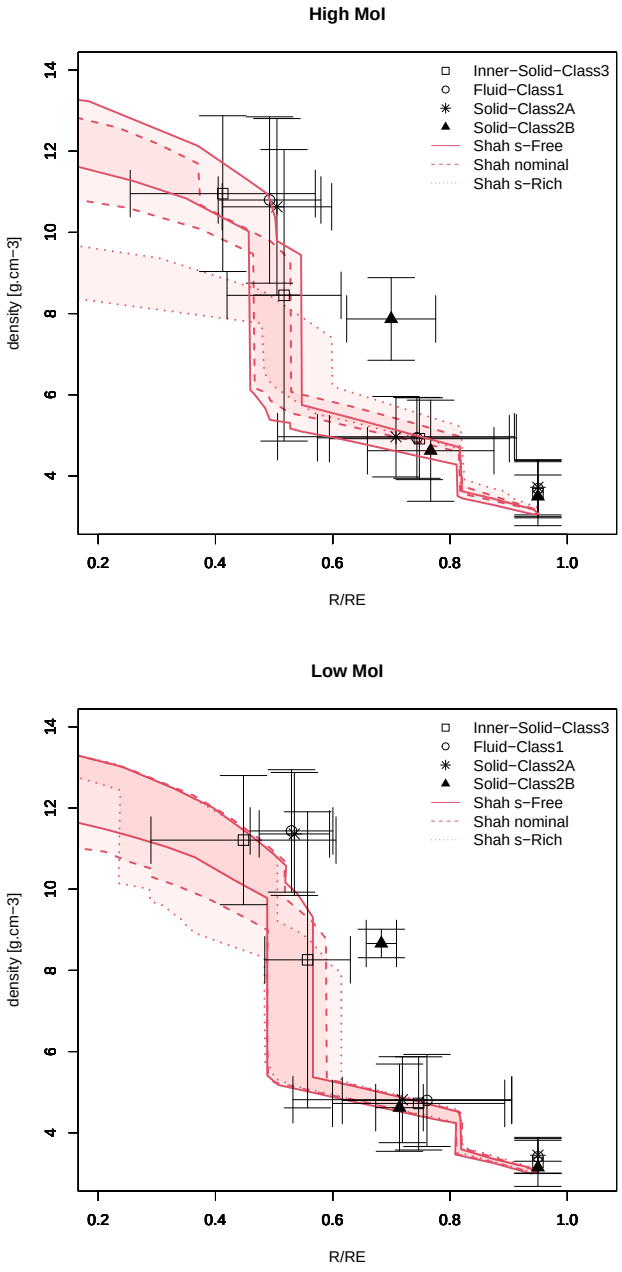

Figure 15: Comparison of the densities obtained with this work with profiles from [48] considering Low and High MoI as defined in [48]. Same x-axis as on Fig. 14. The errorbars are given at 2-σ

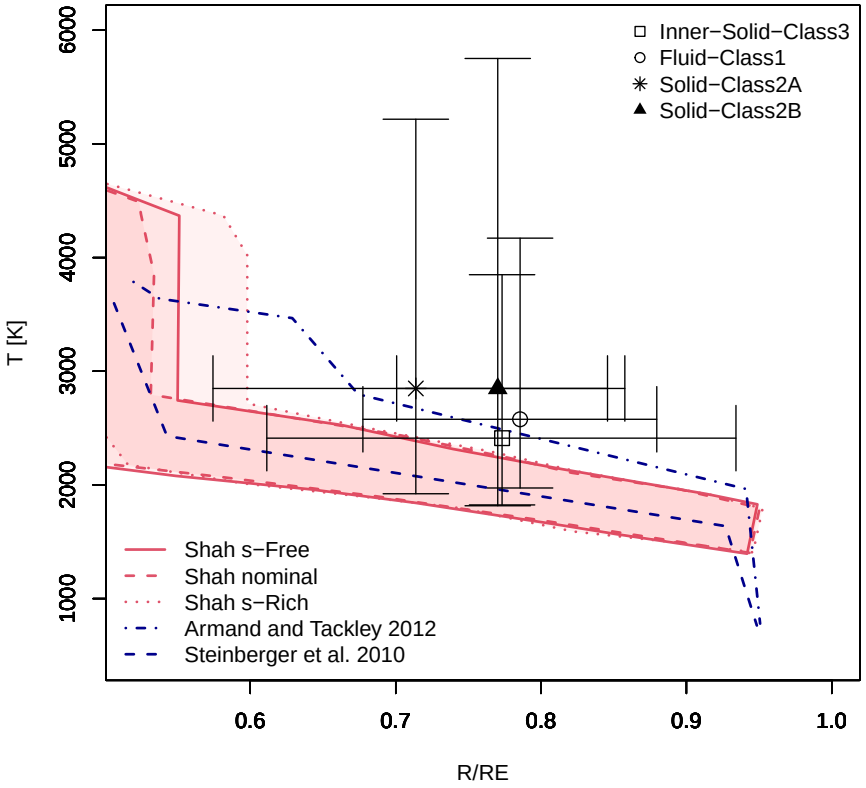

Figure 16: Comparison of the temperatures for the lower mantle for the different classes of models with profiles from [48], [53] and [43]. The temperature of the upper mantle is fixed to 1600 K. Same x-axis as on Fig. 14. The errorbars are given at 2-σ

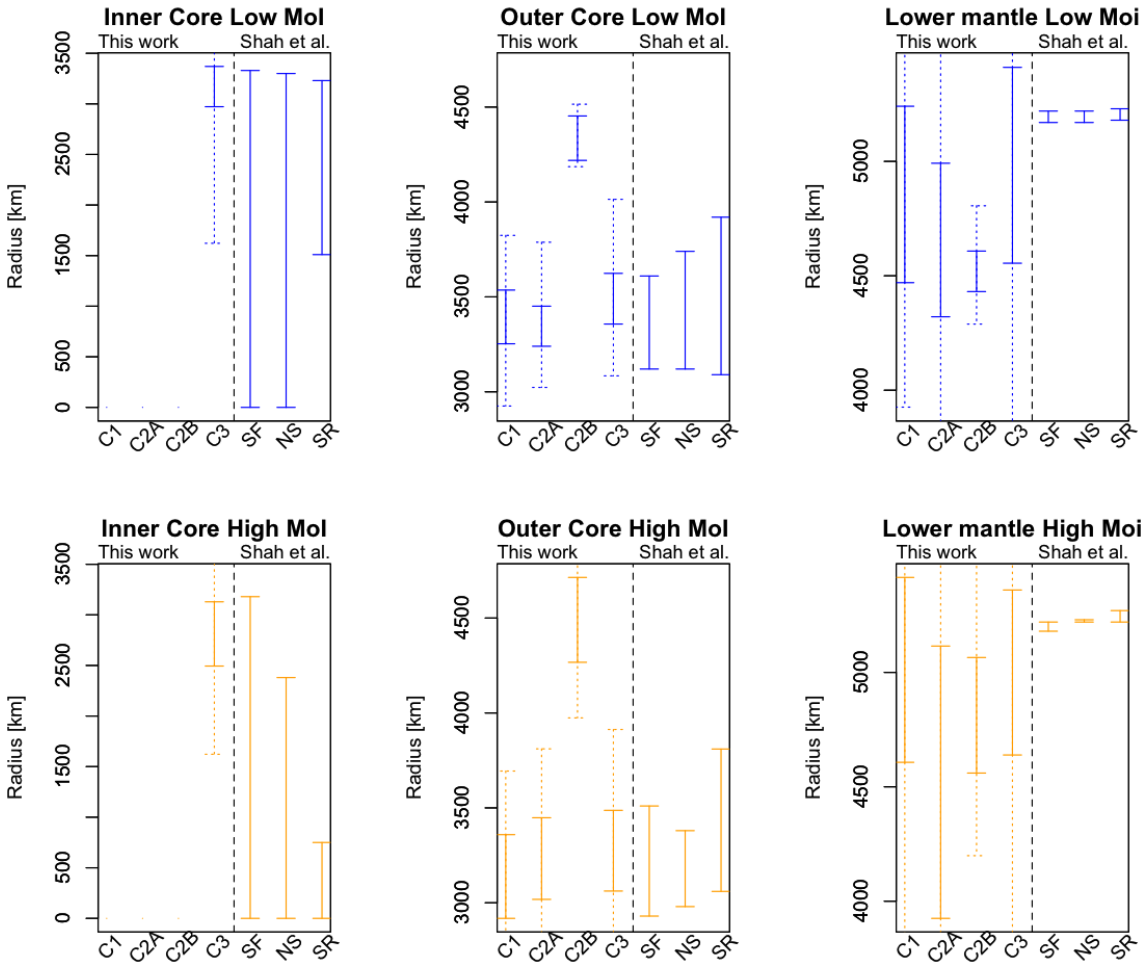

Figure 17: Comparisons between layer boundaries (radii) from [48] and those obtained for the different classes considering MoI subcategories as presented in [48]. C1, C2A, C2B, C3 stand for **Class 1**, **Class 2A**, **Class 2B** and **Class 3** respectively and SF, NS and SR stand for S-free, Nominal-S and S-rich core models as defined in [48], respectively. The errorbars are given at 2-σ

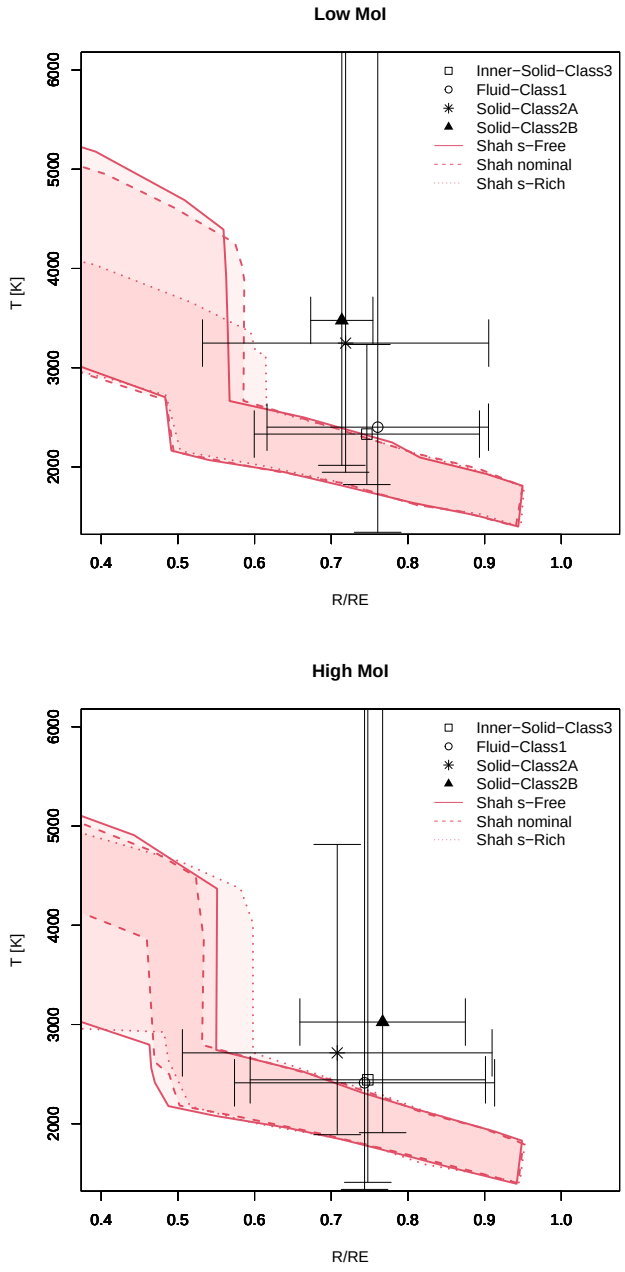

Figure 18: Comparison of the temperatures for the lower mantle obtained with this work for the different classes of models with the profiles from [48] considering Low and High MoI as defined in [48]. Same x-axis as on Fig. 14. The errorbars are given at 2-σ

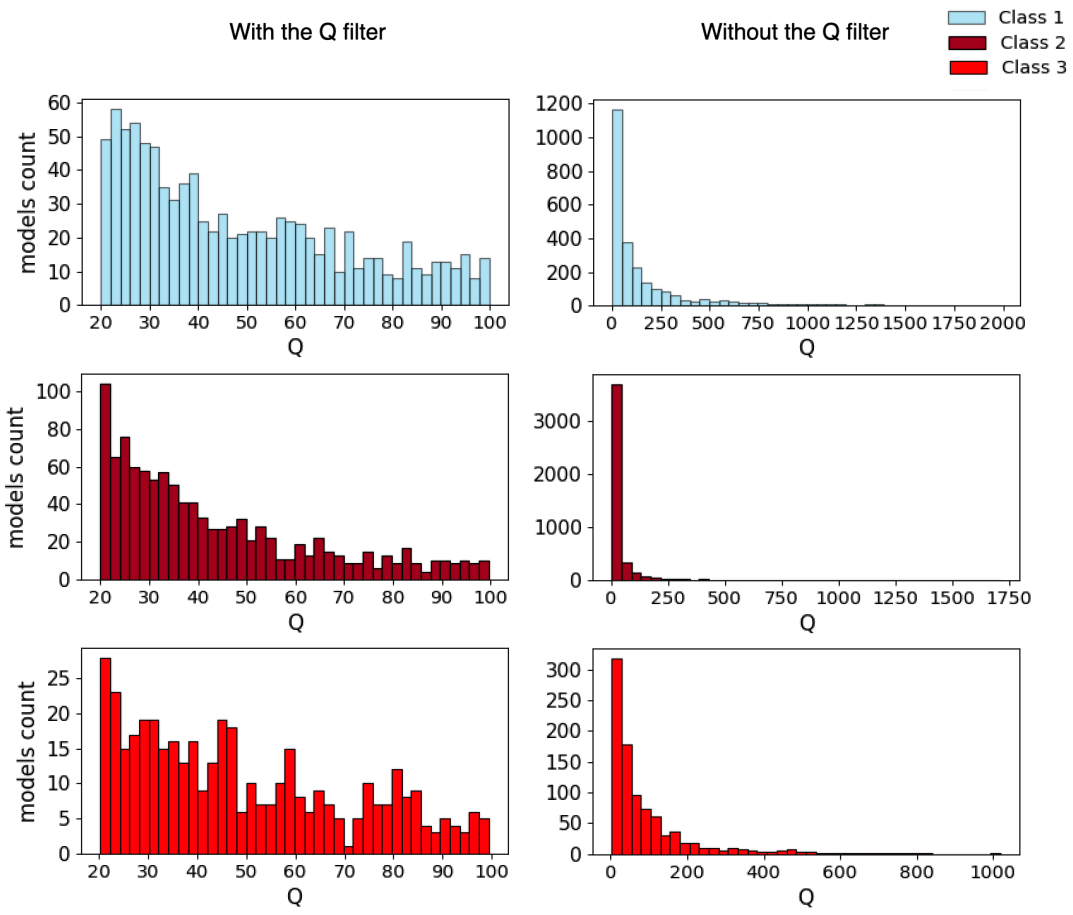

Figure A1: Histograms of the quality factor Q distribution from **Classes 1**, **2** and **3** with (left) and without (right) the quality factor Q filter.

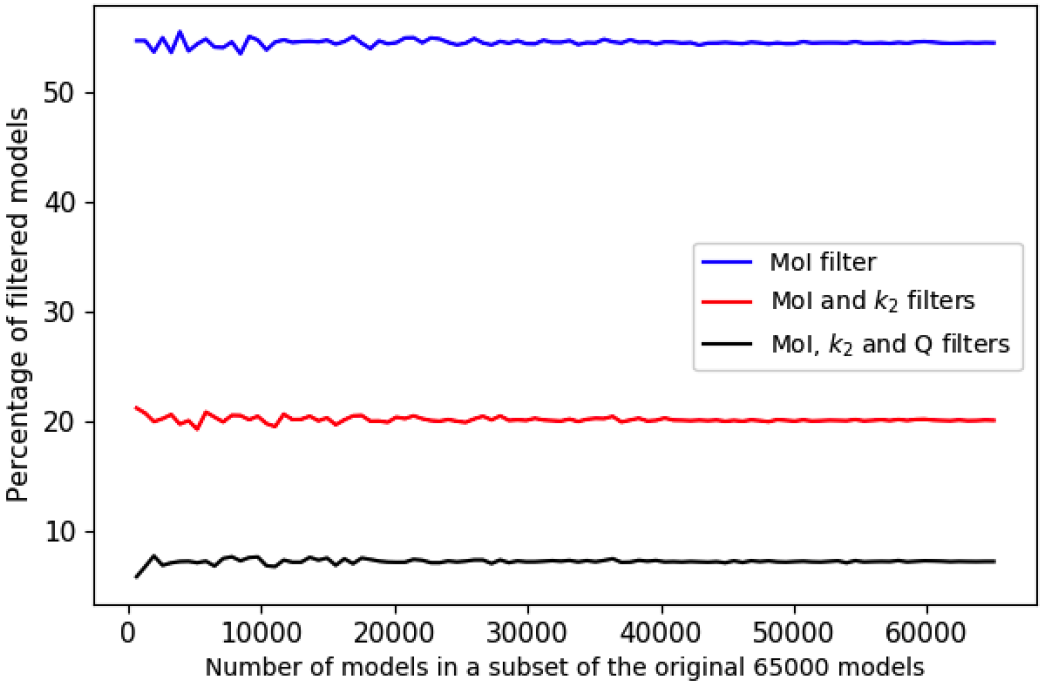

Figure B1: The number of filtered models after each additional filter: MoI ($\pm$1-σ), k_2 ($\pm$2-σ) and Q (from 20 to 100). The x-axis illustrates the number of models in each randomly selected subset of the original 65000 models.

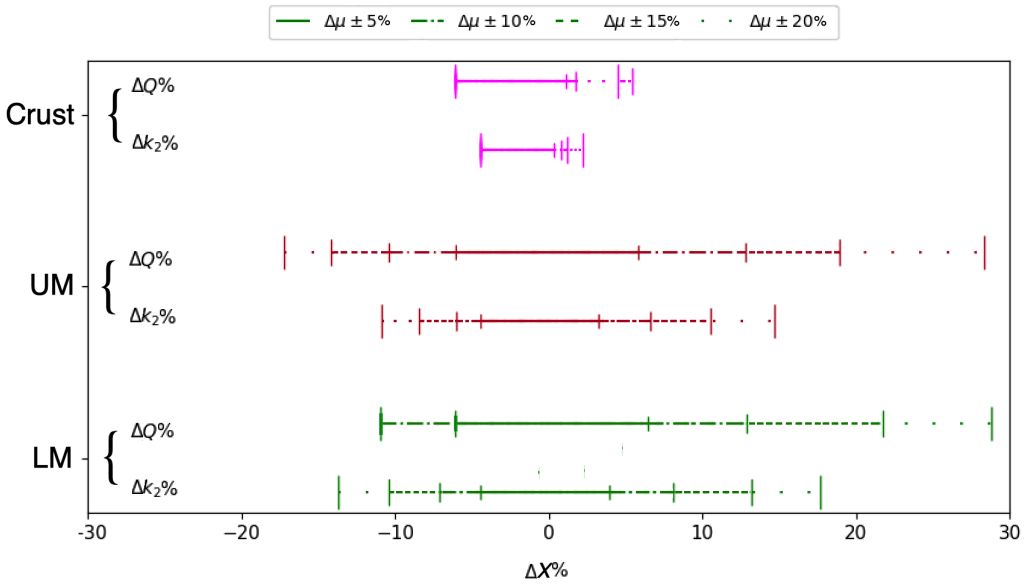

Figure B2: The difference in percentage for the real part of k_2 and Q between the new results and the original results after varying the rigidities (μ). The x-axis is the difference in percentage either to k_2 or to Q, therefore X being either k_2 or Q.

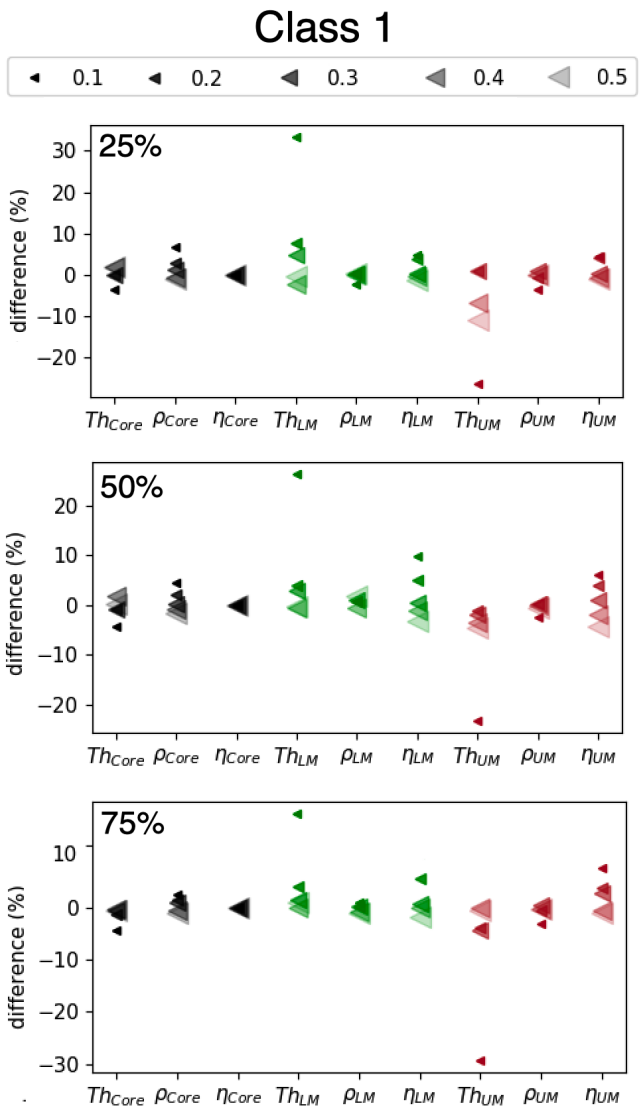

Figure C1: The difference in percentage (%) for **Class 1** between the new results with α between 0.1 and 0.5 and $\alpha = 1/3$. The x-axis corresponds to the layer parameters and the y-axis is the percentage difference. From top to bottom, the supblots correspond to the first quartile (25%), second quartile or median (50%) and third quartile (75%).

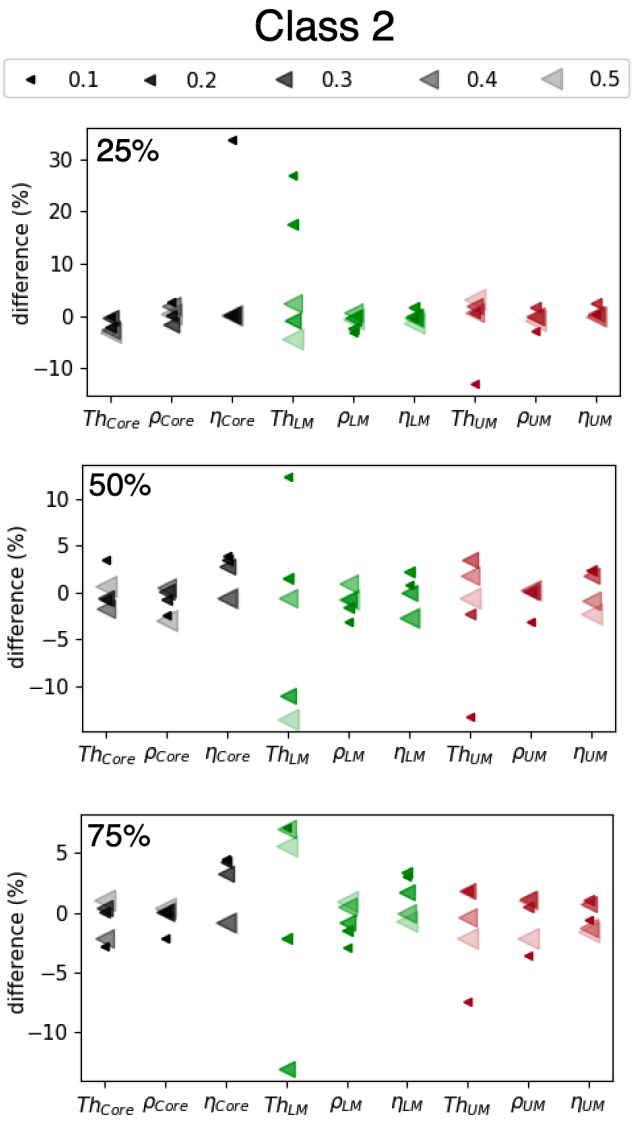

Figure C2: The difference in percentage (%) for **Class 2** between the new results with α between 0.1 and 0.5 and $\alpha = 1/3$. The x-axis corresponds to the layer parameters and the y-axis is the percentage difference. From top to bottom, the supblots correspond to the first quartile (25%), second quartile or median (50%) and third quartile (75%).

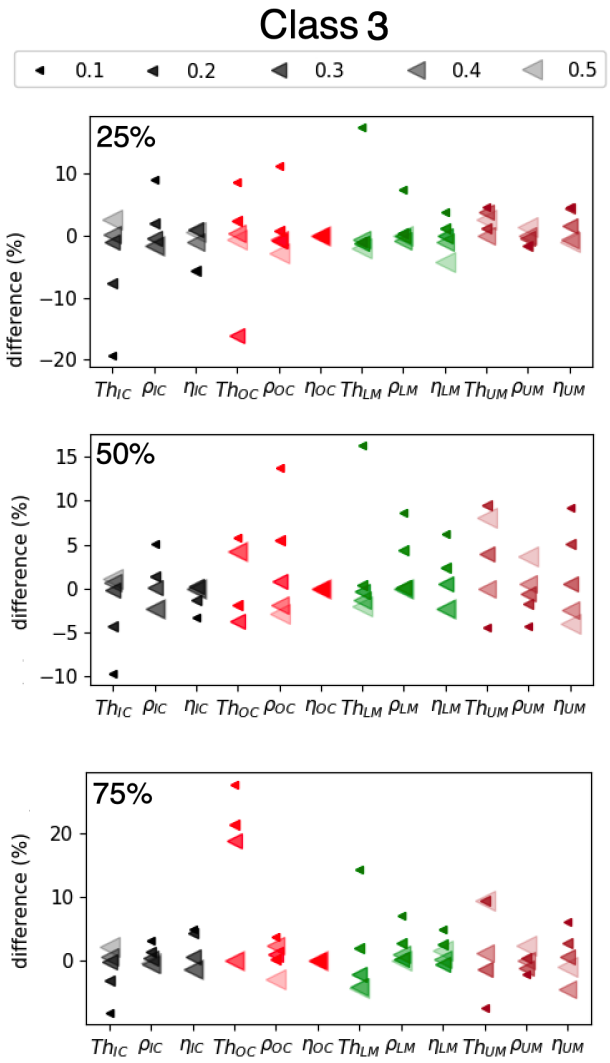

Figure C3: The difference in percentage (%) for **Class 3** between the new results with α between 0.1 and 0.5 and $\alpha = 1/3$. The x-axis corresponds to the layer parameters and the y-axis is the percentage difference. From top to bottom, the supblots correspond to the first quartile (25%), second quartile or median (50%) and third quartile (75%).

Appendix B: Additional figures and tables

We represent the 1D and 2D histograms of the Monte-Carlo sampling from chapter 3 section 3.2 before the density filters for the lower mantle ($\rho_{\mathrm{LM}} < 6000$ kg/m^3) and core/inner core ($\rho_{\mathrm{Core/IC}} < 13000$ kg/m^3) [Trønnes et al., 2019; Shah et al., 2021].

Table A.1: The layers thicknesses (km), densities (kg/m^3) and viscosities (log10 (Pa $\cdot$ s)) values for each core structure before the density filters.

Models	Layers	thickness (km)	density (kg.m^{-3})	viscosity log10(Pa $\cdot$ s)
Fluid (**Class 1**)	upper mantle	2312^{2910}_{1508}	4036^{4320}_{3757}	$20.00^{22.00}_{18.95}$
	lower mantle	1184^{1726}_{637}	6927^{9259}_{5312}	$20.00^{21.90}_{19.30}$
	core	2588^{2955}_{2258}	13401^{16684}_{11024}	-5
Solid (**Class 2**)	upper mantle	2423^{3024}_{1610}	4131^{4395}_{3829}	$20.9^{22.95}_{19.7}$
	lower mantle	691^{1289}_{305}	6876^{9196}_{5393}	$20.78^{22.85}_{19}$
	core	2707^{3249}_{2298}	12665^{16342}_{9628}	$16.85^{19.9}_{14}$
Fluid/Solid (**Class 3**)	upper mantle	2305^{1683}_{1464}	4059^{4322}_{3811}	$20.6^{22.3}_{19.3}$
	lower mantle	1097^{1683}_{575}	6091^{7953}_{4984}	$20.7^{22.3}_{19.48}$
	outer core	520^{938}_{230}	10390^{12520}_{8217}	-5
	inner core	2006^{2383}_{1665}	18210^{22840}_{14300}	$15.6^{17.78}_{12.95}$

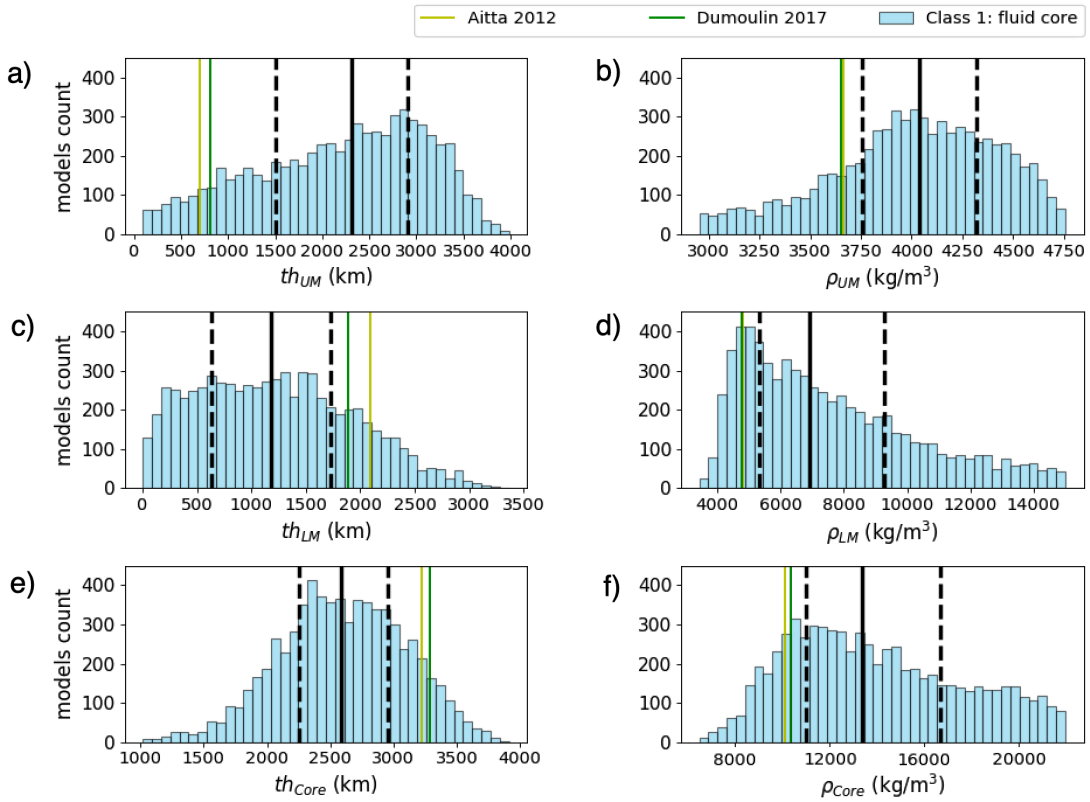

Figure A.1: 1D histograms for (a), (c) and (e) each layer thickness and (b), (d) and (f) each layer density - without the density filters. The solid black line corresponds to the 50% quartile and the dashed black lines correspond respectively to the 25% and 75% quartiles.

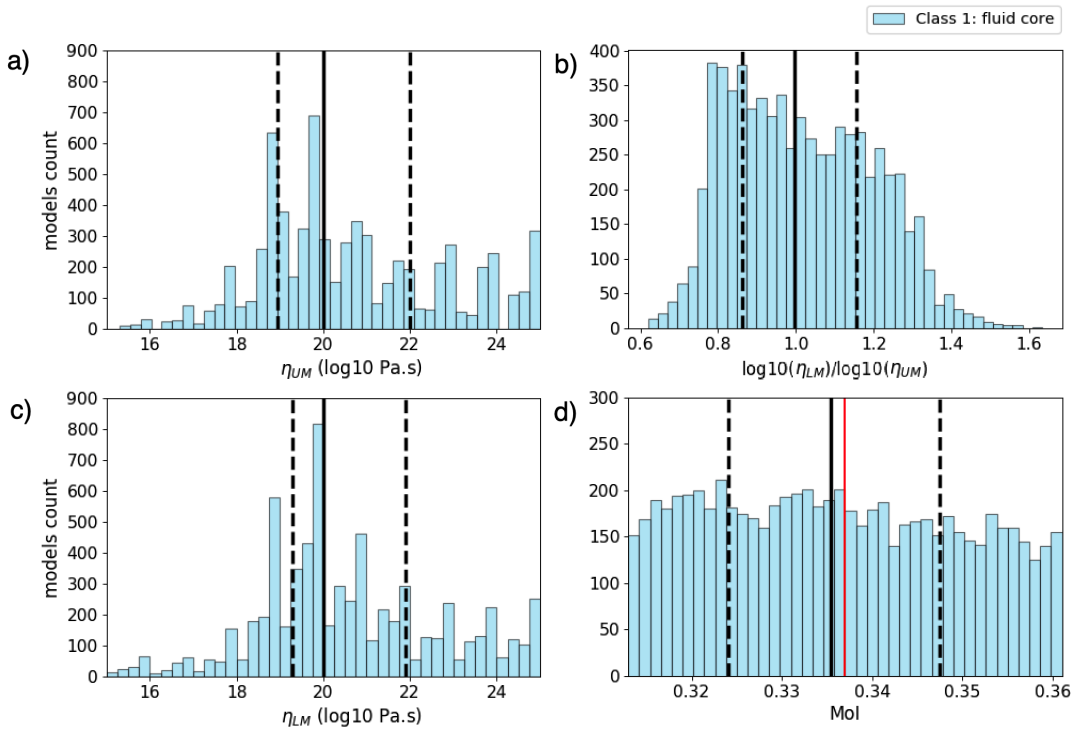

Figure A.2: 1D histograms for (a) and (c) the upper mantle and lower mantle viscosities respectively, (b) their ratios and (d) the MoI - without the density filters. Same representation for the solid and dashed lines as Fig. A.1.

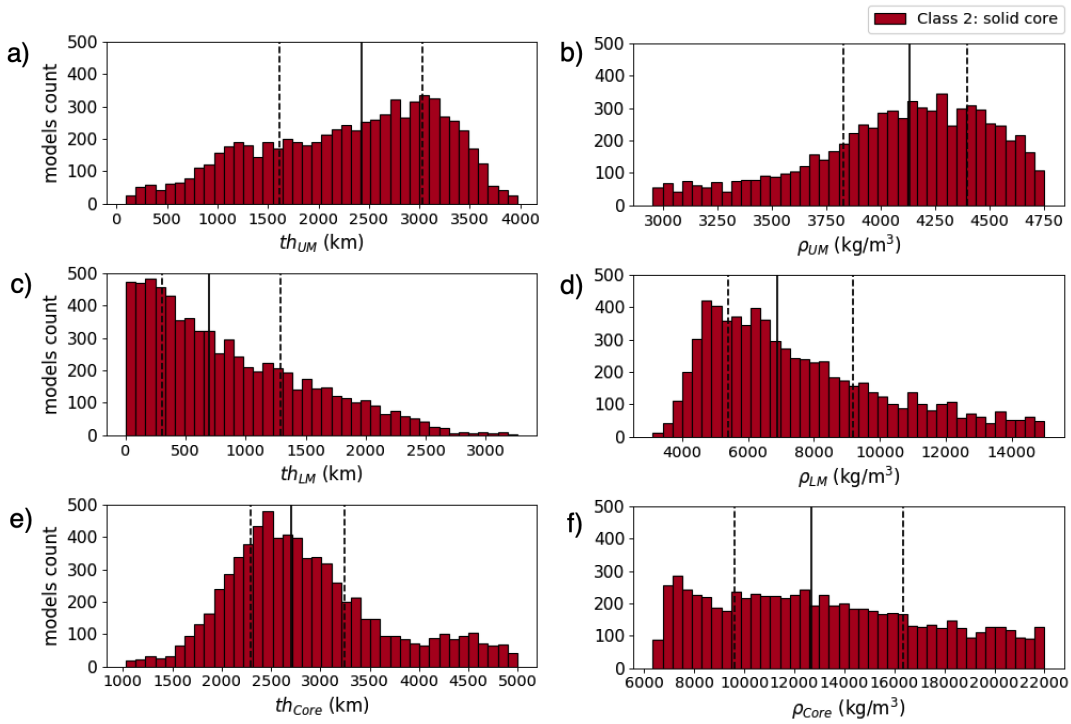

Figure A.3: 1D histograms for (a), (c) and (e) each layer thickness and (b), (d) and (f) each layer density - without the density filters. Same representation for the solid and dashed lines as Fig. A.1.

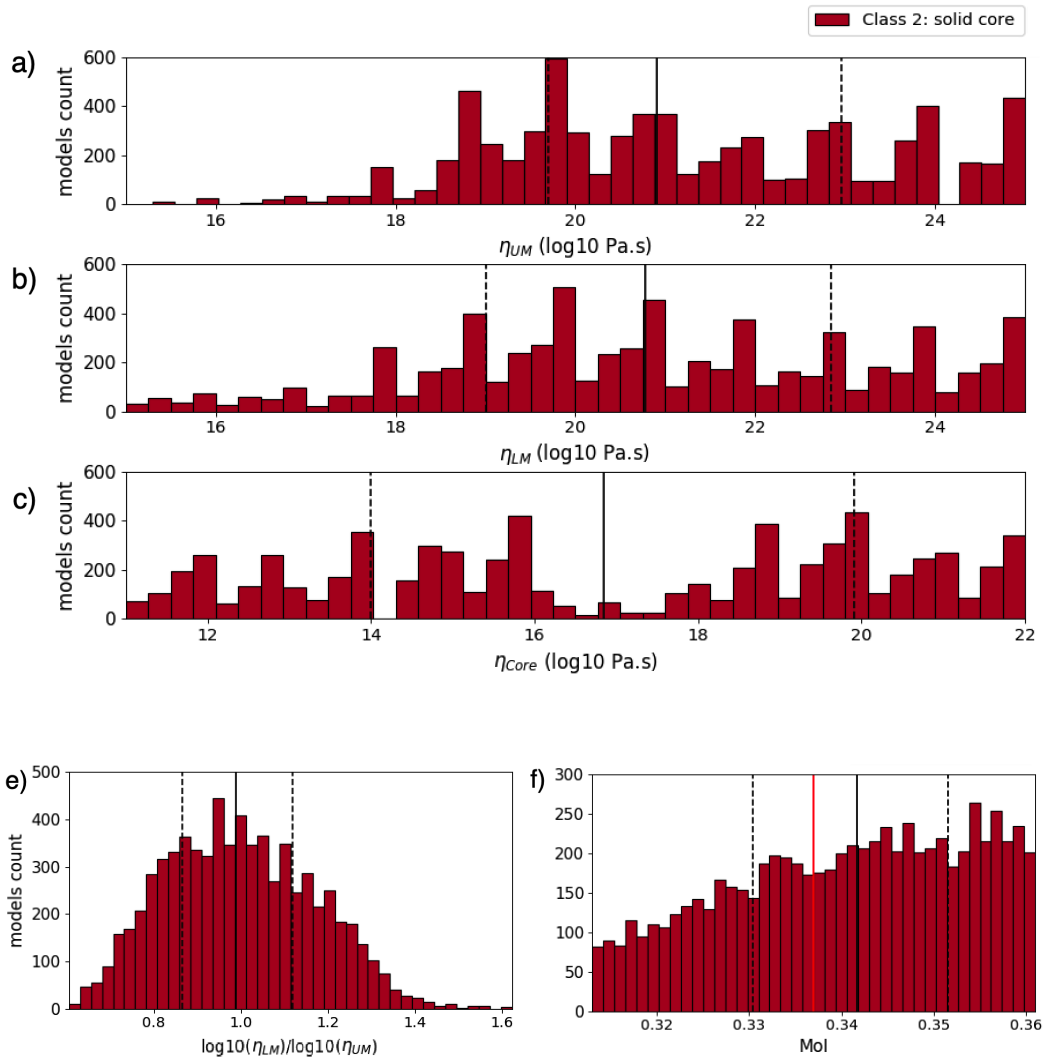

Figure A.4: 1D histograms for each layer (a), (b) and (c) viscosity, (e) lower mantle and upper mantle viscosity ratio and (f) MoI - without the density filters. Same representation for the solid and dashed lines as Fig. A.1.

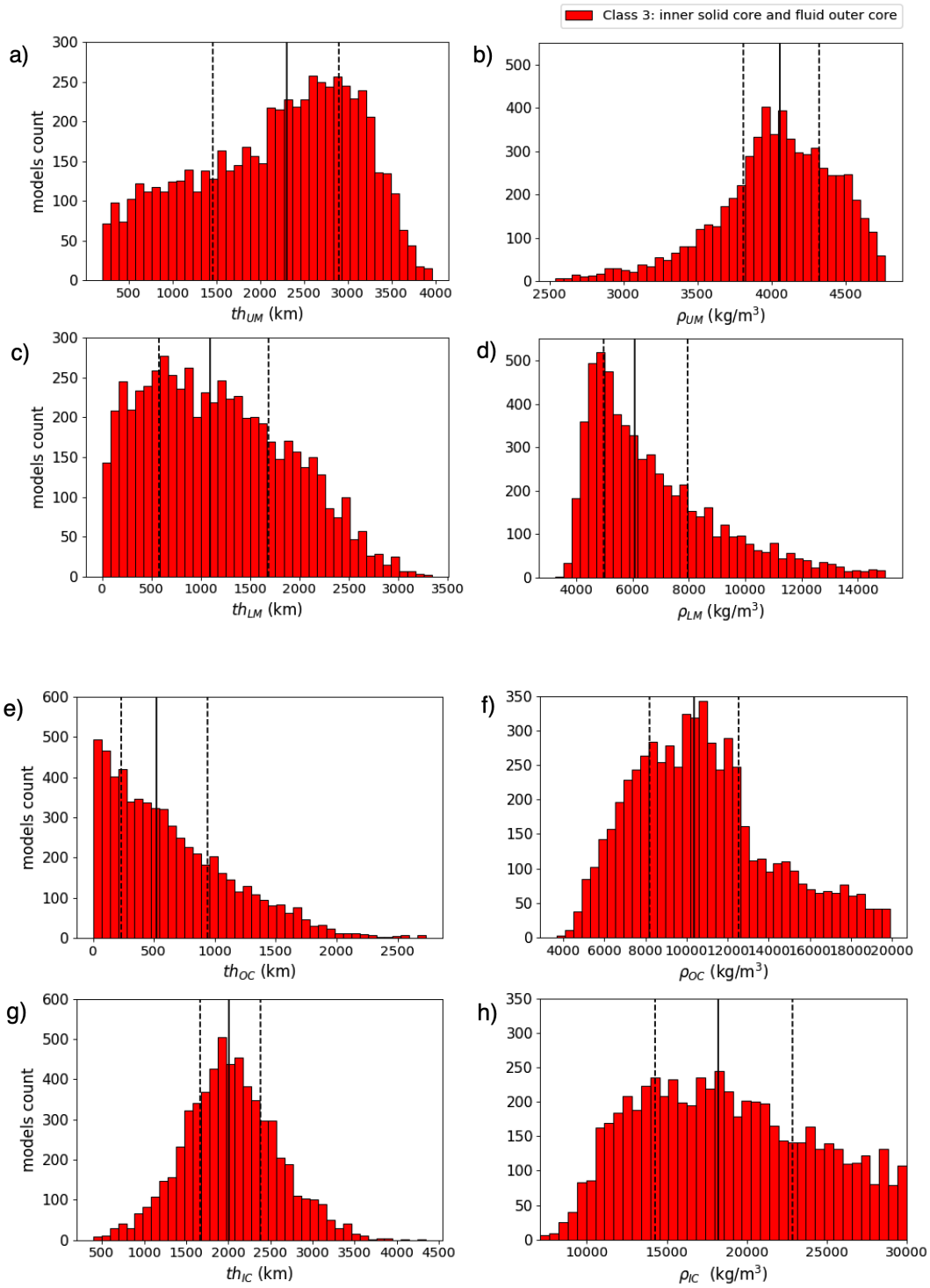

Figure A.5: 1D histograms for each layer (a), (c), (e) and (g) thickness and (b), (d), (f) and (h) density - without the density filters. Same representation for the solid and dashed lines as Fig. A.1.

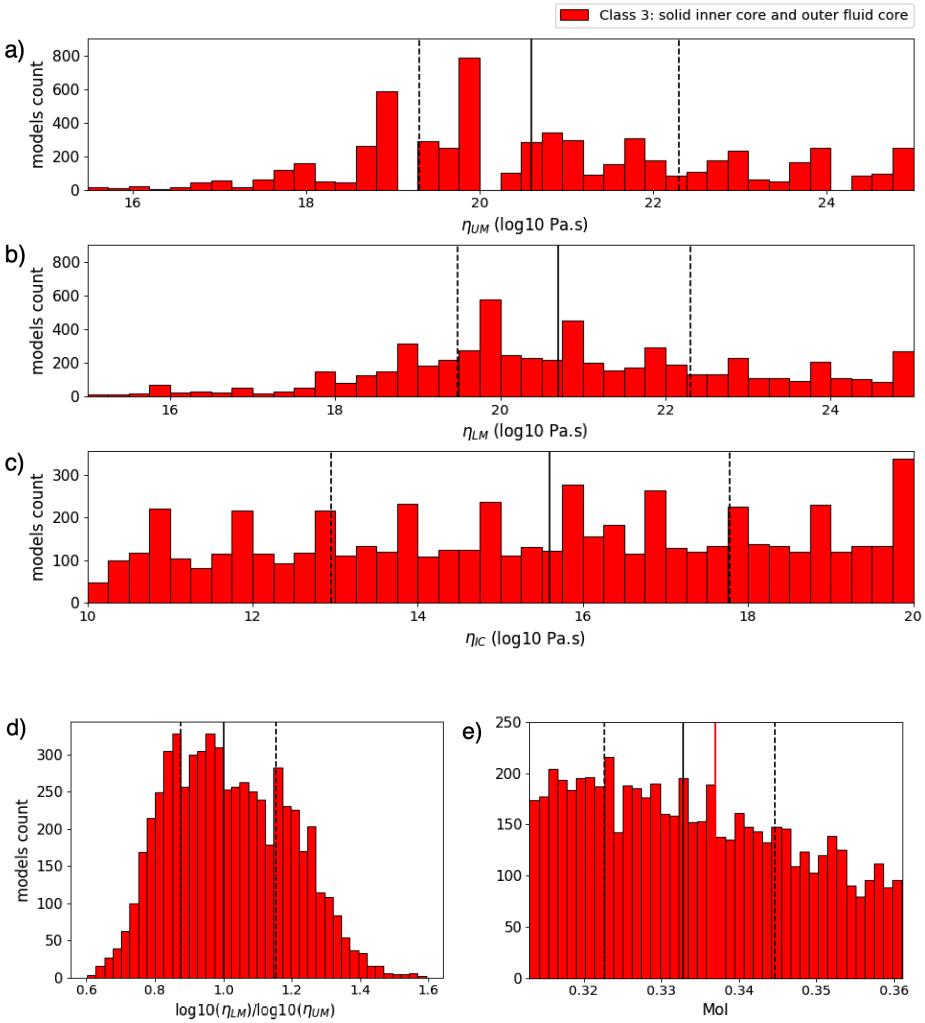

Figure A.6: 1D histograms for each layer (a), (b) and (c) viscosity, (d) the lower mantle and the upper mantle viscosity ratio and (e) MoI - without the density filters. Same representation for the solid and dashed lines as Fig. A.1.

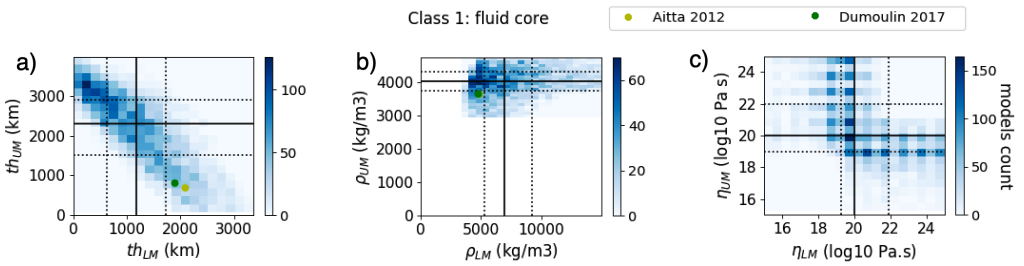

Figure A.7: 2D histograms for **Classes 1**: fluid core - without the density filters. Same representation for the solid and dashed lines as Fig. A.1.

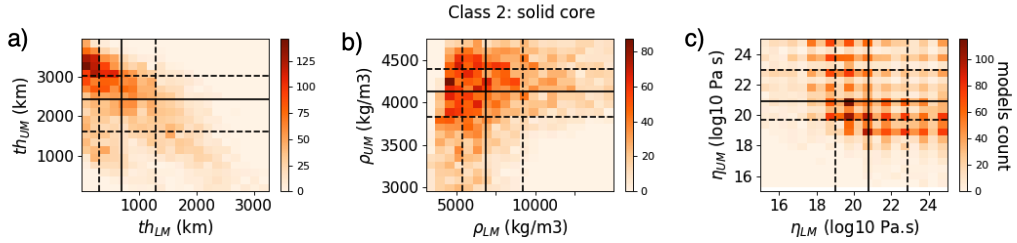

Figure A.8: 2D histograms for **Class 2**: solid core - without the density filters. Same representation for the solid and dashed lines as Fig. A.1.

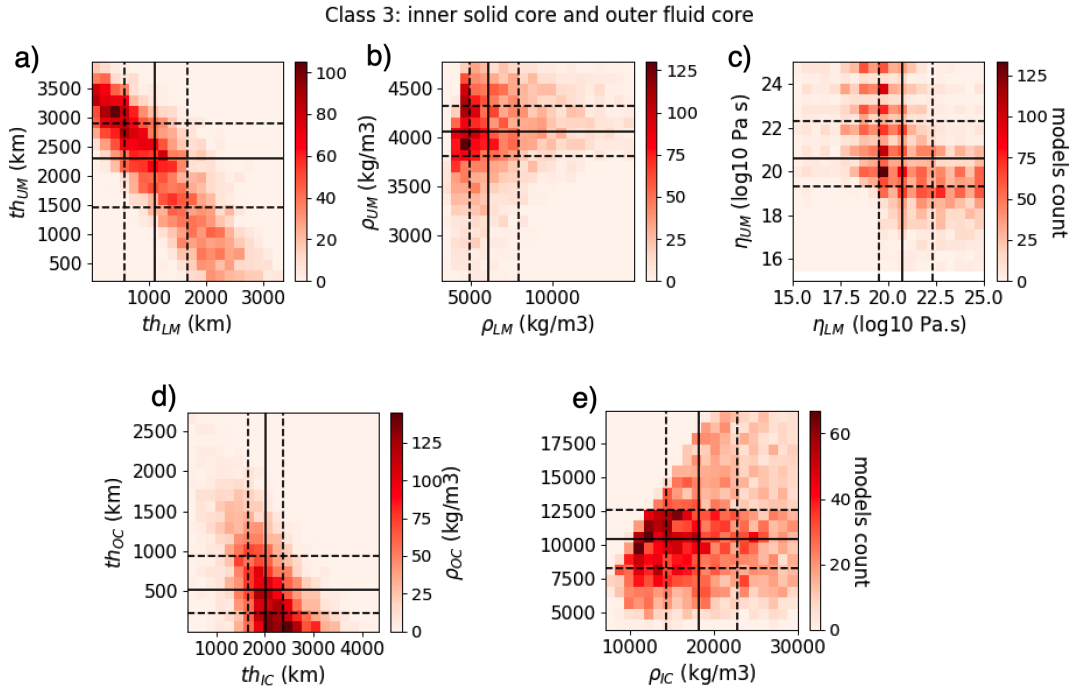

Figure A.9: 2D histograms for **Class 3**: solid inner core and fluid outer core - without the density filters. Same representation for the solid and dashed lines as Fig. A.1.